# Higher Order Corrections to Photon Production in Hadronic Collisions at the LHC

**Dissertation**

**zur**

**Erlangung der naturwissenschaftlichen Doktorwürde**
**(Dr. sc. nat.)**

**vorgelegt der**

**Mathematisch-naturwissenschaftlichen Fakultät**

**der**

**Universität Zürich**

**von**

**Marius Höfer**

**aus**

**Deutschland**

**Promotionskommission**
Prof. Dr. Thomas Gehrmann (Leitung der Dissertation)
Prof. Dr. Massimiliano Grazzini
Prof. Dr. Gino Isidori

Zürich, 2020

# Contents

# 1. Introduction

In his infamous 1905 work on the photoelectric effect [1] Einstein suggested that there is some real physical interpretation of the quanta of energy introduced by Planck in 1900 [2] in his heuristic approach to explaining the spectrum of black-body radiation. The idea of the photon as quantum of light was then later embedded in the quantum mechanical description of the interaction of light and matter [3, 4], which would eventually become quantum electrodynamics (QED). Due to the unification of QED with the weak theory and quantum chromodynamics (QCD) in the Standard Model (SM) of particle physics, the photon as mediator of one of the fundamental forces of nature plays an integral role in the description of high energy particle physics.

Since the photon and its interactions with matter have been extensively studied and are understood to a very large degree, it can help to both probe the less constraint parts of the SM and define the background in searches for physics beyond the SM (BSM physics or "new physics", NP).

Inclusive photon and photon-plus-jet production at a hadron collider for example provide a means to probe the parton distribution function (PDF) of the gluon in the proton already at the leading order (LO) in QCD perturbation theory [5–9] via the partonic process of QCD Compton scattering [10, 11]. At the same time the production of a single photon against a jet with high transverse momentum contributes to the background in missing transverse energy (MET) searches for NP [12]. Inclusive photon production has been investigated in early experiments at the ISR [13–15] and Sp$\bar{\text{p}}$S [16, 17] colliders, followed by precision studies at the Tevatron [18, 19] and by the ATLAS [20–24] and CMS [25–27] experiments at the LHC. Inclusive photon production at low transverse momenta has been investigated by the ALICE experiment [28]. The production of a photon pair has been looked at by ATLAS [29], while photon production in association with one jet has been measured at the Tevatron [30, 31] and by ATLAS [32–34] and CMS [26, 35–37]. Recently ATLAS [38] published a first photon-plus-dijet study.

The production of a photon pair played a crucial role in the discovery of the Higgs boson in 2012 [39, 40] and in the subsequent studies of its properties [41, 42]. Like single isolated photon production, diphoton production is conductive to the search for NP [43, 44], too.

It is clear that in order to fully exploit the high precision of the experiments we need theory predictions which are equally well positioned. As with the current mathematical tools it is not possible to find closed solutions for even the simplest of systems described by the SM, we usually resort to approximations formalised as a truncated power series expansion in the small coupling parameters of the theory. The most relevant expansion for hadronic collisions is that in the strong QCD coupling $\alpha_s$. The accuracy of a prediction can thus be increased, and its uncertainty decreased, by including formerly neglected higher order terms. This comes with

the compromise of vastly growing complexity, both in the mathematical formulae describing the process and in their behaviour in critical regions of the phase-space. To properly treat infrared (IR) divergences appearing in the intermediate steps of calculation, clever procedures have to be contrived [45–60]. Using those and recent developments in the calculation of loop amplitudes it was possible to provide predictions for many processes relevant for physics at the Large Hadron Collider (LHC) up to next-to-next-to leading order (NNLO) in QCD or even beyond. An overview can be found in the introductory chapter of the recent Les Houches report [61].

For the calculation presented in this thesis we adopt the antenna subtraction method [46, 48], which is implemented up to NNLO QCD in the parton-level event generator NNLOJET. It has been successfully used for the calculation of $e^+e^- \to 3j$ [62, 63], jet and dijet production in DIS [64, 65], $pp \to j + X$ [66], $pp \to 2j$ [67], $pp \to Z + j$ [68, 69], $pp \to W + j$ [70], $pp \to H + j$ [71], $pp \to VH$ [72], Higgs production in vector boson fusion (VBF) [73] and last but not least $pp \to \gamma + X/j$ [74], which will be the topic of a large part of this thesis.

Besides the computational complexity another difficulty arises related to the treatment of the photon itself, both in experiment and theory. In the environment of a hadronic collision we find a large number of photons which are produced during the hadronisation process and do not come from the actual hard scattering. As the former are usually accompanied by a large amount of hadronic radiation, looking for well isolated photons is a means to distinguish between their different origins. Unfortunately the fixed cone photon isolation prescription used in the experiment cannot be implemented in a theory calculation in a straightforward manner. Quark-photon collinear configurations in connection with the requirement of a resolved final state photon induce a dependence on the non-perturbative photon fragmentation functions. Their contribution can be suppressed by adopting the so called smooth cone isolation which vetoes any hadronic radiation directly collinear to the photon. Due to the finite resolution of the detector it is not possible to apply this kind of isolation in the experiment, resulting in a discrepancy between the prescriptions used in experiment and theory. In this work we make use of a novel isolation prescription, the hybrid cone isolation, which is supposed to reduce this discrepancy, still avoiding to induce a sensitivity on fragmentation. At the same time it allows us to study the dependence of the cross section on the experimental isolation parameters.

Increasing the statistics by exploring ever higher and higher orders in the strong coupling $\alpha_s$ might raise the question about the other interactions present in the SM. And indeed, a comparison of the numerical size of the strong and electromagnetic coupling constants, $\alpha_s$ and $\alpha$, suggest that the NLO QED corrections are of similar importance as NNLO QCD. Since $\alpha$ also relates to the strength of the weak interaction, the above statement equally holds for the full electroweak (EW) theory.

This thesis is organised as follows:

In Part I we set up the stage for the subsequent studies by briefly reviewing the SM in chapter 2, before focussing on the theory of QCD in the collider environment in chapter 3. We then discuss some important aspects for processes involving photons and introduce the notion of photon isolation in chapter 4. In chapter 5 we explain the program NNLOJET we are using to make our predictions.

Part II is then dedicated to studies of NNLO QCD corrections for inclusive photon and photon-plus-jet production. We begin by summarizing all the necessary ingredients in chapter 6. In chapter 7 we perform some studies on certain technical aspects of the photon isolation, before turning to the discussion of our phenomenology results and their comparison to data in chapter 8. We conclude part II in chapter 9.

The last part of the thesis, part III, is focussed towards the NLO EW corrections for diphoton and inclusive photon production. After investigating important aspects of EW corrections in chapter 10 and a detailed description of the corresponding implementation in NNLOJET in chapter 11, we first discuss their impact on diphoton production in chapter 12. We repeat the task for inclusive photon production in chapter 13, before we summarise and conclude part III in chapter 14.

# Part I.

# Theory prologue

# 2. The Standard Model of particle physics

This chapter serves to set the theoretical foundation from which we will proceed in order to calculate both NNLO QCD and NLO EW corrections to isolated photon production. We will summarise the key features of the SM and the problems one encounters when considering processes beyond tree level. Its application in the collider environment will be subject of chapter 3.

## 2.1. Symmetries and fields

The fundamental revelation which led to the inception of the Standard Model of particle physics was that the behaviour of elementary and composite particles we can observe follows a pattern dictated by symmetries inherent to nature. In an interplay of experimental evidences and theoretical deduction work one could eventually conclude that the underlying symmetry of all fundamental interactions between elementary particles is given by the group

$$G_{\mathrm{SM}} = SU(3)_C \otimes SU(2)_L \otimes U(1)_Y \,, \tag{2.1}$$

where the subscripts indicate to what properties of the elementary particles the individual groups correspond to. How a certain particle behaves is then determined by its transformation properties with respect to that group, which in turn are given by its respective group representation and quantum numbers. The quantum number relevant to $SU(3)_C$ is the colour charge or just colour, originally introduced by Greenberg [75], Han and Nambu [76] to explain the existence of hadrons seemingly violating the Pauli-exclusion principle. The part of the standard model describing the interactions of particles carrying colour charges is called quantum chromodynamics (QCD) and the fundamental force it is assigned to is the strong force. $SU(2)_L \otimes U(1)_Y$ on the other hand is the symmetry group of the electroweak interactions, unifying QED with the parity violating weak interaction. The subscript $Y$ describes the hypercharge of a particle, similar to the electromagnetic charge, to which it is related. The subscript $L$ indicates that only left-handed particles transform non-trivially under $SU(2)_L$.

Since the SM is a quantum field theory, all the particles are in fact quantum fields, and their interactions are described with the help of the SM Lagrangian $\mathcal{L}_{\mathrm{SM}}$, which respects all symmetries of $G_{\mathrm{SM}}$. In its classical (un-quantised) form, it can be separated into four pieces,

$$\mathcal{L}_{\mathrm{SM}}^{\mathrm{cl.}} = \mathcal{L}_{\mathrm{YM}} + \mathcal{L}_{\mathrm{M}} + \mathcal{L}_{\mathrm{H}} + \mathcal{L}_{\mathrm{Yuk}} \,. \tag{2.2}$$

The first piece is the Yang-Mills (YM) Lagrangian, describing the gauge fields of the theory, which are the mediators of the respective fundamental force. It can be written as

$$\mathcal{L}_{\text{YM}} = -\frac{1}{4} G^a_{\mu\nu} G^{a,\mu\nu} - \frac{1}{4} W^\alpha_{\mu\nu} W^{\alpha,\mu\nu} - \frac{1}{4} B_{\mu\nu} B^{\mu\nu} \,, \tag{2.3}$$

where the field-strength tensors are given by

$$G^a_{\mu\nu} = \partial_\mu G^a_\nu - \partial_\nu G^a_\mu - g_s f^{abc} G^b_\mu G^c_\nu \,, \qquad (SU(3)_C) \tag{2.4a}$$

$$W^\alpha_{\mu\nu} = \partial_\mu W^\alpha_\nu - \partial_\nu W^\alpha_\mu - g \varepsilon^{\alpha\beta\gamma} W^\beta_\mu G^\gamma_\nu \,, \qquad (SU(2)_L) \tag{2.4b}$$

$$B_{\mu\nu} = \partial_\mu B_\nu - \partial_\nu B_\mu \,. \qquad (U(1)_Y) \tag{2.4c}$$

The introduction of the gauge fields $G^a_\mu, W^\alpha_\mu$ and $B_\mu$ is direct consequence of promoting the global symmetry given by $G_{\text{SM}}$ to a local gauge symmetry. Demanding the symmetry to be respected in all space-time points requires us to promote the ordinary derivatives of the matter fields, $\partial_\mu \Phi$, to covariant derivatives, $D_\mu \Phi$ (see eq. (2.9)), so that infinitesimally separated points in space-time can be compared in a gauge invariant way. This connection is precisely given by the gauge fields. They transform under the adjoint representation of their respective group, hence there are eight gluons $G^{a=1,\dots,8}_\mu$, three weak gauge bosons $W^{\alpha=1,2,3}_\mu$ and a single hypercharge boson $B_\mu$. While $U(1)_Y$ is an abelian group, just like the $U(1)_{\text{em}}$ of QED, $SU(3)_C$ and $SU(2)_L$ are non-abelian, i.e. their generators do not commute. We therefore find the totally anti-symmetric tensors or structure constants $f^{abc}$ and $\varepsilon^{\alpha\beta\gamma}$ in above equations. Together with the commutator they define the Lie algebra of the corresponding group,

$$[T^a_{SU(3)}, T^b_{SU(3)}] = i f^{abc} T^c_{SU(3)} \,, \qquad [T^\alpha_{SU(2)}, T^\beta_{SU(2)}] = i \varepsilon^{\alpha\beta\gamma} T^\gamma_{SU(2)} \,. \tag{2.5}$$

In a given irreducible representation $R$ of the group the generators are normalised,

$$\text{Tr}\big[T^a_R T^b_R\big] = T_R \delta^{ab} \tag{2.6}$$

which holds for all groups $SU(N)$. The constants $T_R$ are called the Dynkin indices and their value is to some degree a matter of convention. In the literature one often finds the normalisation given for the fundamental representation, with the Dynkin index $T_F$ set either to $1/2$ or 1. From this the other $T_R$ follow.

The fermionic matter content of the theory is collected in $\mathcal{L}_{\text{M}}$,

$$\mathcal{L}_{\text{M}} = \bar{Q}_L (i \not{D}) Q_L + \bar{u}_R (i \not{D}) u_R + \bar{d}_R (i \not{D}) d_R + \bar{E}_L (i \not{D}) E_L + \bar{e}_R (i \not{D}) e_R \,, \tag{2.7}$$

where the first three terms describe the quarks and the last two the leptons and left-handed neutrinos. We explicitly distinguished between the left-handed and right-handed two component

Weyl spinors, indicated with the subscripts $L$ and $R$. This is necessary as all the left-handed fields come as doublets of the group $SU(2)_L$,

$$Q_L = \begin{pmatrix} u_L \\ d_L \end{pmatrix}, \qquad E_L = \begin{pmatrix} \nu_L \\ e_L \end{pmatrix}, \tag{2.8}$$

and the right handed fields are singlets. We ignore for a moment that there are actually three copies of each of the fields, called the (flavour) generations. Note that in the SM there are no right-handed neutrinos $\nu_R$. One can in principle write down a corresponding term, but since in this thesis we are interested in pure SM processes, we will not consider right handed neutrinos any further.

The covariant derivatives we find in above Lagrangian (2.7) are defined as

$$D_\mu = \partial_\mu - ig_s G^a_\mu T^a_{SU(3)} - igW^\alpha_\mu T^\alpha_{SU(2)} - ig' B_\mu T_{U(1)}\,, \tag{2.9}$$

where the generators of the groups are given in the irreducible representation of the field the derivative acts on. The generators of the $U(1)_Y$ are just numbers, the hypercharges, while those of the other two groups can be written as matrices. In the following we will denote the $SU(3)_C$ generators as $T^a$, which in the fundamental representation are proportional to the Gell-Mann matrices, the $SU(2)_L$ generators as $\tau^\alpha$, in the fundamental representation related to the Pauli matrices, and the hypercharge $T_{U(1)}$ as $Y$. While the $\partial_\mu$-terms describes the kinematical part of the fermion Lagrangian, the other terms define the coupling of a fermion to the gauge bosons of the respective group. A field which transforms trivially under a certain group $G$ does not couple to its force carrier, so that the corresponding term is then absent from the covariant derivative.

The matter Lagrangian (2.7) describes massless particles only, but form observation it is clear that most of the elementary particles in the SM have an intrinsic mass. With the setup of the theory so far this is a serious problem, as we cannot write down a mass term for those fields which fully respects the global symmetry, as left- and right-handed fermions transform differently under $SU(2)_L$. The solution to this dilemma is presented in form of the Higgs mechanism, which at the same time explains why at low energies we observe the electromagnetic force as described by QED instead of the full $SU(2)_L \otimes U(1)_Y$. The Higgs field is a complex scalar field $\phi$, which transforms as a doublet under $SU(2)_L$ and carries hypercharge $+\frac{1}{2}$. Its Lagrangian reads

$$\mathcal{L}_{\mathrm{H}} = (D_\mu \phi)^\dagger (D^\mu \phi) + V(\phi) \tag{2.10}$$

with the potential

$$V(\phi) = \mu^2(\phi^\dagger\phi) - \lambda\big(\phi^\dagger\phi\big)^2 \qquad \big(\mu^2, \lambda > 0\big) \tag{2.11}$$

such that it acquires a vacuum expectation value (vev) which partially breaks the $SU(2)_L \otimes U(1)_Y$ symmetry by choosing a specific direction in the abstract space spanned by the group generators,

$$\langle\phi\rangle = \frac{1}{\sqrt{2}}\begin{pmatrix} 0 \\ v \end{pmatrix}, \tag{2.12}$$

where $v = \sqrt{\mu^2/\lambda}$. The vev is still invariant under the phase shift

$$\langle\phi\rangle \to \exp\left(i\beta\left(\tau_3 + \frac{1}{2}\mathbb{1}\right)\right)\langle\phi\rangle\ , \tag{2.13}$$

where $\tau_3$ is the diagonal generator of $SU(2)$ in the fundamental representation. This residual gauge symmetry is precisely the $U(1)_{\text{em}}$ of QED, so that the electromagnetic charge (operator) is given by

$$Q = \tau_3 + Y\,. \tag{2.14}$$

The physical Higgs boson is given by expanding the field $\phi$ around its vev. Choosing the unitary gauge in which all pseudo Nambu-Goldstone bosons related to the symmetry breaking are absorbed into the longitudinal component of the gauge fields[1], we can write

$$\phi(x) = U(x)\frac{1}{\sqrt{2}}\begin{pmatrix}0\\ v + h(x)\end{pmatrix}, \tag{2.15}$$

where we made the space-time dependence explicit. Here $U(x)$ is a general $SU(2)$ rotation and $h(x)$ the physical Higgs boson.

Since the covariant derivative in the Lagrangian (2.10) couples the Higgs field to the gauge bosons $W_\mu^\alpha$ and $B_\mu$,

$$D_\mu\phi = \left(\partial_\mu - igW_\mu^\alpha\tau^\alpha - i\frac{1}{2}g'B_\mu\right)\phi\,, \tag{2.16}$$

the electroweak symmetry breaking (EWSB) mechanism has a non-trivial effect on them. Substituting the vev part of $\phi$ gives rise to mass terms for certain linear combination of the gauge fields, which we can identify as the $W^\pm$ and $Z$ bosons:

$$W_\mu^\pm = \frac{1}{2}\left(W_\mu^1 \mp W_\mu^2\right), \qquad m_W = \frac{v}{2}g\,, \tag{2.17a}$$

$$Z_\mu = \frac{1}{\sqrt{g^2+g'^2}}\left(gW_\mu^3 - g'B_\mu\right), \qquad m_Z = \frac{v}{2}\sqrt{g^2+g'^2}\,. \tag{2.17b}$$

The photon field $A_\mu$ is associated with the combination of generators aligned with the unbroken direction, defining $U(1)_{\text{em}}$,

$$A_\mu = \frac{1}{\sqrt{g^2+g'^2}}\left(gW_\mu^3 + g'B_\mu\right), \qquad m_A \equiv 0\,. \tag{2.18}$$

[1] Exactly how the Nambu-Goldstone bosons end up as the longitudinal components of the gauge fields and giving them the masses we define below can be understood by carefully examining the quantisation procedure of spontaneously broken gauge symmetries. See for example chapter 21 in [77].

Expressing the covariant derivative (2.16) in terms of these mass eigenstates, we can relate the couplings $g$ and $g'$ to the physical, i.e. measurable couplings $e$ and $G_F$,

$$e = \frac{gg'}{\sqrt{g^2 + g'^2}} = g \sin\theta_W \,, \qquad G_F = \frac{g^2}{4\sqrt{2}} m_W^{-2} \,, \tag{2.19}$$

where $G_F$ is the Fermi constant[2]. The weak mixing angle is defined as

$$\sin^2\theta_W = \frac{g'^2}{g^2 + g'^2} = 1 - \frac{m_W^2}{m_Z^2} \,. \tag{2.20}$$

We can now turn back to the initial problem of the fermion masses. The last part of the SM Lagrangian (2.2) is the Yukawa-Lagrangian,

$$\mathcal{L}_{\text{Yuk}} = -Y^d_{ij} \bar{Q}^i_L \phi d^j_R - Y^u_{ij} \bar{Q}^i_L \tilde{\phi} u^j_R - Y^e_{ij} \bar{L}^i_L \phi e^j_R + \text{h.c.} \,, \tag{2.21}$$

describing the Yukawa interaction between the scalar Higgs field and the fermionic matter fields. Here we defined the conjugate Higgs field $\tilde{\phi} = i\sigma_2 \phi^*$ and made the generation indices $i, j = 1, 2, 3$ explicit. The $Y_{ij}$ are the non-diagonal Yukawa matrices which induce a mixing of different generations. After the EWSB the Lagrangian reads

$$\mathcal{L}_{\text{Yuk}} = -\frac{v+h}{\sqrt{2}} Y^d_{ij} \bar{d}^i_L d^j_R - \frac{v+h}{\sqrt{2}} Y^u_{ij} \bar{u}^i_L u^j_R - \frac{v+h}{\sqrt{2}} Y^e_{ij} \bar{e}^i_L e^j_R + \text{h.c.} \,, \tag{2.22}$$

where we used the parametrisation given in eq. (2.15), in unitary gauge, i.e. $U(x) = \mathbb{1}$. We can identify couplings between the fermions and the physical Higgs boson $h$, but also bilinears proportional to $v$, which almost look like mass terms. However, since the $Y_{ij}$ are in general not diagonal, the above Lagrangian is not given in the mass basis, but rather in the so called flavour basis. One can go from one to the other by diagonalising the Yukawa matrices by means of a unitary rotation of the fermion fields,

$$u^i_L \to U^{ij}_{u,L} u^j_L \,, \qquad u^i_R \to U^{ij}_{u,R} u^j_R \,, \tag{2.23a}$$

$$d^i_L \to U^{ij}_{d,L} d^j_L \,, \qquad d^i_R \to U^{ij}_{d,R} d^j_R \,, \tag{2.23b}$$

$$e^i_L \to U^{ij}_{e,L} e^j_L \,, \qquad e^i_R \to U^{ij}_{e,R} e^j_R \,. \tag{2.23c}$$

The fermion masses are then given by

$$m_{f,i} = \frac{v}{\sqrt{2}} \hat{Y}^f_i \,, \tag{2.24}$$

where $f = u, d, e$ and the $\hat{Y}^f$ are the diagonalised versions of the Yukawa matrices $Y^f$. $i$ is the generation index again.

Of course, one has to rotate the fields consistently everywhere in the Lagrangian, thus one expects the transformation matrices to show up in the matter Lagrangian $\mathcal{L}_{\text{M}}$ (2.7). Interestingly in most terms the matrices exactly cancel (i.e. $U^\dagger U = \mathbb{1}$) except for the charged current

[2] Later we will denote it $G_\mu$ to stress the fact that is measured in muon decay.

interactions, i.e. in the couplings with the $W^\pm$ bosons, which mix up-type and down-type flavours, such that

$$\mathcal{L}_\mathrm{M} \supset \mathcal{L}_{qq'W} = \frac{e}{\sqrt{2}\sin\theta_W}\left[\bar{u}_L^i V_{ij} \not{W}^+ d_L^j + \bar{d}_L^i \left(V^\dagger\right)_{ij} \not{W}^- u_L^j\right], \tag{2.25}$$

where

$$V \coloneqq U_{u,L}^\dagger U_{d,L} \tag{2.26}$$

is the Cabibbo-Kobayashi-Maskawa (CKM) matrix [78, 79]. Note that as long as we do not include right-handed neutrinos, we can always freely rotate $\nu_L$ in flavour space. In particular we can choose a transformation such that it completely compensates the rotation of the charged leptons in eq. (2.23c). For the leptons the flavour basis is thus identical to the mass basis. On the other hand, it is well known from the observation of neutrino oscillations that neutrinos must have a non-vanishing mass. If one writes down a corresponding mass term[3], we find a CKM like mixing, which is parametrised in the Pontecorvo–Maki–Nakagawa–Sakata (PMNS) matrix [80].

## 2.2. Quantisation

At the very core of a given quantum field theory sits the generating functional, which encodes all correlation or Green's functions that in turn are linked to the S-matrix through the LSZ reduction formula. The generating functional of a scalar field theory for example is given by

$$Z[J] = \int \mathcal{D}\phi \exp\left[i \int \mathrm{d}^4x [\mathcal{L}(\phi) + J(x)\phi(x)]\right] \tag{2.27}$$

with the source field $J(x)$. Correlation functions are now obtained through derivatives with respect to the sources,

$$(-i)^n \frac{1}{Z[0]} \frac{\partial^n Z[J]}{\partial J(x_1)\dots\partial J(x_n)}\bigg|_{J=0} = \langle\Omega|T\{\hat{\phi}(x_1)\dots\hat{\phi}(x_n)\}|\Omega\rangle \,. \tag{2.28}$$

In case of the free theory we can explicitly solve the path integral, and for the free scalar field we find

$$Z_0[J] = Z_0[0] \exp\left[-\frac{1}{2}\int \mathrm{d}^4x\, \mathrm{d}^4y\, J(x) D(x-y) J(y)\right], \tag{2.29}$$

where $D(x)$ is the Fourier transform of the scalar propagator. Interactions between fields can best be described by separating the Lagrangian in its free part $\mathcal{L}_0$ and the interacting part $\mathcal{L}_I$, such that

$$\mathcal{L} = \mathcal{L}_0 + \mathcal{L}_I \,. \tag{2.30}$$

[3] There a various ways how to write down such terms and explain the very small masses the neutrinos must have. When introducing right handed neutrinos, we can have a Dirac but potentially also a Majorana mass term. Alternatively one can define higher dimensional operators using only left handed neutrinos.

If the strength of the interaction is parametrised with a small coupling $\lambda$, we can expand the corresponding exponential in the generating functional into a power series in that parameter, which gives rise to a perturbative expansion. Using the fact that the fields in $\mathcal{L}_I$ can be expressed as functional derivatives with respect to the sources, we can write the generating functional of the interacting theory as a series of an increasing number of derivatives acting on the free field functional $Z_0$, where the number of derivatives correlates with the power of $\lambda$. Suppose we can write $\mathcal{L}_I = \lambda V(\phi)$, we then find for the scalar field theory:

$$Z[J] = \left(1 + i\lambda\left[\int \mathrm{d}^4x\, V\left(\frac{\delta}{\delta J}\right)\right] + \frac{(i\lambda)^2}{2}\left[\int \mathrm{d}^4x V\left(\frac{\delta}{\delta J}\right)\right]\left[\int \mathrm{d}^4y V\left(\frac{\delta}{\delta J}\right)\right] + \mathcal{O}(\lambda^3)\right)\int Z_0[J]\,. \quad (2.31)$$

We can now derive all the Feynman rules of the theory by calculating the corresponding correlation functions as in eq. (2.28). This way of quantising the fields also works for fermions, as long as one accommodates for the fact that they are anti-commuting objects, which can readily be achieved by defining the sources as Grassmann-valued fields.

For gauge fields, however, we run into a problem when trying to adopt the same approach. Since by construction the Lagrangian is gauge invariant, there are in fact infinitely many equivalent configurations of the gauge fields, all connected by some gauge transformation, which will give the same physical result. Integrating over all these configurations in the path integral will therefore yield a divergent result. A solution to this problem has been presented by Faddeev and Popov. The idea is to introduce a gauge fixing term $G(A) = 0$, so that for each equivalent class of the gauge fields, also called the gauge orbit, we only integrate over a single representative member. The gauge fixing can be put into the path integral by exploiting the functional identity

$$1 = \int \mathcal{D}\alpha(x)\delta(G(A^\alpha))\det\left(\frac{\delta G(A^\alpha)}{\delta\alpha}\right). \quad (2.32)$$

Here $\alpha$ is the parameter of the gauge orbit given by a gauge transformation of the field $A^a_\mu$,

$$(A^\alpha)^a_\mu = A^a_\mu + \frac{1}{g}\partial_\mu\alpha^a + f^{abc}A^b_\mu\alpha^c\,. \quad (2.33)$$

The determinant can be written as a path integral over anti-commuting scalar fields $\eta$ and $\bar\eta$ transforming under the adjoint representation of the group,

$$\det\left(\frac{\delta G}{\delta\alpha}\right) = \int \mathcal{D}\bar\eta\mathcal{D}\eta\exp\left[i\int \mathrm{d}^4x\bar\eta\left(-\frac{\delta G}{\delta\alpha}\right)\eta\right], \quad (2.34)$$

such that eventually

$$Z[0] \sim \int \mathcal{D}A\mathcal{D}\bar\eta\mathcal{D}\eta\exp\left[i\int \mathrm{d}^4x\left(\mathcal{L}(A)\underbrace{-\frac{1}{2}(G)^2}_{\mathcal{L}_{\text{g.f.}}}\right) + \underbrace{\bar\eta\left(-\frac{\delta G}{\delta\alpha}\right)\eta}_{\mathcal{L}_{\text{ghost}}}\right], \quad (2.35)$$

where we dropped the source terms of the fields for brevity. The fields $\bar{\eta}$ and $\eta$ are unphysical, as they openly violate the spin-statistics theorem. This is, however, not a problem since they only appear as virtual particles and never as external physical states. Due to their strange nature they are also called ghosts. While in abelian gauge theories they completely decouple from the theory, in the non-abelian case they are needed to cancel the non-physical polarisation degrees of freedom of the gluon[4].

The precise form of the gauge fixing term $G$ depends on the application we have in mind, and a particular class of gauges which proved useful especially for spontaneously broken symmetries are the $R_\xi$ gauges, which are parametrised in terms of the parameter $\xi$. For general values of $\xi$ the pseudo Nambu-Goldstone bosons are not removed from the theory and one can see how they connect to the longitudinal polarisations of the gauge bosons. For practical applications the parameter $\xi$ can then be chosen such that the Nambu-Goldstone bosons vanish and the propagators of the massive gauge bosons take their well known form

$$\mu \underset{k}{\overset{\longleftarrow}{\sim\sim\sim\sim\sim}} \nu \; = \frac{-ig_{\mu\nu}}{k^2 - m^2} \,. \tag{2.36}$$

The full quantised SM Lagrangian then reads

$$\mathcal{L}_{\text{SM}} = \mathcal{L}_{\text{YM}} + \mathcal{L}_{\text{M}} + \mathcal{L}_{\text{H}} + \mathcal{L}_{\text{Yuk}} + \mathcal{L}_{\text{g.f.}} + \mathcal{L}_{\text{ghost}} \,, \tag{2.37}$$

where $\mathcal{L}_{\text{g.f.}}$ and $\mathcal{L}_{\text{ghost}}$ now contain the gauge fixing terms and ghost fields for all gauge fields present in the theory. Note that the explicit choice of a gauge by construction destroys the gauge invariance of the Lagrangian. It remains, however, invariant under a set of abstract global symmetry transformations, a property which goes by the name of BRST invariance. The BRST symmetries are a crucial element in the proof of renormalisability of non-abelian gauge theories.

## 2.3. Renormalisation, pole masses and the running coupling

When following the approach described in the previous section to find the Feynman diagrams contributing to a process at a given fixed order, we will encounter diagrams with closed loops. When translating such diagrams into their respective mathematical expressions, we have to integrate over the momenta of the virtual particles in the loop. In general the momentum integrals can be divergent for two reasons:

1. The momentum flowing in the loop becomes infinite. This type of behaviour is called an ultraviolet (UV) divergence.

2. The virtuality of one or more of the particles in the loop vanishes completely. If the particle is massless the corresponding propagator is then on-shell and diverges. We call this type of infinities the infrared (IR) divergences.

[4] If one chooses an axial gauge in which only the transverse polarisations propagate, the ghosts also decouple in non-abelian gauge theories.

While at first sight this looks like a huge blow to the validity and consistency of our theory, it is in fact not a problem and even expected to happen. We can cure the divergent behaviour of the loop diagrams by both reinterpreting the coefficients and quantities we used to write down the Lagrangian (for the UV divergences) and carefully defining our observables to include *all* contributions to a given order (for the IR divergences). The latter is a more process dependent task and will be the main topic of chapter 3. The treatment of the pathological UV behaviour can be done in a very general way at the level of the Lagrangian defining the theory and goes by the name of renormalisation, which is well established and the concepts of which we will briefly summarise in the following.

Before dealing with the divergences they have to be regularised in some form, so that we can investigate their behaviour as the parameter regulating the singularity tends to its critical value. Several regularisation prescriptions have been used in the past, the most intuitive being the introduction of some form of cut-off keeping the loop momentum away from the divergent regions. However, the problem with this is that it will in general violate a lot of the original symmetries of the theory, including Lorentz invariance. Most modern approaches to loop calculations therefore adopt a more technical approach, called dimensional regularisation. The crucial observation is that the loop integrals diverge when calculated in the ordinary four space time dimensions, but converge if instead we use a different dimensionality $d \neq 4$. Keeping the dimensions of space time arbitrary during the evaluation of the integrals and defining $d = 4 - 2\epsilon$ will yield results in form of a Laurent series in $\epsilon$ around $\epsilon = 0$. How badly divergent a given loop integral is, is then parametrised by the inverse powers of $\epsilon$ and the corresponding coefficients. As the action $S = \int \mathrm{d}^d x \, \mathcal{L}$ should remain dimensionless, we choose to assign a mass dimension to the coupling constants, which can be done by introducing the regularisation scale $\mu$ and defining $g \to g\mu^\epsilon$. The main advantage of dimensional regularisation, besides the conservation of gauge- and Lorentz-invariance, is that it can treat both UV and IR divergences, as the parameter $\epsilon$ is arbitrary at all stages of the calculation and only send to 0 at the very end. While in principle one can trace the poles in $\epsilon$ back to their respective origin by defining an $\epsilon_{\mathrm{UV}}$ and and $\epsilon_{\mathrm{IR}}$, one often just drops the subscripts and describes the singularity structure using a single parameter.

The technical execution of the procedure has many subtleties related to different choices of how to treat inherently four dimensional objects such as the polarisation vectors of physical states or quantities like $\gamma^5$, leading to different regularisation schemes. Usually one uses the scheme which simplifies the calculation at hand the most. In the end one can use general conversion formulae to relate calculations performed in different schemes. We will use this fact when deriving the matrix elements for inclusive photon and photon-plus-jet production in appendix B.

Once we know the divergent behaviour of the loop diagrams appearing at a given order in the perturbative expansion of our theory, we can try to remove the UV poles entirely by absorbing them into a redefinition of the individual quantities in the Lagrangian. This approach is justified by the fact that the bare couplings, masses and fields with which we constructed the Lagrangian must not necessarily coincide with the corresponding measured quantities. The latter contain

all the effects of all the contributions we had to neglect due to the inability to solve the theory exactly. Thus we redefine all fields, couplings and masses. Symbolically

$$\Psi_0 = Z_\Psi \Psi_R \,, \tag{2.38a}$$

$$g_0 = Z_g g_R \,, \tag{2.38b}$$

$$m_0 = Z_m m_R \,, \tag{2.38c}$$

where the subscript 0 indicates the bare quantities which we used to define the Lagrangian and the renormalised quantities receive a label $R$. In a next step we rewrite the renormalisation factors as $Z_i = 1 + \delta_i$, such that we can split the bare Lagrangian into two pieces,

$$\mathcal{L}_0 = \mathcal{L}_R + \mathcal{L}_{\text{c.t.}} \,, \tag{2.39}$$

where the renormalised Lagrangian $\mathcal{L}_R$ is given by the bare Lagrangian with all quantities replaced by their renormalised version. $\mathcal{L}_{\text{c.t.}}$ is the counterterm Lagrangian, collecting the terms which come with the counterterms $\delta_i$. Just like for any other Lagrangian we can derive corresponding Feynman rules which contain the $\delta_i$ as interaction terms. As we want to identify the quantities in $\mathcal{L}_R$ with finite, physical quantities, we demand that the correlation functions derived with the renormalised Feynman rules are all finite, which we can then use to fix the counterterms $\delta_i$. Based on the relation in eq. (2.39) we can express the renormalised correlation functions in terms of bare diagrams, which exhibit explicit singularities, and counterterm diagrams. We can then define the quantities $\delta_i$ precisely such, that they cancel or subtract the UV poles and render the total result finite, up to the remaining IR divergences[5]. Since the $\delta_i$ can be formally expanded in the couplings, we can achieve a cancellation order by order in perturbation theory. The statement that a finite number of redefinitions we can perform in a given Lagrangian is sufficient to subtract all UV divergences is a highly non-trivial statement, and in general not true. If it is sufficient, then the theory is called renormalisable[6]. Renormalisability is a crucial feature for a theory to have, as it means that we can completely determine all its parameters with a finite number of measurements. One might worry that any spontaneous symmetry breaking like we have it in the SM could spoil the counterterm approach, but one can prove that this is not the case. The renormalisability of the full SM has been shown in a series of papers in the early seventies [82–87].

There is some freedom in how we can actually fix the counterterms $\delta_i$. As long as they subtract the UV pole of the loop integrals, we can add to this subtraction whatever finite piece we want. Choosing a certain subtraction scheme amounts to defining a certain set of renormalisation conditions for the counterterms. In the minimal subtraction (MS) scheme for example we subtract the poles only, and no finite terms are absorbed. A more widely used variant is the modified minimal subtraction ($\overline{\text{MS}}$ ) scheme, which in addition to the poles also absorbs the in loop calculations ubiquitous factors $\ln(4\pi)$ and $\gamma_E$, the Euler-Mascheroni constant. Contrary

[5] We postpone the discussion about how those can be handled to the next chapter, in particular section 3.3.

[6] Confusingly this does not mean that non-renormalisable theories are cannot be renormalised, it is just that we have to include all possible additional terms to the Lagrangian which respect the underlying symmetries. See for example chapter 21 in [81].

to what we initially said, in those schemes the relation between the renormalised masses and couplings and their measured, physical counterparts is not obvious at all. The schemes are still extremely useful, because they simplify the calculation of loop amplitudes considerably.

More physical schemes which are also widely used are the on-shell (OS) scheme and variations thereof for the renormalisation of the masses. The premise is that the renormalised mass of particle should coincide with the pole of the corresponding renormalised propagator

$$iG_R(p^2) = \frac{i}{p^2 - m_R^2 + \Sigma_R(p^2)}\,, \tag{2.40}$$

here for example given for a scalar particle. $\Sigma_R(p^2)$ is the sum of all 1PI self-energy graphs derived in renormalised perturbation theory, i.e. with the counterterm insertions. The pole mass $m_P$ is now defined such that $iG_R(p^2)$ has a single pole at $p^2 = m_P^2$ with residue $i$, implying

$$\Sigma_R(m_P^2) = m_R^2 - m_P^2\,, \qquad \frac{\mathrm{d}}{\mathrm{d}p^2}\Sigma_R(p^2)\bigg|_{p^2=m_P^2} = 0\,. \tag{2.41}$$

Demanding $m_R = m_P$ we can expand $\Sigma_R$ to the desired order in the coupling and from this derive the renormalisation conditions for the counterterms it contains. This approach ensures that the renormalised mass is fixed at all orders in perturbation theory and by construction does not receive any radiative corrections. The situation becomes a little bit more complicated if we consider unstable particles with a finite decay width $\Gamma$. In this case the self-energy $\Sigma_R(p^2)$ obtains a non-vanishing imaginary part,

$$\mathrm{Im}\,\Sigma_R(m_P^2) = m_P\Gamma \qquad \text{for } \Gamma \ll m_P\,, \tag{2.42}$$

which directly follows from the optical theorem. But then the pole mass defined by eqs. (2.41) obviously becomes complex, obstructing its direct interpretation as the physical mass of the particle. We can circumvent this problem by defining the on-shell mass $m_{os}$, or sometimes called the Breit-Wigner mass, as the real part of the pole of the propagator, which amounts to modifying the first of eqs. (2.41) to

$$\mathrm{Re}\,\Sigma_R(m_{\mathrm{os}}^2) = m_R^2 - m_{\mathrm{os}}^2\,. \tag{2.43}$$

$m_{\mathrm{os}}$ can then be directly related to its corresponding measured value. An alternative approach is to write the complex pole $\mu_P$ of the propagator as

$$\mu_P^2 = m_{\mathrm{pole}}^2 - i m_{\mathrm{pole}}\Gamma_{\mathrm{pole}}\,. \tag{2.44}$$

Eqs. (2.41) then holds for $m_P \to \mu_P$. Often $m_{\mathrm{pole}}$ is referred to as *the* pole mass. Note that the distinction between $m_{\mathrm{os}}$, $m_{\mathrm{pole}}$ and our original $m_P$ is only relevant if $\Gamma \neq 0$, i.e. if we are

dealing with unstable particles. One can define simple conversion formulae between the OS mass and width $m_{\text{os}}$, $\Gamma_{\text{os}}$ and the pole mass and width $m_{\text{pole}}$, $\Gamma_{\text{pole}}$ [88, 89],

$$m_{\text{pole}} = \frac{m_{\text{os}}}{\sqrt{1 + (\Gamma_{\text{os}}/m_{\text{os}})^2}}\,, \qquad \Gamma_{\text{pole}} = \frac{\Gamma_{\text{os}}}{\sqrt{1 + (\Gamma_{\text{os}}/m_{\text{os}})^2}}\,. \tag{2.45}$$

Numerically the difference is small but not negligible. We will encounter the conversion given above in part III of the thesis when we discuss the choice of input parameters in EW calculations.

Besides the masses also the coupling constants, in particular the electromagnetic coupling $e = \sqrt{4\pi\alpha}$, can be related to their corresponding measured values. Again, there is some freedom to this approach. We will discuss possible EW renormalisation schemes directly affecting the numerical value of $\alpha$ in our calculations in more detail in section 10.5.2. QCD and its coupling constant $g_s = \sqrt{4\pi\alpha_s}$ are conventionally renormalised in the $\overline{\text{MS}}$ scheme.

A very important observation is that the quantities in the renormalised Lagrangian now depend on the unphysical scale $\mu$ we introduced when calculating loop integrals in dimensional regularisation in order to keep the renormalised couplings dimensionless. $\mu$ is often understood as the scale at which we renormalise the theory, therefore it is also called the renormalisation scale. Since the original bare parameters and fields must be independent of $\mu$ and we know how the renormalised quantities are related to them (eqs. (2.38)), we can write down differential equations describing the dependence. Take a generic coupling for example,

$$0 \overset{!}{=} \mu \frac{\mathrm{d}}{\mathrm{d}\mu} g_0 = \mu \frac{\mathrm{d}}{\mathrm{d}\mu} (Z_g g_R \mu^\epsilon)\,. \tag{2.46}$$

We know that the renormalisation factor $Z_g$ has a formal expansion in $g_R$,

$$Z_g = 1 + \delta_g^{(1)} + \delta_g^{(2)} + \dots \tag{2.47}$$

where $\delta_g^{(l)}$ is the $l$-loop counterterm for which $\delta_g^{(l)} \sim \mathcal{O}\big(g_R^{2l}\big)$. Moreover, the counterterms only implicitly depend on $\mu$ through the coupling $g_R$,

$$\mu \frac{\mathrm{d}}{\mathrm{d}\mu} \delta_g^{(l)} = \mu \frac{\mathrm{d}g_R}{\mathrm{d}\mu} \frac{\partial}{\partial g_R} \delta_g^{(l)}\,. \tag{2.48}$$

Using all this information we can expand the r.h.s. of eq. (2.46) in $g_R$ and thus derive a differential equation for the renormalised coupling, which up to one-loop order reads

$$\beta(g_R) = \mu \frac{\mathrm{d}}{\mathrm{d}\mu} g_R = -\epsilon g_R + \epsilon g_R^2 \frac{\partial}{\partial g_R} \delta_g^1\,. \tag{2.49}$$

Here we defined the so called beta-function $\beta(g_R)$. Note that the $\epsilon$ in front of the second term will cancel against the explicit $1/\epsilon$ pole in $\delta_g^{(1)}$. Thus, in the limit $\epsilon \to 0$ only the coefficient of the pole contributes. Consequently to one-loop order the beta-function is subtraction scheme

independent. We often define the beta-function in terms of $\alpha_R = g_R^2/(4\pi)^2$ instead, so that in its formal expansion in $\alpha$ it reads

$$\beta(\alpha) = \mu \frac{\mathrm{d}}{\mathrm{d}\mu}\alpha = -\epsilon\alpha - 2\alpha\left[\left(\frac{\alpha}{4\pi}\right)\beta_0 + \left(\frac{\alpha}{4\pi}\right)^2\beta_1 + \mathcal{O}(\alpha^3)\right]. \tag{2.50}$$

This equation can be solved (setting $\epsilon = 0$) and at one-loop order we find the leading dependence of the coupling on the scale $\mu$,

$$\alpha(\mu) = \frac{\alpha(\mu_0)}{1 + \frac{\beta_0}{2\pi}\alpha(\mu_0)\ln\frac{\mu}{\mu_0}} = \frac{2\pi}{\beta_0}\frac{1}{\ln\frac{\mu}{\Lambda}}, \tag{2.51}$$

where both the value of the coupling $\alpha(\mu_0)$ at some reference scale $\mu_0$ and the parameter $\Lambda$ as a boundary condition can be fixed by relating $\alpha(\mu)$ to some experimental measurement. While the first part of the equation describes the evolution of the coupling starting from some predefined value $\alpha(\mu_0)$, the second part is useful to find the energy scales at which we expect the perturbative expansion to be no longer valid, i.e. $\alpha \sim \mathcal{O}(1)$. The scale $\Lambda$ at which $\alpha$ diverges is called the Landau pole of the theory. Note that the two equations (2.50) and (2.51) give us valuable information on the behaviour of the coupling in asymptotic limits. Depending on the sign of the leading term $\beta_0$ the coupling either increases or decreases with growing $\mu$. This in turn determines whether the theory in form of a perturbative expansion is valid above or below the Landau pole $\Lambda$. For QCD and QED we find [77, 81]

$$\beta_0^{\mathrm{QED}} = -\frac{4}{3}, \qquad \Lambda_{\mathrm{QED}} \approx 10^{277}\ \mathrm{GeV}, \tag{2.52a}$$

$$\beta_0^{\mathrm{QCD}} = \frac{11}{3}N - \frac{2}{3}N_F, \qquad \Lambda_{\mathrm{QCD}} \approx 200\ \mathrm{GeV}, \tag{2.52b}$$

where the precise value of $\Lambda$ depends on the renormalisation conditions. $\Lambda_{\mathrm{QED}}$ is an incredibly large value, far beyond the Planck scale. QED as a perturbation theory is therefore valid for all reasonable energy scales we can encounter in our experiments, with its coupling (very slowly) growing with the energy. For QCD we observe quite the opposite, at least as long $\frac{11}{2}N > N_F$. The coupling diverges for energy scales as low as a few hundred MeV, and the theory loses its perturbative character for $\mu \lesssim 1$ GeV. For large energies instead, the coupling decreases so that in the limit of infinite energy QCD is free of any interactions, a property which goes by the name of asymptotic freedom. This has some important consequences; while in nature we will never observe free quarks and gluons, because the strongly interacting soft physics will always confine them into bound states, we can treat quarks as free particles if our experiments just provide enough energy. We will refine this statement at the beginning of the next chapter.

# 3. QCD in the collider environment

Now that we set up the theoretical framework of high energy particle physics, we have to make the connection to the calculation of actual collider cross sections we can compare to experimental data. We will begin by making a basic assumption about how the elementary states we use in our calculations relate to measurable, observable quantities and how we can organise ourselves based on the perturbative expansion (section 3.1). We then show how we can use the underlying symmetry of the theory to simplify expressions (section 3.2) and discuss the universal behaviour of these expressions in the IR (section 3.3). With our new knowledge we can then refine the initial approach (section 3.4), before discussing how the treatment of IR singular configurations can be dealt with in an actual calculation by introducing the antenna subtraction formalism (section 3.5). At last the notion of jets is briefly reviewed (section 3.6).

## 3.1. The naïve parton model

The asymptotic freedom of QCD enables us to describe high energy interactions using a perturbative expansion in the coupling, but the states we eventually observe and measure in the experiment are hadrons, i.e. QCD bound states as determined by the low energy, non-perturbative regime of the theory. At the same time the particles we collide at a hadron collider are, as the name suggests, hadrons and not free quarks and gluons. A very important and non-trivial feature of QCD therefore is that the long and short distance (i.e. low and high energy) interactions factorise[1] [90]: We can describe the scattering of two highly energetic hadrons into some partonic final state using perturbative QCD, and then obtain the full result by weighting the individual partonic interactions with the probability to find the corresponding particles within the colliding hadrons[2],

$$\mathrm{d}\sigma_{ab} = \sum_{ij} \int \frac{\mathrm{d}x_1}{x_1} \frac{\mathrm{d}x_2}{x_2} f^0_{i/a}(x_1) f^0_{j/b}(x_2) \mathrm{d}\hat{\sigma}_{ij}(x_1, x_2)\,. \tag{3.1}$$

Here $\mathrm{d}\sigma_{ab}$ is the differential (in some arbitrary observables) cross section of the scattering of two hadrons $a$ and $b$ and $\mathrm{d}\hat{\sigma}_{ij}$ the partonic cross section for the scattering of partons $i$ and $j$. The number density of a parton $i$ within hadron $a$, carrying the momentum $p_i = x p_a$ with $x \in [0, 1]$, is given by the parton distribution function (PDF) $f^0_{i/a}(x)$. In QCD $i, j$ can correspond to all possible quark and ant-quark flavours as well as the gluon. Since we are focussing on $pp$-colliders,

[1] Unfortunately factorisation has not been proven universally for arbitrary processes, yet. Its success in applications, however, is regarded as a sign for its validity.

[2] This equation actually holds true up to terms of $\mathcal{O}(\Lambda_{\mathrm{QCD}}/Q)$ for some characteristic energy scale $Q$ of the process. This precisely reflects the fact that QCD is only really perturbative for $Q \gg \Lambda_{\mathrm{QCD}}$.

we will drop the subscripts $a, b$ in the following. Eq. (3.1) can be regarded as the master formula for the calculation of hadronic scattering cross sections.

The partonic final states of the process described with eq. (3.1) can be matched onto the hadronic final state using parton showers and hadronisation models [9, 91]. For the purpose of this thesis jet-algorithms, see section 3.6, will be used to make the connection between our results and experimental data, thus we will not discuss this topic any further.

The partonic cross section can be calculated in perturbation theory, i.e. it can be written as a formal expansion in the strong coupling constant,

$$\mathrm{d}\hat{\sigma}_{ij} = \mathrm{d}\hat{\sigma}_{ij}^{LO} + \tilde{\alpha}_s \mathrm{d}\hat{\sigma}_{ij}^{NLO} + \tilde{\alpha}_s^2 \mathrm{d}\hat{\sigma}_{ij}^{NNLO} + \mathcal{O}\left(\tilde{\alpha}_s^3\right), \tag{3.2}$$

where we defined $\tilde{\alpha}_s = \alpha_s/(2\pi)$. Here $\mathrm{d}\hat{\sigma}_{ij}^{LO}$, $\mathrm{d}\hat{\sigma}_{ij}^{NLO}$, $\mathrm{d}\hat{\sigma}_{ij}^{NNLO}$ describe the leading order (LO), the next-to-leading order (NLO) and the next-to-next-to leading order (NNLO) contributions to the cross section. In the above formula the powers in $\alpha_s$ have to be understood relative to the leading order contribution, which is defined as, for the process $i + j \to n$ final state particles,

$$\mathrm{d}\hat{\sigma}_{ij\to n}^{LO} = \mathcal{N}^B \int \mathrm{d}\Phi_n \frac{1}{S_n} M_n^B J_n^{(m)} \equiv \int_n \mathrm{d}\hat{\sigma}_{ij\to n}^B . \tag{3.3}$$

Here $\mathcal{N}^B$ is a normalisation factor, $\mathrm{d}\Phi_n$ the Born phase-space, $S_n$ a symmetry factor depending on the external states of the Born matrix element $M_n^B$. $J_n^{(m)}$ is the so called jet function, which describes how $m$ jets can be constructed out of the $n$ final state partons. We will come back to the definition of a jet in section 3.6. In fact $J_n^{(m)}$ should be further understood as measurement function that incorporates any kind of cuts and selection rules to the partonic event.

The NLO and NNLO terms can be written in the same way, as long as we consider that there now are contributions from real (R) and virtual (V) corrections,

$$\mathrm{d}\hat{\sigma}_{ij\to n}^{NLO} = \int_{n+1} \mathrm{d}\hat{\sigma}_{ij\to n+1}^{R} + \int_n \mathrm{d}\hat{\sigma}_{ij\to n}^{V} , \tag{3.4}$$

$$\mathrm{d}\hat{\sigma}_{ij\to n}^{NNLO} = \int_{n+2} \mathrm{d}\hat{\sigma}_{ij\to n+2}^{RR} + \int_{n+1} \mathrm{d}\hat{\sigma}_{ij\to n+1}^{RV} + \int_n \mathrm{d}\hat{\sigma}_{ij\to n}^{VV} . \tag{3.5}$$

Here RR denotes the double-real, RV the real-virtual and VV the double virtual corrections. It is not hard to see that the corresponding matrix elements in general are very complicated objects. It is thus important to study their structure and when possible break them apart into smaller pieces which are easier to handle. A very useful tool in this regard is the colour decomposition of the un-squared amplitudes, as we shall see in the next section.

## 3.2. Colour decomposition of matrix elements

The matrix element given as the square of the scattering amplitude yields the probability density to observe a specific set of external states in a certain infinitesimal region of the phase-space. As a whole, scattering amplitudes are complicated objects depending on the kinematical configuration given by the external states and governed by the symmetry of the underlying theory. However,

one can make use of that symmetry to split the amplitudes into smaller gauge invariant parts, which on their own are much easier to handle. For hadron collisions the relevant symmetry is provided by QCD and its gauge group $SU(3)$. We can make use of the fact that we can factorise a given amplitude in a part describing its dependence on the kinematics, and its QCD colour structure,

$$\mathcal{A}(c, p, \lambda) = n \sum_j \mathcal{C}_j(c) \cdot \mathcal{A}_j(p, \lambda) \,, \tag{3.6}$$

where $\mathcal{A}(c, p, \lambda)$ is the full amplitude for a given kinematics $p$ with the external states in the helicity configuration $\lambda$. $c$ is its colour structure which for the subamplitudes factorises into the object $\mathcal{C}_j(c)$. $n$ collects all the coupling constants and other overall factors. The $\mathcal{A}_j(p, \lambda)$ are called partial amplitudes. They are colour-ordered objects, which means coloured particles, i.e. quarks and gluons, have a fixed ordering within the amplitude. This is particularly helpful when investigating the IR singularity structure of the amplitude and related factorisation properties, as IR limits of colour-ordered amplitudes only occur between particles which are colour connected, i.e. adjacent in the colour ordering [92, 93]. Tree level partial amplitudes are always fully colour stripped, i.e. they do not explicitly depend on the number of colours $N$. For loop amplitudes that is in general not the case, and one can decompose the partial amplitudes further into gauge invariant primitive amplitudes [94], which come with different powers of $1/N$, depending on the colour flow within the loop. The primitive amplitudes are fully colour stripped.

The colour coefficients $\mathcal{C}_j(c)$ are constructed by factoring out all the colour structures from the Feynman rules, that is $T^a_{ij}$ from quark-gluon vertices, $f^{abc}$ from gluon self-interactions, $\delta^{ab}$ for gluon propagators and $\delta_{ij}$ for quark propagators. All diagrams which have the same colour coefficient are then combined into one partial amplitude.

Using the definition of the Lie algebra (2.5) and the normalisation of the generators (2.6) the structure constants can be rewritten as

$$f^{abc} = -\frac{i}{T_F} \operatorname{Tr}\big[\big[T^a, T^b\big] T^c\big] \,. \tag{3.7}$$

Adjoint indices can be contracted using the Fierz identity

$$T^a_{ij} T^a_{kl} = T_F \left( \delta_{il}\delta_{jk} - \frac{1}{N} \delta_{ij}\delta_{kl} \right) , \tag{3.8}$$

from which we can derive some basic rules which help us to simplify the $\mathcal{C}_j(c)$. For later convenience we introduce a shorthand notation for the colour strings and traces,

$$(T^{a_1} T^{a_2} \dots T^{a_n})_{ij} \equiv (a_1 a_2 \dots a_n)_{ij} \,, \tag{3.9a}$$

$$\operatorname{Tr}[T^{a_1} T^{a_2} \dots T^{a_n}] \equiv [a_1 a_2 \dots a_n] \,. \tag{3.9b}$$

Using that the generators are traceless, $[a] = 0$, and $\delta_{ii} = [\mathbb{1}] = N$, we find

$$[aa] = NC_F\,, \tag{3.10a}$$

$$T_F^{-1}[aAaB] = [A][B] - \frac{1}{N}[AB]\,, \tag{3.10b}$$

$$T_F^{-1}[aA][aB] = [AB] - \frac{1}{N}[A][B]\,, \tag{3.10c}$$

$$T_F^{-1}(AaB)_{ij}[aC] = (ACB)_{ij} - \frac{1}{N}(AB)_{ij}[C]\,, \tag{3.10d}$$

$$T_F^{-1}(AaB)_{ij}(CaD)_{kl} = (AD)_{il}(CB)_{kj} - \frac{1}{N}(AB)_{ij}(CD)_{kl} \tag{3.10e}$$

for some $SU(N)$ matrices (i.e. products of generators) $A, B, C$. Here $C_F = T_F(N^2-1)/N$ is the Casimir operator in the fundamental representation[3]. With the help of those relations and the explicit replacement of the structure constants (3.7) the $C_j(c)$ can be written purely in terms of strings and traces of the generators $T^a_{ij}$. They carry adjoint and (anti-)fundamental indices of the group according to the external states of the amplitude. The $n$-gluon tree level amplitude for example can be decomposed as [92, 93]

$$\mathcal{A}_{ng}(c, p, \lambda) = g^{n-2} \sum_{\sigma \in S_n/\mathbb{Z}_n} [\sigma(1)\dots\sigma(n)] a_{ng}(\sigma(p), \lambda)\,, \tag{3.11}$$

with the partial amplitudes $a_{ng}(p, \lambda)$. The $n$ generators in the trace $[1\dots n]$ precisely correlate with the $n$ external gluons. The sum runs over all the non-cyclic permutations $\sigma$ of the gluons, since the trace is invariant under cyclic permutations. When we have an additional external quark pair, the tree level colour decomposition reads [94, 95]:

$$\mathcal{A}_{2qng}(c, p, \lambda) = g^n \sum_{\sigma \in S_n} (\sigma(1)\dots\sigma(n))_{q\bar{q}} b_{2qng}(\sigma(p), \lambda)\,, \tag{3.12}$$

with the partial amplitudes $b_{2qng}(p, \lambda)$. The $q\bar{q}$ indices of the string reflect the colour flow through the external quark legs.

When we square the amplitude to obtain the matrix element[4],

$$M(p) \equiv \sum_\lambda |\mathcal{A}(c, p, \lambda)|^2 = n^2 \sum_\lambda \sum_{ij} \mathcal{C}_i^\dagger(c)\mathcal{C}_j(c)\mathcal{A}_i^\dagger(p, \lambda)\mathcal{A}_j(p, \lambda)\,, \tag{3.13}$$

we can use the relations (3.10) based on the Fierz identity (3.8) again to contract the colour indices in $\mathcal{C}_i^\dagger(c)\mathcal{C}_j(c)$. The result can be expressed in terms of an expansion in $1/N$,

$$M(p) = M_0(p) + \frac{1}{N^2}M_1(p) + \frac{1}{N^4}M_2(p) + \dots \tag{3.14}$$

where we absorbed the summation over the helicity configurations $\lambda$ into the definition of the colour-ordered matrix elements $M_i(p)$. The first term in the expansion is called the leading

[3] In the literature one often sees $C_F = (N^2-1)/2N$, which comes precisely from the choice $T_F = 1/2$.
[4] This works analogously for interferences between amplitudes, as we encounter them for example in the virtual corrections.

colour (LC) contribution, the coefficient of $1/N^2$ the subleading colour (SLC) and so on. This terminology also reflects the naive estimate of the relative size of their contribution to the total matrix element.

The leading colour matrix element $M_0(p)$ can always be written as an incoherent sum of squared partial amplitudes,

$$M_0(p) \propto \sum_{\lambda} \sum_{i} |\mathcal{A}_i(p,\lambda)|^2 \,, \tag{3.15}$$

while for the subleading contributions this is in general not possible. For less than six coloured external states, however, they are given as sum over squared abelian or photonic amplitudes, in which one or more gluons behave in an abelian fashion, that is they couple to quarks only, just as photons. Those amplitudes can be written as a superposition of the ordinary partial amplitudes (see appendix B.2). For six or more coloured legs interference terms occur, which cannot be expressed as photonic amplitudes (see appendix B.6.1), but their structure in terms of the partial amplitudes is well understood.

Since the abelian gluons only couple to quarks, they can also only be colour connected to quarks, hence the colour connection of the corresponding matrix element will factorise. Symbolically for two quarks, $n$ ordinary gluons and one abelian gluon $\tilde{g}$ [48, 96]

$$(q, \{p\}_n, \bar{q}; \tilde{g}) \sim (q, \{p\}_n, \bar{q}) \otimes (q, \tilde{g}, \bar{q}) \,, \tag{3.16}$$

where the first structure on the r.h.s. is the ordinary QCD colour structure of a two quark $n$ gluon matrix element, and the second term describes the QED-like coupling of the abelian gluon. We will use this factorisation when we consider QED real radiation in NLO EW corrections in section 10.4.

## 3.3. Infrared divergences

In a fixed order calculation the cross section or any other observable is only well defined, if we include both the virtual and the real corrections at a given order in perturbation theory. With respect to unresolved real emissions we have to be fully inclusive. This can intuitively be understood by realising that if we cannot measure the extra radiation its presence should not make a difference to the observable. The actual mathematical reason is more fundamental and lies within the IR structure of the theory.

When calculating the loop diagrams contributing to the virtual corrections in $d = 4 - 2\epsilon$ dimensions, the final result will in general contain both UV and IR poles in $\epsilon$. While the former can be removed through renormalisation, the latter, coming from massless particles with vanishing virtuality in the loop, cannot. The real corrections on the other hand do not have explicit poles, but rather implicit divergences related to precisely those regions in phase-space where a particle becomes unresolved. When performing the integral over the final state phase-space, those implicit singularities will be turned into explicit $\epsilon$ poles. Kinoshita, Lee and Nauenberg proved [97, 98], that these poles exactly cancel the ones in the virtual corrections at

any given order in perturbation theory. This statement goes by the name of the KLN theorem and is one of the fundamental statements of quantum field theory. Schematically,

$$\mathrm{d}\hat{\sigma}^{NLO} = \underbrace{\int_{\Phi_R} \underbrace{\mathrm{d}\hat{\sigma}^R}_{\text{implicitly divergent}} + \int_{\Phi_B} \underbrace{\mathrm{d}\hat{\sigma}^V}_{\text{explicit } \epsilon \text{ poles}}}_{\text{finite}} . \tag{3.17}$$

A complication arises when describing scattering events at a hadron collider: the species of the initial states in a given channel of the hard scattering process are fixed by the convolution with the PDFs. Thus, when we consider a final state particle becoming collinear to an initial state particle, we cannot be fully inclusive with respect to that configuration. The problem is overcome by a redefinition of the PDFs, which then absorbs the initial state collinear pole. The relevant theoretical background is formulated in the perturbation theory or QCD improved parton model (see section 3.4).

### 3.3.1. Unresolved real radiation

An important observation regarding unresolved real radiation is that in the IR limits the colour-ordered matrix elements factorise into a function describing the singular behaviour and a reduced matrix element which is, apart form a potential shift of its momenta compared to those of the original matrix element, completely unaware of the unresolved particle. This holds both for the leading colour matrix elements and the subleading colour photonic matrix elements. In a fixed order calculation up to NNLO there are essentially three types of unresolved limits we have to consider:

- Single unresolved radiation off a tree level matrix element.
- Single unresolved radiation off a one-loop matrix element.
- Double unresolved radiation off a tree level matrix element.

In the remainder of this chapter we will use the following notation for the colour-ordered matrix elements:

- $M_n^0(\{p\}_n) = \sum_\lambda \left|\mathcal{A}^0(\{p\}_n, \lambda)\right|^2$ – A tree level matrix element with $n$ external legs is just the absolute square of an colour-ordered tree level amplitude, summed over the helicites.
- $M_n^1(\{p\}_n) = \sum_\lambda 2\,\mathrm{Re}\{\mathcal{A}^{0\dagger}(\{p\}_n, \lambda)\mathcal{A}^1(\{p\}_n, \lambda)\}$ – A one-loop matrix element is not the square but rather the interference of a one-loop amplitude with the corresponding tree level amplitude, summed over helicites. The one loop squared matrix element is denoted $M_n^{1\times 1}$.
- $M_n^2(\{p\}_n) = \sum_\lambda 2\,\mathrm{Re}\{\mathcal{A}^{0\dagger}(\{p\}_n, \lambda)\mathcal{A}^2(\{p\}_n, \lambda)\}$ – Analogous to the one-loop case, the colour-ordered two-loop matrix element is the interference of a two-loop amplitude with a tree level amplitude.

Note that in this notation the matrix elements are completely stripped of any colour or coupling factors.

#### Single unresolved - tree level

We encounter singularities in the colour-ordered matrix element when either a particle becomes soft, i.e. is radiated off with zero momentum, or when it becomes collinear to one of its neighbours in the colour ordering. In the former case the factorisation formula reads [99], for $j$ the soft particle and $i$ and $k$ colour adjacent to $j$,

$$M^0_{n+1}(\dots,i,j,k,\dots) \xrightarrow{j\to 0} S_{ijk} M^0_n(\dots,i,k,\dots)\,, \tag{3.18}$$

where

$$S_{ijk} = \frac{2s_{ik}}{s_{ij}s_{jk}} \tag{3.19}$$

is the soft eikonal factor. Note that a single soft (anti-)quark does not represent a divergent limit, as this would violate fermion number conservation. It can, however, like a gluon become collinear to a colour connected particle, in which case we find [100]

$$M^0_{n+1}(\dots,i,j,\dots) \xrightarrow{i||j} \frac{1}{s_{ij}} \hat{P}^{ss'}_{ij\to I}(z) M^0_{n,ss'}(\dots,I,\dots)\,, \tag{3.20}$$

where the composite or mapped momentum $I$ is formed out of the individual momenta $i$ and $j$. Note that all the quantum numbers (spin, colour, etc.) of particles $i$ and $j$ have to be combined appropriately[5] to form particle $I$. The splitting $\hat{P}^{ss'}_{ij\to I}$ functions are matrices in spinor space. When particle $I$ is a (anti-)quark, or fermion in general, the splitting is just proportional to the identity matrix $\delta^{ss'}$, and we can treat it as a simple multiplicative factor to the reduced matrix element. However, if it is a gluon this is not the case, but we can define the spin averaged splitting functions [101], which are related to the normal ones by a set of angular terms, so that

$$\frac{1}{s_{ij}} \hat{P}^{ss'}_{ij\to I}(z) M^0_{n,ss'}(\dots,I,\dots) = \frac{1}{s_{ij}} P_{ij\to I}(z) M^0_n(\dots,I,\dots) + \text{angular terms}\,. \tag{3.21}$$

One can show that those terms, which are in general homogeneous linear functions in $\cos 2\phi$, where $\phi$ is defined as the azimuthal angle between $i$ and $j$ about their collinear axis, cancel non-locally when integrating over the whole phase-space. In the following we will resort to spin averaged splitting functions only. A full list of final state NLO splitting functions can be found in [100]. From them the corresponding expressions for initial state splittings can be derived [47].

[5] This leads to some complications when considering initial state collinear configurations, as we will see later

### Single unresolved - one-loop

When we deal with real radiation coming from a one-loop matrix element, we need to slightly alter the above factorisation formulae. In the case of the soft (gluon) limit, it now reads [102]

$$M^1_{n+1}(\dots,i,j,k,\dots) \xrightarrow{j\to 0} S^{(1)}_{ijk} M^0_n(\dots,i,k,\dots) + S_{ijk} M^1_n(\dots,i,k,\dots)\,, \tag{3.22}$$

where $S_{ijk}$ is the soft eikonal factor defined as before, now factorising onto a one-loop reduced matrix element, and $S^{(1)}_{ijk}$ its one-loop equivalent. The formula for the single collinear limit follows the same structure [103],

$$\begin{aligned} M^1_{n+1}(\dots,i,j,\dots) &\xrightarrow{i\|j} \\ &\frac{1}{s_{ij}} P^{(1)}_{ij\to I}(z) M^0_n(\dots,I,\dots) + \frac{1}{s_{ij}} P_{ij\to I}(z) M^1_n(\dots,I,\dots) + \text{angular terms}\,, \end{aligned} \tag{3.23}$$

with the one-loop splitting functions $P^{(1)}_{ij\to I}(z)$.

### Double unresolved - tree level

Once we allow for two additional real radiation particles, we can also have double unresolved limits. One has to distinguish between cases where the two unresolved particles are colour connected or not. In the latter case the splitting at tree level is just an iteration of the single unresolved splittings described by eqs. (3.18) and (3.20). In the other case, new structures are needed do describe the factorisation appropriately.

In the case that two colour connected particles become soft, the factorisation reads

$$M^0_{n+2}(\dots,i,j,k,l,\dots) \xrightarrow{j,k\to 0} S(i,j,k,l) M^0_n(\dots,i,j,\dots)\,. \tag{3.24}$$

Note that now also a colour connected $q\bar{q}$ pair can become soft without violating fermion number conservation. depending on the species of the soft particles the soft function is defined differently,

$$S(i,j,k,l) = S_{ijkl} \qquad \text{for soft gg [104]}, \tag{3.25a}$$

$$S(i,j,k,l) = S_{il}(j_q,k_{\bar{q}}) \qquad \text{for soft } q\bar{q} \text{ [46]}. \tag{3.25b}$$

If a gluon becomes soft and is colour connected to a collinear pair, then the factorisation formula is given by [105]

$$M^0_{n+2}(\dots,i,j,k,l,\dots) \xrightarrow{j\to 0, k\|l} S_{i,jkl}(z) \frac{P_{kl\to K}(z)}{s_{kl}} M^0_n(\dots,i,K,\dots) + \text{angular terms}\,, \tag{3.26}$$

with the ordinary tree level spin averaged splitting function $P_{kl\to K}$ and a new singular function $S_{i,jkl}(z)$, describing the soft limit in presence of the collinear pair.

Instead of only two particles becoming collinear to each other, we can also have three colour connected particles in a collinear configuration. For these triple collinear limits the factorisation reads [105]

$$M^0_{n+2}(\dots,i,j,k,\dots) \xrightarrow{i||j||k} P_{ijk\to I}(x,y,z) M^0_n(\dots,I,\dots) + \text{angular terms}\,,\,, \tag{3.27}$$

where the triple collinear splitting function now depends on three momentum fraction variables $x, y, z$. One can in principle be eliminated due to momentum conservation[6], $x + y + z = 1$. The angular terms vanish for these configurations, too, once we integrate over the final state phase-space.

The last class of double unresolved configurations we encounter is that of the double collinear limits, where we have two independent collinear pairs. Note that this involves always four particles and that there has to be at least one particle in one of the collinear configurations which is colour disconnected from any particle in the other collinear configuration. Otherwise we would just go back to the triple collinear case. Symbolically:

$$(\dots,i,j,k,l,\dots) \to (\dots,[ij],[kl],\dots)\,, \tag{3.28}$$

where the momenta in square brackets are collinear. While $j$ is colour connected to $k$, $i$ is disconnected from both constituents of the pair $[kl]$. A direct consequence of this is, that we can write the factorisation formula as a simple composition of single collinear tree level splittings,

$$M^0_{n+2}(\dots,i,j,k,l,\dots) \xrightarrow{i||j,k||l} \frac{P_{ij\to I}(z)}{s_{ij}} \frac{P_{kl\to K}(z)}{s_{kl}} M^0_n(\dots,I,K,\dots) + \text{angular terms}\,. \tag{3.29}$$

### 3.3.2. IR pole structure of loop amplitudes

The explicit IR pole structure of both one and two-loop amplitudes can be described in a universal way, as has been done in [106]. In a slightly different approach to what we did in section 3.2, in the reference the colour structure of the amplitude is explicitly kept by defining the amplitude as a vector in an abstract vector space called the colour space. Following the notation of [106] closely, a generic one-loop amplitude can be written as

$$\left|\mathcal{M}^{(1)}_n(\{p\}_n)\right\rangle = \boldsymbol{I}^{(1)}(\epsilon;\{p\}_n)\left|\mathcal{M}^{(0)}_n(\{p\}_n)\right\rangle + \left|\mathcal{M}^{(1),\text{fin}}_n(\{p\}_n)\right\rangle\,. \tag{3.30}$$

Here the complete IR $\epsilon$ pole structure is encoded in the so called one loop I-operator $\boldsymbol{I}^{(1)}$ acting on a tree level amplitude. The finite remainder $\left|\mathcal{M}^{(1),\text{fin}}_n\right\rangle$ collects all terms which do not factor onto a tree amplitude. It is free from any explicit $\epsilon$ poles. The I-operator reads

$$\boldsymbol{I}^{(1)}(\epsilon;\{p\}_n) = \frac{1}{2}\frac{e^{\epsilon\gamma}}{\Gamma(1-\epsilon)} \sum_i \frac{1}{\boldsymbol{T}_i^2}\left(\boldsymbol{T}_i^2\frac{1}{\epsilon^2} + \gamma_i\frac{1}{\epsilon}\right)\sum_{j\neq i}\boldsymbol{T}_i\cdot\boldsymbol{T}_j\left(\frac{\mu^2 e^{-i\lambda_{ij}\pi}}{2p_i\cdot p_j}\right)^{\epsilon}\,, \tag{3.31}$$

[6] Just like in the case of two collinear particles which carried the momentum fractions $z$ and $(1-z)$ of the combined momentum, respectively.

where $\lambda_{ij} = 1$ if $i$ and $j$ are both incoming or outgoing states and $\lambda_{ij} = 0$ otherwise. The coefficient $\gamma_i$ depends on the species of particle $i$,

$$\gamma_q = \gamma_{\bar{q}} = \frac{3}{2} C_F \,, \qquad \gamma_g = \frac{11}{6} C_A - \frac{2}{3} T_F N_F \,, \tag{3.32}$$

where $C_A = N$ is the quadratic Casimir of the adjoint representation. When acting on an amplitude the operator $\boldsymbol{T}_i$, called the colour charge, projects out an $SU(N)$ generator in the irreducible representation associated with particle $i$, i.e. the adjoint representation for gluons and the (anti-)fundamental representation for (anti-)quarks. Thus

$$(T_i)^a_{bc} = i f_{bac} \qquad i: \text{ gluon}\,, \tag{3.33a}$$

$$(T_i)^a_{bc} = T^a_{bc} \qquad i: \text{final state } q \text{ or initial state } \bar{q} \tag{3.33b}$$

$$(T_i)^a_{bc} = -T^a_{bc} \qquad i: \text{initial state } q \text{ or final state } \bar{q}\,. \tag{3.33c}$$

They furthermore fulfil the properties

$$\boldsymbol{T}_q^2 = \boldsymbol{T}_{\bar{q}}^2 = C_F \,, \qquad \boldsymbol{T}_g^2 = C_A \,. \tag{3.34}$$

Colour conservation is represented by

$$\sum_{i \neq j} \boldsymbol{T}_i = -\boldsymbol{T}_j \,, \tag{3.35}$$

where the sum is over all external states $i$, except for $j$, of the amplitude the operators act on.

The poles of the full one-loop matrix element

$$M_n^1 = 2\,\mathrm{Re}\left\langle \mathcal{M}_n^{(0)} \middle| \mathcal{M}_n^{(1)} \right\rangle \tag{3.36}$$

are then simply given by

$$\mathcal{P}oles\big(M_n^1(\{p\}_n)\big) = 2\,\mathrm{Re}\Big\{ \boldsymbol{I}^{(1)}(\epsilon; \{p\}_n) \Big\} M_n^0(\{p\}_n)\,. \tag{3.37}$$

For colour-ordered amplitudes the I-operator can be written as a sum of simpler colour-ordered I-operators describing the poles related to two colour adjacent particles $i$ and $j$,

$$\boldsymbol{I}^{(1)} = \sum_{\text{pairs } (ij)} \boldsymbol{I}^{(1)}_{ij} \,, \tag{3.38}$$

where the sum runs over all colour connected pairs. The set of the colour-ordered I-operators can be found in [46]. Note that the one-loop I-operator is enough to also describe the pole structure of one loop squared amplitudes $M_n^{1\times 1} = \left\langle \mathcal{M}_n^{(1)} \middle| \mathcal{M}_n^{(1)} \right\rangle$.

At two-loop order the equivalent decomposition of the amplitude reads

$$\begin{aligned}\left|\mathcal{M}_n^{(2)}(\{p\}_n)\right\rangle = &\quad \boldsymbol{I}^{(2)}(\epsilon;\{p\}_n)\left|\mathcal{M}_n^{(0)}(\{p\}_n)\right\rangle \\ &+ \boldsymbol{I}^{(1)}(\epsilon;\{p\}_n)\left|\mathcal{M}_n^{(1)}(\{p\}_n)\right\rangle \\ &+ \left|\mathcal{M}_n^{(2),\text{fin}}(\{p\}_n)\right\rangle , \end{aligned} \tag{3.39}$$

where the two-loop I-operator $\boldsymbol{I}^{(2)}$ can be written in terms of the one-loop I-operators and a new process dependent structure $\boldsymbol{H}^{(2)}$,

$$\begin{aligned}\boldsymbol{I}^{(2)}(\epsilon;\{p\}_n) = &-\frac{1}{2}\boldsymbol{I}^{(1)}(\epsilon;\{p\}_n)\left(\boldsymbol{I}^{(1)}(\epsilon;\{p\}_n) + 4\pi\beta_0\frac{1}{\epsilon}\right) \\ &+ \frac{e^{-\epsilon\gamma}\Gamma(1-2\epsilon)}{\Gamma(1-\epsilon)}\left(2\pi\beta_0\frac{1}{\epsilon}+K\right)\boldsymbol{I}^{(1)}(2\epsilon;\{p\}_n) \\ &+ \boldsymbol{H}^{(2)}(\epsilon;\{p\}_n)\,. \end{aligned} \tag{3.40}$$

The constant $K$ is defined as

$$K = \left(\frac{67}{18}-\frac{\pi^2}{6}\right)C_A - \frac{10}{9}T_F N_F\,. \tag{3.41}$$

Since $\boldsymbol{H}^{(2)}(\epsilon) = \mathcal{O}(1/\epsilon)$ the most divergent piece of the two-loop I-operator is $\mathcal{O}\big(1/\epsilon^4\big)$. The poles of the full two-loop matrix element

$$M_n^2 = 2\,\text{Re}\left\langle \mathcal{M}_n^{(0)}\middle|\mathcal{M}_n^{(2)}\right\rangle \tag{3.42}$$

are then given by

$$\begin{aligned}\mathcal{P}oles\big(M_n^2(\{p\}_n)\big) = &\quad 2\,\text{Re}\Big\{\boldsymbol{I}_n^{(1)}(\epsilon;\{p\}_n)\Big\}\left(M_n^1(\{p\}_n) - \frac{\beta_0}{\epsilon}M_n^0(\{p\}_n)\right) \\ &- 2\,\text{Re}\Big\{\boldsymbol{I}_n^{(1)}(\epsilon;\{p\}_n)^2\Big\}M_n^0(\{p\}_n) \\ &+ 2e^{-\epsilon\gamma}\frac{\Gamma(1-2\epsilon)}{\Gamma(1-\epsilon)}\left(\frac{\beta_0}{\epsilon}+K\right)\text{Re}\Big\{\boldsymbol{I}_n^{(1)}(2\epsilon;\{p\}_n)\Big\}M_n^0(\{p\}_n) \\ &+ 2\,\text{Re}\Big\{\boldsymbol{H}^{(2)}(\epsilon)\Big\}M_n^0(\{p\}_n)\,. \end{aligned} \tag{3.43}$$

## 3.4. The QCD improved parton model

The naïve parton model as introduced in section 3.1 makes the assumption that all the constituents of a hadron move in exactly the same direction as the hadron itself. This is only true as a leading order approximation, as nothing prevents the partons from emitting any number of gluons in arbitrary directions, thus obtaining some non-vanishing transverse momentum component. Treating those emissions perturbatively requires us to redefine the bare PDFs $f_i^0(x)$ at some scale $\mu_F$, which is achieved by convoluting them with the so called splitting kernels

$\Gamma_{ij}$ [107], which describe the probability that a particle $i$ will transform into $j$ due to a series of collinear emissions,

$$f_i(x,\mu_F^2) = \int \mathrm{d}y\,\mathrm{d}z\, f_j^0(y)\Gamma_{ji}(z,\mu_F^2)\delta(x-yz)\,. \tag{3.44}$$

The scale $\mu_F$ is called the factorisation scale, and like the renormalised quantities in the previous chapter had a non-trivial dependence on the renormalisation scale $\mu_R$, the renormalised PDFs depend non-trivially on $\mu_F$. The splitting kernels contain some explicit $\epsilon$ poles, just like the renormalisation counterterms, but with the difference that now their origin lies in the IR. One can show that they precisely cancel the poles we obtain by integrating over the unresolved phase-space of initial state collinear configurations of the matrix elements.

Writing out the splitting kernels as a formal expansion in $\alpha_s$,

$$\Gamma_{ij}(z,\mu_F^2) = \delta_{ij}\delta(1-z) + \tilde{\alpha}_s(\mu_F^2)\Gamma_{ij}^{(1)}(z,\mu_F^2) + \tilde{\alpha}_s^2(\mu_F^2)\Gamma_{ij}^{(2)}(z,\mu_F^2) + \mathcal{O}\big(\tilde{\alpha}_s^3(\mu_F^2)\big) \tag{3.45}$$

we can invert eq. (3.44) to express the bare PDFs in terms of their renormalised, physical counterpart,

$$f_i^0(x) = \int \mathrm{d}y\,\mathrm{d}z\, f_j(y,\mu_f^2)\Gamma_{ji}^{-1}(z,\mu_F^2)\delta(x-yz)\,, \tag{3.46}$$

where

$$\begin{aligned}\Gamma_{ij}^{-1}(z,\mu_F^2) = \delta_{ij}\delta(1-z) - \tilde{\alpha}_s(\mu_F^2)\Gamma_{ij}^{(1)}(z,\mu_F^2) \\ - \tilde{\alpha}_s^2(\mu_F^2)\left[\Gamma_{ij}^{(2)}(z,\mu_F^2) - \sum_k \left[\Gamma_{ik}^{(1)}\otimes\Gamma_{kj}^{(1)}\right](z,\mu_F^2)\right] + \mathcal{O}\big(\tilde{\alpha}_s^3(\mu_F^2)\big)\,.\end{aligned} \tag{3.47}$$

Inserting eq. (3.44) into the master formula (3.1) and expanding $\mathrm{d}\hat{\sigma}_{ij}$ and $\Gamma_{ij}^{-1}$ in the coupling according to eqs. (3.2) and (3.47) we find

$$\begin{aligned}\mathrm{d}\sigma = \sum_{ij}\int \frac{\mathrm{d}x_1}{x_1}\frac{\mathrm{d}x_2}{x_2} f_i(x_1)f_j(x_2)\Big[ & \quad \mathrm{d}\hat{\sigma}_{ij}^{LO}(x_1,x_2) \\ & + \tilde{\alpha}_s\Big(\mathrm{d}\hat{\sigma}_{ij}^{NLO}(x_1,x_2) + \mathrm{d}\hat{\sigma}_{ij,NLO}^{MF}(x_1,x_2)\Big) \\ & + \tilde{\alpha}_s^2\Big(\mathrm{d}\hat{\sigma}_{ij}^{NNLO}(x_1,x_2) + \mathrm{d}\hat{\sigma}_{ij,NNLO}^{MF}(x_1,x_2)\Big)\Big] \\ & + \mathcal{O}\big(\tilde{\alpha}_s^3\big)\,,\end{aligned} \tag{3.48}$$

where the power of $\tilde{\alpha}_s$ has to be understood relative to the leading order contribution as before. $\mathrm{d}\hat{\sigma}_{ij,NLO}^{MF}$ and $\mathrm{d}\hat{\sigma}_{ij,NNLO}^{MF}$ are the NLO and NNLO mass factorisation (MF) terms, respectively. The NLO term reads

$$\mathrm{d}\hat{\sigma}_{ij,NLO}^{MF}(x_1,x_2) = -\int \frac{\mathrm{d}z_1}{z_1}\frac{\mathrm{d}z_2}{z_2}\mathbf{\Gamma}_{ij;kl}^{(1)}(z_1,z_2)\mathrm{d}\hat{\sigma}_{kl}^{LO}(z_1x_1,z_2x_2) \tag{3.49}$$

with the NLO mass factorisation kernel

$$\mathbf{\Gamma}^{(1)}_{ij;kl}(z_1,z_2) = \delta_{lj}\Gamma^{(1)}_{ki}(z_1)\delta(1-z_2) + \Gamma^{(1)}_{lj}(z_2)\delta_{ki}\delta(1-z_1)\,. \tag{3.50}$$

We dropped the $\mu_F^2$ for better clarity. The NNLO term is conveniently separated into two parts,

$$\mathrm{d}\hat{\sigma}^{MF}_{ij,NNLO} = \mathrm{d}\hat{\sigma}^{MF,1}_{ij,NNLO} + \mathrm{d}\hat{\sigma}^{MF,2}_{ij,NNLO}\,, \tag{3.51}$$

depending on whether the splitting kernels are convoluted with the LO or NLO partonic cross section:

$$\begin{aligned}&\mathrm{d}\hat{\sigma}^{MF,1}_{ij,NNLO}(x_1,x_2)\\ &\qquad = -\int \frac{\mathrm{d}z_1}{z_1}\frac{\mathrm{d}z_2}{z_2}\mathbf{\Gamma}^{(1)}_{ij;kl}(z_1,z_2)\Big(\mathrm{d}\hat{\sigma}^{NLO}_{ij}(z_1x_1,z_2x_2) + \mathrm{d}\hat{\sigma}^{MF}_{ij,NLO}(z_1x_1,z_2x_2)\Big)\,,\end{aligned} \tag{3.52}$$

and

$$\mathrm{d}\hat{\sigma}^{MF,2}_{ij,NNLO}(x_1,x_2) = -\int \frac{\mathrm{d}z_1}{z_1}\frac{\mathrm{d}z_2}{z_2}\mathbf{\Gamma}^{(2)}_{ij;kl}(z_1,z_2)\mathrm{d}\hat{\sigma}_{kl,LO}(z_1x_1,z_2x_2)\,, \tag{3.53}$$

The NNLO kernel is defined as

$$\mathbf{\Gamma}^{(2)}_{ij;kl}(z_1,z_2) = \delta_{lj}\Gamma^{(2)}_{ki}(z_1)\delta(1-z_2) + \Gamma^{(2)}_{lj}(z_2)\delta_{ki}\delta(1-z_1) + \Gamma^{(1)}_{ki}(z_1)\Gamma^{(1)}_{ki}(z_2)\,. \tag{3.54}$$

The explicit expressions for $\Gamma^{(1)}_{ij}$ and $\Gamma^{(2)}_{ij}$ can be found in [48]. Note that the brackets in eq. (3.48),

$$\Big(\mathrm{d}\hat{\sigma}^{NLO}_{ij}(x_1,x_2) + \mathrm{d}\hat{\sigma}^{MF}_{ij,NLO}(x_1,x_2)\Big)\,, \tag{3.55a}$$

$$\Big(\mathrm{d}\hat{\sigma}^{NNLO}_{ij}(x_1,x_2) + \mathrm{d}\hat{\sigma}^{MF}_{ij,NNLO}(x_1,x_2)\Big)\,, \tag{3.55b}$$

are now free of any singularities related to initial state collinear configurations. In the following when we talk about $\mathrm{d}\hat{\sigma}^{NLO}_{ij}$ or $\mathrm{d}\hat{\sigma}^{NNLO}_{ij}$ the corresponding mass factorisation term is often implicitly included.

While the splitting kernels $\Gamma_{ij}(z,\mu_F^2)$ are perturbative objects, the renormalised PDFs are not, because ultimately they parametrise the non-perturbative bound state we call the proton in terms of its constituents. As such they cannot be predicted from first principles with the methods at hand. However, similar to what has been done with the running coupling in section 2.3 we can derive a set of differential equations which describe their behaviour depending on the factorisation scale $\mu_F$. Starting from the observation that the bare PDFs $f_i^0$ are independent of $\mu_F$, we find the Dokshitzer-Gribov-Lipatov-Alterelli-Parisi (DGLAP) equations [100, 108, 109],

$$\mu_F^2\frac{\partial}{\partial\mu_F^2}f_i(x,\mu_F^2) = \tilde{\alpha}_s(\mu_F^2)\int_x^1\frac{\mathrm{d}z}{z}P_{ij}\Big(\frac{x}{z},\mu_F^2\Big)f_j(z,\mu_F^2)\,. \tag{3.56}$$

The splitting functions $P_{ij}$ have a formal expansion in $\alpha_s$ and are directly related to the splitting kernels $\Gamma_{ij}$ [48]. Solving these equations allows us to measure the PDFs at a certain scale, thus

fixing the boundary conditions of their evolution, and then use the solutions to obtain their values at any other scale.

## 3.5. Antenna subtraction

The NLO contribution to the partonic cross section $\mathrm{d}\hat{\sigma}_{ij}$ consists of the real radiation correction, the virtual corrections, and the mass factorisation term,

$$\mathrm{d}\hat{\sigma}_{ij}^{NLO} = \int_{n+1} \mathrm{d}\hat{\sigma}_{ij}^{R} + \int_{n} \left[\mathrm{d}\hat{\sigma}_{ij}^{V} + \mathrm{d}\hat{\sigma}_{ij,NLO}^{MF}\right]. \tag{3.57}$$

While the latter two contain explicit IR poles in $\epsilon$, the real radiation contribution is formally divergent in certain regions of the final state phase-space. Ideally one would like to evaluate the phase-space integrals in (3.57) analytically in $d = 4-2\epsilon$ dimensions. The implicit IR divergences of $\mathrm{d}\hat{\sigma}_{ij}^{R}$ would then lead to explicit poles in $\epsilon$ which exactly cancel against the poles of $\mathrm{d}\hat{\sigma}_{ij}^{V}$ and those of the mass factorisation contribution. In practice, however, for a larger number of final state particles or in the presence of phase-space cuts the phase-space integrals cannot be evaluated analytically. A numerical integration, on the other hand, can only be performed if the integral is finite. One therefore needs to find a way to isolate and remove the unresolved singular configurations and explicit $\epsilon$ poles from $\mathrm{d}\hat{\sigma}_{ij}^{R}$ and $\mathrm{d}\hat{\sigma}_{ij}^{V} + \mathrm{d}\hat{\sigma}_{ij,NLO}^{MF}$, respectively, before evaluating the phase-space integrals. Several approaches how to achieve this have been proposed [45, 46, 48–60], and while at NLO the problem has been solved for all processes for example using the formulation of the Catani-Seymour dipole subtraction [110], at NNLO it is still an active field of research. For this work we rely on the method of Antenna subtraction [46–48], implemented up to NNLO QCD in NNLOJET. As the name already suggests it is part of a class of methods labelled IR subtraction, the concepts of which will be discussed in the following.

### 3.5.1. IR Subtraction

The main idea is to define a counterterm (subtraction term) $\mathrm{d}\hat{\sigma}_{ij}^{S}$ for $\mathrm{d}\hat{\sigma}_{ij}^{R}$ which exactly mirrors the IR behaviour of the real radiation contribution, such that the difference $\mathrm{d}\hat{\sigma}_{ij}^{R} - \mathrm{d}\hat{\sigma}_{ij}^{S}$ is rendered finite. The subtraction term has to be constructed such that it can be integrated analytically over the phase-space of the unresolved particle, yielding explicit poles in $\epsilon$, which cancel the poles of $\mathrm{d}\hat{\sigma}_{ij}^{V}$ and $\mathrm{d}\hat{\sigma}_{ij,NLO}^{MF}$, once the integrated subtraction term is added back. The whole procedure thus amounts in rewriting equation (3.57) as

$$\mathrm{d}\hat{\sigma}_{ij}^{NLO} = \int_{n+1} \left[\mathrm{d}\hat{\sigma}_{ij}^{R} - \mathrm{d}\hat{\sigma}_{ij,NLO}^{S}\right] + \int_{n} \left[\mathrm{d}\hat{\sigma}_{ij}^{V} + \mathrm{d}\hat{\sigma}_{ij,NLO}^{MF} + \int_{1} \mathrm{d}\hat{\sigma}_{ij,NLO}^{S}\right], \tag{3.58}$$

where the terms in the square brackets are now finite and free of any explicit $\epsilon$ poles, so that they can be integrated numerically. For convenience, one defines the virtual subtraction term

$$\mathrm{d}\hat{\sigma}_{ij,NLO}^{T} \coloneqq -\mathrm{d}\hat{\sigma}_{ij,NLO}^{MF} - \int_{1} \mathrm{d}\hat{\sigma}_{ij,NLO}^{S}. \tag{3.59}$$

The whole concept can readily be extended to NNLO, where we now have to consider contributions living in the $n+2$, $n+1$ and $n$ particle phase-space,

$$\mathrm{d}\hat{\sigma}_{ij}^{NNLO} = \int_{n+2} \mathrm{d}\hat{\sigma}_{ij}^{RR} + \int_{n+1} \left[\mathrm{d}\hat{\sigma}_{ij}^{RV} + \mathrm{d}\hat{\sigma}_{ij,NNLO}^{MF,1}\right] + \int_{n} \left[\mathrm{d}\hat{\sigma}_{ij}^{VV} + \mathrm{d}\hat{\sigma}_{ij,NNLO}^{MF,2}\right]. \tag{3.60}$$

In the double real (RR) contribution $\mathrm{d}\hat{\sigma}_{ij}^{RR}$ we can have up to two unresolved particles, while in the real virtual (RV) contribution we encounter both explicit $\epsilon$ poles from the loop amplitudes and a potentially unresolved particle. To the double virtual (VV) level we have contributions from both two-loop×tree interferences and one-loop squared amplitudes, hence explicit poles up to $\epsilon^{-4}$. The mass factorisation terms appear both at the RV and VV level. Following the approach at NLO, we rewrite the NNLO cross section as

$$\mathrm{d}\hat{\sigma}_{ij}^{NNLO} = \int_{n+2} \left[\mathrm{d}\hat{\sigma}_{ij}^{RR} - \mathrm{d}\hat{\sigma}_{ij}^{S}\right] + \int_{n+1} \left[\mathrm{d}\hat{\sigma}_{ij}^{RV} - \mathrm{d}\hat{\sigma}_{ij}^{T}\right] + \int_{n} \left[\mathrm{d}\hat{\sigma}_{ij}^{VV} - \mathrm{d}\hat{\sigma}_{ij}^{U}\right], \tag{3.61}$$

where the terms in square brackets are again finite and free of explicit poles. The RR subtraction terms can be split in two pieces,

$$\mathrm{d}\hat{\sigma}_{ij}^{S} \coloneqq \mathrm{d}\hat{\sigma}_{ij}^{S,1} + \mathrm{d}\hat{\sigma}_{ij}^{S,2} \tag{3.62}$$

corresponding to single and double unresolved limits, respectively. After integration they will reappear either at the RV or VV level. The RV subtraction term then reads[7]

$$\mathrm{d}\hat{\sigma}_{ij}^{T} \coloneqq -\mathrm{d}\hat{\sigma}_{ij,NNLO}^{MF,1} + \mathrm{d}\hat{\sigma}_{ij}^{V,S} - \int_{1} \mathrm{d}\hat{\sigma}_{ij}^{S,1}, \tag{3.63}$$

where $\mathrm{d}\hat{\sigma}_{ij}^{V,S}$ serves to subtract the single unresolved configurations of the RV matrix elements. Its integrated form is reintroduced in the VV subtraction term, which is given by

$$\mathrm{d}\hat{\sigma}_{ij}^{U} \coloneqq -\mathrm{d}\hat{\sigma}_{ij,NNLO}^{MF,2} - \int_{1} \mathrm{d}\hat{\sigma}_{ij}^{V,S} - \int_{2} \mathrm{d}\hat{\sigma}_{ij}^{S,2}. \tag{3.64}$$

### 3.5.2. Antenna functions

The basic idea of antenna subtraction is to use the IR factorisation formulae given in section 3.3 as a blueprint for the construction of the real radiation subtraction term, symbolically at NLO

$$\int_{n+1} \mathrm{d}\hat{\sigma}^{S} \sim \int_{n+1} X(i,j,k) \cdot M_n(\dots, I, K, \dots) J_n^{(m)}(\dots, I, K, \dots), \tag{3.65}$$

for $j$ a possibly unresolved particle and $I, K$ the mapped momenta in the reduced matrix element $M_n$, just as in the factorisation formulae[8]. $J_n^{(m)}$ is the jet function. In the limit of $j$ becoming

[7] The MF terms are defined such that they are free of implicit IR singularities, see for example eqs. (3.2) and (3.3) in [48].

[8] Eqs. (3.18), (3.21), (3.22), (3.23), (3.24), (3.26), (3.27), (3.29).

unresolved, the functions $X(i,j,k)$ correctly mirror the IR behaviour of the soft or collinear functions in eqs. (3.18) and (3.20), here denoted $u_{ijk}$, such that

$$M_{n+1}(\dots,i,j,k) - X(i,j,k)\cdot M_n(\dots,I,K,\dots) \xrightarrow{j \text{ unres.}} [u_{ijk} - X(i,j,k)]M_n(\dots,I,K,\dots) \quad (3.66)$$

is finite. The functions $X(i,j,k)$ are called antenna functions [111–115]. In fact only a limited number of them is needed to correctly account for all possible IR limits which can occur at a given order in the perturbative expansion. They are conventionally classified according to the species, quark or gluon, of the two hard radiators $i$ and $k$. For each class the antenna functions are derived from the decay of a certain particle into these radiators plus additional QCD radiation $X$, capturing all of the associated IR singular configurations.

- Quark-anti-quark antennae: decay of an off-shell photon, $\gamma^* \to q\bar{q} + X$ [116]
- Quark-gluon antennae: decay of a neutralino into a gluino and a gluon, $\tilde{\chi} \to \tilde{g}g + X$ [112]
- Gluon-gluon antennae: decay of a Higgs boson into two gluons in the $m_t \to \infty$ limit, $H \to gg + X$ [111]

The tree level antenna functions involving one possibly unresolved particle $j$ are then defined as

$$X_3^0(i,j,k) = \mathcal{S}\frac{M_3^0(i,j,k)}{M_2^0(I,K)}\,, \quad (3.67)$$

where $\mathcal{S}$ collects relevant symmetry factors and $I,K$ in the two-particle matrix element are the mapped momenta of the hard radiators. At NLO those are the only antennae we need. At NNLO we encounter two new types of antennas, reflecting the factorisation structure of one-loop matrix elements (3.22), (3.23) and that of double unresolved limits (3.24), (3.26), (3.27), (3.29), respectively. The later require the introduction of four-particle antennas,

$$X_4^0(i,j,k,l) = \mathcal{S}\frac{M_4^0(i,j,k,l)}{M_2^0(I,L)}\,, \quad (3.68)$$

where now $j$ and $k$ can become unresolved. For the subtraction of the implicit IR singularities of one-loop matrix elements we need new one-loop three particle antenna functions,

$$X_3^1(i,j,k) = \mathcal{S}\frac{M_3^1(i,j,k)}{M_2^0(I,K)} - X_3^0(i,j,k)\frac{M_2^1(I,K)}{M_2^0(I,K)}\,, \quad (3.69)$$

in order to subtract the parts in (3.22), (3.23) associated to the one-loop soft and collinear functions, respectively. As the parts associated to the tree level unresolved functions, factoring onto a reduced one-loop matrix element, are already subtracted by an $X_3^0 M_n^1$ structure, we have to compensate for those bits in the one-loop antenna, which is why we have the second term proportional to $X_3^0$ in eq. (3.69). A complete list of the antenna functions relevant for NLO and NNLO QCD calculations can be found in [48].

All of the antenna functions must be analytically integrable over the phase-space of the unresolved particles, so that the implicit singularities of the antennae appear as explicit poles in $\epsilon$, which then cancel the poles of the virtual correction matrix elements and the mass factorisation contribution. The phase-space therefore must factorise in a similar manner as the matrix elements. Symbolically for NLO:

$$\mathrm{d}\Phi_{n+1}\left(\ldots,i,j,k,\ldots;p_1,p_2\right)=\mathrm{d}\Phi_n\left(\ldots,I,K,\ldots;\hat{p}_1,\hat{p}_2\right)\mathrm{d}\Phi_{X_{ijk}}\,, \tag{3.70}$$

where $\mathrm{d}\Phi_{X_{ijk}}$ is the unresolved or antenna phase-space, and $\mathrm{d}\Phi_n$ that of the remaining hard partons[9]. The concrete factorisation is derived from the form of the mapping functions relating the full momentum set to the reduced one, which in turn depend on whether the hard radiators are in the final or initial state. We have to consider three different momentum mappings, final-final (FF), initial-final (IF), initial-initial (II). Those mappings are subject to some constraints, besides the fact that they should lead to a factorising phase-space:

- All mapped momenta must be on-shell.
- Initial state momenta must remain in direction of the beam axis.
- For each limit the mapped momenta must smoothly tend to the correct resolved momenta.

The appropriate mappings for the final-final configuration were presented in [117] for single unresolved radiation and in [118] for double unresolved radiation. The initial-final and initial-initial mappings can be found in [47], both for single and double unresolved limits. Given the phase-space factorisation we can then rewrite the symbolic formula (3.65) (here for a single unresolved subtraction):

$$\int_{n+1}\mathrm{d}\hat{\sigma}^S=\int\mathrm{d}\Phi_{n+1}\,X_3^\ell M_n^{\ell'}J_n^{(m)}=\underbrace{\int\mathrm{d}\Phi_{X_{ijk}}\,X_3^\ell}_{\sim\mathcal{X}_3^\ell}\int\mathrm{d}\Phi_n\,M_n^{\ell'}J_n^{(m)}\,, \tag{3.71}$$

where $\ell,\ell'=0,1$, and where we defined the integrated antenna $\mathcal{X}_3$, up to a normalisation constant. Following this classification of the mappings we find three different types of integrated antennas, which we denote by FF, IF, II, depending on the type of factorised phase-space $\mathrm{d}\Phi_{X_{ijk}}$ used to integrate them. The integrated antennae can be found in [46] (FF), [113] (IF) and [115] (II).

### 3.5.3. Antenna subtraction at NLO

It is instructive to study the NLO IR subtraction using antennas, because it already shows many of the key features which become relevant at NNLO. As we will explicitly construct NLO QED antenna subtraction terms later on when we consider EW corrections, see section 10.4, we will

[9]
$$\mathrm{d}\Phi_n\left(p_3,\ldots,p_{n+2};p_1,p_2\right)=\frac{\mathrm{d}^{d-1}p_3}{2E_3(2\pi)^{d-1}}\frac{\mathrm{d}^{d-1}p_{n+2}}{2E_{n+2}(2\pi)^{d-1}}(2\pi)^d\delta^{(d)}(p_1+p_2-p_3-\cdots-p_{n+2})$$

present the general structure at NLO in the following. For brevity we will consider only the leading colour, but based on the discussion about the photonic matrix elements at the end of section 3.2 the method can readily applied to the subleading colour as well[10].

The general form of the real and virtual correction cross sections is given by (dropping the $ij$ subscripts)

$$\mathrm{d}\hat{\sigma}^R = \mathcal{N}^R \sum_{\text{perm.}} \mathrm{d}\Phi_{n+1}\left(\{k\}_{n+1}; p_1, p_2\right) \frac{1}{S_{n+1}} M^0_{n+1}(\{k\}_{n+1}; p_1, p_2) J^{(m)}_n(\{k\}_m)\,, \tag{3.72}$$

$$\mathrm{d}\hat{\sigma}^V = \mathcal{N}^V \sum_{\text{perm.}} \mathrm{d}\Phi_{n}\left(\{k\}_{n}; p_1, p_2\right) \frac{1}{S_{n}} M^1_{n}(\{k\}_{n}; p_1, p_2) J^{(m)}_n(\{k\}_m)\,, \tag{3.73}$$

where the normalisation $\mathcal{N}$ collects the overall colour factor, initial state averaging factors and the couplings. The sum runs over all permutations in the colour ordering and $\mathrm{d}\Phi_n$ is the phase-space for the $2 \to n$ kinematics, with $p_1, p_2$ the initial state momenta and $\{k\}_n$ the set of final state momenta. $S_n$ is a final state symmetry factor. And $J^{(m)}_n$ the jet function introduced in eq. (3.3). Following the basic idea of antenna subtraction that in an unresolved limit the real matrix element factorises and tends to an reduced matrix element multiplied with an antenna function,

$$M^0_{n+1}(\{k\}_{n+1}; p_1, p_2) \xrightarrow[j \text{ unres.}]{} X^0_3(\cdot, j, \cdot) M^0_n(\{\tilde{k}\}_n; \tilde{p}_1, \tilde{p}_2)\,, \tag{3.74}$$

we can readily write down the general form of the NLO real subtraction term,

$$\mathrm{d}\hat{\sigma}^S_{NLO} = \mathcal{N}^R \sum_{\text{perm.}} \sum_j \mathrm{d}\Phi_{n+1}\left(\{k\}_{n+1}; p_1, p_2\right) \frac{1}{S_{n+1}} \times X^0_3(\cdot, j, \cdot) M^0_n(\{\tilde{k}\}_n; \tilde{p}_1, \tilde{p}_2) J^{(m)}_n(\{\tilde{k}\}_n)\,, \tag{3.75}$$

$X^0_3(\cdot, j, \cdot)$ is the tree level three particle antenna defined as above, with the dots representing the hard radiators and $j$ the potentially unresolved momentum. In the $2 \to n$ reduced matrix element $M^0_n(\{\tilde{k}\}_n; \tilde{p}_1, \tilde{p}_2)$ the mapped momenta are used, denoted by the $\sim$ accent. Which momenta are actually affected by the mapping and how, depends on the precise configuration of the limit considered. To construct the full subtraction term, $j$ sums over all potentially unresolved particles.

### The final-final configuration

In the final-final configuration the three final state momenta $i, j$ and $k$ are mapped onto the composite final state momenta $I$ and $K$, such that the IR structure of the real radiation matrix element $M^0_{n+1}$ associated to parton $j$ is captured by [48]

$$M^0_{n+1}(\ldots, i, j, k, \ldots; p_1, p_2) \to X^0_3(i, j, k) M^0_n(\ldots, I, K, \ldots; p_1, p_2)\,. \tag{3.76}$$

[10] The terms which can not be written as squared amplitudes, neither partial amplitudes nor photonic amplitudes, and which occur for six or more coloured external states need some extra work. But since their factorisation properties at the amplitude level are well understood, they are not a conceptual problem.

The concrete form of the mapping is defined in [117] in such a way that in the unresolved limits:

$$j \to 0: \qquad I \to i, \qquad K \to k\,, \tag{3.77a}$$

$$j||i: \qquad I \to i+j, \qquad K \to k\,, \tag{3.77b}$$

$$j||k: \qquad I \to i, \qquad K \to j+k\,. \tag{3.77c}$$

The phase-space then factorises into an $2 \to n$ phase-space $\mathrm{d}\Phi_n$ with the mapped momentum set and a final-final antenna phase-space $\mathrm{d}\Phi^{FF}_{X_{ijk}}$,

$$\mathrm{d}\Phi_{n+1}\left(\ldots,i,j,k,\ldots;p_1,p_2\right) = \mathrm{d}\Phi_n\left(\ldots,I,K,\ldots;p_1,p_2\right)\mathrm{d}\Phi^{FF}_{X_{ijk}}\,, \tag{3.78}$$

where [46]

$$\mathrm{d}\Phi^{FF}_{X_{ijk}} = 2^{3-2\epsilon}\pi^{1-\epsilon}\frac{\Gamma(2-2\epsilon)}{\Gamma(1-\epsilon)}(s_{ijk})^{\epsilon}\,\mathrm{d}\Phi_3\left(i,j,k;p_1,p_2\right), \tag{3.79}$$

with $s_{ijk} = s_{ij} + s_{ik} + s_{jk}$. The final-final integrated antenna is then given by

$$\mathcal{X}_3^{0,FF}(s_{ijk}) = \frac{1}{C(\epsilon)}\int \mathrm{d}\Phi^{FF}_{X_{ijk}}\, X_3^0(i,j,k)\,, \tag{3.80}$$

where we defined

$$C(\epsilon) = \frac{(4\pi)^{\epsilon}e^{-\gamma\epsilon}}{8\pi^2}\,. \tag{3.81}$$

Using that the normalisation of the virtual correction (3.73) is related to that of the real correction (3.72) through

$$C(\epsilon)\mathcal{N}^R = \mathcal{N}^V\,, \tag{3.82}$$

we can explicitly write down the virtual subtraction term,

$$\begin{aligned}\mathrm{d}\hat{\sigma}^T_{NLO} = -\mathcal{N}^V \sum_{\text{perm.}}\sum_{I,K}\mathrm{d}\Phi_n\left(\ldots,I,K,\ldots;p_1,p_2\right)\frac{1}{S_n} \\ \times \boldsymbol{J}_2^{(1)}(I,K)M_n^0(\ldots,I,K,\ldots;p_1,p_2)J_n^{(m)}(\{\tilde{k}\}_m)\,,\end{aligned} \tag{3.83}$$

where $I,K$ sums over all integrated dipoles $\boldsymbol{J}_2^{(1)}(I,K)$, similar to $j$ in the real subtraction term (3.75). Since the final-final unresolved limits do not get a contribution form the mass factorisation the integrated dipoles are directly proportional to the integrated antenna functions

$$\boldsymbol{J}_2^{(1)}(I,K) = S_{\mathcal{X}}\mathcal{X}_3^{0,FF}(s_{IK})\,, \tag{3.84}$$

where the proportionality factor $S_{\mathcal{X}}$ depend on the concrete species of antenna. In [48] a complete list including the respective factors is available.

### The initial-final configuration

In the initial-final configuration the phase-space map introduced above cannot be applied, because the initial state momentum 1 must remain in the direction of the beam axis. Instead of defining the mapped initial state momentum as a composition of momenta, it is therefore rescaled, $\bar{1}$, while the two final state momenta are mapped onto a single final state composite momentum $K$. In the IR limits associated to $j$ we find [48]

$$M^0_{n+1}(\dots,j,k,\dots;1_a,p_2) \to X^0_{3,a\to b}(1_a,j,k)M^0_n(\dots,K,\dots;\bar{1}_b,p_2)\,. \tag{3.85}$$

The species of the initial state parton in the reduced matrix element can change from $a$ to $b$. Imagine for example a final state quark becoming collinear to an initial state gluon. In that case the rescaled initial state momentum in the reduced matrix element would be assigned to a quark, in order to get the right quantum numbers in the reduced set of particles. The whole subtraction term, however, has to be convoluted with a gluon PDF in order to ensure the correct cancellation between $\mathrm{d}\hat{\sigma}^R$ and $\mathrm{d}\hat{\sigma}^S$. This is explicitly pointed out by marking the antenna function with the subscript $a \to b$. When $a = b$ the subscript is conventionally dropped.

The mapping initial-final mapping itself is defined such, that [47]

$$j \to 0: \qquad \bar{1} \to 1, \qquad K \to k\,, \tag{3.86a}$$

$$j||1: \qquad \bar{1} \to 1-j, \qquad K \to k\,, \tag{3.86b}$$

$$j||k: \qquad \bar{1} \to 1, \qquad K \to j+k\,. \tag{3.86c}$$

The corresponding phase-space factorisation reads

$$\mathrm{d}\Phi_{n+1}\left(\dots,j,k,\dots;1,p_2\right) = \mathrm{d}\Phi_n\left(\dots,K,\dots;\bar{1},p_2\right)\frac{\mathrm{d}x}{x}\,\mathrm{d}\Phi^{IF}_{X_{1jk}}\,, \tag{3.87}$$

with the initial-final antenna phase-space

$$\mathrm{d}\Phi^{IF}_{X_{1jk}} = \mathrm{d}\Phi_2\left(j,k;p_1,q\right)\frac{Q^2}{2\pi}\delta(\hat{x}-x)\,. \tag{3.88}$$

Here $Q^2 = -q^2 = -(j+k-1)^2$ and $\hat{x} = s_{1jk}/(s_{1j}+s_{1k})$. For the initial-final integrated antenna we then find

$$\mathcal{X}^{0,IF}_{3,a\to b}(s_{1jk};x) = \frac{1}{C(\epsilon)}\int \mathrm{d}\Phi^{IF}_{X_{ijk}}\,X^0_{3,a\to b}(1,j,k)\,. \tag{3.89}$$

The virtual subtraction term is given by

$$\begin{aligned}\mathrm{d}\hat{\sigma}^T_{NLO} = -\mathcal{N}^V\int\frac{\mathrm{d}x}{x}\sum_{\text{perm.}}\sum_K \mathrm{d}\Phi_n\left(\dots,K,\dots;\bar{1},p_2\right)\frac{1}{S_n}\\ \times \boldsymbol{J}^{(1)}_{2,a\to b}(\bar{1},K;x)M^0_n(\dots,K,\dots;\bar{1}_b,p_2)J^{(m)}_n(\{\tilde{k}\}_m)\,,\end{aligned} \tag{3.90}$$

where now the integrated antenna contains part of the mass factorisation contribution,

$$\boldsymbol{J}^{(1)}_{2,a\to b}(\bar{1},K;x) = S_{\mathcal{X}}\mathcal{X}^{0,IF}_{3,a\to b}(s_{\bar{1}K};x) - S_{\Gamma}\Gamma^{1}_{ba}(x)\,. \tag{3.91}$$

$S_\Gamma$ is another numerical factor depending on the antenna species. Note that only the splitting associated with the initial state momentum 1 contributes, so we could carry out the now trivial integration over $z_2$ in the NLO mass factorisation formula (3.49). The other splitting in the NLO mass factorisation kernel (3.50) ends up in an equivalent subtraction term involving the second initial state particle.

### The initial-initial configuration

When both hard radiators are in the initial state, yet another mapping is needed. As for the initial-final case the initial state momenta are rescaled. In order to ensure momentum conservation all final state momenta need to be boosted in a certain way [47], $\{k\}_n \to \{\tilde{k}\}_n$, since unlike before we cannot construct a composite momentum out of the final state momenta in the antenna in order to adjust for this rescaling; we just have the potentially unresolved $j$ to work with. This leads us to

$$M^0_{n+1}(k_1,\dots,j,\dots,k_n;1_a,2_b) \to X^0_{3,a\to c,b\to d}(1_a,j,2_b)M^0_n(\{\tilde{k}\}_n;\bar{1}_c,\bar{2}_d)\,. \tag{3.92}$$

In the limits associated with $j$ the mapping ensures that

$$j\to 0: \qquad \bar{1}\to 1, \qquad \bar{2}\to 2, \qquad \tilde{k}_i \to k_i\,, \tag{3.93a}$$

$$j||1: \qquad \bar{1}\to 1-j, \qquad \bar{2}\to 2, \qquad \tilde{k}_i \to k_i\,, \tag{3.93b}$$

$$j||2: \qquad \bar{1}\to 1, \qquad \bar{2}\to 2-j, \qquad \tilde{k}_i \to k_i\,. \tag{3.93c}$$

For the phase-space factorisation we have

$$\mathrm{d}\Phi_{n+1}\left(k_1,\dots,j,\dots,k_n;1,2\right) = \mathrm{d}\Phi_n\left(\{k\}_n;\bar{1},\bar{2}\right)\frac{\mathrm{d}x_1}{x_1}\frac{\mathrm{d}x_2}{x_2}\,\mathrm{d}\Phi^{II}_{X_{1j2}}\,, \tag{3.94}$$

with

$$\mathrm{d}\Phi^{II}_{X_{1j2}} = \frac{\mathrm{d}^d k_j \delta^+(k_j^2)}{(2\pi)^{d-1}} x_1 x_2 \delta(\hat{x}_1 - x_1)\delta(\hat{x}_2 - x_2)\,. \tag{3.95}$$

The explicit form of the rescaling parameters $x_{1,2}$ can be found in [47]. The integrated initial-initial antenna is then given by

$$\mathcal{X}^{0,II}_{3,a\to c,b\to d}(s_{1j2};x_1,x_2) = \frac{1}{C(\epsilon)}\int \mathrm{d}\Phi^{II}_{X_{1j2}}\, X^0_{3,a\to c,b\to d}(1,j,2)\,. \tag{3.96}$$

For the integrated subtraction term we find

$$\mathrm{d}\hat{\sigma}^{T}_{NLO} = -\mathcal{N}^{V} \int \frac{\mathrm{d}x_1}{x_1}\frac{\mathrm{d}x_2}{x_2} \sum_{\text{perm.}} \mathrm{d}\Phi_n\left(\{k\}_n; \bar{1}, \bar{2}\right)\frac{1}{S_n} \times \boldsymbol{J}^{(1)}_{2,a\to c,b\to d}(\bar{1},\bar{2};x_1,x_2) M^0_n(\{\tilde{k}\}_n;\bar{1}_c,\bar{2}_d) J^{(m)}_n(\{\tilde{k}\}_m)\,, \quad (3.97)$$

with the initial-initial integrated antenna

$$\boldsymbol{J}^{(1)}_{2,a\to c,b\to d}(\bar{1},\bar{2};x_1,x_2) = S_{\mathcal{X}}\mathcal{X}^{0,II}_{3,a\to c,b\to d}(s_{\bar{1}\bar{2}};x_1,x_2) - S_{\Gamma,1}\Gamma^1_{ca}(x_1)\delta(1-x_2) - S_{\Gamma,2}\Gamma^1_{db}(x_2)\delta(1-x_1)\,, \quad (3.98)$$

which now contains the NLO mass factorisation contribution of both initial states.

### 3.5.4. Antenna subtraction at NNLO

At NNLO the construction of the subtraction term is more involved due to the more complicated singularity structure. In the following we will describe how the individual pieces are set up and how they interact. Figure 3.1 depicts the general blueprint of the interplay between the different terms. There are many subtleties one has to be aware of, but we will not discuss them here in detail, as the corresponding solutions have been well established in the literature [48, 119, 120], and the actual construction of the subtraction is not the main focus of this thesis.

#### The double real subtraction term

As mentioned earlier the double real subtraction term has to subtract both the single unresolved and double unresolved singularities from the double real contribution to the cross section, which is why we have split it into two separate terms, $\mathrm{d}\hat{\sigma}^{S,1}_{ij}$ and $\mathrm{d}\hat{\sigma}^{S,2}_{ij}$. In fact, in order to better describe the interplay of the different subtraction terms it is helpful to subdivide it even further:

$$\mathrm{d}\hat{\sigma}^{S}_{ij,NNLO} = \underbrace{\mathrm{d}\hat{\sigma}^{S,a}_{ij,NNLO}}_{\mathrm{d}\hat{\sigma}^{S,1}_{ij}} + \underbrace{\mathrm{d}\hat{\sigma}^{S,b1}_{ij,NNLO} + \mathrm{d}\hat{\sigma}^{S,b2}_{ij,NNLO} + \mathrm{d}\hat{\sigma}^{S,c}_{ij,NNLO} + \mathrm{d}\hat{\sigma}^{S,d}_{ij,NNLO}}_{\mathrm{d}\hat{\sigma}^{S,2}_{ij}}\,. \quad (3.99)$$

The different terms are shown in the bottom section of figure 3.1. After integration they reappear either at the real virtual (middle section in figure 3.1) or the double virtual level (top section in figure 3.1). The individual purposes of those different contributions are summarised in the following.

$\mathrm{d}\hat{\sigma}^{S,a}_{ij}$ - This term targets the single unresolved configurations. As a complete analogue of the NLO real subtraction term it is constructed out of $X^0_3$ antennae and an $n+1$ final state particle reduced matrix element. Note that the reduced matrix element itself has IR singularities which have to be subtracted elsewhere. After integration the subtraction term will be reintroduced at the real virtual level to cancel the explicit poles of $\mathrm{d}\hat{\sigma}^{RV}_{ij}$.

$\mathrm{d}\hat{\sigma}^{S,b_1}_{ij}$ - Double unresolved limits with two colour connected particles are subtracted by this term. It is constructed out of $X^0_4$ antennae and after integration over the unresolved phase-space

will reappear in the double virtual subtraction term. The $X_4^0$ antenna, however, has some spurious limits in cases where only one particle or two almost colour connected particles become unresolved. Those unwanted limits have to be compensated in another part of $\mathrm{d}\hat{\sigma}^S_{ij,NNLO}$.

$\mathrm{d}\hat{\sigma}^{S,b_2}_{ij}$ - The spurious single unresolved limits of the $X_4^0$ antennae in $\mathrm{d}\hat{\sigma}^{S,b_1}_{ij}$ are subtracted by treating the $X_4^0$s just like ordinary matrix elements, for which we can construct a subtraction out of $X_3^0$ antennas, but now instead of reduced matrix elements we have $X_3^0$ antennas. Consequently we find terms containing the product $X_3^0 \times X_3^0$ factorizing onto the same reduced matrix element as the corresponding $X_4^0$ in $\mathrm{d}\hat{\sigma}^{S,b_1}_{ij}$. While subtracting the single unresolved limits correctly, this introduces further spurious limits of the almost colour connected kind. After integration over the unresolved phase-space this part is reintroduced at the real virtual level.

$\mathrm{d}\hat{\sigma}^{S,c}_{ij}$ - In the case of two almost colour connected particles becoming unresolved the limit is subtracted twice by $\mathrm{d}\hat{\sigma}^{S,a}_{ij}$, and at the same time $\mathrm{d}\hat{\sigma}^{S,b_2}_{ij}$ oversubtracts the spurious limits of a certain class of $X_4^0$ antennas. Those double counting and oversubtraction issues are resolved by defining appropriate terms in $\mathrm{d}\hat{\sigma}^{S,c}_{ij}$, which again are based on a product of $X_3^0$ antennas, but with a carefully chosen mapping sequence. Moreover we encounter additional spurious limits related to single soft configurations, but which can not be compensated by any ordinary antenna function and require the introduction of so called large angle soft terms [96, 121]. After integration over the unresolved phase-space $\mathrm{d}\hat{\sigma}^{S,c}_{ij}$ will reappear as part of the real virtual subtraction term.

$\mathrm{d}\hat{\sigma}^{S,d}_{ij}$ - In the same way that double unresolved limits of the almost colour connected kind got subtracted twice by $\mathrm{d}\hat{\sigma}^{S,a}_{ij}$ the double unresolved configurations with two colour disconnected particles are. To compensate for this oversubtraction $\mathrm{d}\hat{\sigma}^{S,d}_{ij}$ is constructed around a product of $X_3^0$ antennas. Since the unresolved particles are colour disconnected the two antennae do not share any momenta and, unlike in $\mathrm{d}\hat{\sigma}^{S,c}_{ij}$, the ordering in which they appear is not important. This term will be integrated directly to the double virtual level.

#### The real virtual subtraction term

The real virtual subtraction term serves two purposes:

1. Cancellation of the explicit poles of the one-loop matrix elements.
2. Subtraction of the divergences associated with the real radiation.

It therefore contains part of the double real subtraction term integrated over single unresolved configurations, combined with the appropriate part of the NNLO mass factorisation contribution, and new subtractions with un-integrated antennas, which will be reintroduced at the double virtual level after integration over the single unresolved phase-space. It is conventionally subdivided into five distinct pieces, constituting the middle section of figure 3.1.:

$$\mathrm{d}\hat{\sigma}^T_{ij,NNLO} = \mathrm{d}\hat{\sigma}^{T,a}_{ij,NNLO} + \mathrm{d}\hat{\sigma}^{T,b_1}_{ij,NNLO} + \mathrm{d}\hat{\sigma}^{T,b_2}_{ij,NNLO} + \mathrm{d}\hat{\sigma}^{T,b_3}_{ij,NNLO} + \mathrm{d}\hat{\sigma}^{T,c}_{ij,NNLO}\,. \tag{3.100}$$

$\mathrm{d}\hat{\sigma}_{ij}^{T,a}$ - This term is the counterpart of the double real subtraction contribution $\mathrm{d}\hat{\sigma}_{ij}^{S,a}$. It contains the corresponding integrated antenna functions $\mathcal{X}_3^0$ with the appropriate parts of the mass factorisation, joined in the integrated antenna string $\boldsymbol{J}_{n+1}^{(1)}$, to cancel the explicit poles of the one-loop real virtual matrix elements. In a sense $\mathrm{d}\hat{\sigma}_{ij}^{S,a}$ and $\mathrm{d}\hat{\sigma}_{ij}^{T,a}$ form an independent NLO subtraction for all configurations where only one of the two real radiation partons becomes unresolved.

$$\mathrm{d}\hat{\sigma}_{ij}^{T,a} \sim \boldsymbol{J}_{n+1}^{(1)} M_{n+1}^0 \,. \tag{3.101}$$

$\mathrm{d}\hat{\sigma}_{ij}^{T,b_1}$ - Corresponding to the tree×one-loop terms in the one-loop factorisation formulae (3.22) and (3.23), this term is constructed out of tree level antennae and one-loop reduced matrix elements. It removes a part of the implicit IR singularities of the real virtual matrix element, but it introduces explicit poles in the one-loop reduced matrix element. Those poles are removed by introducing the appropriate integrated antenna string $\boldsymbol{J}_n^{(1)}$, which contains the correct part of the NNLO mass factorisation contribution.

$$\mathrm{d}\hat{\sigma}^{T,b_1} \sim X_3^0 M_n^1 + X_3^0 \boldsymbol{J}_n^{(1)} M_n^0 \,. \tag{3.102}$$

$\mathrm{d}\hat{\sigma}_{ij}^{T,b_2}$ - The one-loop×tree part of the one-loop factorisation formulae (3.22) and (3.23) is considered in $\mathrm{d}\hat{\sigma}_{ij}^{T,b_2}$, combining one-loop antennae $X_3^1$ with tree level reduced matrix elements. The one-loop antenna itself has explicit $\epsilon$ poles which need to be removed. This is only partially achieved by the string $\boldsymbol{J}_X^{(1)}$ coming from the integration of $\mathrm{d}\hat{\sigma}_{ij}^{S,b_2}$ over the single unresolved phase-space. To take care of all poles a integrated antenna string $\boldsymbol{J}_2^{(1)}$ unrelated to the double real subtraction has to be introduced. This term has to be compensated in the double virtual subtraction term, like the one-loop antenna function. Both integrated strings, the one coming from the double real level and the unrelated one, receive contributions from the NNLO mass factorisation.

$$\mathrm{d}\hat{\sigma}^{T,b_2} \sim X_3^1 M_n^0 + \boldsymbol{J}_X^{(1)} X_3^0 M_n^0 - M_X X_3^0 \boldsymbol{J}_2^{(1)} M_n^0 \,. \tag{3.103}$$

$\mathrm{d}\hat{\sigma}_{ij}^{T,b_3}$ - The one-loop antennae $X_3^1(i,j,k)$ introduced as part of $\mathrm{d}\hat{\sigma}_{ij}^{T,b_2}$ is subject to renormalisation at the scale $s_{ijk}$. To match the renormalisation scale to that used for the matrix elements, $\mu^2$ the antenna is modified using the running of $\alpha_s$,

$$X_3^1 \to X_3^1 + \frac{\beta_0}{\epsilon} X_3^0 \left( \left( \frac{|s_{ijk}|}{\mu^2} \right)^{-\epsilon} - 1 \right) . \tag{3.104}$$

The extra terms proportional to the beta function coefficient $\beta_0$ are collected in $\mathrm{d}\hat{\sigma}_{ij}^{T,b_3}$. After integration over the single unresolved phase-space it will be reintroduced as part of the double virtual subtraction.

$$\mathrm{d}\hat{\sigma}^{T,b_3} \sim -\frac{\beta_0}{\epsilon} X_3^0 M_n^0 + \frac{\beta_0}{\epsilon} X_3^0 \left( \frac{|s|}{\mu^2} \right)^{-\epsilon} M_n^0 \,. \tag{3.105}$$

$\mathrm{d}\hat{\sigma}_{ij}^{T,c}$ - This term originates from the almost colour connected subtraction term $\mathrm{d}\hat{\sigma}_{ij}^{S,c}$. After its integration over the single unresolved phase-space, including the large angle soft terms, it still needs to be combined with additional new terms to render it IR finite. $\mathrm{d}\hat{\sigma}_{ij}^{T,c}$ is further decomposed into $\mathrm{d}\hat{\sigma}_{ij}^{T,c_1}$ and $\mathrm{d}\hat{\sigma}_{ij}^{T,c_2}$ containing the new terms, and the genuine integrated double real terms. Both terms will reappear in different parts of the double virtual subtraction term.

$$\mathrm{d}\hat{\sigma}^{T,c} \sim -\int_1 \mathrm{d}\hat{\sigma}^{S,c} + \mathrm{d}\hat{\sigma}^{T,c_1} + \mathrm{d}\hat{\sigma}^{T,c_2}\,. \tag{3.106}$$

**The double virtual subtraction term**

The double virtual subtraction contains all the integrated structures from the double real and real virtual level, as well as mass factorisation contributions necessary to cancel all explicit $\epsilon$ poles of the two-loop matrix elements. In its construction it follows Catani's two-loop factorisation formula (3.43), leading to a formal separation of the subtraction term into three pieces,

$$\mathrm{d}\hat{\sigma}_{ij,NNLO}^{U} = \mathrm{d}\hat{\sigma}_{ij,NNLO}^{U,A} + \mathrm{d}\hat{\sigma}_{ij,NNLO}^{U,B} + \mathrm{d}\hat{\sigma}_{ij,NNLO}^{U,C}\,, \tag{3.107}$$

as given in the top section of figure 3.1.

$\mathrm{d}\hat{\sigma}_{ij}^{U,A}$ - This term receives contributions from $\mathrm{d}\hat{\sigma}_{ij}^{T,b_1}$ and $\mathrm{d}\hat{\sigma}_{ij}^{T,b_3}$. Combined with the appropriate MF term it cancels all $1/\epsilon^4$ and $1/\epsilon^3$ poles of the double virtual matrix element, contained in the first two lines of eq. (3.43).

$$\mathrm{d}\hat{\sigma}^{U,A} \sim -\frac{\beta_0}{\epsilon}\boldsymbol{J}_n^{(1)} M_n^1 + \boldsymbol{J}_n^{(1)} M_n^{(1)}\,. \tag{3.108}$$

$\mathrm{d}\hat{\sigma}_{ij}^{U,B}$ - The part in $\mathrm{d}\hat{\sigma}_{ij}^{T,b_1}$ introduced to subtract the explicit poles of the one-loop matrix element is after integration of the single unresolved phase-space reintroduced in this term, together with the integrated $\mathrm{d}\hat{\sigma}_{ij}^{T,c_1}$ and $\mathrm{d}\hat{\sigma}_{ij}^{S,d}$ and the appropriate mass factorisation contribution. $\mathrm{d}\hat{\sigma}_{ij}^{U,B}$ cancels the remaining $\epsilon^{-2}$ and $\epsilon^{-1}$ poles present in the first two lines of eq. (3.43).

$$\mathrm{d}\hat{\sigma}^{U,B} \sim \frac{1}{2}\boldsymbol{J}_n^{(1)} \otimes \boldsymbol{J}_n^{(1)} M_n^0\,. \tag{3.109}$$

$\mathrm{d}\hat{\sigma}_{ij}^{U,C}$ - The remaining terms appear, after integration over the corresponding unresolved phase-space, in this contribution. Those include $\mathrm{d}\hat{\sigma}_{ij}^{S,b_1}$, $\mathrm{d}\hat{\sigma}_{ij}^{T,b_2}$, $\mathrm{d}\hat{\sigma}_{ij}^{T,c_2}$ and the part of $\mathrm{d}\hat{\sigma}_{ij}^{T,b_3}$ not considered in $\mathrm{d}\hat{\sigma}_{ij}^{U,A}$. Together with the rest of the NNLO mass factorisation term it cancels all the leftover poles in the last two lines of eq. (3.43).

$$\mathrm{d}\hat{\sigma}^{U,C} \sim \boldsymbol{J}_n^{(2)} M_n^0\,. \tag{3.110}$$

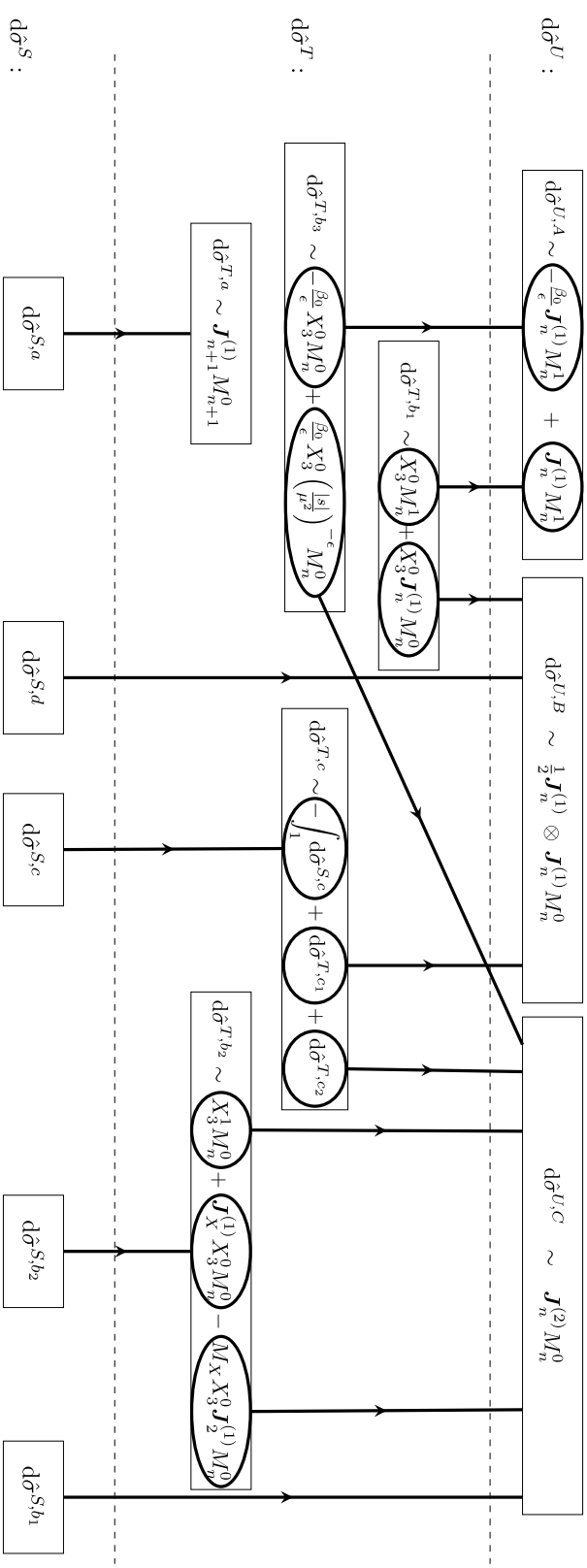


Figure 3.1.: Figure 3 from [48] depicting the interplay of the different pieces of the double real, real virtual and double real subtraction terms. The arrow indicate the connection of integrated and un-integrated contributions.

## 3.6. Jet algorithms

The procedure we described so far enables us to calculate cross sections for the production of elementary particles in hadronic collisions. We also argued that coloured particles, i.e. quarks and gluons, will never be observed as free objects, but rather in form of hadronic bound states. The transition from partonic final states to hadronic final states, the hadronisation, could be ignored due to the idea of factorisation, which allowed us to separate the high energy, short distance interactions from the non-perturbative long distance effects. It is also true that at the energies available at a modern collider the partons will not only form a handful of hadrons, but a plethora of them. Depending on the momentum of the one final state parton starting the hadronisation cascade, we will see a collimated deposit of hadronic energy in our detector, pointing in a clear direction, thus defining a jet. The point is that despite the complicated substructure of an object like a jet its total momentum, i.e. the sum of the momenta of all its constituents, should be largely determined by that of the one parton coming out of the hard scattering. We therefore find a clear relation between the jets measured in an experiment and the composition of the coloured final states as described by the partonic cross section [122].

At leading order the correspondence is clear and one-to-one between quarks/gluons and jets. If, however, we allow for additional coloured final state particles, we have to account for the possibility that two of those partons are close enough that their respective jets merge and cannot be distinguished from a jet originating from a single particle. It is therefore mandatory to come up with some method to cluster the products of the hard interaction at the parton level depending on some distance criterion, in order to obtain an accurate estimate of how the event might be seen in a detector. This methods are what we nowadays call jet algorithms. In hindsight modern algorithms might seem simple, but they are the result of some very sophisticated development, at the beginning of which it was not at all clear how they should be defined consistently between experiment and theory [123]. The most important property they must have is that of IR safety, which means that their definition must not depend on any soft or collinear radiation[11]

In the following we will briefly discuss a class of the most common jet algorithms, the $k_T$ algorithms, a variant of which we use for all of our calculations. Many other, equally valid approaches exists and many of them are reviewed in [124].

The idea of the $k_T$ algorithms is to define two distance measures,

$$d_{ij} = \min\left(k_{T_i}^{2n}, k_{T_j}^{2n}\right) \frac{\sqrt{(\Delta y_{ij})^2 + (\Delta\phi_{ij})^2}}{R^2}\,, \tag{3.111a}$$

$$d_{iB} = k_{T_i}^{2n}\,, \tag{3.111b}$$

where the first describes a separation between particles $i$ and $j$ in the rapidity-azimuth plane, normalised to some jet radius parameter $R$ and weighted with some factor depending on the transverse momenta of the two particles, hence the name of the algorithm. The latter is the distance of particle $i$ from the beam axis, simply parametrised as a power of its transverse momentum again.

[11] IR safety is a feature *all* sensible observables must exhibit.

We then proceed as follows:

1. Evaluate $d_{ij}$ and $d_{iB}$ for all final state particles.
2. Find the smallest element in the set of all distances $\{d\} \coloneqq \bigcup_{i>j}\{d_{ij}, d_{iB}\}$. Then check:
   - $\min\{d\} = d_{ij}$ for some $i, j$. Then the particles $i$ and $j$ are combined to form a composite particle and the algorithm is repeated with the new particle list.
   - $\min\{d\} = d_{iB}$ for some $i$. Then $i$ is regarded as a jet and removed from the list of particles, before starting again with step 1.
3. Terminate when no more particles remain as they are all clustered into jets.

The parameter $n$ in eqs. (3.111) determines the order in which the particles are clustered and consequently also the precise form of the result. While there are arguments for each of the different values of $n$ which have been used in the past, the anti-$k_T$ algorithm [125] ($n = -1$) is nowadays preferred over for example the original $k_T$-algorithm [126, 127] ($n = 1$) or the Cambridge/Aachen (C/A) algorithm [128, 129] ($n = 0$), which can be ascribed to the particular shape of the resultant jets.

# 4. Photons in hadronic collisions

A photon produced in a high energy collision at a hadron collider can serve as an important tool to understand the basic structure of the Standard Model, and maybe even beyond. Understanding the production of an energetic photon pair in a hadronic collision is mandatory for both the estimation of QCD background in Higgs production and in searches for new physics, either in form of new exotic particles decaying into a diphoton state or in off-resonant studies [43, 44]. At the same time the production of an isolated photon with large transverse momentum, inclusively or in association with one or multiple jets, is a means to directly study the underlying QCD dynamics and provides access to the gluon PDF [5–9] already at LO in QCD. Therefore measuring photon production cross sections has always been part of the experimental agenda, from early experiments [13–17] to more recent precision studies [18–38].

In principle hard photons have a clear experimental signature as electromagnetic showers in the detector. In practice the experimental environment is polluted by a plethora of photons not coming from the actual scattering process. For example, during an ordinary hadronic collision event a lot of neutral pions are produced during the hadronisation process after the actual scattering event, which then in turn often decay into a photon pair, $\pi^0 \to \gamma\gamma$. Depending on how boosted the pion was, the photons might even be miscounted as a single photon, in case they are very collimated. It is therefore important to find methods to distinguish the photons originating from the actual scattering, the so called promt photons, from all the others.

Due to the detector effects implementing any kind of photon identification in experiment is a very sophisticated process [130–132], but in principle it boils down to looking for photons well isolated from any hadronic activity, as photons created during hadronisation are very likely to be accompanied by a lot of hadronic radiation. To turn the logic around, a well isolated photon is unlikely to stem from anything else but the hard scattering process. This method of separating the photon is called photon isolation. For each candidate photon in the event some kind of cut on the allowed hadronic energy in the vicinity of the photon is defined. A photon is regarded as an isolated photon, if it passes the test. There are different ways how the isolation can be implemented in practise, both in experiment and theory. They mainly differ by how the vicinity of the photon is defined concretely, or how much hadronic energy we allow, and how it may be distributed around the photon. Independently of how it is eventually done, the actual experimental implementation of photon isolation, which is applied at the event level, is in general very different from the parton level isolation we usually apply in fixed order theory calculations. The experimental isolation can, however, be mapped onto a parton level isolation using unfolding techniques [133, 134], and for the majority of current experiments the isolations used are at the parton level equivalent to a so called fixed cone isolation.

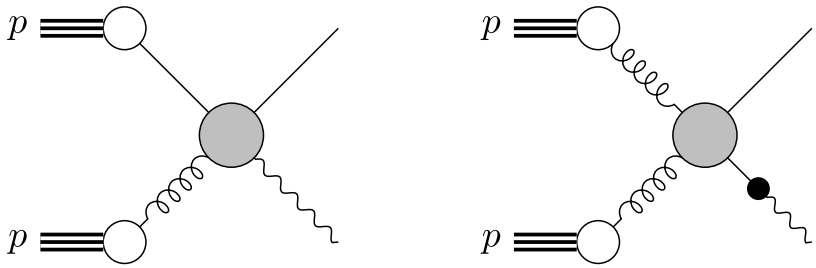


(a) direct contribution (b) fragmentation contribution

Figure 4.1.: The two different production mechanisms for final state photons. Direct production in the hard scattering (a) or non-perturbative fragmentation of a hard parton into a photon (b).

The idea is to define a distance $R$ from the photon in the $\eta - \phi$ plane, $R^2 = \Delta\eta^2 + \Delta\phi^2$, which describes a cone around the photon momentum axis. We then sum up all (transverse) hadronic energy inside the cone, $E_T^{\text{had}}(R)$ and set an upper limit for it,

$$E_T^{\text{had}}(R) < E_T^{\text{max}} \,. \tag{4.1}$$

Only if this inequality is fulfilled, the photon is regarded as isolated. We will describe the class of cone based isolations in more detail in section 4.1. While this type of isolation can be directly implemented on the theory side, the actual calculation is not free of complications, which have their origin in the IR singularity structure of the process. With sufficiently many particles in the final state, nothing prevents a quark to become collinear to the photon, which in QED is an IR divergent limit. Since we explicitly demand the photon to be resolved, we cannot subtract the singularity with our usual techniques. In other words, we are not fully inclusive in the final state any more, hence the KLN theorem is not applicable. This becomes obvious when considering the virtual correction which would normally compensate such collinear divergences. As in the corresponding amplitude the photon appears as a virtual particle, the requirement set by the process definition is not met, we do not have a real final state photon, and thus the correction does not contribute.

Instead the divergence is compensated by the non-perturbative photon fragmentation functions [135, 136], $D_{i\to\gamma}$, which describe the splitting of a parton $i$ into a photon. This is very much like the situation for initial state collinear singularities, which are absorbed by the mass factorisation terms coming from a redefinition of the PDFs. We are therefore forced to split the cross section for isolated photon production into two contributions, the direct contribution, which describes the production of photons as part of the hard partonic scattering, and the fragmentation contribution, describing a jet production process, for which one of the hard partons eventually fragments into a photon, see figure 4.1.

$$\mathrm{d}\sigma^{\gamma} = \mathrm{d}\sigma^{\gamma}_{\text{dir}} + \mathrm{d}\sigma^{\gamma}_{\text{frag}} \,. \tag{4.2}$$

This factorisation is proven to be valid to all orders in QCD [137], in particular also in the presence of photon isolation. The fragmentation contribution can be written as

$$\mathrm{d}\sigma^{\gamma}_{\mathrm{frag}} = \sum_i \int_0^1 \mathrm{d}z\, \mathrm{d}\sigma^i(z) D^{\mathrm{bare}}_{i\to\gamma}(z)\,, \tag{4.3}$$

where $\mathrm{d}\sigma^i$ is the cross section of the inclusive production of parton $i$ instead of the photon and $D^{\mathrm{bare}}_{i\to\gamma}$ the bare (unrenormalised) fragmentation function. The convolution variable $z$ is conventionally defined as the momentum fraction the photon inherits after the splitting of parton $i$. Note that requiring a non-vanishing photon $p_T$ hence directly implies a lower bound $z_{\min} > 0$ for $z$. Like the PDFs the fragmentation functions are renormalised through the introduction of appropriate splitting kernels $\mathbf{\Gamma}_{i\to\gamma}$ (see section 3.4), such that at LO we find[1]

$$D^{(0),bare}_{i\to\gamma}(z) = D^{(0)}_{i\to\gamma}\big(z,\mu_A^2\big) + \tilde{\alpha}\big(\mu_A^2\big)\mathbf{\Gamma}^0_{i\to\gamma}(z,\mu_A^2) + \mathcal{O}\big(\tilde{\alpha}^2\big(\mu_A^2\big)\big) \tag{4.4}$$

with $\tilde{\alpha} = \alpha/2\pi$. The scale $\mu_A^2$ is called the fragmentation scale[2]. Given that it is an unphysical quantity, the dependence of the renormalized fragmentation function on $\mu_A$ must vanish in the all orders result. From this we can derive an evolution equation for the fragmentation function similar to the DGLAP equations for the PDFs. Solving these equations requires input from experiment to fix the boundary conditions. To date only two measurements with sensitivity to the fragmentation functions are available, one of photon production inside jets by ALEPH [138] at LEP and one of inclusive photon production by OPAL [139], also at LEP. Since all other measurements of photon production rely on some form of the cone isolation mentioned above, the dependence on the fragmentation contribution is reduced and influenced by the isolation in a way that an extraction of the fragmentation functions is not possible. Due to the limited data the fragmentation functions suffer from large uncertainties. Therefore, and also because the fragmentation functions are complicated objects on their own, the general wish is to keep their impact on the theory calculation as small as possible.

Note that while the simple photon isolation we mentioned above does suppress the quark-photon collinear configurations and with them also the fragmentation contribution to large extent, the dependence can never fully be removed. As long as the energy of the quark collinear to the photon is smaller than the cut on the hadronic energy, decreased by the energy of other QCD particles in the isolation cone of course, the event will pass the isolation. Lowering this cut to zero in a finite sized phase-space region around the photon would remove the collinear configurations and with it the dependence on the fragmentation functions completely, however, it would also cut away any soft radiation in the cone needed for the proper cancellation of QCD IR singularities in any fixed order calculation.

[1] There is some ongoing controversy whether the non-perturbative photon fragmentation function should be counted with an relative coupling factor of $\alpha$ or $\alpha/\alpha_s$. Here we choose the former option, hence the LO fragmentation function $D^{(0)}_{i\to\gamma}$ contributes at the same order as the splitting kernel, $\tilde{\alpha}\mathbf{\Gamma}^0_{i\to\gamma}$.

[2] We avoid denoting it $\mu_f$ or $\mu_F$ to prevent confusion with the factorisation scale of initial state collinear radiation.

This leaves us with two options:

1. Employ a modified photon isolation prescription, which vetoes any collinear configurations between photon and quark in an IR safe manner. At the same time this will remove any dependency on the fragmentation functions $D_{i\to\gamma}$. The downside of this approach is that we introduce an artificial discrepancy between experimental and theoretical photon isolation, which is a potential source of systematic error to be investigated carefully.

2. Incorporate the fragmentation function into the calculation, despite all the technical complications this approach entails, including a possibly required adaptation of the method used for treating the IR singularities.

We will discuss general approaches to photon isolation first, with some particular examples used to eliminate the fragmentation contribution, in section 4.1. Later on in section 4.2 we will have a brief look how fragmentation could be implemented within the antenna subtraction framework at NLO.

## 4.1. Photon isolation

Different ways to implement photon isolation in a theoretical calculation have been used in the past. In recent studies of photon production at high energy hadron collisions it was almost exclusively the class of cone based isolations. We will therefore, and also because the isolation prescription used throughout this thesis falls into that category, focus mainly on different types of cone isolation. Later on in section 4.1.2 we will shortly discuss other approaches and what advantages they might have over the more traditional isolation prescriptions.

### 4.1.1. Cone based isolation

As already mentioned above, the basic feature of cone based isolations is the definition of a cone around the photon axis, described by the distance $R$ in the $\eta - \phi$ plane,

$$R^2 = \Delta\eta^2 + \Delta\phi^2 \,. \tag{4.5}$$

The transverse energy of any hadronic radiation, which at parton level consists of gluons and (anti-)quarks, within the cone is then summed up an compared to a predefined maximum ,

$$\sum_{R^{i\gamma}<R} E_T^i \equiv E_T^{\mathrm{had}}(R) < E_T^{\mathrm{max}}(E_T^\gamma; r)\,, \tag{4.6}$$

where the sum runs over all partons $i$ inside the cone. Whenever this threshold is exceeded, the candidate photon is not considered as isolated and rejected. The allowed maximum $E_T^{\mathrm{max}}(E_T^\gamma; r)$ is dependent on the photon transverse energy, and can also be defined as a profile in the distance $r$ from the photon. Then more or less energy can be permitted within a given concentric subcone, depending on its radius $r$. In the following we categorise the cone based isolations depending on the precise form of $E_T^{\mathrm{max}}(E_T^\gamma; r)$.

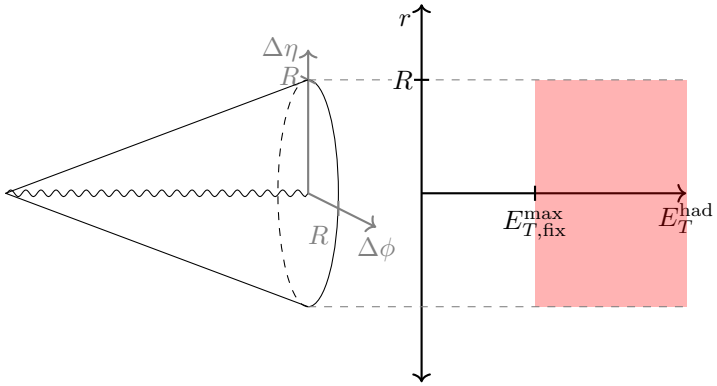


Figure 4.2.: Schematic depiction of the fixed cone isolation criterion. Within a cone around the photon, defined through the radius $R$ in the $\eta - \phi$ plane, only a certain fixed amount of hadronic energy is allowed. How the energy is distributed within the cone is irrelevant. Based on figure I.5(a) in [61].

#### Fixed cone isolation

The fixed cone isolation describes all prescriptions for which the profile defined by $E_T^{\mathrm{max}}(E_T^\gamma; r)$ is independent of $r$, therefore setting a fixed upper cut on the allowed hadronic energy in the whole cone. This is sketched in figure 4.2. Usually one defines

$$E_{T,\mathrm{fix}}^{\mathrm{max}}(E_T^\gamma) = \varepsilon E_T^\gamma + E_T^{\mathrm{thres}}\,, \tag{4.7}$$

such that the amount of tolerated hadronic energy around the photon increases as it becomes more energetic. Basically all photon isolation prescriptions implemented in recent experiments are at the parton level equivalent to this type of cone isolation. Note $E_T^{\mathrm{max}}$ is always strictly greater than 0 ($E_T^{\mathrm{thres}} > 0$, and $E_T^\gamma$ is usually subject to a lower cut). In experiment because of the finite energy resolution of the detector and also in order to not suppress too many events, and in theory to ensure proper treatment of the IR singularity structure. As we mentioned above, this will lead to a dependence on the fragmentation contribution.

Another problem arises in the calculation, even for this comparatively simple setup. In [137] it has been observed that for small values of the cone size the isolated photon NLO cross section exceeds the fully inclusive cross section. Given that the photon isolation actually vetoes part of the events, this is clearly an unphysical result. The origin of this behaviour lies in the artificial separation of the partonic phase-space due to the introduction of the isolation cone. The contributions to the NLO total cross section from both outside and inside the cone show a logarithmic dependence on the cone size $R$,

$$\mathrm{d}\sigma^{\mathrm{in}} \sim \ln R\,, \qquad\qquad \mathrm{d}\sigma^{\mathrm{out}} \sim \ln \frac{1}{R}\,. \tag{4.8}$$

If no isolation is applied, the logarithmic dependence cancels in the sum, so that the total inclusive cross section is independent from the unphysical parameter $R$. However, when the phase-space within the cone is restricted due to any isolation cuts, the exact cancellation between $\mathrm{d}\sigma^{\mathrm{in}}$ and $\mathrm{d}\sigma^{\mathrm{out}}$ is spoiled and a residual logarithmic dependence on $R$ remains. For small radii

this leads to a significant, and in particular unphysical, enhancement of the isolated cross section, which can only be cured by a resummation of the logarithms, which for the fixed cone isolation has been performed to leading logarithmic (LL) accuracy in [140]. The effect proved to be negligible for realistic cone sizes $R \sim 0.4$, but should be considered when going to values of $R < 0.1$.

As mentioned previously, the fixed cone isolation is the predominant isolation prescription used in current experiments. In the mid 1990s and early 2000s the $D0$ experiment at the Tevatron used a slight modification of the fixed cone isolation, dubbed hollow cone isolation [141–143]. Here a second cone around the photon is defined, within the actual isolation cone. Inside this inner cone no isolation is applied whatsoever. This should account for the complications in defining the event level experimental isolation in the detector cells hit by the electromagnetic shower representing the photon. In [140] the impact of a small inner cone radius $R_h$ was investigated. For this setup the total cross section shows a behaviour inverse to that of the narrow fixed cone[3], with an unphysical logarithmic suppression of the cross section. The authors of [140] conclude, that at least a LL resummation of the problematic terms is needed to get reliable NLO results when using the hollow cone prescription.

We should note that current experiments use more sophisticated methods to deal with the difficulties of defining photon isolation in the region of the electromagnetic cluster, in away that the hollow cone isolation has been abandoned in favour of the standard fixed cone isolation.

### Smooth cone isolation

Smooth cone isolation, sometimes called dynamical and often Frixione isolation [144], makes the cut on the allowed hadronic energy explicitly dependent some $r \leq R$, such that for a given concentric subcone with radius $r$

$$E_{T,\mathrm{dyn}}^{\mathrm{max}}(E_T^\gamma; r) = \chi(r) E_{T,\mathrm{fix},d}^{\mathrm{max}}(E_T^\gamma) = \chi(r)\left(\varepsilon_d E_T^\gamma + E_{T,d}^{\mathrm{thres}}\right), \tag{4.9}$$

with the profile function $\chi(r)$ defined for all $r \leq R$. Its main purpose is to veto any hadronic radiation collinear to the photon in order to completely remove the dependence on the fragmentation contribution. To this end, $\chi(r)$ needs to tend to 0 as $r \to 0$ in a smooth way,

$$\chi(r) \xrightarrow[r\to 0]{} 0\,. \tag{4.10}$$

In principle the exact form of the profile is arbitrary, conventionally one uses

$$\chi(r) = \left(\frac{1-\cos r}{1-\cos R}\right)^n \tag{4.11}$$

or

$$\chi(r) = \left(\frac{r}{R}\right)^{2n}. \tag{4.12}$$

[3] Which makes sense, as the hollow part of the hollow cone isolation is nothing but an "inverse" isolation cone.

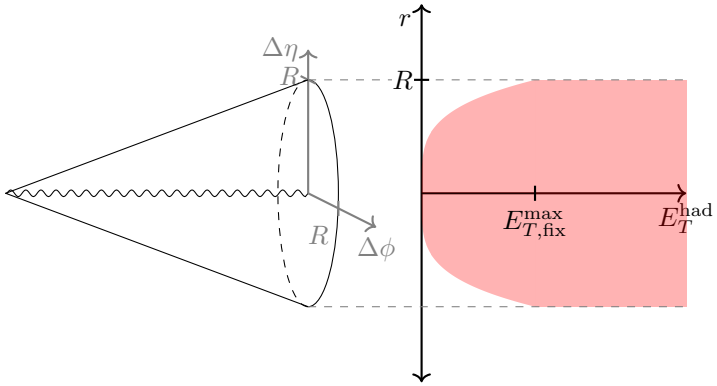


Figure 4.3.: Schematic depiction of the smooth cone isolation criterion. The maximum allowed hadronic energy within the cone is now an $r$-dependent quantity, according to eq. (4.9). The profile $\chi(r)$ smoothly tends to zero as $r \to 0$, thus suppressing any radiation collinear to the photon. For the plot we used the specific form given in eq. (4.12) with $n = 2$. Based on figure I.5(b) in [61].

Note that the latter form is nothing but the first term in the expansion of the first profile for small $r$ and $R$. Unless stated otherwise we will exclusively consider the first profile when talking about smooth isolation. A schematic depiction of the smooth cone isolation is presented in figure 4.3. While applying smooth cone isolation simplifies the theory calculation quite significantly by removing the fragmentation contribution, it inevitably introduces a systematic error, as it differs from the fixed cone isolation prescription used in experiments. In order to minimize the impact of this discrepancy a tight isolation accord has been proposed [145–147], defining a range of parameters to be used in the smooth cone isolation to mimic the fixed cone isolation as closely as possible. While a small uncertainty remains, the advantages from dropping the fragmentation contribution have been considered greater, such that the smooth cone isolation has been used in almost all recent fixed order calculations for isolated photon and diphoton studies [148–151].

Given the finite resolution of the detectors, it is not possible to remove the discrepancy by applying a smooth cone isolation in experiment. There have been studies of how the smooth profile could be approximated by using a discretised form, matched to the layout of the detector cells [152–154], see figure 4.4. The problem with this, however, is, that we have to allow for a small finite amount of hadronic energy in the innermost cone to ensure proper cancellation of the IR singularities in the calculation. This in turn reintroduces a sensitivity on the fragmentation contribution, thus nullifying the reason why we implemented the smooth cone isolation in the first place.

Like the fixed cone isolation the smooth cone isolation suffers from unphysical logarithmic enhancements when the cone radius is small. A resummation of these terms at LL accuracy has been performed recently in [155]. For a realistic choice of isolation parameters as proposed in the tight isolation accord the effects are again negligible. In [155] it was also pointed out that non-global logarithms appear in both the fixed and smooth cone isolation preventing up to now an understanding of their all-order structure.

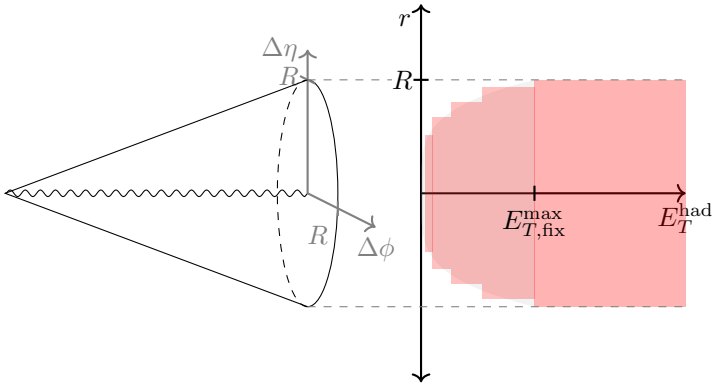


Figure 4.4.: A discretised version of the smooth cone isolation, matched to the granularity of the detector.

### Hybrid isolation

A way how the difference between the experimental and theoretical isolation prescriptions can be reduced, is the implementation of the so called hybrid isolation, first introduced in [156] and used by ATLAS in their 13 TeV study of photon-plus-jet production [34] in order to compare the data to NLO predictions produced with SHERPA [156–158]. The basic idea is to perform a staged isolation, combining both the fixed cone and the smooth cone isolation, such that

$$E_{T,\mathrm{hyb}}^{\mathrm{max}}(E_T^\gamma; r; R_d) = \begin{cases} \min\left(E_{T,\mathrm{fix}}^{\mathrm{max}}(E_T^\gamma), E_{T,\mathrm{dyn}}^{\mathrm{max}}(E_T^\gamma; r)\right), & (0 \le r < R_d) \\ E_{T,\mathrm{fix}}^{\mathrm{max}}(E_T^\gamma), & (R_d \le r < R) \end{cases} . \tag{4.13}$$

While overall a fixed cone isolation is applied to the photon, in a small concentric sub-cone of size $R_d < R$ we invoke an additional smooth cone isolation, so that any radiation collinear to the photon is vetoed and the fragmentation contribution removed. Figure 4.5 gives an impression of the isolation profile. Note that for $R_d = 0$ we just reproduce the fixed cone isolation. Because we neglect the fragmentation contribution the limit $R_d \to 0$, however, is not smooth. We will discuss this issue in more detail later on.

In the following we will often refer to the region in which the smooth cone isolation is defined as the *inner cone*, while the rest of the isolation cone is the *outer cone*. The advantage of the hybrid isolation is, that the parameters of the fixed cone isolation can be matched exactly to the fiducial parameters used in a given experiment. The only discrepancy between the theoretical and experimental isolation is then related to the parameters of the smooth isolation in the inner cone. When we choose $R_d^2 \ll R^2$, only a small fraction of the isolation cone is affected and the dependence on the technical parameters of $E_{T,\mathrm{dyn}}^{\mathrm{max}}(E_T^\gamma; r)$ should be much reduced compared to the standard smooth cone isolation. At the same time it should provide a good approximation of the fixed cone isolation, without the need to introduce the fragmentation contribution. The hybrid isolation has been used recently for the NNLO QCD calculations of inclusive photon and photon-plus-jet production [74, 159] and diphoton production [160, 161].

The concrete setup, however, is not without pitfalls, and a careful investigation of the interplay of the different isolation parameters is advisable. The first issue one encounters lies in the precise

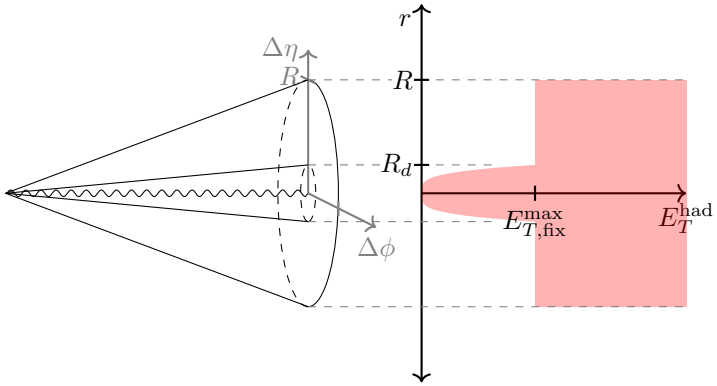


Figure 4.5.: Schematic depiction of the hybrid cone isolation criterion. A small smooth cone regulates the quark-photon collinear singularity, while the larger fixed cone isolation exactly mimics the isolation used in the experiment. The profile shown here corresponds to the matched hybrid isolation as defined in eq. (4.18). Based on figure I.5(c) in [61].

setup of the inner cone. In principle nothing prevents us from choosing a different $E_{T,\mathrm{fix}}^{\mathrm{max}}(E_T^\gamma)$ in the definition of the smooth cone than for the actual fixed cone isolation, i.e.

$$E_{T,\mathrm{fix},d}^{\mathrm{max}}(E_T^\gamma) \neq E_{T,\mathrm{fix}}^{\mathrm{max}}(E_T^\gamma) \qquad (\text{inner cone})\,. \tag{4.14}$$

In addition the profile $\chi(r)$ might be chosen such that

$$E_{T,\mathrm{dyn}}^{\mathrm{max}}(E_T^\gamma; r = R_d) \neq E_{T,\mathrm{fix}}^{\mathrm{max}}(E_T^\gamma)\,. \tag{4.15}$$

Both configurations (see figures 4.6a,4.6b) can lead to either a reduced effective size of the inner cone, or a discontinuity at $r = R_d$, potentially introducing instabilities in the calculation [45, 147]. Those problems are entirely avoided by defining the so called matched hybrid isolation. It puts the additional constraints that

$$E_{T,\mathrm{fix},d}^{\mathrm{max}}(E_T^\gamma) = E_{T,\mathrm{fix}}^{\mathrm{max}}(E_T^\gamma) \tag{4.16}$$

and

$$\chi(r < R_d) \leq 1\,, \qquad \chi(r = R_d) = 1\,. \tag{4.17}$$

The definition (4.13) can then be rewritten as

$$E_{T,\mathrm{hyb,matched}}^{\mathrm{max}}(E_T^\gamma; r; R_d) = E_{T,\mathrm{fix}}^{\mathrm{max}}(E_T^\gamma) \begin{cases} \chi(r)\,, & (0 \leq r < R_d) \\ 1\,, & (R_d \leq r < R) \end{cases}, \tag{4.18}$$

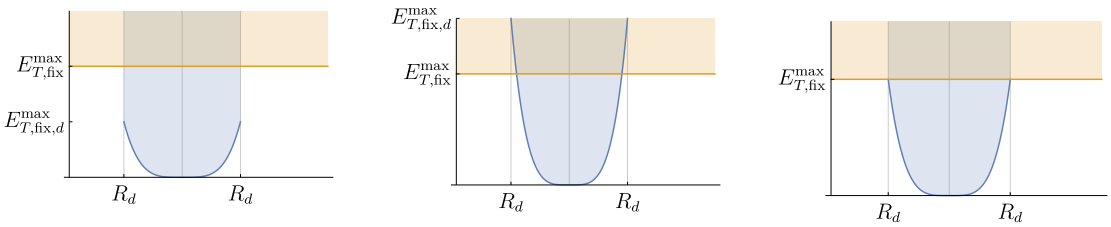


(a) "jump" in the isolation profile

(b) inner cone radius effectively reduced

(c) matched hybrid isolation

Figure 4.6.: Hybrid isolation with different parameters for the inner cone, independent of the outer cone parameters (a),(b) and matched to the outer cone parameters (c). The first two cases potentially lead to numerical instabilities.

with $\chi(r)$ as in eq. (4.17) (see figure 4.6c). Note that above formula shows that the hybrid isolation is in a sense a special form of the smooth cone isolation, with the profile

$$\chi(r)_{\mathrm{matched}} = \begin{cases} \chi(r)\,, & (0 \leq r < R_d) \\ 1\,, & (R_d \leq r < R) \end{cases} \qquad \text{(matched hybrid)}\,. \tag{4.19}$$

In the 2019 Les Houches report [61] a detailed study of the matched hybrid isolation has been performed. Comparing to the study of hybrid isolation in [74], which does not use the matched version, it becomes evident that the impact of the mismatch at the inner cone boundary is negligible, at least as long as tight isolation parameters are chosen for the smooth cone. In both cases, matched and non-matched, the behaviour is much more affected by the radius $R_d$ of the inner cone.

Following the argument about narrow cones we presented above, at NLO we expect to encounter an unphysical $\log(1/R_d)$ behaviour as $R_d \to 0$. This is a purely geometric effect and will not be compensated by the inclusion of higher order corrections. In general their logarithmic behaviour will be more complicated, but this does not mean higher order corrections will inevitably lead to an aggravation of the effect. The parameter $R_d$ therefore has to be chosen with care; not too small, in order to avoid to end up in the unphysical configuration, and not too large, so that the condition $R_d^2 \ll R^2$ which we based the motivation for the hybrid isolation on is not violated. The dependence of total and differential cross sections on the parameters of the hybrid isolation will be subject of chapter 7.

### 4.1.2. Other isolation methods

While the cone based isolations are clearly the predominant approach to photon isolation in both theory and experiment, there are other ways to set about it. Defining a cone dissecting the parton phase-space is a very direct and graphical ansatz, but it does not really consider the underlying processes of photon production. In some cases it might be useful to construct the isolation precisely around these structures.

### Democratic clustering

In [162] it has been proposed to treat photons and QCD partons democratically in the jet clustering algorithm, thus forming clusters with a certain amount of photonic energy,

$$E_\gamma = z(E_\gamma + E_{\text{had}})\,, \tag{4.20}$$

where $z \leq 1$ is defined as the fraction of the clusters' total energy carried by the photon. A cluster is then identified with an isolated photon when $z$ exceeds a certain threshold value $z_{\text{cut}}$. In a setup like this the fragmentation contribution is *enhanced*, a situation which we tried to avoid when employing the cone based isolations, in particular the smooth cone and hybrid isolation. For the extraction of the photon fragmentation function from experimental data[4], however, this is clearly not optimal. Proposing a theoretical means to measure the (quark-to-)photon fragmentation functions at LEP has indeed been the main motivation of the authors of [162].

A isolation prescription like this might also be useful when considering higher order EW corrections to the production of photons in association with jets. Unlike in pure QCD, where for a given process the number of photons is always constant, when considering EW and in particular QED corrections, we can have additional real radiation photons in the final state. These photons can in principle become unresolved, or non-isolated with respect to whatever isolation method is applied, without having the event being rejected (as would happen in QCD, where the number of resolved, isolated photons *defines* the process). For jet observables it is therefore important to know about any photonic component of the cluster, and precisely how big this contribution is. If it is too large, the jet would actually be counted as an isolated photon, thus not entering the jet observable. While for cone based isolations it is not obvious how this can be achieved in a meaningful way, the democratic clustering approach presents itself as a natural solution.

### Soft drop isolation

Related to the democratic clustering is the method dubbed soft drop isolation [163]. Unlike the former it is based on jet *declustering*, in particular the soft drop declustering technique introduced in [164]. The main goal of soft drop declustering is the removal of wide-angle soft radiation from a jet ("jet grooming") and the identification of hard subjets. This is achieved by tracing back the algorithm to construct the jet in the first place, breaking it up into its two main subjets. Those are then subject to the condition

$$\frac{\min\left(p_T^1, p_T^2\right)}{p_T^1 + p_T^2} > z_{\text{cut}} \left(\frac{R_{12}}{R}\right)^\beta\,, \tag{4.21}$$

where $p_T^i$ is the transverse momentum of subjet $i$, $R_{12}$ the distance of the subjets in the $\eta - \phi$ plane, $R$ the jet radius, and $z_{\text{cut}}$ and $\beta$ the technical parameters of the procedure. Whenever the condition is violated, the softer of the two constituents is removed from the jet, thus eliminating any soft contributions. Note that $R_{12}$ increases as the angular separation increases, thus

[4] Remember that the fragmentation functions need input from experiment to fix the boundary conditions of their evolution.

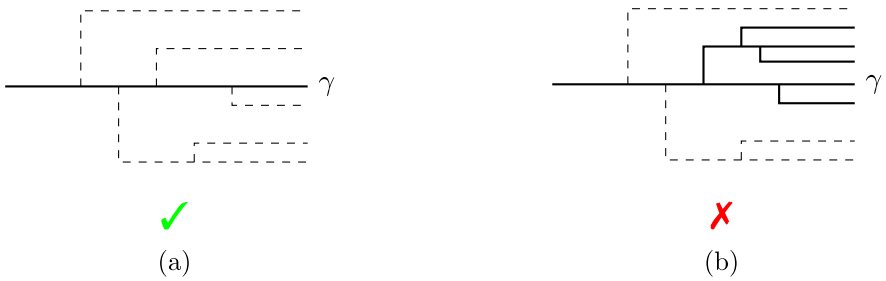


Figure 4.7.: Figure 2 from [163]: Schematic depiction of the soft drop isolation. During the declustering constituents to the photon-jet are dropped (dashed lines) when they violate the soft drop condition (4.21). A photon is deemed as isolated when it is the only particle remaining in the jet after the algorithm stops (a). If other particles remain clustered with the photon, it is not isolated (b).

putting tighter constraints on any wide-angle radiation. We then repeat the procedure with the remaining subjet. The recursion stops as soon as the condition is met and a (sub)jet cannot be dissected any further.

The idea of soft drop isolation is to turn this procedure around: if a given photon-jet cluster fails during the soft drop declustering at all stages, we will eventually arrive at a single particle forming the "jet". If this particle is a photon, it can safely be regarded as an isolated photon. The procedure is sketched in figure 4.7. Note that the particular form of the inequality (4.21) leads to a full suppression of any collinear radiation, thus removing the dependence on the fragmentation contribution: For collinear radiation we have $R_{12} \to 0$, which in turn sets the soft drop threshold to zero. But then the collinear configuration will pass the test, so that the two particles remain clustered and are therefore not isolated. In fact in [163] it is shown that the soft drop isolation is equivalent to smooth cone isolation in the limit of small $z_{\text{cut}}$ and $R$. The authors use this novel technique to expose the QED quark-to-photon splitting function $P_{q\gamma}$ by investigating the kinematics of a photon subjet within a quark-like parent jet, and furthermore suggest to study how the detector granularity, which was the motivation for the discretised smooth cone isolation, could be portrayed using soft drop isolation.

Like the democratic clustering, soft drop isolation in combination with soft drop declustering could also be useful when studying higher order QED corrections.

## 4.2. Photon Fragmentation at NLO

When we do not remove the radiation collinear to the photon, either because we did not use a photon isolation prescription which does so, or did not use any isolation at all in case we are interested in fully inclusive cross sections, we have to account for the fragmentation contribution. The parton level equivalent (stripped off the PDFs) of the symbolic factorisation formula (4.2) reads

$$\mathrm{d}\hat{\sigma}^{\gamma}_{ij} = \mathrm{d}\hat{\sigma}^{\gamma}_{ij,\text{dir}} + \mathrm{d}\hat{\sigma}^{\gamma}_{ij,\text{frag}}\,, \tag{4.22}$$

where the direct component up to NLO takes its usual form,

$$\mathrm{d}\hat{\sigma}^{\gamma}_{ij,\mathrm{dir}} = \int_n \mathrm{d}\hat{\sigma}^{\gamma,B}_{ij} + \int_{n+1} \mathrm{d}\hat{\sigma}^{\gamma,R}_{ij} + \int_n \left[\mathrm{d}\hat{\sigma}^{\gamma,V}_{ij} + \mathrm{d}\hat{\sigma}^{\gamma,MF}_{ij}\right] \tag{4.23a}$$

$$= \int_n \mathrm{d}\hat{\sigma}^{\gamma,B}_{ij} + \int_{n+1} \left[\mathrm{d}\hat{\sigma}^{\gamma,R}_{ij} - \mathrm{d}\hat{\sigma}^{\gamma,S}_{ij}\right] + \int_n \left[\mathrm{d}\hat{\sigma}^{\gamma,V}_{ij} - \mathrm{d}\hat{\sigma}^{\gamma,T}_{ij}\right]. \tag{4.23b}$$

We explicitly introduced the real and virtual subtraction terms, which we split in two parts each. One corresponds to the subtraction of all QCD IR singularities and the other will subtract the quark-photon collinear limit ,

$$\mathrm{d}\hat{\sigma}^{\gamma,S}_{ij} = \mathrm{d}\hat{\sigma}^{\gamma,S}_{ij,QCD} + \mathrm{d}\hat{\sigma}^{\gamma,S}_{ij,\gamma}\,, \tag{4.24a}$$

$$\mathrm{d}\hat{\sigma}^{\gamma,T}_{ij} = \mathrm{d}\hat{\sigma}^{\gamma,T}_{ij,QCD} + \mathrm{d}\hat{\sigma}^{\gamma,T}_{ij,\gamma}\,. \tag{4.24b}$$

The QCD virtual subtraction term is constructed as usual out of the integrated real subtraction combined with the mass factorisation contribution,

$$\mathrm{d}\hat{\sigma}^{\gamma,T}_{ij,QCD} = -\int_1 \mathrm{d}\hat{\sigma}^{\gamma,S}_{ij,QCD} - \mathrm{d}\hat{\sigma}^{\gamma,MF}_{ij}\,. \tag{4.25}$$

If we were inclusive over the photon, i.e. allowing it to become soft or collinear to the initial states, too, we could define the photonic integrated subtraction term in precisely the same way,

$$\mathrm{d}\hat{\sigma}^{\gamma,T}_{ij,\gamma}\Big|_{\mathrm{incl.}} = -\int_1 \mathrm{d}\hat{\sigma}^{\gamma,S}_{ij,\gamma} - \mathrm{d}\hat{\sigma}^{\gamma,MF}_{ij,\gamma}\,. \tag{4.26}$$

The explicit $\epsilon$ poles of this term will then cancel against those of the corresponding virtual QED correction. However, since we are explicitly demanding a resolved photon in the final state a few things change. For one thing we will not have to worry about the soft or initial state collinear limits associated with the photon. The photonic mass factorisation term $\mathrm{d}\hat{\sigma}^{\gamma,MF}_{ij,\gamma}$ drops out and there will not be any virtual QED corrections at the given order in $\alpha$, the poles of which we would have to cancel. On the other hand we are then left with the final state photon-quark collinear divergence. One can show that when integrating over the phase-space it can again be turned into an explicit $\epsilon$ pole which will eventually cancel against a term coming from the fragmentation contribution, which up to NLO reads

$$\mathrm{d}\hat{\sigma}^{\gamma}_{ij,\mathrm{frag}} = \sum_a \int_{z_{\min}}^1 \mathrm{d}z \int_n \mathrm{d}\hat{\sigma}^{B,a}_{ij} D^{(0),\mathrm{bare}}_{a\to\gamma}(z)\,. \tag{4.27}$$

At NLO[5] we can have only $a = q, \bar{q}$. The lower bound $z_{\min}$ on convolution variable $z$ is directly related to the fiducial and isolation cuts we impose on the photon. Using eq. (4.4) we can expand the bare fragmentation function into the renormalised fragmentation function and a

[5]Remember that we count the LO fragmentation function with an additional power of $\alpha$ instead of $\alpha/\alpha_s$, so that it contributes at the NLO level. If we had made the other choice, we would also get contributions from higher orders from the fragmentation function introducing $g \to \gamma$ splittings.

piece containing the parton-to-photon splitting kernel, which we will call the final state mass factorisation (FSMF)

$$\mathrm{d}\hat{\sigma}^{\gamma}_{ij,\mathrm{frag}} = \sum_a \int_{z_{\min}}^1 \mathrm{d}z \int_n \mathrm{d}\hat{\sigma}^{B,a}_{ij} D^{(0)}_{a\to\gamma}(z,\mu_A^2) + \int_{z_{\min}}^1 \mathrm{d}z \underbrace{\int_n \frac{\alpha}{2\pi} \sum_a \mathrm{d}\hat{\sigma}^{B,a}_{ij} \mathbf{\Gamma}^0_{a\to\gamma}(z,\mu_A^2)}_{\mathrm{d}\hat{\sigma}^{\gamma,FSMF}_{ij}} . \tag{4.28}$$

We can then write down the photonic virtual subtraction term as

$$\mathrm{d}\hat{\sigma}^{\gamma,T}_{ij,\gamma} = -\int_{z_{\min}}^1 \mathrm{d}z \left[ \int_{1/\{z\}} \mathrm{d}\hat{\sigma}^{\gamma,S}_{ij,\gamma} + \mathrm{d}\hat{\sigma}^{\gamma,FSMF}_{ij} \right], \tag{4.29}$$

where the $\int_{1/\{z\}}$ denotes the integration over the unresolved phase-space while remaining differential in $z$. The term in the square brackets is free from explicit $\epsilon$ poles, as they cancel between the (partially) integrated subtraction term and the final state mass factorisation contribution. Note that going from eq. (4.29) to the inclusive case eq. (4.26) cannot trivially be achieved by sending $z_{\min} \to 0$. In fact the integral over the FSMF contribution will diverge in this limit, reflecting the soft photon singularity which can only be properly absorbed into the corresponding virtual corrections.

The fragmentation contribution up to NLO in $D_{i\to\gamma}$ has been implemented for diphoton, dihadron and photon-plus-hadron production in the DIPHOX [165–167] program, and similarly in its sibling dedicated to inclusive photon and photon-plus-jet production, JETPHOX [137, 168, 169]. Both programs use the BFG parametrisation [170] of the photon fragmentation functions[6]. Despite their age they are the state of the art tool used by experimental collaborations to produce Monte Carlo samples at NLO accuracy for comparison to data. This is also because there are no other implementations of the fragmentation available which go beyond NLO QCD. We will use JETPHOX in chapter 7, when we study the dependence of the inclusive photon and photon-plus-jet cross sections on the parameters of the hybrid isolation.

Both DIPHOX and JETPHOX rely on a combination of Catani-Seymour [110, 171] subtraction and phase-space slicing as used in [172–174] to subtract IR singularities. In the following we will present a short outline how the fragmentation contribution can be implemented when using antenna subtraction at the NLO level. The two new key ingredients we need compared to the QCD subtraction are a refined phase-space factorisation, making the dependence on $z$ explicit, and new (partially) integrated antenna functions, differential in $z$. This discussion can serve as a base for the extension to NNLO, which is subject of current research.

### 4.2.1. Fragmentation with antennae at NLO

We start construction the real subtraction terms by analysing which unresolved configurations can actually occur, and how this reduces the number of antennae needed. Since in the antenna subtraction method a photon is equivalent to an abelian gluon, which can be colour connected to (anti-)quarks only, the only antenna we need for the NLO real subtraction term is

[6] Programs from the PHOX family take the non-perturbative fragmentation functions as $\mathcal{O}(\alpha/\alpha_s)$ in the power counting.

the $A_3^0(q,g,\bar{q})$ [48] , which sandwiches a gluon/photon between a $q\bar{q}$-pair and subtracts all potential IR limits in which the gluon/photon becomes unresolved. Moreover the photon is required to be always in the final state, as well as one of the hard radiators, reducing the phase-space mappings to be considered to final-final and initial-final[7]. The real subtraction term for the photon becoming collinear to quark $i$ in the final-final configuration then reads

$$\begin{aligned}\mathrm{d}\hat{\sigma}^{\gamma,S,FF} = \mathcal{N}^R \sum_{\text{perm.}} \mathrm{d}\Phi_{n+1}\left(\dots, i_q, j_\gamma, \check{k}_{\bar{q}}, \dots; p_1, p_2\right) \frac{1}{S_{n+1}} \\ \times Q_q^2 A_3^0(i_q, j_\gamma, \check{k}_{\bar{q}}) M_n^0(\dots, I, \check{K}, \dots) J_n^{(m)}(\{\tilde{k}\}_n; z)\,, \end{aligned} \tag{4.30}$$

where the photon momentum fraction $z$ of the mapped momentum $I$ is defined as

$$z = \frac{s_{jk}}{s_{ik} + s_{jk}}\,. \tag{4.31}$$

The crucial point is that now the jet function $J_n^{(m)}$ explicitly depends on $z$. Because it applies the jet algorithm and any cuts on the photon, it needs to know the momentum of the photon in the collinear quark-photon cluster. In contrast to the ordinary QCD subtraction we now also have an explicit quark charge factor $Q_q^2$. Here the anti-quark has the role of a spectator parton, indicated by the check-mark assigned to its momentum, $\check{k}_{\bar{q}}$. While the $A_3^0$ antenna could in principle properly account for the $\bar{q}||\gamma$ limit, $z$ vanishes for this configuration and the jet function is constructed such that it evaluates to zero, as we expect a $z > 0$ for a resolved photon. This is a purely technical issue, which can be compensated by introducing an equivalent subtraction term for the $\bar{q}||\gamma$ limit.

To integrate the subtraction term we have to rewrite the three body phase-space appearing in the final-final phase-space factorisation (3.78) so that we can pull out an explicit integration over $z$,

$$\mathrm{d}\Phi_{n+1}\left(\dots, i_q, j_\gamma, \check{k}_{\bar{q}}, \dots; p_1, p_2\right) = \mathrm{d}\Phi_n(\dots, I_q, \check{K}_{\bar{q}}, \dots; p_1, p_2)\, \mathrm{d}\Phi^{FF}_{X_{ijk}/\{z\}}\, \mathrm{d}z\,. \tag{4.32}$$

We can then integrate the final-final real subtraction over the unresolved phase-space while staying differential in $z$. We obtain

$$\begin{aligned}\int_{1/\{z\},\gamma} \mathrm{d}\hat{\sigma}^{\gamma,S,FF} = -\mathcal{N}^V \frac{1}{S_n} \sum_{perm.} \mathrm{d}\Phi_n(\dots, I_q, \check{K}_{\bar{q}}, \dots; p_1, p_2) \\ \times Q_q^2 \mathcal{A}_3^{0,FF}(s_{IK}; z) M_n^0(\dots; I_q, \check{K}_{\bar{q}}; \dots) J_n^{(m)}(\{\tilde{k}\}_m; z)\,, \end{aligned} \tag{4.33}$$

with the now $z$ dependent integrated antenna function

$$\mathcal{A}_3^{0,FF}(s_{IK}; z) = \frac{1}{C(\epsilon)} \int \mathrm{d}\Phi^{FF}_{X_{ijk}/\{z\}}\, A_3^0(i_q, j_\gamma, \check{k}_{\bar{q}})\,. \tag{4.34}$$

[7] We are only interested in collinear limits and not the soft photon limit, as we are looking for a hard resolved photon in the final state. Configurations with a soft photon allow for both hard radiators in the initial state, but would be rejected by the event cuts. The situation changes when we consider real QED radiation as part of EW corrections, see chapter 10.

The explicit poles of $\mathcal{A}_3^{0,FF}$ are cancelled by the final state mass factorisation kernel. We can write out the final state mass factorisation term in eq. (4.29),

$$\begin{aligned}\mathrm{d}\hat{\sigma}^{\gamma,FSMF} =& \frac{\alpha}{2\pi}\mathrm{d}\hat{\sigma}_{ij}^{B,q}\mathbf{\Gamma}^0_{q\to\gamma}(z,\mu_A^2)\\ =& \mathcal{N}'\mathcal{N}^V\sum_{\text{perm.}}\mathrm{d}\Phi_n\left(\{k\}_n;p_1,p_2\right)\frac{1}{S_n}M_n^0(\dots;i_q,k_{\tilde{q}};\dots)\\ &\times Q_q^2\Gamma^0_{q\gamma}(z,\mu_A^2)J_n^{(m)}(\{k\}_m;z)\,,\end{aligned} \tag{4.35}$$

where we used[8]

$$\mathrm{d}\hat{\sigma}^{B,q} = \mathcal{N}_{\text{jet}}^{LO}\sum_{\text{perm.}}\mathrm{d}\Phi_n\left(\{k\}_n;p_1,p_2\right)\frac{1}{S_n}M_n^0(\dots;i_q,k_{\tilde{q}};\dots)J_n^{(m)}(\{k\}_m;z)\,, \tag{4.36}$$

and

$$\mathbf{\Gamma}^0_{q\to\gamma}\left(z,\mu_A^2\right) = 8\pi^2C(\epsilon)Q_q^2\Gamma^0_{q\gamma}\left(z,\mu_A^2\right), \tag{4.37}$$

with $8\pi^2C(\epsilon) = (4\pi)^\epsilon e^{-\gamma\epsilon}$ (see eq. (3.81)). The quantity $\Gamma^0_{q\gamma}$ is directly linked to the quark-to-photon splitting function [162, 175][9],

$$\Gamma^0_{q\gamma}(z,\mu_A^2) = \frac{1}{\epsilon}\mu_A^{-2\epsilon}P_{q\gamma}(z)\,. \tag{4.38}$$

The normalisation factors are related through $\mathcal{N}^V = C(\epsilon)\mathcal{N}^R = C(\epsilon)(4\pi\alpha)\mathcal{N}_{\text{jet}}^{LO}$. In eq. (4.35) $\mathcal{N}'$ is a dimensionless constant compensating potential differences in the normalisation of the photonic and jet matrix elements[10]. The full final-final virtual subtraction term is then given by

$$\begin{aligned}\mathrm{d}\hat{\sigma}^{\gamma,T,FF} = -\int_{z_{\text{cut}}}^1\mathrm{d}z\,\Bigg[&\mathcal{N}^V\frac{1}{S_n}\sum_{perm.}\mathrm{d}\Phi_n(\dots,I_q,\check{K}_{\bar{q}},\dots;p_1,p_2)\\ &\times Q_q^2\mathbf{J}_2^{(1)}(I_q,\check{K}_{\bar{q}};z)M_n^0(\dots,I_q,\check{K}_{\bar{q}},\dots;p_1,p_2)J_n^{(m)}(\{\tilde{k}\}_n;z)\Bigg]\,,\end{aligned} \tag{4.39}$$

with the integrated dipole

$$\mathbf{J}_2^{(1)}(i_q,k_{\tilde{q}};z) = \mathcal{A}_3^{0,FF}(s_{IK};z) - \mathcal{N}'\Gamma^0_{q\gamma}\left(z,\mu_A^2\right). \tag{4.40}$$

In the initial-final configuration we have

$$\begin{aligned}\mathrm{d}\hat{\sigma}^{\gamma,S,IF} =& \mathcal{N}^R\sum_{\text{perm.}}\mathrm{d}\Phi_{n+1}\left(\dots,i_q,j_\gamma,\dots;\check{1}_{\bar{q}},p_2\right)\frac{1}{S_{n+1}}\\ &\times Q_q^2A_3^0(i_q,j_\gamma,\check{1}_{\bar{q}})M_n^0(\dots,I,,\dots;\check{\check{1}}_{\bar{q}},p_2)J_n^{(m)}(\{\tilde{k}\}_n;z)\,,\end{aligned} \tag{4.41}$$

[8] The jet function depends on $z$ because the momentum of the quark is written in terms of the photonic momentum, $k_q = k_\gamma/z$.
[9] A factor $\mu^{2\epsilon}$ introduced by working in $d = 4-2\epsilon$ dimensions has been absorbed in the overall normalisation.
[10] In NNLOJET this factor is 1/2 for historical reasons.

with

$$z = \frac{s_{j1}}{s_{i1} + s_{j1}} \,. \tag{4.42}$$

The initial state hard radiator will always take the role of the spectator as we are only interested in the final-final quark-photon collinear limit. Again we have to make the $z$ integration explicit in the initial-final phase-space factorisation (3.87) in order to obtain the integrated $z$-dependent antenna function,

$$\mathrm{d}\Phi_{n+1}\left(\ldots, i_q, j_\gamma, \ldots; \check{1}_{\bar{q}}, p_2\right) = \mathrm{d}\Phi_n\left(\ldots, I_q, \ldots; \check{\check{1}}_{\bar{q}}, p_2\right) \frac{\mathrm{d}x}{x}\, \mathrm{d}\Phi^{IF}_{X_{ijk}/\{z\}}\, \mathrm{d}z \,. \tag{4.43}$$

For the integrated subtraction term we then get

$$\begin{aligned}\int_{1/\{z\},\gamma} \mathrm{d}\hat{\sigma}^{\gamma,S,IF} = -\mathcal{N}^V \int \frac{\mathrm{d}x}{x} \frac{1}{S_n} \sum_{perm.} \mathrm{d}\Phi_n(\ldots, I_q, \ldots; \check{\check{1}}_{\bar{q}}, p_2) \\ \times Q_q^2 \mathcal{A}_3^{0,IF}(s_{1I}; z) M_n^0(\ldots, I_q, \ldots; \check{\check{1}}_{\bar{q}}, p_2) J_n^{(m)}(\{\tilde{k}\}_n; z)\,,\end{aligned} \tag{4.44}$$

with the initial-final $z$ dependent integrated antenna

$$\mathcal{A}_3^{0,IF}(s_{1I}; z) = \frac{1}{C(\epsilon)} \int \mathrm{d}\Phi^{IF}_{X_{ijk}/\{z\}}\, A_3^0(i_q, j_\gamma, \check{1}_{\bar{q}})\,. \tag{4.45}$$

Combining the integrated subtraction term with the final state mass factorisation contribution we obtain the full initial-final virtual subtraction term,

$$\begin{aligned}\mathrm{d}\hat{\sigma}^{\gamma,T,IF} = -\int_{z_{\mathrm{cut}}}^1 \mathrm{d}z \Bigg[\mathcal{N}^V \int \frac{\mathrm{d}x}{x} \frac{1}{S_n} \sum_{perm.} \mathrm{d}\Phi_n(\ldots, I_q, \ldots; \check{\check{1}}_{\bar{q}}, p_2) \\ \times Q_q^2 \mathbf{J}_2^{(1)}(I_q, \bar{1}_{\bar{q}}; z) M_n^0(\ldots, I_q, \ldots; \check{\check{1}}_{\bar{q}}, p_2) J_n^{(m)}(\{\tilde{k}\}_n; z)\Bigg]\,.\end{aligned} \tag{4.46}$$

The integrated dipole is now given by

$$\mathbf{J}_2^{(1)}(I_q, \bar{1}_{\bar{q}}; z) = \mathcal{A}_3^{0,IF}(s_{1I}; z) - \mathcal{N}' \Gamma^0_{q\gamma}\left(z, \mu_A^2\right) \delta(1-x)\,, \tag{4.47}$$

where we had to introduce the $\delta(1-x)$ to trivialise the $x$ integration in eq. (4.46) for the final state mass factorisation part.

# 5. NNLOJET

The necessary infrastructure to calculate differential cross sections up to NNLO QCD accuracy using the antenna subtraction method is implemented within the computational framework NNLOJET. In this chapter we present a brief overview of the program and the auto-generation routines used to implement new processes. The NNLOJET code is still under development and subject to continuous adaptations and improvement. For a more detailed description of the conceptual basics of the code we refer to other PhD theses such as [119, 176–178]. During the respective projects discussed therein important contributions to the code were developed.

## 5.1. General overview

At the core of the NNLOJET program, written in FORTRAN 95, sits the Monte Carlo integrator Vegas [179], used to numerically evaluate the phase-space integrals and convolutions with the PDFs needed to calculate the cross section as defined by eq. (3.1). In this the program is not limited to hadron collider processes. For a large set of processes all relevant matrix elements are available in analytic form, as well as all antenna functions necessary for calculations at the NNLO QCD level[1], together with the pertinent phase-space mappings. NNLOJET is interfaced to LHAPDF [180], which provides the PDFs selected by the user and also takes care of the running of the strong coupling $\alpha_s$.

For the actual evaluation of the cross section the program contains all the necessary routines to apply jet-algorithms, the photon isolation (both cone based and democratic clustering approaches), and any kind of fiducial cuts. The results can be booked fully automatically into multi-differential histograms. The concrete setup of a run can be steered by the user through dedicated `runcard` files. With those files one can define:

- The process and contribution (leading order, real corrections, etc.) to calculate.
- Physics input such as masses and widths and their corresponding schemes.
- The LHAPDF PDF sets to use.
- The parameters for the jet algorithm and photon isolation, if needed.
- The fiducial cuts.
- The histograms to book, with free choice of the binning.
- Further technical parameters.

[1] As we shall see in part III we can use the same antennae for the subtraction of NLO QED limits.

Besides the infrastructure for the calculation of differential cross sections NNLOJET contains a set of testing routines for internal consistency checks of the matrix element and subtraction term implementation, see also section 6.3.2.

So far NNLOJET has been used to calculate the processes $e^+e^- \to 3j$ [62, 63], jet and dijet production in DIS [64, 65], $pp \to j + X$ [66], $pp \to 2j$ [67], $pp \to Z + j$ [68, 69], $pp \to W + j$ [70], $pp \to H + j$ [71], $pp \to VH$ [72], Higgs production in vector boson fusion (VBF) [73], $pp \to \gamma + X/j$ [74] and $pp \to \gamma\gamma$ [160, 161].

## 5.2. Process auto-generation - part 1

As a large part of the program (or `driver`) structure is universal for all processes, we can resort to a set of Maple scripts to auto-generate the necessary code and link all the relevant routines, whenever we want to implement a new process into the NNLOJET framework. The auto-generation can be separated into two parts:

1. The setup of the `driver`-structure and linking of the Vegas routines with the matrix elements and the subtraction terms.

2. Generation of the subtraction terms as FORTRAN code.

For the first step some key parameters of the process, like the overall power of the couplings and colour factor of the Born level have to be specified in a steering file for the auto-generation. For a given process `X` it is denoted `X.map` and in the following often called "the `.map` file". It also contains a full list of identifiers for the colour-ordered matrix elements with their respective colour factor. We will look at an explicit example in Part III of this thesis when discussing the implementation of NLO EW corrections within NNLOJET (chapter 11). The matrix elements have to be implemented manually as FORTAN functions. The Maple scripts will then read the `.map` file and generate all crossings contributing to the process, as well as the FORTRAN files containing the subroutines needed to dress the matrix elements with colour, symmetry and coupling factors and convolute them with the PDFs. The scripts will also make sure that everything is properly linked to the integrator. In addition some files (the `driver`-bridge files) are generated to link the FORTAN source code of the subtraction terms. Those files, however, require some manual adjustments. That way one can make use of the fact that different channels can be subtracted with different crossings of the same subtraction term, reducing the amount of independent functions significantly.

Like the matrix elements the subtraction terms have to be put in by hand, as they are very process specific and there is no algorithm automating the generation of antenna subtraction terms at the NNLO level. To simplify their implementation they are coded in the form of short Maple files using a set of short-hand notations, which are then translated into FORTRAN code in the second step of the auto-generation.

## 5.3. OpenLoops2 interface - part 1

For some processes the analytic form of the matrix elements is not available. In that case it is useful to resort to some amplitude provider, which can help us out with numerically evaluated amplitudes[2]. Numerical matrix elements can also be used to validate their analytic counterparts. In NNLOJET we implemented a link to OpenLoops2 [181], using its native FORTRAN interface. At the moment the OpenLoops2 interface can be used as a substitute of the matrix elements only, but not for the reduced matrix elements in the subtraction terms, because OpenLoops2 does not provide a colour decomposition of the squared amplitudes as we need it for the application of the antenna subtraction method. A direct consequence of this is that the auto-generated `driver-bridge` files linking the subtraction source code have to be modified in such a way that they combine multiple terms to subtract all colour levels at once. As long as the colour decomposition of the matrix element is known, this is not a problem. Note that we *do not* need to know the form of the colour-ordered matrix elements, just the decomposition.

The auto-generation scripts are constructed such that they will link the appropriate OpenLoops2 routines instead of the matrix element source code, once the user sets some specific flags in the process `.map` file. As we essentially build the whole infrastructure for the NLO EW corrections around the OpenLoops2 interface, we will postpone a more detailed description to chapter 11.

[2] At least for tree level and one-loop amplitudes. To date there is no general algorithm available which would allow the automated numerical evaluation of two-loop amplitudes.

# Part II.

# NNLO QCD corrections for $\gamma + X/j$

# Introduction

The production of a single photon with high transverse momentum at a hadron collider, inclusively or in association with a jet, is an interesting process to study for several reasons. An isolated photon has an electromagnetic signature clearly distinct from any hadronic activity and can serve as a probe of the underlying strong dynamics of the process. The two leading order production channels [10, 11] (see figure 5.1) are $q\bar{q}$-annihilation, $q\bar{q} \to g\gamma$, and QCD Compton scattering, $qg \to q\gamma$, the latter of which renders the process sensitive to the gluon PDF already at leading order [5, 6]. It was only recently [7–9] that the inclusion of the photon data into global PDF fits has been reconsidered. It had previously been abandoned because of the theoretical difficulties related to the fragmentation function and the lack of precise enough predictions.

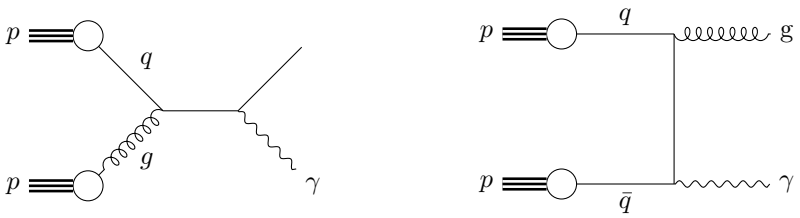


(a) QCD Compton scattering

(b) $q\bar{q}$ annihilation

Figure 5.1.: The two different Born level diagrams contributing to inclusive photon and photon-plus-jet production.

In addition photon-plus-jet production also serves as a means to estimate the SM background in searches for new physics (NP). In [12] for example photon-plus-jet production played a role in interpolating the $Z(\nu\bar{\nu})$+jet background in NP searches with a high energy jet recoiling against missing transverse momentum.

From these applications it is clear that isolated photon production within the SM has to be understood very accurately. The precision studies of inclusive photon [18–27] and photon-plus-jet [26, 30–37] production published in the recent years pushed down the experimental uncertainties to the few percent level. To make proper use of this progress we need the theory predictions to keep up and reduce their uncertainty, too. The conventional approach is to include previously neglected higher orders in the perturbative expansion. Here the main focus lies on higher order QCD corrections, which in an hadron collider environment are expected to have a much bigger impact than the EW corrections, given the order of magnitude difference in the numerical size of their respective coupling constant.

So far fixed order NNLO QCD predictions for inclusive photon and photon-plus-jet production are available by the MCFM group [148, 149]. Those calculations were performed using the conventional smooth cone isolation in order to completely remove the sensitivity on the photon

fragmentation functions. Almost two decades after the publication of the JETPHOX code [137] for the calculation of the NLO QCD corrections including the fragmentation component, there is no code available which extends this calculation to NNLO. Thus, a systematic discrepancy between the isolation used in the precision measurements and the most recent theory prediction persists. With our calculation we try to reduce that discrepancy by applying the hybrid isolation criterion introduced in section 4.1.1, and offer a prediction at NNLO QCD accuracy fully independent from [148, 149], which serves as a good check for the validity of the underlying theory. In addition the hybrid isolation allows us to study the dependence on the experimental isolation parameters in an approximative way, which is not possible for the conventional smooth cone isolation, and can only fully be done at that level once the fragmentation functions up to NNLO QCD are implemented and fixed cone isolation can be used.

Part II of the thesis is organised as follows: In chapter 6 we will discuss all the necessary ingredients, i.e. matrix elements and subtraction terms, for the implementation of inclusive photon and photon-plus-jet production up to NNLO QCD. In chapter 7 we study the dependence of the isolated photon cross sections on the technical parameters of the hybrid isolation, before in chapter 8 we move on to a phenomenology study based on the recent measurements [21–23, 26, 28, 34, 37] by the LHC experiments. We summarise our results and conclude this part in chapter 9.

# 6. Ingredients for $\gamma + X/j$ up to NNLO QCD

In this chapter we will discuss the ingredients needed for the implementation of the inclusive photon and photon-plus-jet processes up to NNLO QCD. They only differ by the final state selection cuts, the underlying channels and amplitudes are exactly the same. In the remainder of this chapter we will therefore, whenever we talk about photon-plus-jet, implicitly refer to inclusive photon production, too. In section 6.1 we will describe the structure of the matrix elements needed, and in section 6.2 we will briefly discuss how the corresponding antenna subtraction terms can be obtained from the already existing subtraction for the $Z$+jet process. In section 6.3 we will explain how both the individual parts and the full implementation have been validated.

## 6.1. Matrix elements for $\gamma + X/j$ up to NNLO QCD

Up to NNLO in QCD we have to consider the following contributions:

- **LO - Born** - The Born level consists of all $\mathcal{O}(\alpha\alpha_s)$ $2 \to 2$ tree level matrix elements contributing to a one-photon final state.
- **NLO - R** - The real corrections consist of all $\mathcal{O}\left(\alpha\alpha_s^2\right)$ $2 \to 3$ tree level matrix elements contributing to a one-photon final state.
- **NLO - V** - The virtual corrections consist of all $\mathcal{O}\left(\alpha\alpha_s^2\right)$ $2 \to 2$ one-loop matrix elements, i.e. the interference of the one-loop amplitudes with the corresponding tree level amplitudes, contributing to a one-photon final state.
- **NNLO - RR** - The double real corrections consist of all $\mathcal{O}\left(\alpha\alpha_s^3\right)$ $2 \to 4$ tree level matrix elements contributing to a one-photon final state.
- **NNLO - RV** - The real virtual corrections consist of all $\mathcal{O}\left(\alpha\alpha_s^3\right)$ $2 \to 3$ one-loop matrix elements, i.e. the one-loop-tree interferences contributing to a one-photon final state.
- **NNLO - VV** - The double virtual corrections consist of all $\mathcal{O}\left(\alpha\alpha_s^3\right)$ $2 \to 2$ two-loop matrix elements, i.e. the one-loop amplitudes squared and the two-loop-tree interferences contributing to a one-photon final state.

In the remainder of this chapter we will discuss all matrix elements contributing to the parts listed above and show how they decompose in their respective colour levels, as it is needed for the

application of the antenna subtraction method. How the actual parts relate to the un-squared amplitudes which can be found in the literature is subject of appendix B. Before we begin some clarification of the nomenclature is in order.

The classification of the amplitudes and matrix elements follows two of their basic properties: the number of loops and the composition of the external states, where the precise crossing does not matter, e.g. the two channels $q\bar{q} \to g\gamma$ and $qg \to q\gamma$ are based on the same tree, one- or two-loop matrix element. When we explicitly talk about the external states we will therefore indicate them as all-final states, i.e. $0 \to 2q1g1\gamma$ or just $2q1g1\gamma$ for above example. This also reflects the fact that the helicity amplitudes are conventionally defined with all outgoing momenta. Different crossings of the same matrix element of course come with different averaging and symmetry factors. In general each matrix element will be multiplied with the following factors:

- All crossings come with a factor $1/4$ for the average over the two helicity states of the two incoming particles.
- An colour averaging factor for the initial states. $1/(NC_F) = 1/8$ for gluons, $1/N = 1/3$ for (anti-)quarks and 1 for an initial state photon. The latter is only relevant if we consider higher order EW corrections, see section 10.2.
- Final state symmetry factors. For $n$ indistinguishable particles $1/n!$.

Those factors only depend on the external states and not on the specific matrix element or even process under consideration. We will therefore neglect them in the following and do not count them into the overall colour and coupling factor, which indeed does depend on the process.

The naming and classification of the matrix elements is explained in the following. The number of external quark pairs determines the "type" of the amplitude or matrix element:

- No quark pairs: A-type.
- One quark pair: B-type.
- Two quark pairs of non-identical flavour: C-type.
- Two quark pairs of identical flavour: D-type. The D-types are actually the interference term between two C-type amplitudes with different ordering of the quarks. We will explain this in more detail later.

As we are discussing a process which at Born level is $2 \to 2$, we cannot have more than two quark pairs, since the maximum number of external particles will be six at the double real level, one of them being the photon. The individual colour stripped matrix elements will be denoted directly according to their type. A subscript informs about the number of external gluons, a superscript about the number of loops. Photonic amplitudes are marked with an superscript $\gamma$. Accents show their belonging to a certain colour level; a tilde symbol ($\tilde{\bullet}$) indicates subleading colour, a hat ($\hat{\bullet}$) is associated to a power of $N_F$. Both symbols stack, i.e. a double tilde means sub-subleading in colour. There are some special accents, which only appear in certain situations. We will point those cases out once we encounter them. Following those conventions $\tilde{B}^{1,\gamma}_{2g}$ will be

the one-loop photonic subleading colour matrix element with one external quark pair and two external gluons, i.e. $0 \to 2q2g1\gamma$. It is part of the real virtual level.

The full matrix elements will be denoted with a capital A, with the type as subscript, as well as the number of external particles, The number of external photons and whether it is a tree or loop matrix element will be written as superscript. To come back to the previous example, $A_{5,B}^{1\gamma,1-\text{loop}}$ will be the full real virtual $0 \to 2q2g1\gamma$ matrix element. The corresponding un-squared amplitude, for a single helicity configuration, will be denoted with a curly $\mathcal{A}$. Here: $\mathcal{A}_{5,B}^{1\gamma,1-\text{loop}}$. The colour decomposed amplitudes are given in appendix B.

### 6.1.1. Leading order - Born contribution

At leading order we can construct only one amplitude,

- B-type: $0 \to 2q1g1\gamma$ at tree level squared.

Since there is no direct gluon-photon coupling, we cannot have any A-type tree level amplitudes, so there is no $3g1\gamma$ contribution at the leading order. This obviously extends to the NLO real and NNLO double real level. Moreover we do not have enough external particles, yet, to have another quark pair. The Born level therefore only consist of all the crossings (with the photon in the final state) of

$$A_{4,B}^{1\gamma,\text{tree}} = \sum_{\text{hel}} \left| \mathcal{A}_{4,B}^{1\gamma,\text{tree}} \right|^2 = \mathcal{N}^B B_{1g}^{0,\gamma} \,, \tag{6.1}$$

where we sum over the individual squared helicity amplitudes. The overall colour and coupling factor is given by

$$\mathcal{N}^B = 4(4\pi\alpha_s)(4\pi\alpha)NC_F \,, \tag{6.2}$$

with $C_F = (N^2-1)/N$. The quark charge factor squared $Q_q^2$ associated with the quark-photon coupling is absorbed into $B_{1g}^{0,\gamma}$; $Q_d^2 = 1/9$, $Q_u^2 = 4/9$.

### 6.1.2. Next-to-leading order - real contribution

At the next-to-leading order we can have one additional real radiation particle in the final state. While this can be an additional gluon to the LO B-type amplitude, with now 4 external particles besides the photon there is also the possibility of having two quark pairs. Thus the matrix elements to consider are

- B-type: $0 \to 2q2g1\gamma$ at tree level squared.
- C-type: $0 \to 2q2Q1\gamma$ at tree level squared.
- D-type: $0 \to 4q1\gamma$, tree level interference.

The overall factor of the matrix elements is related to that of the Born level by an additional power of $\alpha_s$. We can also pull out another factor of $N$,

$$\mathcal{N}^R = (4\pi\alpha_s)N\mathcal{N}^B = 4(4\pi\alpha_s)^2(4\pi\alpha)N^2C_F\,. \tag{6.3}$$

The full B-type matrix element is given by

$$A_{5,B}^{1\gamma,\text{tree}} = \sum_{\text{hel}} \left|\mathcal{A}_{5,B}^{1\gamma,\text{tree}}\right|^2 = \mathcal{N}^R \left( \sum_{S_2(1,2)} B_{2g,12}^{0,\gamma} - \frac{1}{N^2}\tilde{B}_{2g}^{0,\gamma} \right), \tag{6.4}$$

where the sum in the leading colour term runs over all permutations of the two gluons in $B_{2g,ij}^{0,\gamma} \equiv B_{2g}^{0,\gamma}(\bar{q}, g_i, g_j, q, \gamma)$,

$$\sum_{S_2(1,2)} B_{2g,12}^{0,\gamma} = B_{2g}^{0,\gamma}(\bar{q}, g_1, g_2, q, \gamma) + B_{2g}^{0,\gamma}(\bar{q}, g_2, g_1, q, \gamma)\,. \tag{6.5}$$

The subleading colour matrix element $\tilde{B}_{2g}^{0,\gamma}$ is symmetric with respect to an interchange of the quarks and therefore needs no sum.

The full C-type matrix element for two non-identical flavoured quark pairs is given by

$$A_{5,C}^{1\gamma,\text{tree}} = \sum_{\text{hel}} \left|\mathcal{A}_{5,C}^{1\gamma,\text{tree}}\right|^2 = \mathcal{N}^R \left( \frac{1}{N} C_{0g}^{0,\gamma} \right). \tag{6.6}$$

In case of identically flavoured quarks we have to anti-symmetrise the amplitude over the anti-quarks,

$$\mathcal{A}_{5,C+D}^{1\gamma,\text{tree}}(\bar{q}, \bar{Q}, Q, q, \gamma) = \mathcal{A}_{5,C}^{1\gamma,\text{tree}}(\bar{q}, \bar{Q}, Q, q, \gamma) - \mathcal{A}_{5,C}^{1\gamma,\text{tree}}(\bar{Q}, \bar{q}, Q, q, \gamma)\,, \tag{6.7}$$

where $q$ and $Q$ have now the same flavour. The anti-symmetrisation reflects the two possibilities to connect the quark lines when forming the square,

$$A_{5,C+D}^{1\gamma,\text{tree}} = \sum_{\text{hel}} \left|\mathcal{A}_{5,C+D}^{1\gamma,\text{tree}}\right|^2 = A_{5,C}^{1\gamma,\text{tree}}(\bar{q}, \bar{Q}) + A_{5,C}^{1\gamma,\text{tree}}(\bar{Q}, \bar{q}) + A_{5,D}^{1\gamma,\text{tree}}\,, \tag{6.8}$$

with

$$A_{5,D}^{1\gamma,\text{tree}} = -2 \sum_{\substack{\text{hel} \\ (h_q = h_Q)}} \text{Re}\left\{ \mathcal{A}_{5,C}^{1\gamma,\text{tree}\,\dagger}(\bar{q}, \bar{Q}) \mathcal{A}_{5,C}^{1\gamma,\text{tree}}(\bar{Q}, \bar{q}) \right\} = \mathcal{N}^R \left( \frac{1}{N^2} D_{0g}^{0,\gamma} \right). \tag{6.9}$$

We reduced the argument list of the C-type amplitudes to the minimum for better legibility. The helicity sum only runs over configurations with identical helicites for both quark lines, as the others vanish. The C-type matrix elements in eq. (6.8) are the genuine squares of the individual amplitudes in eq. (6.7), while the D-type is their interference. Note that interchanging the antiquarks in the amplitude's momentum assignment corresponds to going from one Mandelstam-like diagram to another, for example changing $\bar{q} \leftrightarrow \bar{Q}$ (in the all-final momentum assignment of the amplitude) in an s-channel $q\bar{q} \to Q\bar{Q}$ diagram will result in an $Q\bar{q} \to Q\bar{q}$

t-channel diagram. The D-types are therefore interferences of different Mandelstam channels, having a much simpler IR singularity structure than the C-types. Most divergences will only appear in one diagram taking part in the interference, hence being integrable.

### 6.1.3. Next-to-leading order - virtual contribution

At the virtual level contributing at NLO we have to consider one-loop corrections to the Born matrix element,

- B-type: $0 \to 2q1g1\gamma$ at one-loop×tree level.

At the one-loop level we can write down a $3g1\gamma$ A-type amplitude, as all the external gauge bosons can couple to an internal quark loop. Only the box diagram contributes to this amplitude, the triangles mutually cancel. Since we do not have a corresponding tree amplitude, the one-loop A-type will not play a role at the NLO virtual level, but reappear as part of the NNLO double virtual correction as a one-loop squared matrix element.

The full B-type virtual matrix element is given by

$$A_{4,B}^{1\gamma,1-\text{loop}} = 2\sum_{\text{hel}} \text{Re}\left\{\mathcal{A}_{4,B}^{1\gamma,\text{tree}\,\dagger}\mathcal{A}_{4,B}^{1\gamma,1-\text{loop}}\right\} = \mathcal{N}^V\left(B_{1g}^{1,\gamma} - \frac{1}{N^2}\tilde{B}_{1g}^{1,\gamma} + \frac{N_F}{N}\hat{B}_{1g}^{1,\gamma}\right), \tag{6.10}$$

where the overall factor is related to that of the Born through

$$\mathcal{N}^V = \frac{1}{8\pi^2}(4\pi\alpha_s)N\mathcal{N}^B = \frac{1}{2\pi^2}(4\pi\alpha_s)^2(4\pi\alpha)N^2C_F\,. \tag{6.11}$$

$N_F$ contributions like in the matrix element 6.10 stem from internal quark loops[1], for which we have to sum over all possible flavours running in the loop. Since the amplitudes we are using are consistently defined in the five flavour scheme, $N_F = 5$.

All matrix elements contributing to the NLO level are listed in table 6.2 in section 6.1.7, together with their corresponding name in the NNLOJET code.

### 6.1.4. Next-to-next-to-leading order - double real contribution

With now two additional real radiation particles we can write down a B-type amplitude with three gluons and dress the real level C- and D-types with one additional gluon,

- B-type: $0 \to 2q3g1\gamma$ at tree level squared.
- C-type: $0 \to 2q2Q1g1\gamma$ at tree level squared.
- D-type: $0 \to 4q1g1\gamma$, tree level interference.

[1] Without coupling to the photon, as this would introduce a sum of the quark charge factors over all the flavours in the loop instead of just a simple sum corresponding to the number of flavours. We do not encounter such cases at the NLO level. Moreover, here the colour stripped matrix element $\hat{B}_{1g}^{1,\gamma}$ associated to the $N_F$ factor is somewhat special, as is does not have a finite part and only contributes to the $\epsilon^{-1}$ coefficient trough the renormalisation, see appendix B.

At NNLO the overall factor obtains another power of $\alpha_s$ and $N$, so that for the double real case

$$\mathcal{N}^{RR} = (4\pi\alpha_s)N\mathcal{N}^R = 4(4\pi\alpha_s)^3(4\pi\alpha)N^3C_F\,. \tag{6.12}$$

The full B-type double real matrix element reads

$$A_{6,B}^{1\gamma,\text{tree}} = \sum_{\text{hel}} \left|\mathcal{A}_{6,B}^{1\gamma,\text{tree}}\right|^2 \tag{6.13a}$$

$$= \mathcal{N}^{RR}\left(\sum_{S_3(1,2,3)} B_{3g,123}^{0,\gamma} - \frac{1}{N^2}\sum_{S_3(1,2,3)} \tilde{B}_{3g,123}^{0,\gamma} + \frac{N^2+1}{N^4}\tilde{\tilde{B}}_{3g}^{0,\gamma}\right), \tag{6.13b}$$

where again we sum over all possible permutations of the three gluons, this time in the leading and subleading colour term. The sub-subleading contribution is totally symmetric with respect to gluon interchange.

The full two quark pair, non-identical flavour C-type matrix element is given by

$$A_{6,C}^{1\gamma,\text{tree}} = \sum_{\text{hel}} \left|\mathcal{A}_{6,C}^{1\gamma,\text{tree}}\right|^2 = \mathcal{N}^{RR}\left(\frac{1}{N}C_{1g}^{0,\gamma} + \frac{1}{N^3}\tilde{C}_{1g}^{0,\gamma}\right), \tag{6.14}$$

where we now have two colour levels due to the additional final state gluon. In case of identically flavoured quarks we have to anti-symmetrise the amplitude over the anti-quarks again,

$$\mathcal{A}_{6,C+D}^{1\gamma,\text{tree}}(\bar{q},g,\bar{Q},Q,q,\gamma) = \mathcal{A}_{6,C}^{1\gamma,\text{tree}}(\bar{q},g,\bar{Q},Q,q,\gamma) - \mathcal{A}_{6,C}^{1\gamma,\text{tree}}(\bar{Q},g,\bar{q},Q,q,\gamma)\,. \tag{6.15}$$

Squaring the above amplitude we find

$$A_{6,C+D}^{1\gamma,\text{tree}} = \sum_{\text{hel}} \left|\mathcal{A}_{6,C+D}^{1\gamma,\text{tree}}\right|^2 = A_{6,C}^{1\gamma,\text{tree}}(\bar{q},\bar{Q}) + A_{6,C}^{1\gamma,\text{tree}}(\bar{Q},\bar{q}) + A_{6,D}^{1\gamma,\text{tree}} \tag{6.16}$$

with

$$A_{6,D}^{1\gamma,\text{tree}} = -2\sum_{\substack{\text{hel}\\(h_q=h_Q)}} \text{Re}\left\{\mathcal{A}_{6,C}^{1\gamma,\text{tree}\,\dagger}(\bar{q},g,\bar{Q},Q,q,\gamma)\mathcal{A}_{6,C}^{1\gamma,\text{tree}}(\bar{Q},g,\bar{q},Q,q,\gamma)\right\} \tag{6.17a}$$

$$= \mathcal{N}^{RR}\left(-\frac{1}{N^2}D_{1g}^{0,\gamma} + \frac{1}{N^4}\tilde{D}_{1g}^{0,\gamma}\right). \tag{6.17b}$$

### 6.1.5. Next-to-next-to-leading order - real virtual contribution

The real virtual level consists of all one-loop×tree interferences involving one-loop virtual corrections to the $2 \to 3$ contributions. We have

- B-type: $0 \to 2q2g1\gamma$ at one-loop×tree level.
- C-type: $0 \to 2q2Q1\gamma$ at one-loop×tree level.
- D-type: $0 \to 4q1\gamma$, one-loop×tree level, interference of antiquark ordering.

The tree level amplitudes with which we interfere are the same that contribute to the NLO real level. Like the A-type at the NLO virtual level we can in principle write down a $4g1\gamma$ one-loop amplitude, but since there is no corresponding tree it will not contribute at the real virtual level. As one-loop squared matrix element it is part of the N$^3$LO real double virtual level, which we do not consider here.

The overall colour and coupling factor is related to those of the NLO contributions like

$$\mathcal{N}^{RV} = \frac{1}{8\pi^2}(4\pi\alpha_s)N\mathcal{N}^{R} = (4\pi\alpha_s)N\mathcal{N}^{V} = \frac{1}{2\pi^2}(4\pi\alpha_s)^3(4\pi\alpha)N^3C_F\,. \tag{6.18}$$

The full B-type real virtual matrix element is then given by

$$A_{5,B}^{1\gamma,1-\text{loop}} = 2\sum_{\text{hel}}\text{Re}\left\{\mathcal{A}_{5,B}^{1\gamma,\text{tree}\,\dagger}\mathcal{A}_{5,B}^{1\gamma,1-\text{loop}}\right\} \tag{6.19a}$$

$$\begin{aligned}= \mathcal{N}^{RV}\Bigg(&\sum_{S_2(1,2)} B_{2g,12}^{1,\gamma} - \frac{1}{N^2}\sum_{S_2(1,2)}\tilde{B}_{2g,12}^{1,\gamma} - \frac{1}{N^2}\tilde{\tilde{B}}_{2g}^{1,\gamma} + \frac{1}{N^4}\tilde{\tilde{B}}_{2g}^{1,\gamma}\\ &+ \frac{N_F}{N}\sum_{S_2(1,2)}\hat{B}_{2g,12}^{1,\gamma} + \frac{N_F}{N^3}\hat{\tilde{B}}_{2g}^{1,\gamma} + \frac{N_F^q}{N}\left(1-\frac{4}{N^2}\right)\check{B}_{2g}^{1,\gamma}\Bigg)\,.\end{aligned} \tag{6.19b}$$

Here $N_F^q$ is the sum of the quark charge factors,

$$N_F^q = \sum_{q=d,u,s,c,b} Q_q = \frac{1}{3}\,, \tag{6.20}$$

coming from the coupling of the photon not to the external quarks but to a closed fermion loop. Note that since we are working in the five flavour scheme, the top quark does not contribute to the sum. In the associated colour stripped matrix element $\check{B}_{2g}^{1,\gamma}$ only an un-squared charge factor $Q_q$ is absorbed, corresponding to the quark-photon coupling in the tree level amplitude participating in the one-loop×tree interference.

The full non-identical flavour C-type matrix element reads

$$A_{5,C}^{1\gamma,1-\text{loop}} = 2\sum_{\text{hel}}\text{Re}\left\{\mathcal{A}_{5,C}^{1\gamma,\text{tree}\,\dagger}\mathcal{A}_{5,C}^{1\gamma,1-\text{loop}}\right\} = \mathcal{N}^{RV}\left(\frac{1}{N}C_{0g}^{1,\gamma} + \frac{1}{N^3}\tilde{C}_{0g}^{1,\gamma} + \frac{N_F}{N^2}\hat{C}_{0g}^{1,\gamma}\right). \tag{6.21}$$

For identically flavoured quarks we have to anti-symmetrise over the anti-quarks again, both the tree and the one-loop amplitude,

$$\mathcal{A}_{5,C+D}^{1\gamma,\text{tree}}(\bar{q},\bar{Q},Q,q,\gamma) = \mathcal{A}_{5,C}^{1\gamma,\text{tree}}(\bar{q},\bar{Q},Q,q,\gamma) - \mathcal{A}_{5,C}^{1\gamma,\text{tree}}(\bar{Q},\bar{q},Q,q,\gamma)\,, \tag{6.22}$$

$$\mathcal{A}_{5,C+D}^{1\gamma,1-\text{loop}}(\bar{q},\bar{Q},Q,q,\gamma) = \mathcal{A}_{5,C}^{1\gamma,1-\text{loop}}(\bar{q},\bar{Q},Q,q,\gamma) - \mathcal{A}_{5,C}^{1\gamma,1-\text{loop}}(\bar{Q},\bar{q},Q,q,\gamma)\,. \tag{6.23}$$

The interference is then given by

$$A_{5,C+D}^{1\gamma,1-\text{loop}} = 2\sum_{\text{hel}}\text{Re}\left\{\mathcal{A}_{5,C+D}^{1\gamma,\text{tree}\,\dagger}\mathcal{A}_{5,C+D}^{1\gamma,1-\text{loop}}\right\} \tag{6.24a}$$

$$= A_{5,C}^{1\gamma,1-\text{loop}}(\bar{q},\bar{Q}) + A_{5,C}^{1\gamma,1-\text{loop}}(\bar{Q},\bar{q}) + A_{5,D}^{1\gamma,1-\text{loop}} \tag{6.24b}$$

with

$$A_{5,D}^{1\gamma,1-\text{loop}} = -2 \sum_{\substack{\text{hel} \\ (h_q=h_Q)}} \text{Re}\Big\{\mathcal{A}_{5,C}^{1\gamma,\text{tree}\dagger}(\bar{q},\bar{Q})\mathcal{A}_{5,C}^{1\gamma,1-\text{loop}}(\bar{Q},\bar{q}) + \mathcal{A}_{5,C}^{1\gamma,\text{tree}\dagger}(\bar{Q},\bar{q})\mathcal{A}_{5,C}^{1\gamma,1-\text{loop}}(\bar{q},\bar{Q})\Big\} \tag{6.25a}$$

$$= \mathcal{N}^{RV}\left(\frac{1}{N^2}D_{0g}^{1,\gamma} + \frac{1}{N^4}\tilde{D}_{0g}^{1,\gamma} + \frac{N_F}{N^3}\hat{D}_{0g}^{1,\gamma}\right). \tag{6.25b}$$

### 6.1.6. Next-to-next-to-leading order - double virtual contribution

There are two contributions to the double virtual level: two-loop×tree interferences and one-loop squared matrix elements. For the B-type we have both of them, but now there is also the A-type $3g1\gamma$ one-loop squared matrix element we mentioned earlier. While there is an A-type two-loop amplitude, we again cannot interfere it with any tree. We therefore have to consider

- A-type: $0 \to 3g1\gamma$, one-loop squared.
- B-type: $0 \to 2q1g1\gamma$ at two-loop×tree level plus one-loop squared.

With the overall colour and coupling factor

$$\mathcal{N}^{VV} = \frac{1}{8\pi^2}(4\pi\alpha_s)N\mathcal{N}^{V} = \frac{1}{16\pi^4}(4\pi\alpha_s)^3(4\pi\alpha)N^3C_F \tag{6.26}$$

the full one-loop squared A-type is given by

$$A_{4,A}^{1\gamma,2-\text{loop}} = \sum_{\text{hel}}\left|\mathcal{A}_{4,A}^{1\gamma,1-\text{loop}}\right|^2 = \mathcal{N}^{VV}\frac{\left(N_F^q\right)^2}{N}\left(1-\frac{4}{N^2}\right)A_{3g}^{2,\gamma}, \tag{6.27}$$

which now comes with a squared sum of the charge factors associated to the flavours in the loop. Since there are no other quarks involved, no charge factors are absorbed into $A_{3g}^{2,\gamma}$.

For the full double virtual B-type matrix element we find

$$A_{4,B}^{1\gamma,2-\text{loop}} = \sum_{\text{hel}}\left(\left|\mathcal{A}_{4,B}^{1\gamma,1-\text{loop}}\right|^2 + 2\,\text{Re}\left\{\mathcal{A}_{4,B}^{1\gamma,\text{tree}\dagger}\mathcal{A}_{4,B}^{1\gamma,2-\text{loop}}\right\}\right) \tag{6.28a}$$

$$= \mathcal{N}^{VV}\left(B_{1g}^{2,\gamma} - \frac{1}{N^2}\tilde{B}_{1g}^{2,\gamma} + \frac{1}{N^4}\tilde{\tilde{B}}_{1g}^{2,\gamma} + \frac{N_F}{N}\hat{B}_{1g}^{2,\gamma} + \frac{N_F^2}{N^2}\hat{\hat{B}}_{1g}^{2,\gamma} + \frac{N_F}{N^3}\hat{\tilde{B}}_{1g}^{2,\gamma} + \frac{N_F^q}{N}\left(1-\frac{4}{N^2}\right)\check{B}_{2g}^{2,\gamma}\right). \tag{6.28b}$$

We now have contributions also to the $N_F^2$ level, coming from either two-loop diagrams with two internal quark loops interfered with the tree or from the square of two one-loop amplitudes with internal quark loop[2]. Since there was no part of the one-loop amplitudes coming with a factor $N_F^q$, we only have a term associated with a single power of $N_F^q$ in the double virtual correction, coming from genuine two-loop amplitudes.

[2] In this specific case the contribution of the one-loop squared matrix element to the $N_F^2$ level stems from the renormalisation counterterm only.

All matrix elements contributing to the NNLO level are listed in table 6.3 in section 6.1.7, together with their corresponding name in the NNLOJET code.

#### Note on the impact of the loop-induced contribution

We have to remark that the loop-induced contribution $A_{3g}^{2,\gamma}$ had initially been forgotten and was implemented a while after the studies presented in chapters 7 and 8 had been performed. We checked that the effect of this missing contribution in context of those studies is negligible. For the setup used therein the loop-induced channels contribute less than 1% to the already small NNLO coefficient, despite being enhanced by the two gluon PDFs. Comparing to the numerical uncertainty of the full NNLO numbers we concluded that a full re-evaluation of the results presented in chapters 7 and 8 is not necessary.

### 6.1.7. Summary of contributing matrix elements

In this section we quickly summarize all matrix elements contributing to inclusive photon and photon-plus-jet production up to NNLO QCD. We also give the corresponding names of the matrix elements in the NNLOJET code. Table 6.1 is a list of all contributions to the leading order. Following the discussion above, there is only one entry. Table 6.2 shows all matrix elements of the NLO level, both the real and virtual corrections, table 6.3 the matrix elements of the NNLO level, consisting of double real, real virtual and double virtual contributions.

| LO | | | |
|---|---|---|---|
| level | channels | ME | NNLOJET |
| B | $0 \to 2q1g1\gamma$ | $B_{1g}^{0,\gamma}$ | `B1g0G(qb,g,q,G)` |

Table 6.1.: Matrix elements (ME) contributing to the leading order of inclusive photon and photon-plus-jet production, the corresponding channels and the name of the matrix elements in the NNLOJET code. There is only a single Born level (B) contribution.

| NLO | | | |
|---|---|---|---|
| level | channels | ME | NNLOJET |
| R | $0 \to 2q2g1\gamma$ | $B_{2g}^{0,\gamma}$ | `B2g0G(qb,g,g,q,G)` |
| | | $\tilde{B}_{2g}^{0,\gamma}$ | `Bt2g0G(qb,g,g,q,G)` |
| | $0 \to 2q2Q1\gamma$ | $C_{0g}^{0,\gamma}$ | `C0g0G(qb,Q,Qb,q,G)` |
| | $0 \to 4q1\gamma$ | $D_{0g}^{0,\gamma}$ | `D0g0G(qb,q,qb,q,G)` |
| V | $0 \to 2q2g1\gamma$ | $B_{1g}^{1,\gamma}$ | `B1g1G(qb,g,q,G)` |
| | | $\tilde{B}_{1g}^{1,\gamma}$ | `Bt1g1G(qb,g,q,G)` |
| | | $\hat{B}_{1g}^{1,\gamma}$ | `Bh1g1G(qb,g,q,G)` |

Table 6.2.: Matrix elements (ME) contributing to the next-to-leading order of inclusive photon and photon-plus-jet production, the corresponding channels and the name of the matrix elements in the NNLOJET code. At NLO we have real (R) and virtual (V) corrections.

| NNLO | | | |
|---|---|---|---|
| level | channels | ME | NNLOJET |
| RR | $0 \to 2q3g1\gamma$ | $B_{3g}^{0,\gamma}$ | `B3g0G(qb,g,g,g,q,G)` |
| | | $\tilde{B}_{3g}^{0,\gamma}$ | `Bt3g0G(qb,g,g,g,q,G)` |
| | | $\tilde{\tilde{B}}_{3g}^{0,\gamma}$ | `Btt3g0G(qb,g,g,g,q,G)` |
| | $0 \to 2q2Q1g1\gamma$ | $C_{1g}^{0,\gamma}$ | `C1g0G(qb,g,Q,Qb,q,G)` |
| | | $\tilde{C}_{1g}^{0,\gamma}$ | `Ct1g0G(qb,g,Q,Qb,q,G)` |
| | $0 \to 4q1g1\gamma$ | $D_{1g}^{0,\gamma}$ | `D1g0G(qb,g,q,qb,q,G)` |
| | | $\tilde{D}_{1g}^{0,\gamma}$ | `Dt1g0G(qb,g,q,qb,q,G)` |
| RV | $0 \to 2q2g1\gamma$ | $B_{2g}^{1,\gamma}$ | `B2g1G(qb,g,g,q,G)` |
| | | $\tilde{B}_{2g}^{1,\gamma}$ | `Bt2g1G(qb,g,g,q,G)` |
| | | $\tilde{\tilde{B}}_{2g}^{1,\gamma}$ | `Btt2g1G(qb,g,g,q,G)` |
| | | $\tilde{\tilde{\tilde{B}}}_{2g}^{1,\gamma}$ | `Bttt2g0G(qb,g,g,q,G)` |
| | | $\hat{B}_{2g}^{1,\gamma}$ | `Bh2g1G(qb,g,g,q,G)` |
| | | $\hat{\tilde{B}}_{2g}^{1,\gamma}$ | `Bth2g1G(qb,g,g,q,G)` |
| | | $\check{B}_{2g}^{1,\gamma}$ | `Bv2g1G(qb,g,g,q,G)` |
| | $0 \to 2q2Q1\gamma$ | $C_{0g}^{1,\gamma}$ | `C0g1G(qb,Q,Qb,q,G)` |
| | | $\tilde{C}_{0g}^{1,\gamma}$ | `Ct0g1G(qb,Q,Qb,q,G)` |
| | | $\hat{C}_{0g}^{1,\gamma}$ | `Ch0g1G(qb,Q,Qb,q,G)` |
| | $0 \to 4q1\gamma$ | $D_{0g}^{1,\gamma}$ | `D0g1G(qb,q,qb,q,G)` |
| | | $\tilde{D}_{0g}^{1,\gamma}$ | `Dt0g1G(qb,q,qb,q,G)` |
| | | $\hat{D}_{0g}^{1,\gamma}$ | `Dh0g1G(qb,q,qb,q,G)` |
| VV | $0 \to 3g1\gamma$ | $A_{3g}^{2,\gamma}$ | `A3g2G(g,g,g,G)` |
| | $0 \to 2q1g1\gamma$ | $B_{1g}^{2,\gamma}$ | `B1g2G(qb,g,q,G)` |
| | | $\tilde{B}_{1g}^{2,\gamma}$ | `Bt1g2G(qb,g,q,G)` |
| | | $\tilde{\tilde{B}}_{1g}^{2,\gamma}$ | `Btt1g2G(qb,g,q,G)` |
| | | $\hat{B}_{1g}^{2,\gamma}$ | `Bh1g2G(qb,g,q,G)` |
| | | $\hat{\hat{B}}_{1g}^{2,\gamma}$ | `Bhh1g2G(qb,g,q,G)` |
| | | $\hat{\tilde{B}}_{1g}^{2,\gamma}$ | `Bth1g2G(qb,g,q,G)` |
| | | $\check{B}_{1g}^{2,\gamma}$ | `Bh1g2G34(qb,g,q,G)` |

Table 6.3.: Matrix elements (ME) contributing to the next-to-next-to-leading order of inclusive photon and photon-plus-jet production, the corresponding channels and the name of the matrix elements in the NNLOJET code. At NNLO we have double real (RR), real virtual (RV) and double virtual (VV) corrections.

## 6.2. IR-subtraction

### 6.2.1. Antenna subtraction with electroweak vector bosons

For the purpose of the numerical phase-space integration as part of the cross section calculation both the explicit IR poles of the loop matrix elements and the implicit soft and collinear limits of the real correction matrix elements have to be subtracted. To achieve this we apply the antenna subtraction formalism [46–48] introduced in section 3.5. The presence of an external electroweak vector boson, the photon in our case, does not spoil the method, as long as we consider a few differences compared to pure QCD. For calculations of higher order corrections in QCD we do not need to worry about configurations with unresolved photons. These cases will be dealt with when considering NLO EW corrections in the last part of this thesis, see section 10.4. For the sake of pure QCD corrections the final state vector bosons (or their respective decay products) will always remain resolved. They will, however, affect how we have to organise the matrix elements and subtraction terms[3]:

- While QCD is flavour blind, the couplings of $\gamma, Z$ and $W^{\pm}$ explicitly depend on the electromagnetic charge factor and/or flavour of the fermions involved in the process. We therefore have to treat channels with different flavour structure as separate contributions.
- In case of real radiation matrix elements involving multiple quark pairs we also have to make sure we pass the correct flavours to the reduced matrix element, once one of the pairs becomes unresolved.
- Due to the chiral structure of the weak gauge boson couplings, amplitudes with external $Z$ or $W^{\pm}$ bosons do not exhibit the line reversal or reflection symmetry of pure QCD amplitudes (see e.g. eq. (A.12)), which has to be considered when relating different matrix elements to simplify their construction.

Apart from these complications the actual colour structure of the matrix elements is not affected by introducing one or more colourless vector bosons. E.g. a $2 \to 4$ double real radiation matrix element for inclusive photon production will have the same colour structure as the corresponding $2 \to 3$ dijet matrix element without the photon[4]. In other words: while we potentially might have to consider *more* individual channels, their respective IR singularity structure, which is directly related to their colour structure, is *simpler* than for pure QCD processes.

Antenna subtraction has been successfully used for the calculation of NNLO QCD corrections to the Drell-Yan process [69, 182], $Z$+jet production [68], and the production of weak gauge bosons in general [70, 183] .

### 6.2.2. Subtraction terms for inclusive photon and photon-plus-jet

The colour structure of the amplitudes contributing to inclusive photon and photon-plus-jet production is identical to that of the amplitudes contributing to inclusive $Z$ and $Z$-plus-jet production, which have already been implemented in the NNLOJET code. The NNLO subtraction

[3] See section 2.6 in [119] for a slightly more detailed discussion.
[4] We make intensive use of this fact when constructing the matrix elements in appendix B.

terms for the photon processes could therefore be constructed in an automated manner by replacing the names of the relevant reduced matrix elements and adjusting the overall coupling factor. The actual combination of antenna strings could be ported without any modifications.

In the $Z$ amplitudes we actually never have a single momentum assigned to the final state vector boson, but rather a pair of momenta representing its decay products $\ell^+\ell^-$. Since the lepton pair is oblivious of colour, this does not interfere with the subtraction in any way. The assigned momenta will appear in the full matrix element in precisely the same way as in the reduced matrix elements. As a consequence we could simply replace the two momenta of the lepton pair by a single momentum representing the photon.

## 6.3. Tests and validation

The implementation of the photon-plus-jet process in NNLOJET has been validated at several stages:

1. Validation of the matrix elements at the level of individual phase-space points.

2. Validation of the proper functioning of the IR subtraction.

3. Validation at the level of the full cross section against third party tools.

### 6.3.1. Validation of the matrix elements

All tree level and one-loop matrix elements have been validated for their various crossings on the level of single phase-space points against the numeric expressions provided by OpenLoops [181, 184]. For the one-loop matrix elements we compared the finite piece and the pole coefficients separately, where we had to consider that the OpenLoops2 matrix elements come without the shift related to the expansion of the loop coefficient $c_\Gamma$ (see eqs. (B.4),(B.49),(B.49) in appendix B).

The comparison was performed with full colour matrix elements, since with the libraries included in the public version of OpenLoops2 it is not possible to access the individual colour levels. Testing several phase-space points for each crossing the tree level matrix elements could be validated with a precision of 12 digits or better. The same accuracy is reached in the validation of the one-loop $2 \to 2$ matrix elements, both for their finite pieces and the pole coefficients. The one-loop $2 \to 3$ matrix elements (i.e. the real virtual contribution for photon-plus-jet) could be validated to 10 digits or better. We had to use a non-public version of the OpenLoops2 libraries which do not include top-loops, since our matrix elements are in the five-flavour scheme. For the one-loop $2 \to 2$ this does not matter, as no fermion loops contribute.

Currently there is no amplitude provider available which we could use to test the two-loop matrix elements at the level of phase-space points. Switching to OpenLoops2, however, enabled us to at least validate the loop-induced $gg \to g\gamma$ matrix element $A_{3g}^{2,\gamma}$. For the various crossings we found agreement to 12 digits or better.

### 6.3.2. Validation of the subtraction terms

The implementation of the subtraction has been validated in several tests and consistency checks, for which NNLOJET provides all the necessary routines and runtime test modes[5]:

1. Check the proper subtraction of IR limits associated to real emissions. This is done in the so called spiketest. Using a modified version of the phase-space generator RAMBO [185], every possible single and double unresolved limit, soft and/or collinear, of a given kinematics is probed. For a given channel and colour level we then calculate the ratio[6] of the real matrix element contribution to the corresponding subtraction term,

$$R(x) = \frac{\mathrm{d}\hat{\sigma}_{\mathrm{ME}}(x)}{\mathrm{d}\hat{\sigma}_{\mathrm{Sub}}(x)} \tag{6.29}$$

   for at least 1000 phase-space points in the limit considered. Here $x$ parametrises how close we reach to the actual singular configuration. There is some ambiguity how precisely $x$ is defined; in NNLOJET we usually relate it to the specific Mandelstam invariant which vanishes in the unresolved limit. Precisely for a single unresolved particle in an $2 \to 3$ kinematics and $\hat{s}$ the total partonic energy in the event:

$$s_{jk} = (1-x)\hat{s} \qquad \text{if } i \text{ soft and } j,k \text{ the remaining final state particles,} \tag{6.30a}$$

$$s_{ij} = x\hat{s} \qquad \text{if } i||j. \tag{6.30b}$$

   This can readily be extended to double unresolved configurations. In the exact limit we expect

$$R(x) \xrightarrow[x\to 0]{} 1\,, \tag{6.31}$$

   since by construction the subtraction should tend to the value of the matrix element. This behaviour can be visualised in so called spikeplots. Figure 6.1 provides an example. It shows the behaviour of the subleading colour contribution to the channel $q_1 g_2 \to g_3 g_4 q_5 \gamma_6$ in the triple collinear limit $g_3||g_4||q_5$. For the green histogram all points considered had an $x$ of $10^{-7}$ or smaller, for the blue histogram $x \leq 10^{-8}$ and finally for the red histogram $x \leq 10^{-11}$. And indeed the closer we are to the actual singularity at $x = 0$, the more the ratio $R$ tends to 1.

2. Check the proper cancellation between the pole coefficients of the virtual correction matrix elements and the integrated subtraction terms. This can be achieved by activating the pole-check runtime mode. NNLOJET will then calculate the ratio of the matrix element's and corresponding subtraction term's pole coefficients for individual generic phase-space points. The test passes, if all these ratios are equal to 1 within machine precision.

[5] A more detailed explanation of the test routines available in NNLOJET can be found in appendix A of [176].

[6] We are not considering the difference as both the matrix element and the subtraction term can have subleading singularities which are not properly cancelled between the two. Thus the difference does not necessarily tend to 0 in the limit. Those subleading singularities are not a problem in the calculation, as their associated phase-space volume is small, so that upon integration they vanish. Forming the ratio we can make sure that we are checking the cancellation of the leading singularity properly, with the contributions of any subleading structures vanishing in the limit.

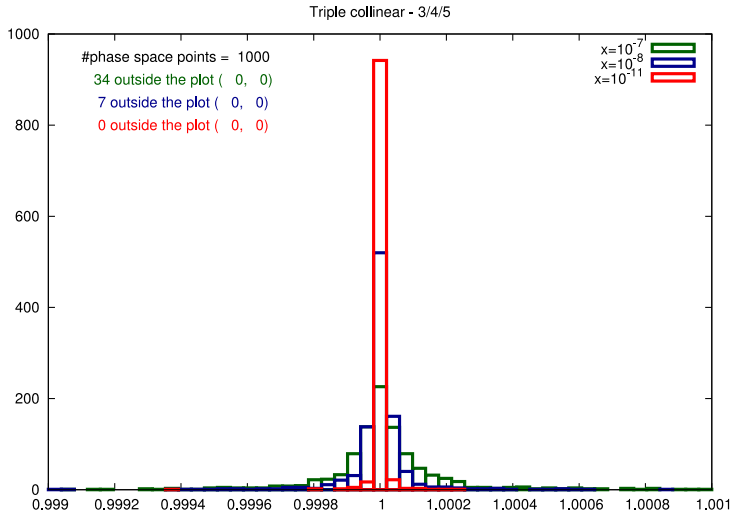


Figure 6.1.: Example spikeplot for the triple collinear $g_3||g_4||q_5$ limit in the subleading colour contribution of the channel $q_1 g_2 \to g_3 g_4 q_5 \gamma_6$. Each colour corresponds to a different degree to which we probe the limit.

3. Check relations between the unintegrated and integrated subtraction term to make sure that everything which is subtracted at the real emission level is added back at the virtual correction level. These layer checks are set up in form of Maple scripts closely related to those used in the auto-generation of the Fortran code for the subtraction terms. The checks will parse the subtraction term Maple files as well as additional code structures to relate each combination of unintegrated antenna function and reduced matrix element appearing in the subtraction terms to the corresponding integrated term, taking the correct symmetry factors into account and exploiting non-trivial relations between different antenna functions and matrix elements.

For the implementation of the NNLO corrections to inclusive photon and photon-plus-jet production all of the above tests were performed successfully. Together with the pointtests of the matrix elements described in section 6.3.1 this already supports the validity of our implementation.

For performance and stability reasons invariants cannot become arbitrarily small during the actual NNLOJET production runs, so that we never go as deep into the unresolved limits as for the spiketests. This behaviour is controlled by the $y_0$ cut which can be set in the runcard. It forces all invariants to be greater than $y_0 \hat{s}$, where $\sqrt{\hat{s}}$ is the total partonic energy of the event. Varying the cut over a certain range is another means to check the consistency of the implementation, as the total result should be independent of the value of this technical and unphysical parameter, provided it is chosen small enough. For the photon-plus-jet process we checked the dependence for the real, double real and real virtual contributions and found that we indeed reach a stable plateau for the cross section. Choosing a value $y_0 \lesssim 10^{-7}$ should remove any dependence on the parameter from the calculation.

| | | LO coeff. | NLO coeff. |
|---|---|---|---|
| GJ | NNLOJET | $(19682.7 \pm 5.7)$pb | $(12012 \pm 35)$pb |
| | SHERPA | $(19687.2 \pm 1.8)$pb | $(12160 \pm 60)$pb |
| GJJ | NNLOJET | $(3900.1 \pm 4.9)$pb | $(2175 \pm 21)$pb |
| | SHERPA | $(3894.8 \pm 8.3)$pb | $(2192 \pm 13)$pb |
| GJJJ | NNLOJET | $(1254.9 \pm 5.3)$pb | |
| | SHERPA | $(1257.0 \pm 1.3)$pb | |

Table 6.4.: Validation numbers for the LO and NLO coefficients for photon plus 1,2 and 3 jets, obtained with NNLOJET and SHERPA.

### 6.3.3. Validation of the full implementation

The full implementation of the process could in large parts be tested by comparing the full cross sections for photon-plus-jet and photon-plus-dijet production at NLO QCD to the results obtained with SHERPA [156–158], interfaced to OpenLoops2 [181, 184]. The photon-plus-dijet results could be obtained by simply demanding an additional jet. While the former cross section provides a means to directly test the Born contribution and the real and virtual corrections including the full subtraction, the latter makes it possible to also access the real virtual corrections (i.e. one-loop $2 \to 3$) and the double real contribution (i.e. tree level $2 \to 4$), with the constraint of an resolved third final state particle. We also did a comparison for photon-plus-trijet production at leading order in order to check the implementation of the $2 \to 4$ matrix elements without any contributions coming from the IR subtraction.

All runs have been performed in a simplified setup for a centre-of-mass energy of $\sqrt{s} = 8$ TeV, with fixed scales $\mu_R = \mu_F = m_Z$. Jets are defined through the anti-$k_T$ algorithm with the radius parameter $R^j = 0.5$. The photon is identified using the smooth cone isolation criterion

$$E_{T,\mathrm{dyn}}^{\mathrm{max}}(E_T^\gamma; r) = \varepsilon_d E_T^\gamma \left( \frac{1 - \cos r}{1 - \cos R} \right)^n , \tag{6.32}$$

with

$$R = 0.5 \qquad \varepsilon_d = 1 , \qquad n = 1 . \tag{6.33}$$

Both the jets and the photon are required to have a minimum $p_T$ of 30 GeV to be accepted. The numerical value of the electromagnetic coupling $\alpha$ was fixed to $\sim 1/132.232$, which corresponds to the value in the $G_\mu$ scheme, see section 10.5.2. All NNLOJET runs use the same matrix elements and IR subtraction infrastructure and only differ by requiring one, two or three resolved jets, respectively. The results are summarised in table 6.4.

The process photon-plus-1jet at NLO QCD has recently been re-validated in the course of the validation of the NLO EW corrections against the computational framework MATRIX [186], see section 13.2. Anticipating the results from this section, which have been obtained in a slightly different setup, we find agreement to a much higher precision than for our initial validation:

| | | LO coeff. | NLO coeff. |
|---|---|---|---|
| GJ | NNLOJET | $(223.266 \pm 0.083)$pb | $(182.013 \pm 0.090)$pb |
| | MATRIX | $(224.273 \pm 0.011)$pb | $(182.005 \pm 0.018)$pb |

To validate also the double unresolved part of the NNLO subtraction as well as the double virtual corrections we compared our predictions for inclusive photon and photon-plus-jet production to the corresponding calculations published by the MCFM group [148, 149]. These comparisons will be subject of sections 8.1.1 and 8.2.1, respectively. The contribution from the loop-induced channel $gg \to g\gamma$ could be validated[7] independently against the "box" contribution implemented in the JETPHOX code [137]:

| | | loop-induced coeff. |
|---|---|---|
| GJ | NNLOJET | $(28.72942 \pm 0.00010)$fb |
| | JETPHOX | $(28.726 \pm 0.015)$fb |

[7] Using the setup presented in section 8.2.2.

# 7. Isolation studies

Given the novelty of the hybrid isolation (`hybIso` in plots) it will be interesting to see how it compares against the more standard smooth/dynamical cone isolation (`dynIso` in plots). All cone based isolations discussed in section 4.1.1 have been implemented in NNLOJET. The fixed cone isolation procedure, however, requires the inclusion of the fragmentation contribution, which is not available, yet. We therefore resort to JETPHOX [137] for the calculation of isolated photon and photon-plus-jet NLO QCD cross sections using a fixed cone. The direct comparison between the JETPHOX numbers and the ones obtained with the hybrid isolation criterion will help to constrain the technical parameters of the latter. Where appropriate, JETPHOX NLO QCD results are therefore displayed in the following. We want to remark that JETPHOX uses the BFG parametrisation [170] for the photon fragmentation functions. This parametrisation is expected to slightly underestimate the region of large longitudinal momentum transfer, which is relevant for the contribution to isolated photon cross sections [187]. The following results have previously been published in our paper [74].

For the smooth cone isolation and the smooth cone of the hybrid isolation we chose the standard profile as given in eq. (4.11)

$$\chi(r) = \left(\frac{1-\cos r}{1-\cos R}\right)^n . \tag{7.1}$$

For both isolation prescriptions we set $E_{T,d}^{\text{thres}}$ (compare eq. (4.9)) to zero. The outer or fixed cone part of the hybrid isolation is always chosen to match the experimental setup under consideration. The functional form of the smooth and hybrid isolation to be used in this and the following section can thus be summarised as follows[1]:

$$E_{T,\text{dyn}}^{\max}(p_T^\gamma; r) = \varepsilon_d p_T^\gamma \left(\frac{1-\cos r}{1-\cos R}\right)^n , \tag{7.2}$$

$$E_{T,\text{hyb}}^{\max}(p_T^\gamma; r; R_d) = \begin{cases} \min\left(E_{T,\text{fix}}^{\max}(p_T^\gamma), \varepsilon_d p_T^\gamma \left(\frac{1-\cos r}{1-\cos R}\right)^n\right), & (0 \le r < R_d) \\ E_{T,\text{fix}}^{\max}(p_T^\gamma), & (R_d \le r < R) \end{cases} , \tag{7.3}$$

with

$$E_{T,\text{fix}}^{\max}(p_T^\gamma) = \varepsilon p_T^\gamma + E_T^{\text{thres}} . \tag{7.4}$$

Note that above definition of the hybrid isolation does not correspond to the matched version described in eq. (4.18). As mentioned earlier, a comparison of the qualitative results obtained in the following to the study of isolation parameters performed in [61], which used the matched

[1] For massless particles $E_T = p_T$.

hybrid and the second version of the profile function eq. (4.12), showed that this does not cause any problems.

In order to investigate the dependence on the parameter choices for both the smooth and the hybrid cone isolation procedures, we use the fiducial cross section definition of the 13 TeV ATLAS $\gamma$ + jet data [34] (see Section 8.2.2 below). The photon has to have a transverse momentum $p_T^\gamma > 125$ GeV and a rapidity $|y^\gamma| < 2.37$, excluding the barrel–endcap region $[1.37, 1.56]$. Each event is required to contain at least one jet, defined through the anti-$k_T$ algorithm [125] with $R^j = 0.4$, with transverse momentum $p_T^j > 100$ GeV and rapidity $|y^j| < 2.37$. A jet must have a separation from the photon axis of $R^{\gamma j} > 0.8$.

We compute the theory predictions at NLO, using the NNPDF3.1 PDF set [188], and both the renormalisation and factorization scale are chosen to be equal to the photon transverse momentum. The theoretical uncertainty arising from the scale choice is estimated by means of a seven-point scale variation:

$$\mu_R = a\, p_T^\gamma\,, \qquad\qquad \mu_F = b\, p_T^\gamma\,, \tag{7.5}$$

where $a, b \in (\frac{1}{2}, 1, 2)$ and we exclude the pairs $(a, b) = (\frac{1}{2}, 2)$ and $(a, b) = (2, \frac{1}{2})$. For the `fixIso` predictions using JETPHOX we superimpose each of the resulting seven scale combinations with a variation of the fragmentation scale $\mu_A$ around a central scale of $p_T^\gamma$ by factors of $\frac{1}{2}, 1, 2$. We observe that the variation of $\mu_A$ has a much smaller impact than the variation of the other two scales.

The smooth cone parameters $\varepsilon_d$ and $n$ are varied in the following ranges:

$$\varepsilon_d \in (0.05, 0.1, 0.15)\,, \qquad\qquad n \in \left(\tfrac{1}{2}, 1, 2\right)\,. \tag{7.6}$$

For these variations, the cone size of the smooth cone is kept fixed at $R_d = 0.4$ for the standard smooth isolation and at $R_d = 0.1$ for the hybrid isolation. The dependence on the smooth cone size is investigated for fixed $(\varepsilon_d, n) = (0.1, 2)$, by taking $R_d \in (0.2, 0.4, 0.8)$ for the smooth isolation and $R_d \in (0.05, 0.1, 0.2)$ for hybrid isolation. In the case of the hybrid isolation the parameters for the outer fixed cone are fixed at (see eq. (4.7))

$$R = 0.4\,, \qquad\qquad E_T^{\text{thres}} = 10 \text{ GeV}\,, \qquad\qquad \varepsilon = 0.0042\,, \tag{7.7}$$

as in the experimental measurement [34]. The results are shown in figure 7.1. We observe a reduced dependence on the technical parameters of the smooth cone when going from smooth to hybrid isolation. This reduction is most pronounced for variations of the cone size $R_d$. This is to be expected, as in the smooth isolation the smooth cone defines the actual catchment area for the photon isolation in the calculation, while in the hybrid isolation this is accounted for by the outer fixed cone.

Although overlapping within their respective scale uncertainties, the predictions using hybrid isolation display a tendency to fall systematically above the predictions obtained using smooth isolation for identical values of $(\varepsilon_d, n)$, which can be understood from more real radiation events being admitted in the hybrid isolation procedure. The JETPHOX [137] fixed cone isolation

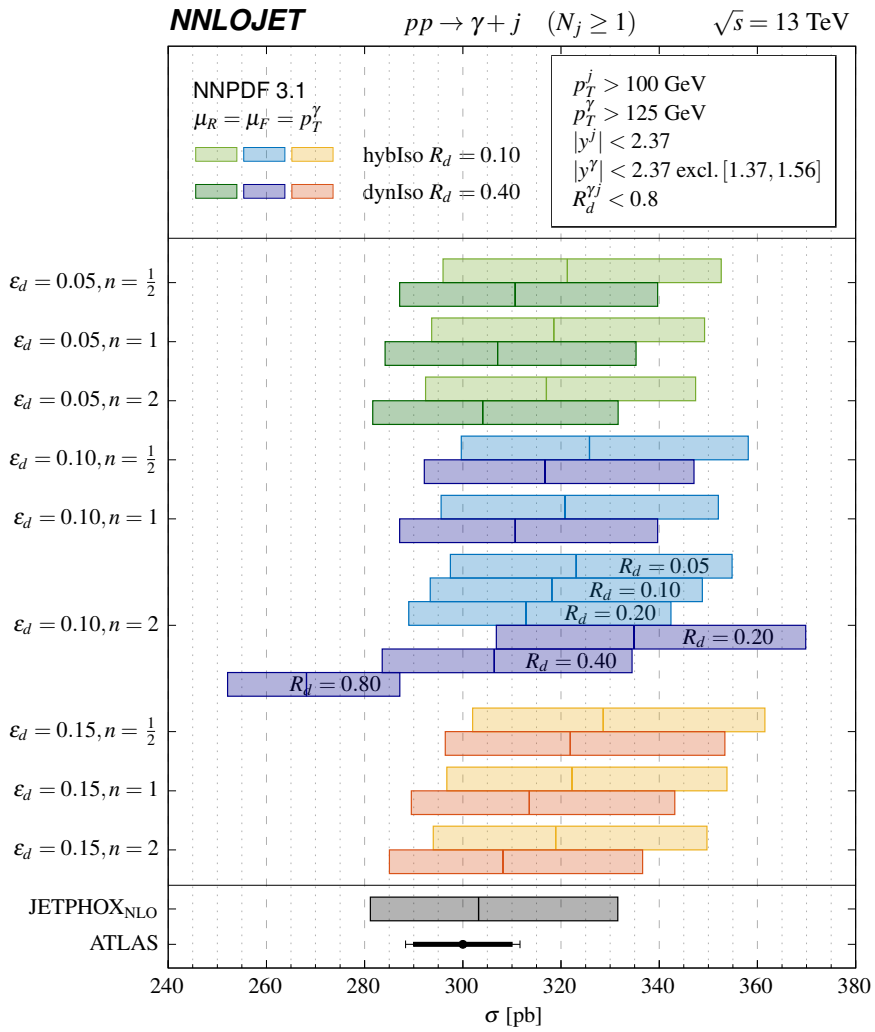


Figure 7.1.: Total cross section for different parameter choices ($\varepsilon_d = 0.05, 0.1, 0.15$, $n = \frac{1}{2}, 1, 2$) for both smooth photon isolation (`dynIso`) [144] (dark colours) and the smooth cone part of the hybrid photon isolation (`hybIso`) (light colours). The default cone size for `dynIso` is $R_d = 0.4$, while for `hybIso` it is $R_d = 0.1$. For the specific parameter choice $\varepsilon_d = 0.1, n = 2$ we also investigate variations of the cone size by factors $\frac{1}{2}$ and 2. The fixed cone parameters of the hybrid isolation are chosen according to the ATLAS measurement [34]. The `fixIso` prediction (using JETPHOX [137]) and the ATLAS measurement are shown for comparison.(Figure 1 from [74])

prediction is slightly below the bulk of the predictions for both hybrid and smooth cone isolation, indicating that the BFG parametrisation [170] of the photon fragmentation functions amounts to a somewhat smaller amount of photon yield in association with partons inside the isolation cone than what is admitted by these prescriptions. We use still use the comparison to the fixed cone result to fix the default values of $\varepsilon_d$ and $n$ to be used in the following. While the overall dependence on these quantities is small in the considered range of variation, we see that

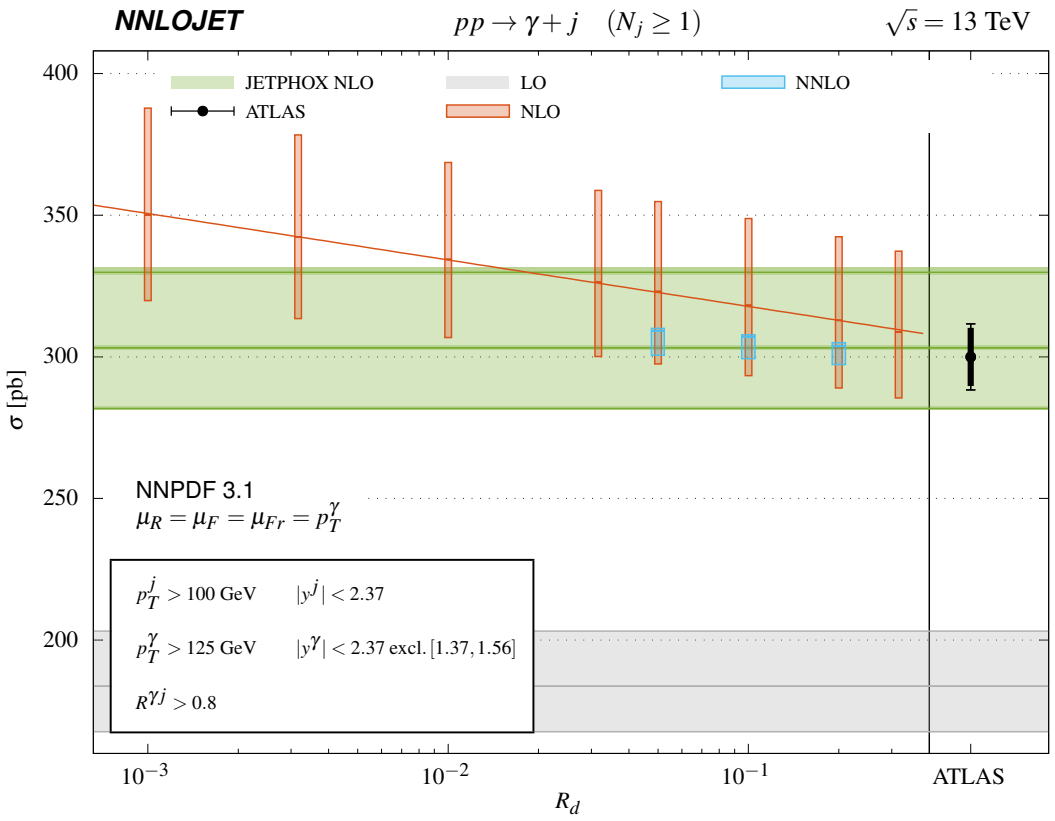


Figure 7.2.: Dependence of the total cross section for photon + jet production (ATLAS 13 TeV measurement [34]) at NLO and NNLO on the conesize $R_d$ of the inner smooth cone used in the hybrid isolation procedure. All other isolation parameters are fixed: $\varepsilon_d = 0.1$, $n = 2$, $R = 0.4$, $E_T^{\text{thres}} = 10$ GeV, $\varepsilon = 0.0042$. The line is a fit of a function with form $f(R_d) = a \cdot \log(1/R_d) + b$ to the NLO prediction at the central scale. The NLO prediction for fixed cone isolation is obtained with the BFG parametrisation [170] of the photon fragmentation functions, and computed with the JETPHOX code [137]. Its uncertainty band contains only variations of the factorization and renormalisation scales, while the small fragmentation scale uncertainty is superimposed on the central and extremal values. The LO prediction is independent on the isolation procedure. (Figure 2 from [74])

with larger values of both we tend towards the JETPHOX result. Following the tight isolation accord [145–147] for the smooth cone isolation, $\varepsilon_d$ should not exceed 0.1. We will follow this advice also for the hybrid isolation and fix

$$\varepsilon_d = 0.1\,, \qquad\qquad n = 2\,, \tag{7.8}$$

as the default values. A more detailed study about the dependence on $n$ can be found in [61].

The remaining residual dependence on the cone size $R_d$ in the hybrid isolation deserves more attention. As we already discussed in section 4.1.1, as $R_d$ approaches zero, one expects the cross section to diverge as $\sigma \sim \log(1/R_d)$, following from the factorisation of the cross section in the photon–quark collinear limits at NLO. While the outer fixed cone vetoes hard quarks in the

vicinity of the photon, relatively soft quarks, that is with $p_T^q < E_T^{\max}$, are in principle allowed within the fixed cone. The smooth inner cone prevents them from becoming collinear to the photon. When we shrink the smooth cone, at some point we will start to probe the quark–photon collinear limit, leading a logarithmic rise, which at NLO amounts to a single power of $\log(R_d)$. We checked this by extending the scan over the cone size $R_d$ in the hybrid isolation to values as low as $R_d = 10^{-3}$. The result is shown in figure 7.2.

The exact limit $R_d \to 0$ corresponds to no photon isolation, resulting in a fully inclusive photon cross section. In this case, the fragmentation contribution to the cross section has to be included, so that the negative final state mass factorisation counterterm (see section 4.2, in particular eqs. (4.28) and (4.29)) compensates the $\log(R_d)$-divergence, yielding a finite result for the cross section. From this cancellation, we can conclude that there exists a finite (but unknown) value of $R_d$ for which the hybrid isolation procedure (without fragmentation contribution) should produce exactly the same results as the fixed-cone isolation (with fragmentation contribution), since the vetoed real radiation cross section inside $R_d$ and the negative fragmentation counterterm exactly compensate each other. The `fixIso` result obtained with JETPHOX contains this counterterm, together with the non-perturbative quark-to-photon fragmentation function from which it is inseparable. Comparison of the `hybIso` and `fixIso` results (and taking into account that the BFG photon fragmentation function parametrisation in JETPHOX likely underestimates [187] the isolated region) indicates that the exact compensation takes place at around $R_d = 0.1$, or even above.

In the following, we use $R_d = 0.1$ throughout as default value for hybrid isolation. Smaller values will start probing the quark–photon collinear divergence and are disfavoured by the comparison with the `fixIso` results. Larger values would violate the condition $R_d^2 \ll R^2$, imposed on the relative cone sizes in the hybrid isolation. It has to be remembered that the hybrid isolation is an approximation to the fixed-cone isolation used in the experimental measurements. It reproduces the correct functional dependence on $R$, but induces potentially a small $R$-independent shift on the cross sections from discarding the collinear fragmentation contributions. The potential magnitude of this shift can be estimated by comparing the NLO `hybIso` prediction at $R_d = 0.1$ with the NLO `fixIso` JETPHOX prediction, which is obtained with the BFG parametrisation of the photon fragmentation functions and predicts a cross section lower by 4.6%, see Figure 7.2. This discrepancy likely overestimates the shift, given the effect of the BFG parametrisation in the isolated photon region, such that we can assume its magnitude to be a conservative upper bound on the residual uncertainty associated with the photon isolation prescription in the theoretical predictions.

At NNLO, the divergent behaviour in the $R_d \to 0$ limit becomes more involved, containing both $\log^2(R_d)$ and $\log(R_d)$ terms. Resolving the NNLO $R_d$-dependence over the full range of values of Figure 7.2 is prohibitively expensive in terms of computation time and numerical stability. To illustrate the behaviour in the vicinity of the default value $R_d = 0.1$ we display the NNLO cross sections for $R_d = 0.05$ and $R_d = 0.2$, observing that the $R_d$-dependence in this region is weaker than at NLO, decreasing from a $(+1.6, -1.7)\%$ variation to a $(+0.9, -1.3)\%$ variation. Following the arguments given above, an exact matching of fragmentation counterterm and inner hybrid isolation cone should be attained for some value $R_d < R$, and the comparison

between NLO `fixIso` and `hybIso` predictions suggests that this value can not be too small. The variation around the default value $R_d = 0.1$ that is observed at NNLO can thus be considered a reasonable estimation of the residual uncertainty associated with the hybrid isolation procedure.

We should remark that for the precise hybrid isolation parameters we use here the prescription is subject to a reduction of the effective inner cone size as discussed in section 4.1.1 (see in particular figure 4.6b). We find

$$\cos R_d^{\text{eff}} = 1 - 3.16228 \sqrt{\frac{0.0042 p_T^\gamma + 10 \text{ GeV}}{p_T^\gamma}} (1 - \cos R_d) \tag{7.9a}$$

$$\Rightarrow \quad R_d^{\text{eff}} < R_d \quad \text{for} \quad p_T^\gamma > 104.4 \text{ GeV} . \tag{7.9b}$$

At the fiducial threshold we find $R_d^{\text{eff}}(125 \text{ GeV})/R_d \approx 0.96$; the difference grows for larger transverse momenta, so that for 1 TeV we have $R_d^{\text{eff}}(1 \text{ TeV})/R_d \approx 0.61$. This is still not a problem concerning the statements made above, for the following reasons:

- The transverse momentum distribution of the photon in photon-plus-jet production is rapidly falling, see figure 8.11. Thus, most of the events will lie just above the threshold, so that the dependence of the total cross section on $R_d^{\text{eff}}$ is governed by the value of the effective cone size close to $p_T^\gamma = 125$ GeV.

- The ratio $R_d^{\text{eff}}/R_d$ depends only very mildly on $R_d$ itself. Over the range of $R_d$ we consider it changes by less than one per mille. The difference between $R_d^{\text{eff}}$ and $R_d$ can therefore be seen as a constant shift.

- Most importantly $R_d$ is a technical parameter. Its interpretation as the actual inner cone size is illustrative, but it does not have to be that way for the hybrid isolation to be a valid prescription. Moreover it is not our intention to extract the parameters of the line drawn in figure 7.2, fitting the logarithmic dependence. The focus lies on the qualitative behaviour.

The overall behaviour on the inner cone $R_d$ *parameter* is, on the level of the differential $p_T^\gamma$ distribution, confirmed in a study we performed for the latest Les Houches report [61]. There we avoided such complications by resorting to the matched hybrid isolation from the start.

# 8. Phenomenology

In this chapter we will present the phenomenological results we obtained for inclusive photon and photon-plus-jet production at NNLO QCD accuracy. Most of them have been published previously in our paper [74] and in the Moriond 2019 proceedings [159]. We will therefore follow the presentation in those references closely.

The calculations are performed within the NNLOJET framework, using the implementation of the matrix elements discussed in section 6.1 and employing the antenna subtraction method presented in section 3.5 and section 6.2. Per default the calculations use the NNPDF3.1 [188] PDF set and apply the hybrid isolation procedure as given in eq. (7.3) and studied in the previous chapter 7. The parameters are chosen such that they reflect the fiducial photon isolation criteria used in the respective experiment. Scale uncertainties are estimated using a seven-point scale variation as in chapter 7.

The numerical value of the electromagnetic coupling is set to $\alpha(G_\mu) = 1/132.232$, which in the $G_\mu$-EW renormalisation scheme is derived from the value of the Fermi constant $G_\mu$ measured in muon decay. The concrete schemes are discussed in section 10.5.2 in context of NLO EW corrections. Here the coupling $\alpha$ merely is a multiplicative constant. As the number of photons is fixed for all orders of QCD, so is the power of the electromagnetic coupling, such that it factorises completely. This enables us to calculate cross sections with one value of $\alpha$ and then rescale to any other value at the histogram level, if necessary. Note that conventional choices for $\alpha$ in higher order QCD corrections range from $\alpha(0) \approx 1/137$ to $\alpha(m_Z) \approx 1/128$. For inclusive photon and photon-plus-jet production, which are $\mathcal{O}(\alpha)$ processes, this amounts to a constant $\sim 7\%$ shift between results obtained with either of the two values.

The remainder of this chapter is organised as follows: Section 8.1 will be dedicated to isolated photon production, based on measurements performed by ATLAS [21, 22], CMS [26] and ALICE [28]. Section 8.2 will then discuss photon-plus-jet production, comparing to data from ATLAS [34] and CMS [26, 37]. From the point of the calculation inclusive photon and photon-plus-jet production only differ by the application of a jet reconstruction requirement in the latter. As a non-trivial check of our implementation we directly confront our results with the existing predictions from MCFM, both for inclusive photon [148] and photon-plus-jet production [149]. Those runs were performed using a standard smooth cone isolation.

## 8.1. Inclusive isolated photon production

Isolated photon cross sections are defined through kinematical selection cuts on the observed photon only. By requiring a minimal transverse momentum of the photon, they imply the existence of a partonic recoil. Consequently, predictions for isolated photon production are

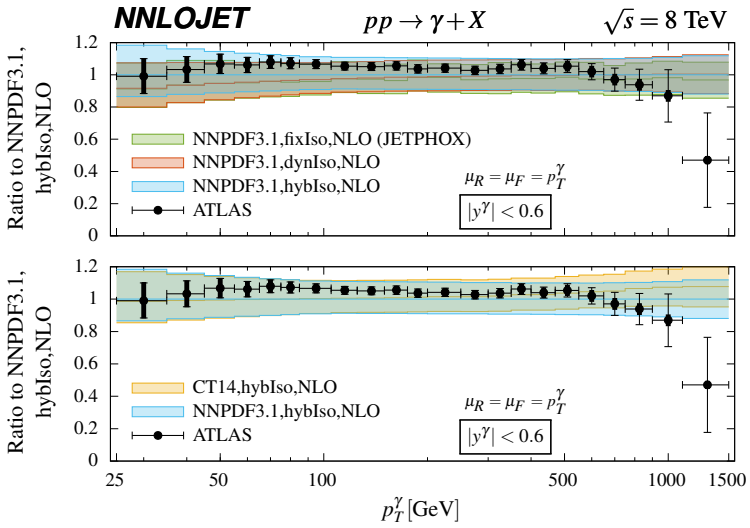


Figure 8.1.: Impact of the choice of the photon isolation criterion (smooth isolation [144] and fixed-cone isolation (produced with JETPHOX [137]) versus hybrid isolation, top frame) and PDF set (CT14 [189] versus NNPDF3.1 [188], bottom frame) at NLO, shown as ratio to our default choice of NNPDF3.1 with hybrid isolation. (Figure 3 from [74])

obtained from the photon-plus-jet calculation by simply dropping the requirement of observing a jet. Experimental measurements of photon production have been performed since the early days of hadron colliders [13–19]. Measurements of isolated photon production at ATLAS [20–22, 24] and CMS [25, 26] are now reaching per-cent level accuracy over a large kinematical range. To interpret these precision data demands an equally high accuracy on the theory predictions. In the following, we confront the 8 TeV ATLAS data [21] and the 13 TeV, 3.2 fb$^{-1}$ ATLAS [22] and CMS [26] data with our newly derived NNLO QCD predictions. The predictions were recently used in the updated 13 TeV, 36 fb$^{-1}$ study by ATLAS [24]. By default, we use the hybrid isolation procedure as given in eq. (7.3). In order to compare our results with the MCFM calculation of the NNLO corrections, we also replicate the setup of [148] by employing a smooth cone isolation with the same parameters as used there, confronted to the ATLAS 8 TeV measurements.

### 8.1.1. Comparison with ATLAS 8 TeV measurements and MCFM calculation

The ATLAS 8 TeV measurement [21] of isolated photon production is performed in four different regions in rapidity

$$|y^\gamma| < 0.6, \quad 0.6 < |y^\gamma| < 1.37, \quad 1.56 < |y^\gamma| < 1.81, \quad 1.81 < |y^\gamma| < 2.37\,, \tag{8.1}$$

and differentially in transverse momentum, with a lower cut off $p_T^\gamma > 25$ GeV. No further cuts are applied.

For the theoretical NNLOJET predictions, we set the central renormalisation and factorization scale to be equal to the photon transverse momentum $p_T^\gamma$. As default, we use the NNPDF3.1 [188] PDF set and apply a hybrid photon isolation (`hybIso`) with parameters

$$\begin{aligned} R_d &= 0.1\,, & \varepsilon_d &= 0.1\,, & n &= 2\,, \\ R &= 0.4\,, & E_T^{\text{thres}} &= 4.8\text{ GeV}\,, & \varepsilon &= 0.0042\,, \end{aligned} \tag{8.2}$$

such that the outer fixed-cone parameters ($R$, $E_T^{\text{thres}}$, $\varepsilon$) reproduce the photon isolation definition used in the experimental measurement [21].

In order to compare with the MCFM calculation [148], we replicate the setup used there, with the CT14 [189] PDF set and a smooth cone isolation (`dynIso`) (see eq. (7.2))

$$R_d = 0.4\,, \qquad \varepsilon_d = 0.1\,, \qquad n = 2\,. \tag{8.3}$$

To investigate the impact of these different settings, we compare the combinations of PDF and isolation procedure at NLO. Finally, at NLO we also use JETPHOX [137] to compute predictions for fixed cone isolation (`fixIso`) with the cone parameters of the experimental measurement, and using the BFG parametrization [170] of the photon fragmentation functions.

In the upper panel of figure 8.1 we compare the `dynIso` and `fixIso` predictions to the default setting of `hybIso`. All three predictions are obtained using NNPDF3.1 parton distributions. We find that the largest differences due to the choice of the isolation procedure occur in the low $p_T^\gamma$ region below approximately 100 GeV, while for $p_T^\gamma > 200$ GeV the difference is negligible. The cross section obtained with `dynIso` or `fixIso` (which yield very similar predictions) is consistently lower than the `hybIso` result, as already observed for the total cross section in Figure 7.1. In the lowest bin the deviation in the central value lies just below 10%. This discrepancy is in principle consistent at NLO within the scale uncertainty. It is noted, however, that unlike scale setting effects, the impact of the photon isolation procedure is not compensated at higher orders, such that the difference reflects a genuine systematic shift in the predictions.

The lower panel of figure 8.1 compares the `hybIso` predictions for NNPDF3.1 and CT14 parton distributions. Here, we observe the opposite kinematical pattern. While there is no significant difference at low $p_T^\gamma$, using CT14 leads to a consistently larger cross section compared to NNPDF3.1 for $p_T^\gamma > 200$ GeV, up to almost 8% in the highest bin. This pattern can be traced back to differences in the large-$x$ gluon and antiquark distributions, which produces similar effects also in gauge-boson-plus-jet observables [183].

The NNLO prediction for the ATLAS 8 TeV isolated photon production is computed for our default setting of NNPDF3.1 and hybrid isolation and, in order to numerically compare with the MCFM study [148], also for their choice, CT14 and smooth isolation.

We also need to take into account the different value of $\alpha(m_Z) = 1/127.9$ used there for the electromagnetic coupling, while our predictions are obtained in the $G_\mu$-scheme with $\alpha|_{G_\mu} = 1/132.232$. Since we are only considering the QCD corrections to one-photon amplitudes, the

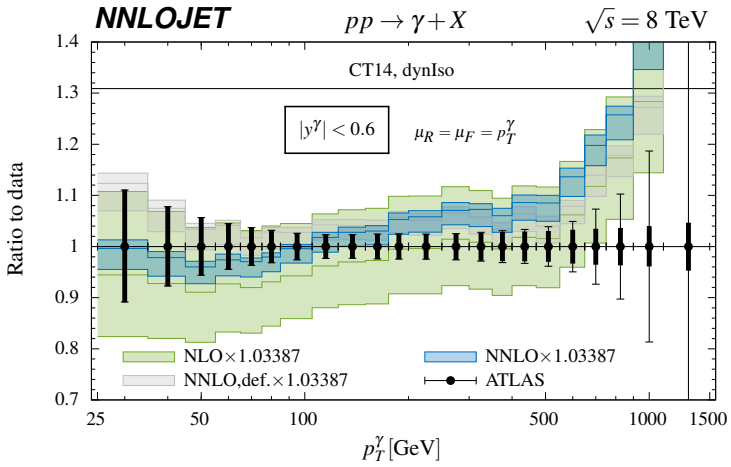


Figure 8.2.: Ratio to ATLAS data [21] for the transverse energy/momentum of the photon at NLO and NNLO, using the PDF and isolation procedure choice of MCFM [148]. The results are rescaled by a factor of 1.03387 to account for the different choice of $\alpha_{\text{em}}$. The NNLO result obtained using the default PDF and isolation procedure choice is shown in grey. (Figure 4 from [74])

results are directly proportional to $\alpha$ and thus the difference in $\alpha$ can readily be accounted for by a constant rescaling factor

$$\frac{\alpha(m_Z)}{\alpha|_{G_\mu}} = \frac{1/127.9}{1/132.232} \approx 1.03387\,. \tag{8.4}$$

Figure 8.2 shows the ratio to ATLAS data at NLO and NNLO. It corresponds to the lower panel of figure 4 in the MCFM study [148], where however the bins below $p_T^\gamma = 65$ GeV are not displayed. Compared to the default setting, we observe a decrease in the low $p_T$ region caused by the smooth isolation as well as an increase in the high $p_T$ region, due to the use of CT14. By construction, this agrees with our findings from figure 8.1.

While our NLO results are in full agreement with the MCFM study [148], we observe discrepancies at NNLO. Especially at low $p_T^\gamma$, our predictions are above the ones obtained in [148]. Moreover, for all values of $p_T^\gamma$ we compute a scale uncertainty that is slightly larger than the one stated in [148]. A most recent re-evaluation of the MCFM results [190] leads to modifications that bring MCFM and our results into mutual agreement within their respective Monte Carlo uncertainties. It should be emphasised that the two calculations rely on independent implementations of the underlying NNLO matrix elements and use completely different methods for the extraction and cancellation of infrared singularities among the different subprocesses. Consequently, the observed agreement amounts to a highly non-trivial check for our result as well as for MCFM [190].

Figure 8.3 shows a detailed comparison of the NNLO predictions obtained with our default setup with the ATLAS 8 TeV data [21]. Compared to NLO, the inclusion of NNLO corrections leads to a substantial reduction of the scale uncertainty on the predictions to less than $(+2, -4)\%$ in the bulk of the $p_T^\gamma$ distributions, with slightly larger uncertainty towards the limits of large

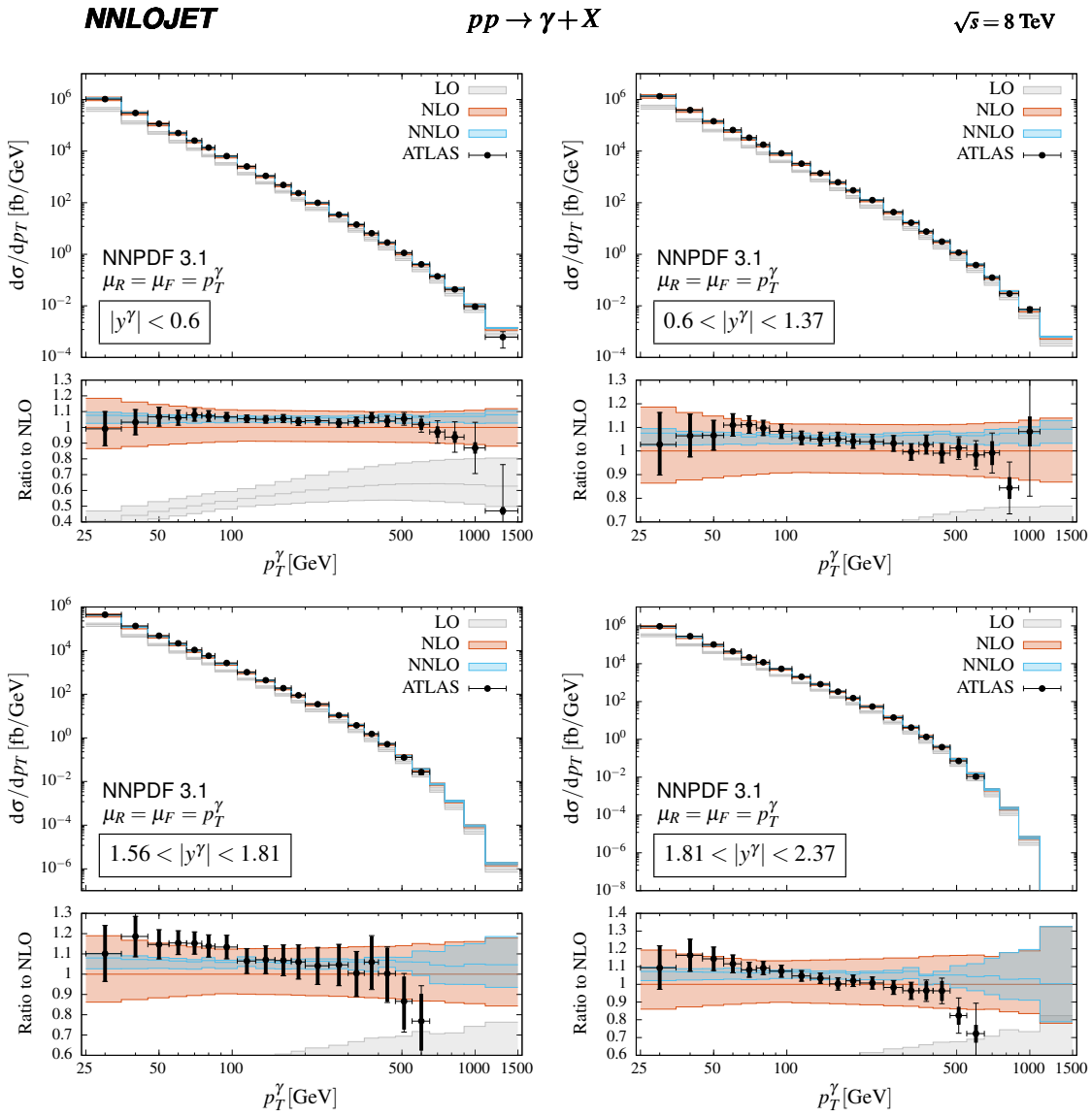


Figure 8.3.: Transverse energy/momentum distribution of isolated photons at LO, NLO, NNLO in four different rapidity bins, from central (top left) to most forward (bottom right). The results are compared to 8 TeV ATLAS data [21]. (Figure 5 from [74])

and small transverse momentum, with the exception of the two forward bins, for which the scale uncertainty grows drastically in the highest $p_T^\gamma$-bins, in which the cross section drops over several orders of magnitude. Throughout the kinematical range, the NNLO scale uncertainty is at most as large as (and mostly smaller than) the measurement errors. The ATLAS data are well-described in normalization and shape for all rapidity ranges. Small deviations observed at the largest transverse momenta are not yet significant within error ranges, but might indicate the onset of electroweak Sudakov logarithms [191, 192].

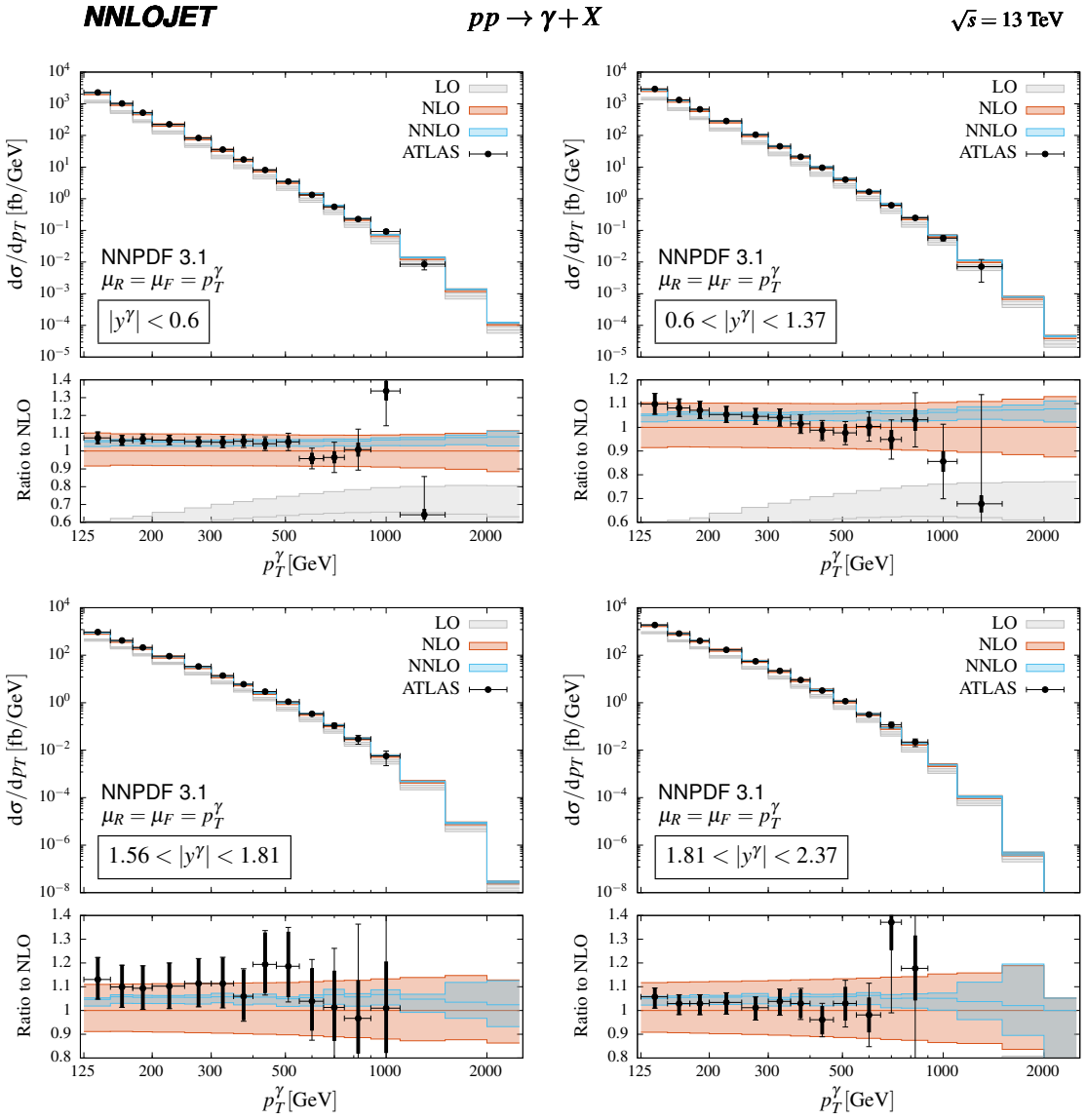


Figure 8.4.: Transverse energy/momentum distribution of isolated photons at LO, NLO and NNLO in four different rapidity bins, from central (top left) to most forward (bottom right). The results are compared to 13 TeV ATLAS data [22]. (Figure 6 from [74])

### 8.1.2. Comparison with ATLAS 13 TeV measurements

The ATLAS 13 TeV isolated photon measurement [22] is performed for the same rapidity bins (8.1) as used at 8 TeV [21] with a fixed-cone based isolation and transverse momentum $p_T^\gamma > 125$ GeV. Compared to the 8 TeV measurement, this larger transverse momentum cut implies a reduced sensitivity on the photon isolation prescription.

For the theoretical predictions, we use NNPDF3.1, and the hybrid isolation procedure with

$$\begin{aligned} R_d &= 0.1\,, & \varepsilon_d &= 0.1\,, & n &= 2\,, \\ R &= 0.4\,, & E_T^{\text{thres}} &= 4.8\ \text{GeV}\,, & \varepsilon &= 0.0042\,, \end{aligned} \tag{8.5}$$

where the parameters for the outer cone correspond to the settings used in the ATLAS measurement. Central renormalisation and factorization scales are again set equal to the photon transverse momentum $p_T^\gamma$. Figure 8.4 shows the four rapidity bins up to $|y^\gamma| = 2.37$, excluding the region $[1.37, 1.56]$ and compared to ATLAS data [22]. The NNLO corrections are positive and largely constant over the whole rapidity and $p_T^\gamma$ range, increasing the prediction for the central scale by approximately $(5-6)\%$. The scale uncertainty at NLO is around $\pm 10\%$ for the central rapidity bin and increases to more than $\pm 15\%$ for the more forward bins. At NNLO this uncertainty is significantly reduced to no more than $(+3.2, -5.1)\%$ in all bins, in most bins to even smaller values, except at very large $p_T^\gamma$ for the last three bins in the two most forward regions. Here the cross section drops quickly and the scale uncertainty increases.

Overall we observe a very good agreement with the data in most bins. Larger discrepancies are observed only for the highest values of $p_T^\gamma$, where data and theory remain nevertheless consistent within increasing experimental errors. In the second rapidity bin, we observe that the slope of the measured $p_T^\gamma$ distribution is less well described than in the other bins, with the theory prediction being slightly harder than the measurement.

### 8.1.3. The ratio $R^\gamma_{13/8}$

In [23] ATLAS measured the ratio $R^\gamma_{13/8}$ of the differential cross sections for inclusive photon production at 13 TeV and 8 TeV presented in the previous sections (figures 8.4 and 8.3, respectively) as a function of the photon transverse momentum. The ratio is evaluated in the same bins and rapidity regions used for the individual measurements, using the overlap of the phase-space regions, with $p_T^\gamma > 125$ GeV. By carefully taking into account the correlations of the experimental systematic uncertainties of the separate measurements, the overall systematic uncertainty of the ratio can be reduced. In particular those related to the photon energy scale, which are dominant in the individual measurements of $\mathrm{d}\sigma/\mathrm{d}p_T^\gamma$, are decreased.

The theory prediction for $R^\gamma_{13/8}$ has not been performed as an independent calculation, but rather has been derived using the two calculations for 8 TeV and 13 TeV. For both the theoretical uncertainty is estimated by means of a seven-point scale variation, as explained above. For the ratio, however, it is not exactly clear how the theoretical uncertainty should be calculated. Remember that the method of the scale variation is used to assess the impact of higher order corrections missing from the truncated perturbative series, because an all-order result must be independent of any unphysical parameters like $\mu_R$ and $\mu_F$. Put differently, the *envelope* of the scale variations is considered as a measure for the potential range in which the all-order result should lie. Considering a totally correlated ratio, i.e. always choosing the same scales in numerator and denominator, will by construction cancel much of the scale dependence, leading to a formally small theoretical uncertainty. However, this approach will likely underestimate the

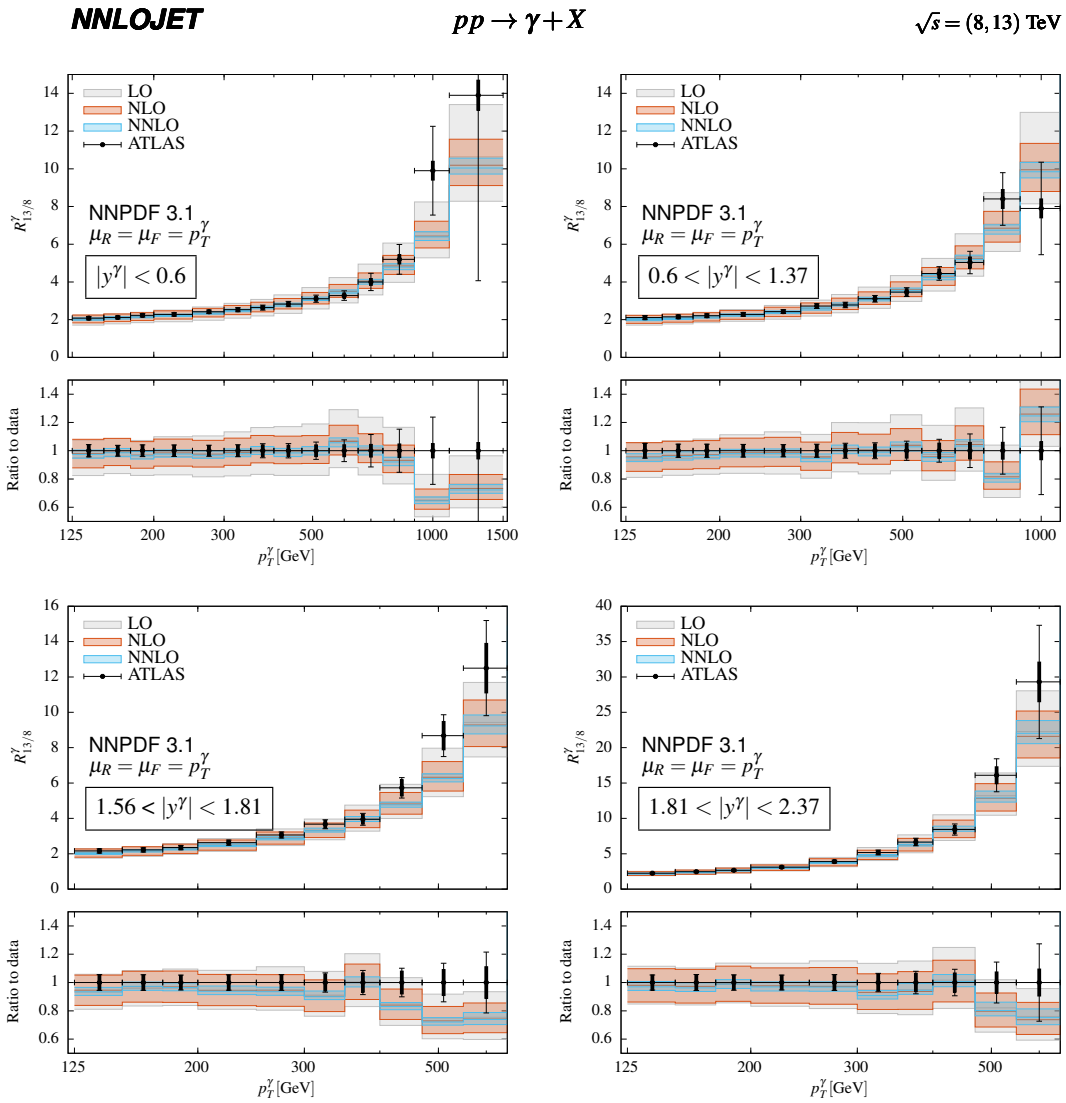


Figure 8.5.: $R^\gamma_{13/8}$ as a function of the transverse energy/momentum of the isolated photon at LO, NLO and NNLO in four different rapidity bins, from central (top left) to most forward (bottom right). The theoretical uncertainty bands are derived by means of an independent variation of factorization and renormalisation scales, both in the numerator and the denominator (see text for details). The results are compared to ATLAS data [23]. (Figure 1 from [159].

actual uncertainty[1]. On the other hand, a fully uncorrelated ratio inflates the error unreasonably. We will therefore choose the middle ground by generalising the conventional seven-point scale variation for two scales, to a 31-point scale variation for four scales, i.e. varying the renormalisation and factorisation scales for both the numerator and denominator independently: $\mu_F^i = a_i\, p_T^\gamma$, $\mu_R^i = b_i\, p_T^\gamma$ with $i \in \{\text{numerator,denominator}\}$ and $a_i, b_i \in \{1/2, 1, 2\}$, where we exclude the configurations with the ratio of any two scales equal to 1/4 or 4.

In figure 8.5 we show the result in the four rapidity bins also used in figures 8.4 and 8.3 and compare to ATLAS data [23]. Except for the highest bins in $p_T^\gamma$ the description of the data is excellent. Like for the calculations [74] for individual $\sqrt{s}$ we see a significant reduction in the uncertainty when going from NLO to NNLO, even with our conservative approach to the scale uncertainty explained above: While at NLO the uncertainty lies between $(+10, -9)\%$ and $(+17, -14)\%$, only slightly growing with $p_T^\gamma$ and $|y^\gamma|$, at NNLO it lies between $(+3.4, -2.8)\%$ and $(+6.5, -4.0)\%$.

### 8.1.4. Comparison with CMS 13 TeV measurements

The CMS 13 TeV measurement of isolated photon production [26] is performed in four bins in rapidity

$$|y^\gamma| < 0.8, \quad 0.8 < |y^\gamma| < 1.44, \quad 1.57 < |y^\gamma| < 2.1, \quad 2.1 < |y^\gamma| < 2.5\,, \tag{8.6}$$

and yields photon transverse momentum distributions for $p_T^\gamma > 190$ GeV. It uses a fixed-cone isolation procedure.

We compute the theory predictions using NNPDF3.1 with a central scale of $p_T^\gamma$, and use the hybrid isolation parameters

$$\begin{aligned} R_d &= 0.1\,, & \varepsilon_d &= 0.1\,, & n &= 2\,, \\ R &= 0.4\,, & E_T^{\text{thres}} &= 5\ \text{GeV}\,, & \varepsilon &= 0\,, \end{aligned} \tag{8.7}$$

with the large cone parameters coinciding with the fixed-cone settings used by CMS. Figure 8.6 shows the result in the four rapidity bins up to $|y^\gamma| = 2.5$, excluding the region $[1.44, 1.57]$. Again we find the NNLO corrections to be positive and largely constant, increasing the NLO predictions by roughly $(4 - 6)\%$ for the central scale. The scale uncertainties are similar as observed in the previous subsection: at NLO approximately $\pm 10\%$ for central rapidities and growing to $\pm 15\%$ for the most forward bin, and no more than $(+1.4, -4.2)\%$ at NNLO.

Most data points agree with the calculation within the respective experimental and theoretical uncertainty, with discrepancies mainly observed in the bins with the largest $p_T^\gamma$. Again, the theory prediction for the slope of the $p_T^\gamma$ distribution in the second rapidity bin is harder than what is observed in the experimental data. This effect is even more pronounced for the CMS data than for the ATLAS data. Given that ATLAS and CMS display a similar pattern in this region using 13 TeV data, this may point towards the need to reconsider the parton distributions in kinematical ranges relevant to this distribution.

[1] See also the discussion about the uncertainties of cross section ratios in [193].

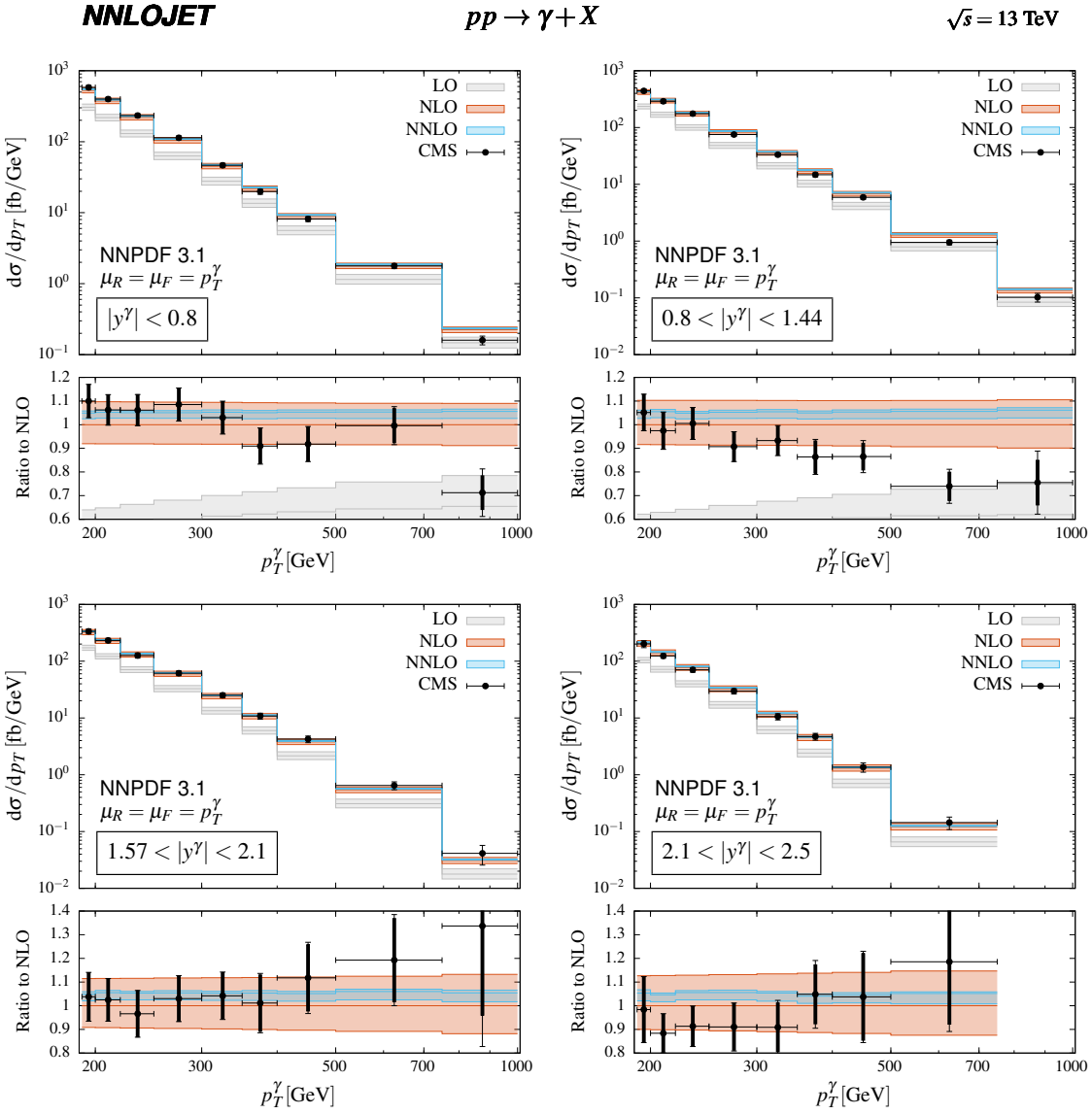


Figure 8.6.: Transverse energy/momentum distribution of the photon at LO, NLO and NNLO in four different rapidity bins, from central (top left) to most forward (bottom right). The results are compared to 13 TeV CMS data [26]. Note that for the sake of comparison the data has been multiplied by the corresponding rapidity bin-width, as CMS presents the data in double-differential form in $p_T^\gamma$, $y^\gamma$. (Figure 7 from [74])

### 8.1.5. Isolated photon production at low transverse momentum

So far we looked into inclusive photon production at comparatively high momenta as measured by the ATLAS and CMS experiments. Due to its special layout the ALICE experiment on the other hand is able to measure photons with considerably smaller transverse momentum. In [28] they report a measurement of the inclusive photon production in the range

$$10 \text{ GeV} \leq p_T^\gamma \leq 60 \text{ GeV} \tag{8.8}$$

in $\sqrt{s} = 7$ TeV proton-proton collisions, using $\mathcal{L} = (473 \pm 33)\text{nb}^{-1}$ of data. The measurement is restricted to the central rapidity region,

$$|y^\gamma| < 0.27\,. \tag{8.9}$$

At the leading order the photon and the recoiling parton are back-to-back in the centre-of-momentum frame and the Bjorken-$x$ values are given by

$$x_1 = \frac{p_T^\gamma}{\sqrt{s}}\left(e^{+y^\gamma} + e^{+y^{\text{recoil}}}\right), \tag{8.10a}$$

$$x_2 = \frac{p_T^\gamma}{\sqrt{s}}\left(e^{-y^\gamma} + e^{-y^{\text{recoil}}}\right). \tag{8.10b}$$

Assuming $y^\gamma \approx y^{\text{recoil}}$ and using the above cuts we can get a rough estimate of how small the $x$-values we probe can get. We find

$$x_{1,2} \gtrsim 2 \cdot 10^{-3}\,. \tag{8.11}$$

Given that inclusive photon production is sensitive to the gluon PDF already at leading order through QCD Compton scattering, it becomes now clear why looking into the low transverse momentum region might be of interest. In practise higher order corrections will blur the direct relation given by eq. (8.10) and a wider range of $x$ values will be probed for a given $p_T^\gamma$. As the authors of [28] argue, photons can still be considered a better probe than for example hadrons, for which the range of examined $x$ values would be even broader.

From an experimental point of view the actual measurement suffers from the low photon purity at small values of $p_T^\gamma$. The huge number of background photons makes the photon isolation particularly challenging, so that it is regarded as the main source of systematic uncertainty.

Employing a hybrid isolation (eq. (7.3)) with the parameters

$$\begin{aligned} R_d &= 0.1\,, & \varepsilon_d &= 0.1\,, & n &= 2\,, \\ R &= 0.4\,, & E_T^{\text{thres}} &= 2 \text{ GeV}\,, & \varepsilon &= 0\,, \end{aligned} \tag{8.12}$$

we calculated the differential cross section in the transverse momentum region given in (8.8). The fixed cone parameters in (8.12) correspond to the fiducial isolation performed by ALICE. To estimate the theoretical uncertainty we performed the conventional seven-point scale variation, with $\mu_R = \mu_F = p_T^\gamma$ as the central scale. The PDFs were again taken from the NNPDF3.1 set.

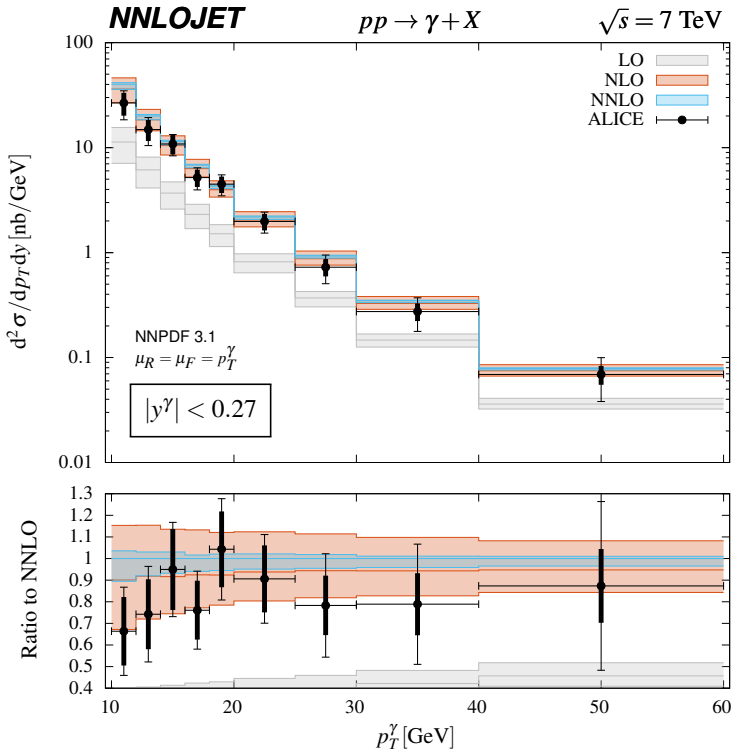


Figure 8.7.: Transverse energy/momentum distribution of the photon at LO, NLO and NNLO. The results are compared to 7 TeV ALICE data [28].

In figure 8.7 we present the results in double differential form in $p_T^\gamma$ and $y^\gamma$. To compare to data we had to rescale our results with the "isolated generated photon fraction" $\kappa^{\text{iso}}$, given in the left panel of figure 6 in [28][2].

We find the NNLO-to-NLO $k$-factor to be almost flat, describing a positive shift of the central scale by about 11% in the lowest bin and then decreasing towards the last bin with a shift of approximately 6%. As already observed for the other predictions above the NNLO result lies well within the NLO scale band, pointing at a good convergence of the perturbative expansion also for low values of the photon transverse momentum. When going from NLO to NNLO the scale uncertainty reduces quite considerably from $(+14, -11)\%$ to $(+1.1, -3.5)\%$ in the highest bin and from $(+28, -25)\%$ to $(+3.6, -10.5)\%$ in the lowest. Our prediction is in exact agreement with the data, both regarding the normalisation and the shape, but given the rather large experimental uncertainties of several tens of percent, we cannot make any statements more precise than that. We see that at the lowest $p_T^\gamma$ the experimental uncertainty is driven by the systematics, which in turn is dominated by the low photon purity.

From the above we conclude that with our setup, using NNLOJET and the hybrid isolation procedure, we are able to produce high accuracy predictions for inclusive photon production even at low transverse momenta without any big difficulties. In the future this might indeed become useful in the extraction of the gluon PDF at small $x$.

[2]For details on the efficiency we refer directly to the ALICE paper [28].

### 8.1.6. Dependence on photon isolation parameters

The hybrid isolation procedure approximates the fixed-cone isolation that is used in the experiment through a theory prescription that vetos collinear quark–photon configurations and eliminates the contribution from the photon fragmentation functions. This behaviour is obtained by applying a smooth isolation procedure inside a small inner cone of radius $R_d$, concentric to the larger isolation cone of radius $R$. As a consequence, some amount of hadronic energy inside the inner cone is not properly treated in the theory calculation, resulting in a systematic mismatch on the cross section prediction. The resulting small offset will vary with the $E_T^{\max}$ that is used in the experimental isolation, but is independent on $R$, as long as $R > R_d$, since it affects only parton radiation inside $R_d$. Consequently, our calculation in hybrid isolation can predict the variation of the isolated photon cross section under changes of the size of the isolation cone $R > R_d$. The neglected photon fragmentation process contributes only inside $R_d$, and potentially leads to an $R$-independent offset on the normalization of the cross section, as discussed in detail in chapter 7 above.

As a test case for the $R$-dependence, we consider the isolated photon cross section of the ATLAS 13 TeV measurement [22] (discussed in section 8.1.2above) integrated in $p_T^\gamma$, for the four different rapidity bins (8.1). We use our default setup with hybrid isolation parameters as in (8.5), varying only $R$. Figure 8.8 displays the $R$-dependence of the cross sections at different perturbative orders. For LO, the cross section is constant, since the number of partons is insufficient to trigger the cone-based isolation. We vary the fixed cone size between $R = 0$ to $R = 0.8$, and observe that the $R$-dependence is very similar in all four rapidity bins. As expected, we see a decrease of the cross section when going to higher values of $R$, as an increasing portion of the phase-space for the extra QCD radiation is vetoed. This decrease is slightly stronger at NNLO than at NLO, likely due to the improved description of extra radiation with increasing number of external partons. The scale uncertainty on the NNLO cross section is not larger than $(+1.3, -2.9)\%$. Once the cone size of the outer fixed cone becomes smaller than the size of the smooth cone $R < R_d$, the hybrid isolation prescription becomes largely identical to a smooth cone isolation with cone size $R_d$, since the catchment area of the fixed cone falls fully inside the smooth cone. This can be seen in the figures for $R < 0.1$, with a near-flat cross section indicating that the behaviour is essentially dictated by the smooth cone isolation step.

## 8.2. Photon-plus-jet production

The measurement of hadronic jets produced in association with an isolated photon allows for the direct reconstruction of the leading-order kinematics of the underlying two-to-two scattering process, thereby constraining in particular the momentum fractions of the incoming partons. Following earlier studies at the Tevatron [30, 31], ATLAS [32–34] and CMS [26, 35–37] provided precision measurements of photon-plus-jet production over a large kinematical range.

The interpretation of these data, and their potential usage in extraction of parton distribution functions, requires precise theory predictions. Our NNLO corrections for photon-plus-jet production are compared to the 8 TeV CMS data [37] and to the 13 TeV ATLAS [34] and CMS [26] data. By default, the hybrid isolation procedure in the form of eq. (7.3) is applied. For compari-

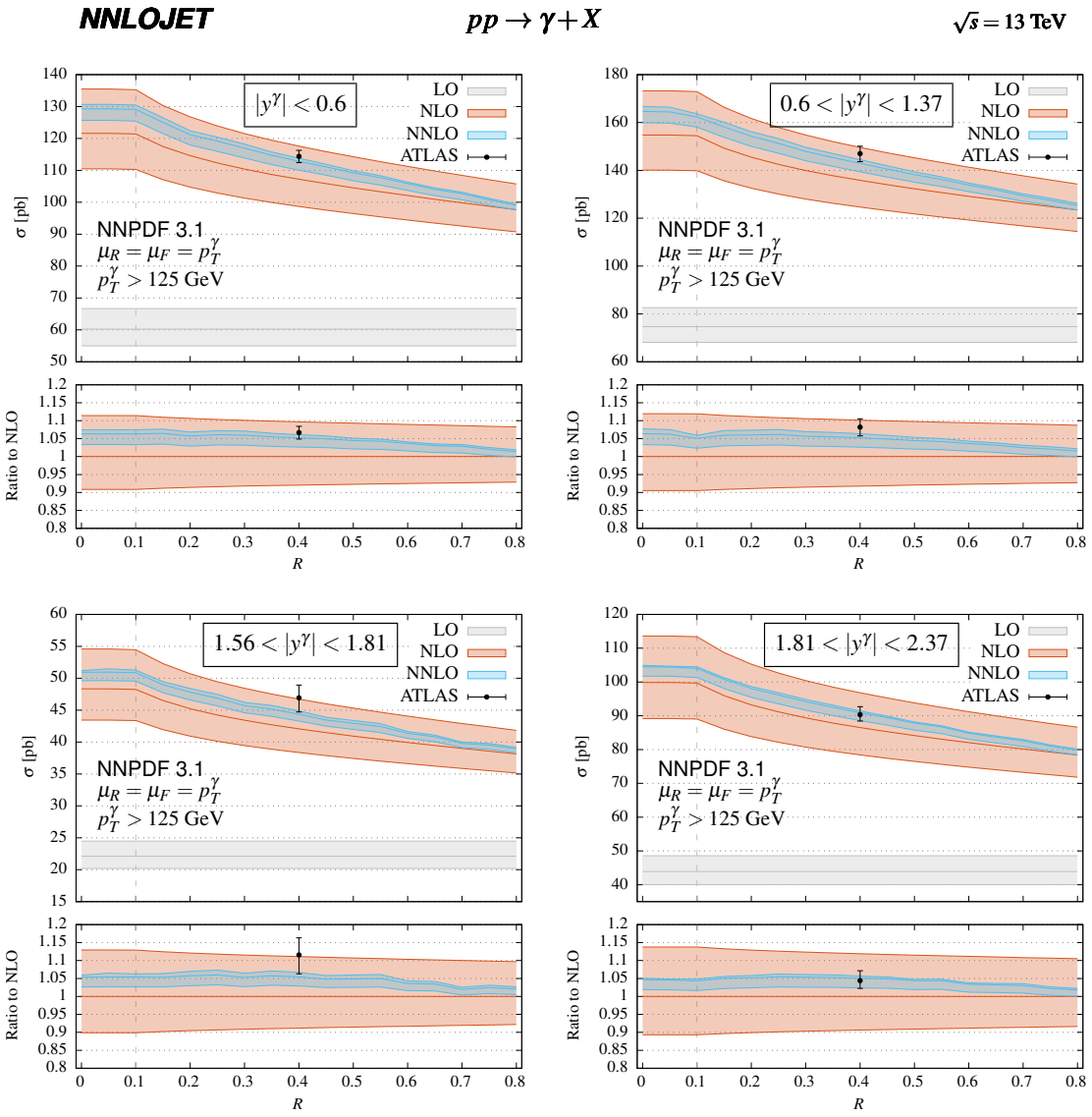


Figure 8.8.: Dependence of the total cross section for inclusive photon production at 13 TeV at LO, NLO and NNLO on the cone size $R$ of the outer fixed cone used in the hybrid isolation procedure, for different regions of the photon rapidity. All other isolation parameters are fixed: $R_d = 0.1$, $\varepsilon_d = 0.1$, $n = 2$, $E_T^{\text{thres}} = 4.8$ GeV, $\varepsilon = 0.0042$. The dashed line marks the cone size $R_d$ of the smooth cone. The ATLAS measurement [22] is performed only for a fixed cone with size $R = 0.4$. (Figure 8 from [74])

son with the MCFM calculation, we also replicate the setup of [149] using a smooth cone isolation with the same parameters as chosen there, confronted with the CMS 8 TeV measurements.

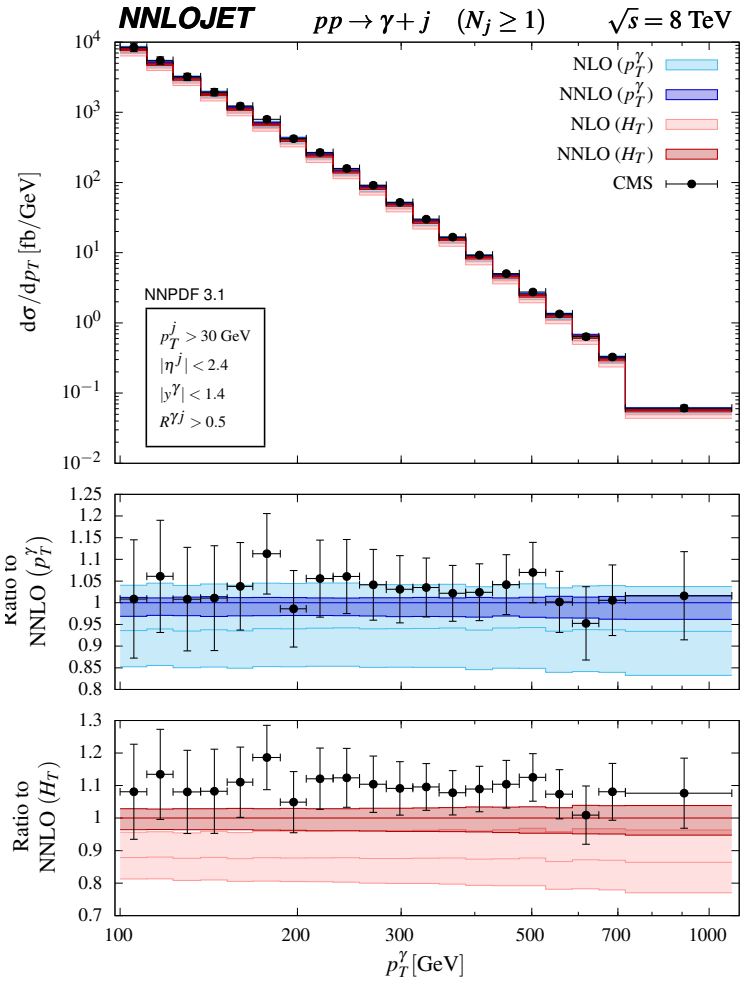


Figure 8.9.: Transverse energy/momentum distribution of the photon at NLO and NNLO for different central scale choices: $p_T^\gamma$ in blue, $H_T$ in red. The calculations are carried out using the NNPDF3.1 NNLO PDF set [188] and the hybrid isolation procedure. The results are compared to 8 TeV CMS data [37]. (Figure 9 from [74])

### 8.2.1. Comparison with CMS 8 TeV measurements and MCFM calculation

The CMS measurement of photon-plus-jet production uses the anti-$k_T$ algorithm [125] with a radius parameter of $R^j = 0.5$ to perform the jet clustering. The following cuts in transverse momentum and pseudorapidity are applied to the jets:

$$p_T^j > 30 \text{ GeV}, \qquad |y^j| < 2.4. \tag{8.13}$$

The measurement is inclusive on the jet multiplicity, meaning that events are retained if they contain at least one jet passing these cuts. Photons are identified with a fixed-cone isolation and must be separated in azimuth and pseudorapidity from the jet axis by $R^{\gamma j} > 0.5$. Their transverse momentum distribution for $p_T^\gamma > 100$ GeV is measured in the central rapidity region $|y^\gamma| < 1.4$.

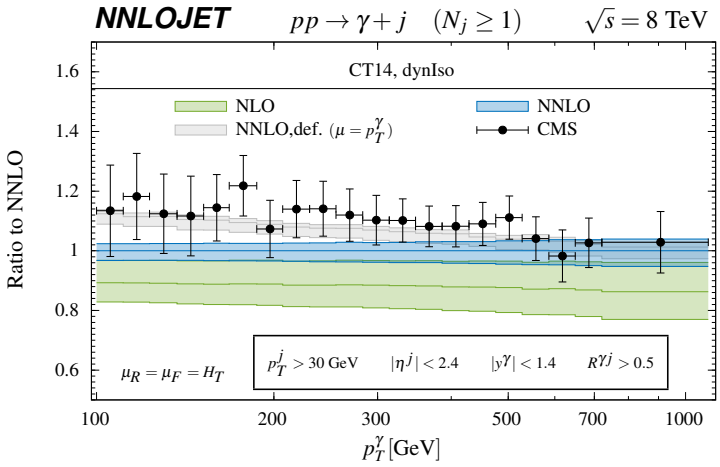


Figure 8.10.: Ratio to NNLO for the transverse energy/momentum of the photon at NLO and NNLO, using the PDF and isolation procedure choice of MCFM [149]. The default NNLO result is shown in grey. (Figure 10 from [74])

Our calculation is performed with the default setting, using NNPDF3.1 parton distributions and hybrid isolation with the same parameters as in (8.7), matching the fixed-cone settings of the CMS measurement [37]. We use two different values for the central scale: $\mu_R = \mu_F = p_T^\gamma$ and $\mu_R = \mu_F = H_T$, where $H_T$ is defined as the scalar sum of the transverse momenta of all final state partons and the photon. A central scale at $p_T^\gamma$ is our standard choice, while $H_T$ has been used in the MCFM calculation [149]. The results are shown in figure 8.9. For both central scale choices we find the NNLO corrections to be positive. For $H_T$, they are typically $(14-16)\%$, which is considerably larger than the $(6.0-7.1)\%$ corrections obtained for $p_T^\gamma$. While in both cases the scale uncertainty at NLO is up to $\pm 11\%$, it is decreased at NNLO to up to $(+1.7, -3.8)\%$ for $p_T^\gamma$ and up to $(+3.9, -5.3)\%$ for $H_T$. In terms of perturbative stability, $p_T^\gamma$ appears thus to be sightly favourable as the central scale choice. Although within experimental and theoretical uncertainties both scale choices are consistent with the data, the calculation carried out using $p_T^\gamma$ yields a better description of data, while the predictions using $H_T$ are below the data in almost all bins.

To compare our result to the MCFM calculation of the NNLO corrections [149], we replicate the setup used there, with CT14 PDF, smooth cone isolation with (see eq. (7.2))

$$R_d = 0.4 \qquad \varepsilon_d = 0.025\,, \qquad n = 2\,, \tag{8.14}$$

and $H_T$ as the central scale choice. The NLO and NNLO results are shown in figure 8.10, which reproduces the lower panel of figure 2 in the MCFM study. We observe a good agreement with the result presented in [149], which provides an important cross-check on both calculations, which were performed with completely different methods, and which rely on fully independent implementations. The specific aspects of the MCFM calculation that required a re-evaluation of the isolated photon results, discussed in section 8.1.1 above, are not expected to have a significant impact on the results for the photon+jet process [190] that are compared here.

### 8.2.2. Comparison with ATLAS 13 TeV measurements

Detailed measurements of kinematical distributions in photon-plus-jet production were performed by the ATLAS collaboration [34], based on data taken at 13 TeV. The study uses the anti-$k_T$ algorithm with $R^j = 0.4$ to identify the jets, and the following parameters for the fixed-cone based photon isolation:

$$R = 0.4\,, \qquad E_T^{\text{thres}} = 10\ \text{GeV}\,, \qquad \varepsilon = 0.0042\,, \tag{8.15}$$

which only differ in the threshold energy $E_T^{\text{thres}}$ from the ones used in the inclusive photon measurement discussed in Section 8.1.2. We take the same parameters for the smooth cone of the hybrid isolation procedure as above:

$$R_d = 0.1\,, \qquad \varepsilon_d = 0.1\,, \qquad n = 2\,. \tag{8.16}$$

The fiducial event selection cuts are as follows:

$$\begin{gathered} p_T^j > 100\ \text{GeV}, \quad |y^j| < 2.37, \\ p_T^\gamma > 125\ \text{GeV}, \quad (|y^\gamma| < 1.37 \text{ or } 1.56 < |y^\gamma| < 2.37), \quad R^{\gamma j} > 0.8. \end{gathered} \tag{8.17}$$

The measurement requires that at least one jet passes the above jet cuts, and is thus inclusive on the number of jets. Distributions involving the jet kinematics always refer to the leading (in transverse momentum) jet. For some observables examining the photon–jet system, additional cuts are imposed:

$$|y^\gamma + y^j| < 2.37\,, \qquad m^{\gamma j} > 450\ \text{GeV}\,, \qquad |\cos\theta^*| < 0.83\,, \tag{8.18}$$

where

$$\cos\theta^* = \tanh\frac{\Delta y^{\gamma j}}{2}\,, \tag{8.19}$$

with $\Delta y^{\gamma j}$ being the rapidity difference between the photon and the leading jet. In the centre-of-momentum system of the underlying two-to-two Born process $\theta^*$ corresponds to the scattering angle. In the following, the fiducial selection cuts are explicitly indicated in the figures.

We compute the theory predictions in our default setting, with NNPDF3.1 and hybrid isolation, using the parameters listed in (8.15) and (8.16) and with $p_T^\gamma$ as central scale. The transverse momentum distribution of the photon $p_T^\gamma$ is compared to the ATLAS data [34] in figure 8.11. We see that going from NLO to NNLO leads to substantial improvements in both scale uncertainty of the prediction as well as description of the data in general.

While in the $p_T^\gamma$ spectra of inclusive photon events discussed earlier, the NNLO corrections were largely flat over the whole range, this is not the case for the inclusive photon-plus-jet process. The corrections are negative for $p_T^\gamma < 175$ GeV and small and positive for $p_T^\gamma > 175$ GeV, they change the shape of the distribution, so that it describes that of the data much better, particularly up to 550 GeV. The improvement in the scale uncertainty is similar to what we

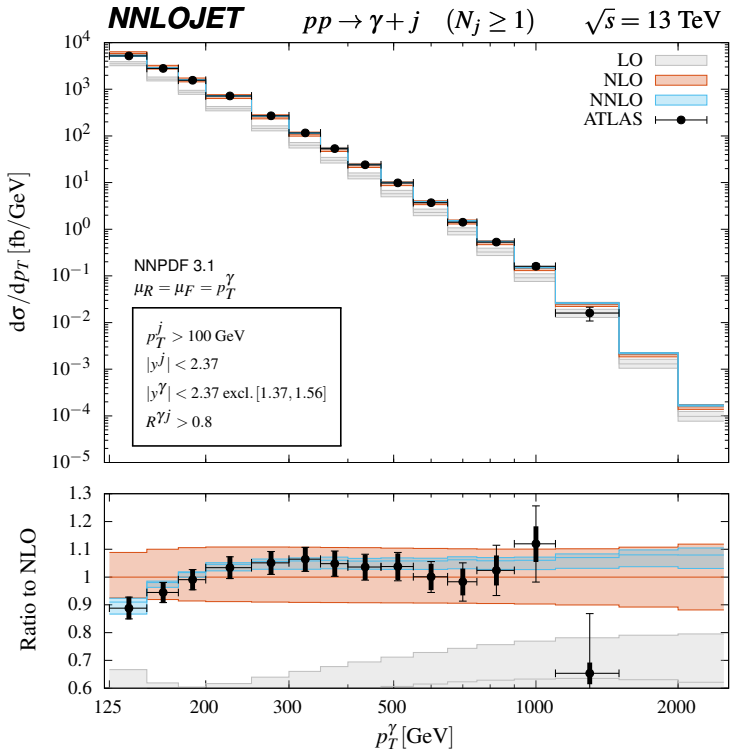


Figure 8.11.: Transverse momentum distribution of the photon in photon-plus-jet events, at LO, NLO and NNLO. The predictions are compared to ATLAS data [34]. (Figure 11 from [74])

have observed previously for inclusive photon production, going down from approximately $\pm 10\%$ at NLO to no more than $(+2.3, -4.7)\%$ at NNLO. In most bins the uncertainty is even smaller than that. The NNLO scale band lies within the NLO band, pointing towards convergence of the perturbative series. In the last bin for which data is available, the calculation overestimates the cross section. In this region, electroweak Sudakov logarithms start to become numerically sizeable [191, 192], and could be resolved with increasingly accurate data.

At leading order, the photon and the leading jet carry identical amounts of transverse momentum. Including higher order corrections, this one-to-one correspondence no longer holds, although typically photon and leading jet largely balance each other's transverse momenta. The leading jet $p_T^j$ distribution is shown in figure 8.12. The fiducial $p_T$-cuts (8.17) on the photon and the jets are slightly different, which leads to a discontinuity in the LO $p_T^j$ spectrum around the value of the $p_T^\gamma$ cut, marked in the plot with a dashed line. Being forced into a strict back-to-back configuration at LO, in all events the jet has at least 125 GeV of transverse momentum, cutting a significant portion from of the first bin ($(100 - 130)$ GeV).

As a consequence the cross section in that bin is underestimated quite significantly. Only from NLO onwards, when additional real radiation can take part of the recoil, we can have a softer leading jet, thereby describing the event kinematics more truthfully, and leading to a better agreement with the data. The cross section in the first bin is therefore described at

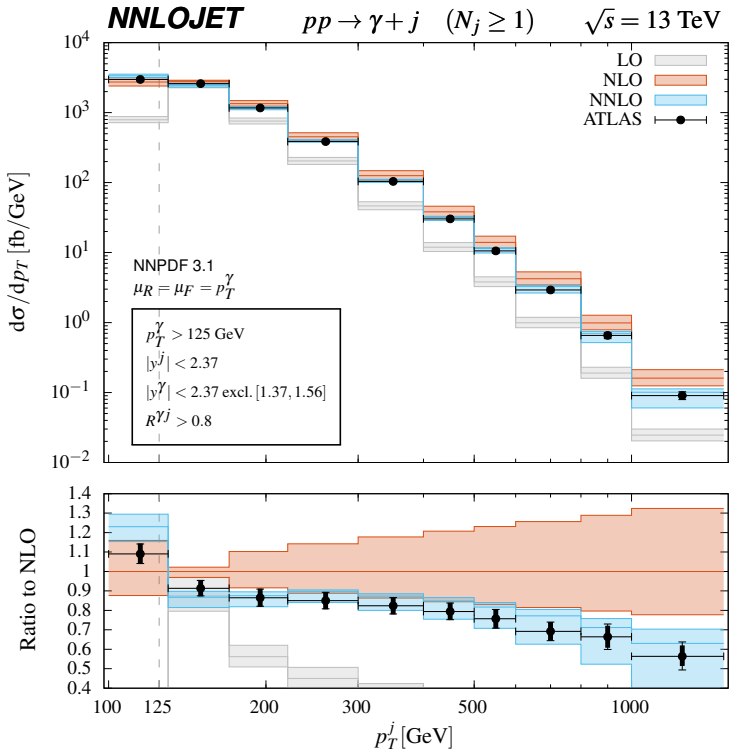


Figure 8.12.: Transverse momentum distribution of the leading jet in photon-plus-jet events, at LO, NLO and NNLO. The grey dashed line marks the cut on the $p_T$ of the photon, the recoil of which mostly goes into the leading jet. The predictions are compared to ATLAS data [34]. (Figure 12 from [74])

one order lower than it is in the other bins, which reflects itself in the size of the NLO scale variation, being significantly larger in the first bin than in the second. The NLO corrections and the associated scale uncertainty increase very substantially towards larger $p_T^j$. This effect stems from configurations with two hard back-to-back jets accompanied by photon at much lower transverse momentum, which is effectively described as a leading order process. All but the first data point lie below the NLO uncertainty band, which fails to describe the shape of the data. It is only upon including the NNLO corrections that the theory prediction matches the measured spectrum, and that scale errors become more uniform at $(+3, -11)\%$ size, at least for the $p_T^j$ range from 130 GeV to 500 GeV. For higher $p_T^j$ the scale uncertainty grows rapidly, up to $(+11, -40)\%$ in the highest bin. The origin of this can be found in the same configurations which already inflated the NLO scale uncertainty at high $p_T^j$.

The invariant-mass distribution of the photon–jet system is shown in figure 8.13. As for the $p_T^j$-distribution, we observe very large and positive NLO corrections. Here the NLO scale uncertainty is again around $(+12, -10)\%$ for the low mass bins and growing moderately to roughly $(+15, -12)\%$ in the bins above 1000 GeV. The NNLO correction is nearly constant and shifts the central value towards the lower edge of the NLO scale band, while decreasing the scale uncertainty to no more than $(+1.4, -7.7)\%$. With this the NNLO result matches the data nicely

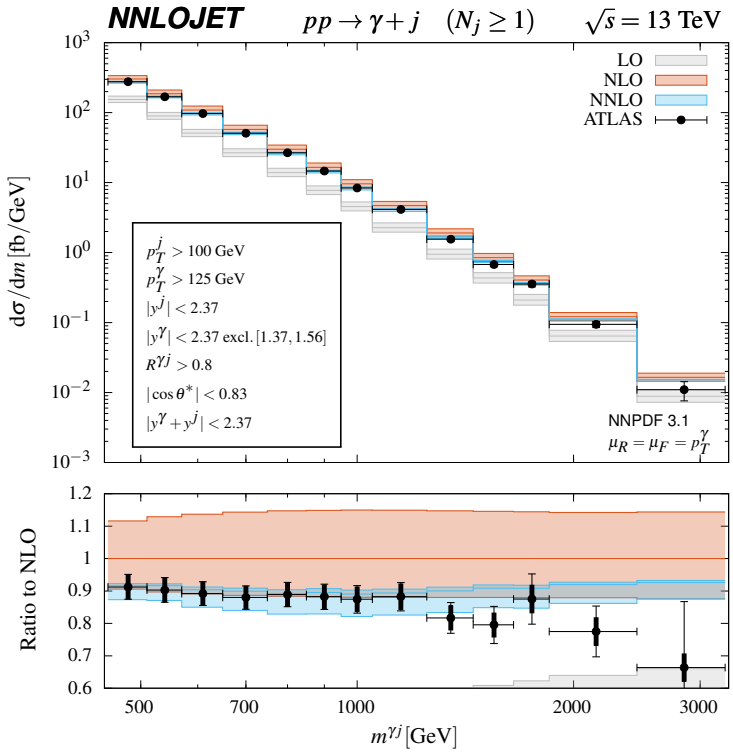


Figure 8.13.: Invariant mass of the photon leading jet system, at LO, NLO and NNLO. The predictions are compared to ATLAS data [34]. (Figure 13 from [74])

up to 1250 GeV. At higher masses the measured cross section lies below the prediction in most bins, yet still being consistent within increasing errors.

The azimuthal separation in the photon–jet system, shown in figure 8.14, is described in a meaningful manner only from NLO onwards, as in the LO configuration photon and the leading jet (the only jet present in the event) are exactly back-to-back and thus $\Delta\phi^{\gamma j}\big|_{\text{LO}} \equiv \pi$. It is closely related to the azimuthal separation in diphoton production, whose perturbative description has been investigated in detail [150, 151]. The NLO description of this observable is still dominated by back-to-back configurations and fails to provide a decent description of the data [34]. Only after including the NNLO corrections, allowing for one more real radiation parton to take part of the recoil and shifting the leading jet away from the back-to-back configuration, we see a significant enhancement in smaller separation angles. In particular in the lowest bin ($\pi/2$ to $3\pi/5$), the prediction is increased by more than a factor of four compared to its NLO value. The scale uncertainty is of similar size at NLO and NNLO, and in particular for smaller angles. At NNLO it decreases from $(+32, -22)\%$ in the lowest bin to $(+3.0, -7.0)\%$ in the back-to-back bin, this one being effectively one order higher than the others. Still the predictions match the data quite well and it becomes obvious that an NNLO calculation is indeed needed to make reasonable theoretical predictions about this specific observable.

Figure 8.15 shows the distribution in $|\cos\theta^*|$, which represents the scattering angle (8.19) in the underlying two-to-two Born process. On this distribution, the additional cuts (8.18)

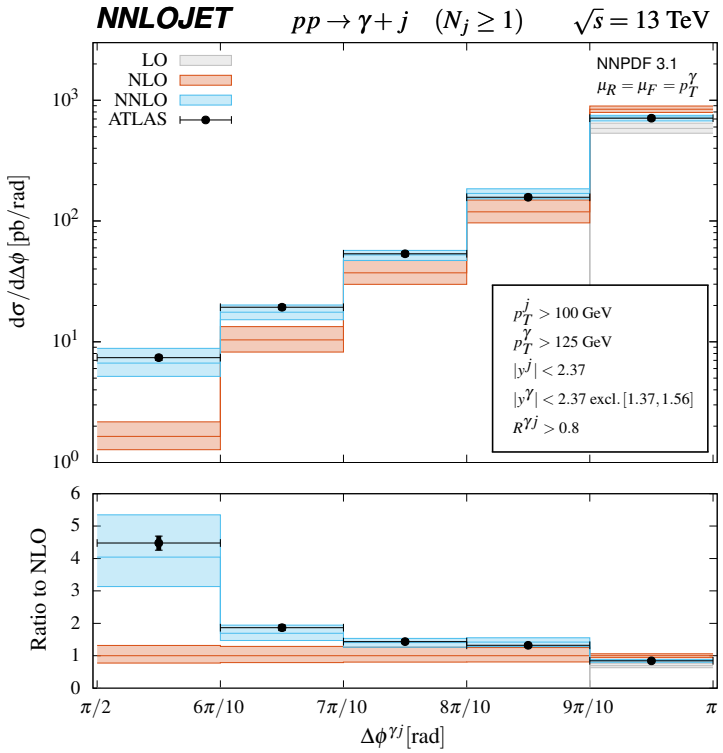


Figure 8.14.: Azimuthal separation of the photon and the leading jet, at LO, NLO and NNLO. The predictions are compared to ATLAS data [34]. (Figure 14 from [74])

were applied, thereby selecting photon–jet systems with high invariant mass. Its perturbative behaviour is thus similar to the $p_T^j$ and $m^{\gamma j}$ distributions, with very large and positive NLO corrections. We also find the NNLO corrections to be negative, shifting the central prediction to the lower edge of the NLO scale band. The scale uncertainty is reduced significantly at NNLO to no more than $(+1.3, -7.5)\%$, in most bins it is even smaller.

This observable was discussed by ATLAS [34] in view of a possible sensitivity to the photon fragmentation function at large $|\cos\theta^*|$, arising from differences in the angular dependence of the underlying Born process for direct production and fragmentation. The hybrid isolation procedure used in our calculation eliminates the photon fragmentation contribution, it is however only an approximation to the fixed-cone isolation used in the ATLAS measurement. Given that our calculation provides already a very good description of the $|\cos\theta^*|$ distribution, being consistent within errors throughout the full kinematical range, we conclude that the data at large $|\cos\theta^*|$ leave only little room for a contribution from photon fragmentation. Instead of investigating specific kinematical regions in isolated photon production, a more promising approach to the determination of the photon fragmentation functions may be through in the study of non-isolated photons inside hadronic jets [162, 194, 195].

The ATLAS measurement [34] of photon-plus-jet production was performed inclusively in rapidity. To gain better insight in the kinematical dependence of the perturbative corrections, and in the potential sensitivity to the parton distributions, figure 8.16 displays the rapidity

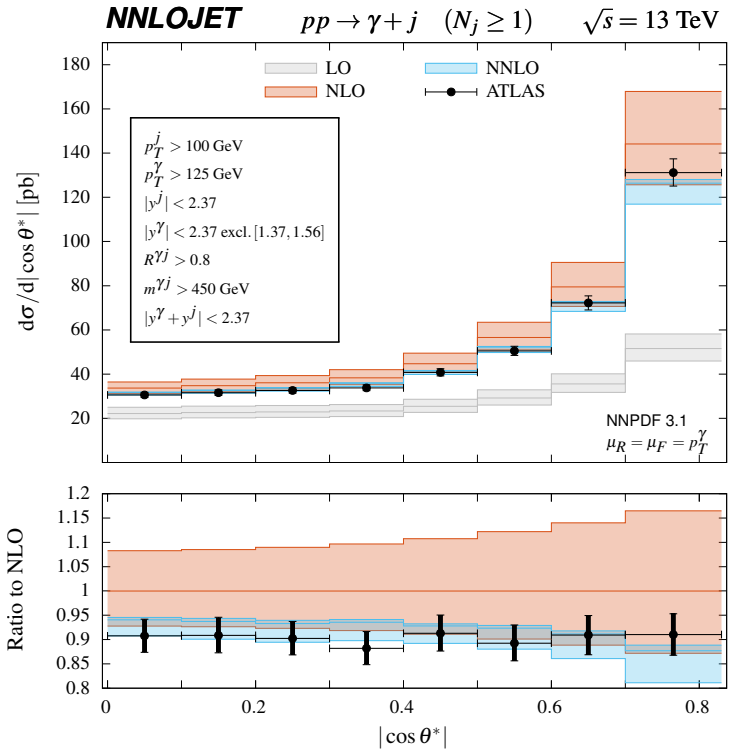


Figure 8.15.: Distribution in $|\cos\theta^*|$ at LO, NLO and NNLO. The predictions are compared to ATLAS data [34]. (Figure 15 from [74])

distributions of the photon and the leading jet, as well as distributions in rapidity sum and difference. While the NNLO corrections appear to be quite uniform in the individual rapidity distributions, we observe some changes of the shapes in the rapidity correlation distributions. In these, the corrections are largest in magnitude for small rapidity sum (symmetric events) and for large rapidity difference (small scattering angle), remaining negative throughout.

### 8.2.3. Comparison with CMS 13 TeV measurements

The 13 TeV CMS study of isolated photon production [26] discussed in Section 8.1.4 above also provides measurements of photon-plus-jet observables. For these, jets are clustered using the anti-$k_T$ algorithm with radius parameter $R^j = 0.4$ and requiring

$$p_T^j > 30 \text{ GeV}\,, \qquad p_T^\gamma > 190 \text{ GeV}\,, \qquad R^{\gamma j} > 0.4\,. \tag{8.20}$$

Results for the photon transverse momentum distribution are presented in different bins in rapidity for the photon and the jet, corresponding to central and forward production:

$$|y^\gamma| \in [0, 1.44] \quad \text{and} \quad |y^\gamma| \in [1.57, 2.5]\,, \tag{8.21a}$$
$$|y^j| \in [0, 1.5] \quad \text{and} \quad |y^j| \in [1.5, 2.4]\,, \tag{8.21b}$$

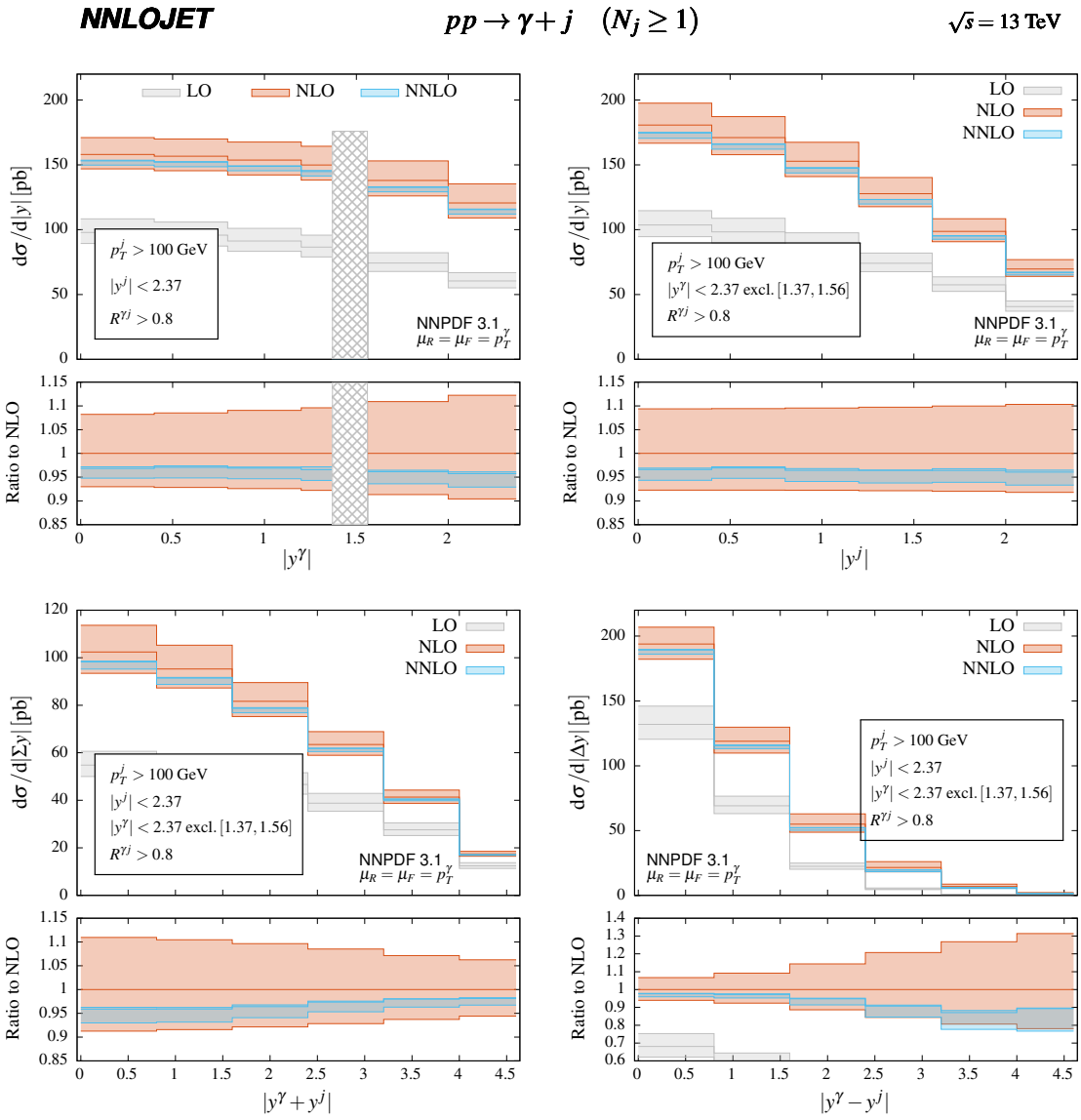


Figure 8.16.: Rapidity distribution of the photon (top left), of the leading jet (top right), distribution of the rapidity sum of both (bottom left) and of the rapidity difference (bottom right), at LO, NLO and NNLO. (Figure 16 from [74])

omitting the region $|y^\gamma| \in [1.44, 1.57]$. With these, four combinations of central/forward photon/jet rapidity regions are measured.

We use our default setup, with NNPDF3.1 and hybrid isolation using the same parameters (8.7) as in Section 8.1.4 and $\mu_R = \mu_F = p_T^\gamma$ as central scale choice. The results are shown in figure 8.17. We find the NLO scale uncertainty to be largely flat over the whole $p_T^\gamma$ range in all four rapidity bins, with a size of about $\pm 10\%$. The NNLO corrections are positive and mostly flat in all bins, increasing the central prediction by $(4-9)\%$. The scale uncertainty is reduced

to less than $(+0.9, -2.8)\%$ for the configurations with a central jet and less than $(+2.1, -4.3)\%$ for those with a forward jet.

Although the predictions are consistent with the data within the respective uncertainties, they do however not yield a good description of the shape of the measurement. It appears that the form of the discrepancy depends on the photon rapidity and not so much on the leading jet rapidity. For the central photon the prediction is too low in the low $p_T^\gamma$ region and too high in the high $p_T^\gamma$ region, irrespectively of the jet rapidity. If the photon is forward, the predictions match the data at low $p_T^\gamma$, but underestimate the cross section in the high $p_T^\gamma$ tail, again independently of the jet rapidity. In other words, the calculation predicts more high-$p_T$ photons in the central region than there are actually observed, but fewer softer photons in the central and fewer hard photons in the forward region. A similar pattern was already observed in the isolated photon distribution measured by CMS, figure 8.6, although somewhat less pronounced.

If this tension in the shape persists and becomes more pronounced, it will be rather unlikely that it could be accommodated by a modification of the parton distribution functions. In the case of the photon-plus-jet measurement, it may indicate that the rather low jet transverse momentum cut leads to potentially large logarithmic corrections, which are poorly described by fixed-order perturbation theory.

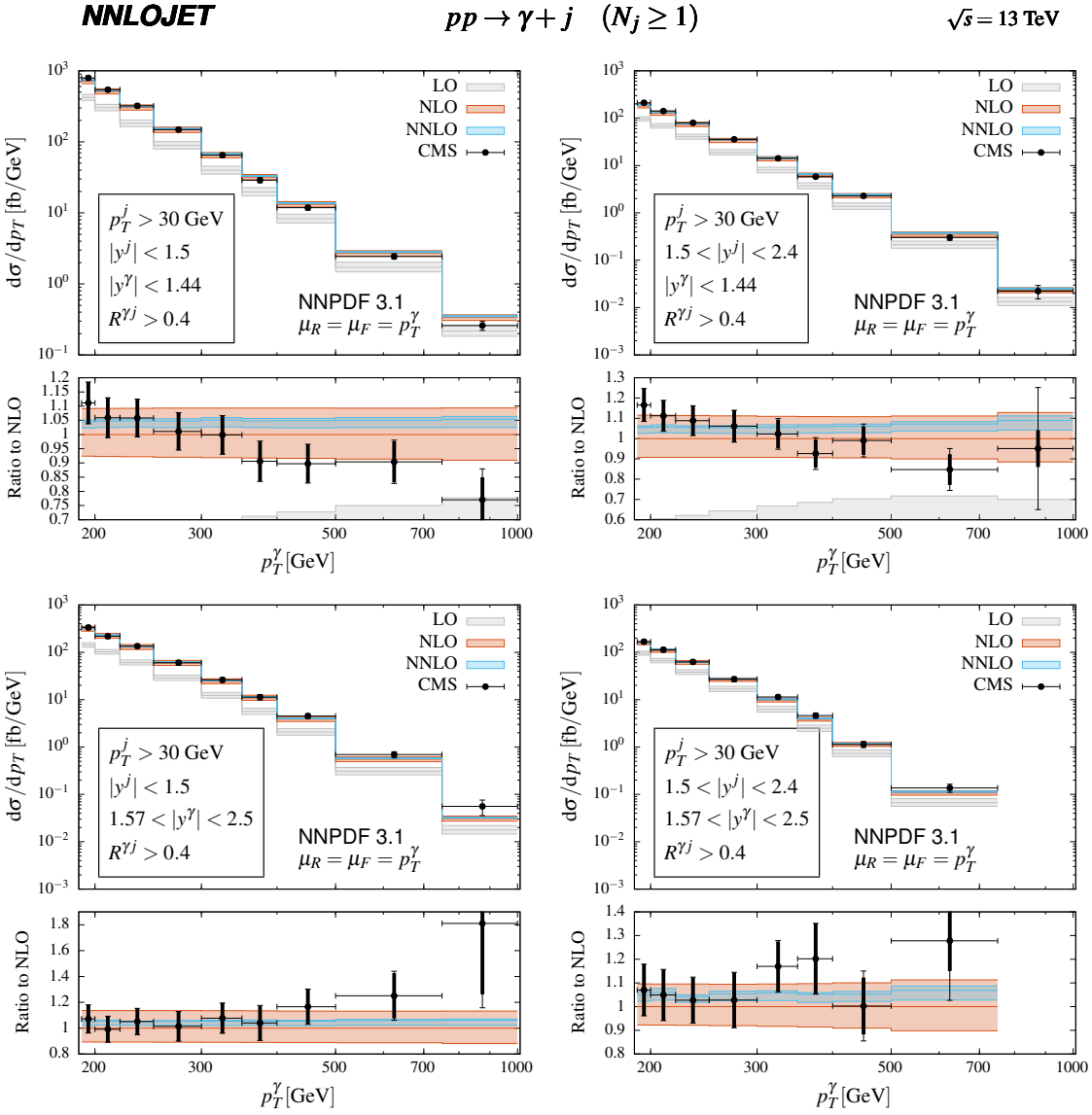


Figure 8.17.: Transverse energy/momentum distribution of the photon at LO, NLO and NNLO in two different rapidity bins for the photon and the leading jet, each. The results are compared to CMS data [26]. Note that the data has been multiplied by the corresponding rapidity bin-widths, as CMS presents the data in triple-differential form in $(p_T^\gamma, y^\gamma, y^j)$. (Figure 17 from [74])

# 9. Summary and conclusion of part II

The recent experimental progress in the measurements of isolated photon and photon-plus-jet production at the LHC requires a reduction of the theoretical uncertainties if the one wishes to make optimal use of the precision data. The conventional approach to improve the theory results is by including ever higher orders in perturbation theory, which however drastically increases the complexity of the calculation, both in terms of the scattering amplitudes to be included and the structure of the IR limits.

Here we described all the ingredients necessary to perform the calculation up to NNLO QCD accuracy. After investigating the colour decomposition of all the tree, one-loop and two-loop matrix elements contributing to the production of a single photon, we briefly discussed how the antenna subtraction terms needed to handle the IR singular limits are related to those of $Z$-plus-jet production. We then proceeded with the description of the various steps undertaken to validate our implementation.

An additional complication arises from the differences in the photon isolation procedure applied in theory and experiment, as described in more detail in part I. With state-of-the-art tools this discrepancy is inevitable at the level of NNLO corrections. However, using the novel hybrid cone isolation procedure we are able to at least reduce this mismatch by applying the same fixed cone isolation with radius $R$ as the experiment, but regulating the problematic collinear region with a smaller smooth cone of size $R_d$. [1] In chapter 7 we performed a detailed study of isolation settings at NLO, which revealed only a moderate sensitivity on the inner cone's parameters of the hybrid prescription, allowing us to infer a much reduced ambiguity associated with this procedure. In the limit of small $R_d$, we further confirmed the correct logarithmic behaviour $\sigma \sim \log(1/R_d)$ as predicted by QCD. This behaviour is compensated in the limit $R_d \to 0$ by a negative final state mass factorisation counterterm from the photon fragmentation function, resulting in a numerical compensation of fragmentation contributions and smooth cone suppression at a finite value of $R_d$, which we estimate to be in the vicinity of $R_d = 0.1$. The associated uncertainty on the cross section predictions is at the level of a few per cent, and largely concentrated at low values of photon transverse momentum. For $p_T^\gamma > 125$ GeV, a very conservative estimate based on comparison at NLO with fixed cone isolation and a model for the photon fragmentation functions results in below 5% uncertainty, while a variation of the $R_d$ parameter at NNLO points to an uncertainty below 2%. Moreover, using the hybrid isolation the exact dependence of the cross section on the fixed cone $R$ can be predicted, as long as $R_d^2 \ll R^2$ is respected. This opens up the possibility to perform more stringent tests of perturbative QCD predictions in the future once measurements are available for different cone sizes.

[1] The following paragraphs are up to small changes taken from the summary in our publication [74].

Up to now, all predictions at NNLO in QCD involving prompt photons have employed a smooth cone isolation. In chapter 8 we presented our calculation of isolated photon and photon+jet processes at NNLO in QCD using the antenna subtraction method and, for the first time, apply the hybrid cone isolation at this order. We performed a detailed comparison of our predictions to the available measurements by the ATLAS and CMS collaborations, which overall show an excellent agreement to the data. Going from NLO to NNLO, we observe a dramatic reduction in scale uncertainties across the entire kinematic range with residual scale uncertainties that are typically at the level of 5% or smaller for genuine NNLO observables. This reduction persists also in the ratio of observables measured at different $\sqrt{s}$. For isolated photon production, the NNLO corrections are rather flat with a positive shift of about +5% in the central prediction. In the photon-plus-jet process, on the other hand, NNLO corrections can induce substantial shape distortions that often could not be resolved at NLO due to the much larger scale uncertainties. The reduced theory errors further expose some minor tensions with the CMS photon+jet measurement at 13 TeV, which are difficult to account for by PDF effects and will require further investigation. A comparison to recent ALICE data proved the applicability of our setup also for very low values of the photon transverse momentum, which could be useful to probe the gluon PDF in the proton at very low $x$, once the comparatively large systematic uncertainties of the measurement related to the low photon purity in that region are under control.

The excellent perturbative convergence displayed in the NNLO prediction combined with a photon isolation treatment that follows closely the procedure used in experiments puts the theory predictions on a solid basis with residual uncertainty estimates that are competitive with the experimental errors, often even surpassing them. Although much smaller than in the smooth cone isolation, the hybrid approach still contains an intrinsic theoretical ambiguity from the removal of the fragmentation component through the narrow inner cone. Further progress in alleviating the mismatch between experiment and theory for the isolation procedure will require the calculation of the fragmentation component at NNLO. With this, the theory calculation can apply identical photon isolation criteria as used in the experimental measurements, however at the expense of introducing a novel dependence on photon fragmentation functions.

# Part III.

# NLO EW corrections for $\gamma\gamma$ and $\gamma + X$

# Introduction

While the expansion in the QCD coupling constant appears natural in the context of hadronic collisions, this leaves out the electroweak sector and with this a large part of the SM interactions. The coupling $g$ of the heavy weak gauge bosons $Z$ and $W^{\pm}$ and the electromagnetic coupling $e$ of the photon are connected and can both be expressed in terms of the QED coupling constant $\alpha$ through the simple relation

$$e^2 = g^2 \sin^2 \theta_W = 4\pi\alpha \,. \tag{9.1}$$

Including EW corrections therefore corresponds to a perturbative expansion in $\alpha$. Comparing the numerical size of the coupling constants $\alpha_s$ and $\alpha$ at a reasonable scale for hadronic collisions gives us a crude estimate of the size of the electroweak corrections[2]. Given that [196]

$$\left.\begin{aligned} \alpha_s(m_Z) &\approx 0.118 \\ \alpha(m_Z) &\approx 1/128 \end{aligned}\right\} \Rightarrow \frac{\alpha_s^2(m_Z)}{\alpha(m_Z)} \approx 1.8 \,, \tag{9.2}$$

NLO EW corrections can be expected to have a similar impact as the NNLO QCD corrections. For processes where NNLO QCD is needed to match the experimental accuracy, the NLO EW corrections should therefore be considered, too. Moreover, EW corrections are known to modify the shape of differential distributions in a non-trivial way, especially in the tails of distributions where the impact of Sudakov double logarithms [197] of the form $\alpha \log^2\left(Q^2/m_i^2\right)$ with $m_i = m_W, m_Z$ becomes seizable [191, 192, 198–200]. This is of particular interest as precisely that region is sensitive to physics beyond the Standard Model [201–203].

A short survey on the processes which are particularly sensitive to EW corrections and are among the most abundant at the LHC can be found in [204]. So far, NLO EW or QED corrections in combination with NLO or NNLO QCD have been calculated for many of the processes relevant at the LHC[3] [205–211].

While the NNLOJET code has originally been constructed to compute QCD corrections up to NNLO accuracy, in the following we will make a first attempt to also include NLO EW corrections. The photon processes for which the QCD corrections are already implemented shall serve as our test cases.

This part of the thesis is organized as follows: In chapter 10 we will discuss the general technical aspects of NLO EW corrections, with the focus on processes with external photons. Chapter 11 is dedicated to the implementation of the EW corrections in NNLOJET. In chapter 12 we investigate the NLO EW corrections for diphoton production. The contributing channels and

[2] For the sake of this argument we can assume $\sin^2 \theta_W$ to be an $\mathcal{O}(1)$ constant.
[3] This list is by no means exclusive.

their corresponding IR structure are discussed. The implementation is then validated against the computational framework MATRIX [186], before we show some phenomenology results based on the 8 TeV ATLAS study [29]. The exercise is repeated for inclusive photon production in chapter 13. We briefly summarise our findings and conclude in chapter 14.

# 10. Aspects of NLO EW corrections

Once we go beyond pure fixed order QCD and also consider NLO EW corrections, modifications in several steps of the calculation are required. The most obvious point is the occurrence of new matrix elements at different relative order in $\alpha$. This matrix elements will naturally introduce new (QED) IR limits which have to be taken care of. Last but not least there a channels with photons and/or leptons crossed into the initial state, so that in principle we need to include photon and lepton PDFs. In the next sections we will first discuss how to organize the matrix elements and their crossings in a calculation based on a two-fold perturbative expansion, i.e. simultaneously in $\alpha_s$ and $\alpha$. We will then discuss the impact of photonic and leptonic PDFs, before investigating the general IR structure we have to expect at the NLO EW level, and how antenna subtraction can be applied to deal with the limits. After some comments on more technical aspects of the calculation we will discuss the consequences of extra real radiation photons on the treatment of photons in general.

## 10.1. Mixed power counting in the matrix elements

When considering QCD and EW corrections simultaneously we have to deal with a two-fold perturbative expansion, one in $\alpha_s$, one in $\alpha$. Consequently structuring the calculation becomes more involved than for a computation of QCD corrections only. While in an expansion in one coupling only we have a clear correspondence between the order of a contribution ($\mathrm{N^kLO}$) and the power of the couplings,

$$\mathrm{N^kLO} \Leftrightarrow \alpha_s^{n+k}\alpha^m \qquad (k \in \mathbb{N}_0), \tag{10.1}$$

this is not the case for the mixed expansion. Here we rather have a correspondence between the total power of the couplings and the perturbative level,

$$\mathrm{N^kLO} \Leftrightarrow \alpha_s^{n+i}\alpha^{m+j} \qquad (k \in \mathbb{N}_0\,, i,j \in \mathbb{Z}\,, k = i+j). \tag{10.2}$$

This is schematically depicted in figure 10.1.

At the LO level we usually define the contribution with the highest possible power of $\alpha_s$, corresponding to $k = i = j = 0$, as the QCD-Born. The other contributions to the LO level, $k = 0$ and $j = -i$, contain two different types of channels:

- Channels with new external state signatures, not present within the QCD-Born, like the $q\bar{q} \to \gamma\gamma$ diphoton channel as part of inclusive photon production.

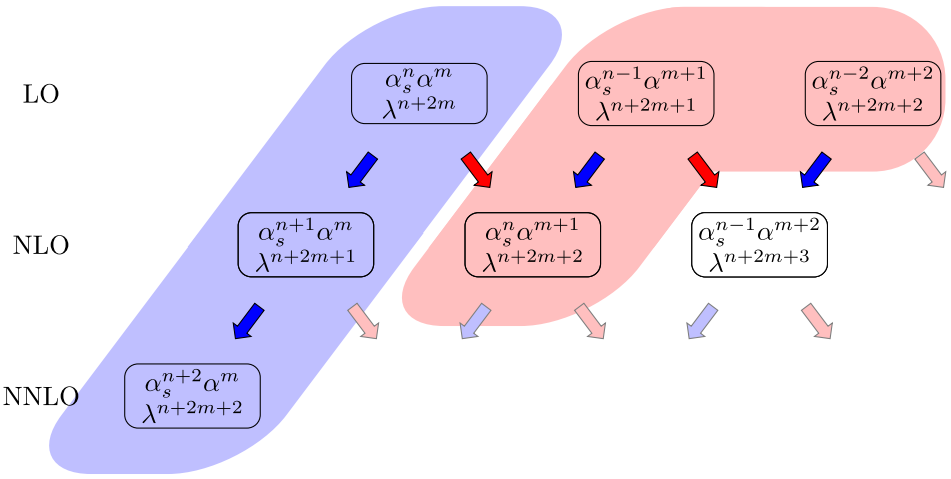


Figure 10.1.: General structure of mixed QCD/EW corrections. At each level (LO, NLO, ...) we have multiple contributions with different powers of the couplings. Each contribution at a given level is connected to two contributions at the next level by either an extra power of $\alpha_s$ (blue arrows) or $\alpha$ (red arrows). The QCD-Born corresponds to the LO contribution with the highest possible power of $\alpha_s$ and the pure QCD corrections correspond to the leftmost chain of blobs (blue background). The $\lambda$s show the estimated size of the contribution. See text for more details.

- Channels with external state signatures already present within the QCD-Born but with different internal coupling structure, and interferences of those channels. An example is the $4q$-channel in dijet production. Depending on whether the two quark lines are connected by a gluon or an electroweak gauge boson, we have $4q$ channels at $\mathcal{O}(\alpha_s^2)$, $\mathcal{O}(\alpha_s\alpha)$ (interference), and $\mathcal{O}(\alpha^2)$.

Each of the different LO contributions is connected to two different contributions at the NLO level, by either adding a power of $\alpha_s$ or $\alpha$. Naively one could interpret this as QCD or EW corrections to a given diagram, however this concept can be misleading, as one can turn the argument around, in the sense that any contribution at NLO is connected to two contributions at LO[1]. It is therefore not always possible to unambiguously identify a given diagram as either a QCD correction to a lower order diagram or an EW correction to a different lower order diagram. The bookkeeping of matrix elements and channels should therefore be based on the external states and the power of the couplings only.

To estimate the size of a given contribution in this scheme, based on the earlier mentioned comparison of the numerical size of the coupling constants, it is useful to define the generic expansion parameter $\lambda \sim \mathcal{O}(0.1)$. We then assign one or two powers of $\lambda$ to the strong and electromagnetic coupling constant, respectively,

$$\alpha_s \sim \lambda\,, \qquad \alpha \sim \lambda^2\,. \tag{10.3}$$

Contributions with the same total power of $\lambda$ should then be of comparable size. The QCD-Born of a given process corresponds to the contribution with the lowest power of $\lambda$ and the QCD

[1] Apart from those which are minimal in one of the couplings.

corrections up to NNLO come with up to two additional powers (blue background in figure 10.1). When including NLO EW corrections, we should therefore consider all those contributions with up to two additional powers of $\lambda$. In the most general case this corresponds to the two subleading Borns with relative (to the QCD-Born) coupling $\alpha/\alpha_s$ and $\alpha^2/\alpha_s^2$, as well as the NLO term of relative order $\alpha$ (red background in figure 10.1). Any further Born or NLO terms are considered to be of negligible size compared to NNLO QCD (i.e of the same size as N$^3$LO QCD or smaller). We will give more explicit examples of this bookkeeping scheme in chapters 12 and 13, when considering NLO EW corrections to diphoton and inclusive photon production, respectively.

## 10.2. EW PDFs, leptonic real radiation and the Higgs boson

Including additional powers of $\alpha$ with respect to the QCD Born channels allows us to cross photons and in principle also leptons into the initial state. Thus, we need to discuss the inclusion of PDFs which account for the photon and lepton content in the proton. The precise determination of these PDFs requires an extension of the DGLAP evolution equations and splitting functions to also include QED effects [212–214]. Compared to the quark and gluon PDFs the photon (lepton) PDF is suppressed by $\mathcal{O}(\alpha)$ ($\mathcal{O}(\alpha^2)$) and hence the impact is expected to be small. This has been investigated for some key processes at hadron colliders in [213]. While the photon PDF does have an impact on phenomenology, the (charged) lepton PDFs are completely negligible for a realistic set of event cuts. It is for that reason that lepton PDFs are not widely available, while there has been quite some development on the photon PDFs [212, 215–218].

In the following we will therefore only consider the possibility of photons in the initial state and discard all crossings with initial state leptons. This has the consequence that lepton pairs can only appear in the final state, both when they are already present at the Born level (for example as decay products of heavy weak gauge bosons) or as additional EW real radiation. The latter case, however, will be a subleading EW correction, which we do not consider following the argument in the previous section. The point is that in order to generate a lepton pair it needs to couple to either a $\gamma, Z$ or $W^\pm$ (in which case we get a lepton-neutrino pair), amounting to an overall factor of $\alpha^2$ in the squared amplitude; one $\alpha$ coming from the coupling of the lepton pair to the gauge boson, one $\alpha$ from the coupling of the gauge boson to the rest of the diagram. See figure 10.2 for an illustration. Note that the leptons cannot couple to a final state photon already present at LO QCD, because this would obviously eliminate the photon from the list of final states, but at LO QCD all final state photons are part of the definition of the process, so they must be kept at all stages. We will call those photons the QCD-Born photons in the following. At leading order final state photons not part of the process definition can only occur as part of a subleading ($\mathcal{O}(\alpha/\alpha_s)$) Born. Splitting such a non-QCD-Born photon into a lepton pair is then again a subleading $\mathcal{O}(\alpha/\alpha_s) \times \mathcal{O}(\alpha)$ effect. As a consequence we do not have any additional external leptons, neither in the initial nor in the final state, at the NLO EW level as we define it. They can, however, appear in closed fermion loops as part of the EW virtual corrections.

As for the final state weak gauge bosons, which due to their short life-time are never detected directly but rather through their respective decay products, they will in general be part of the

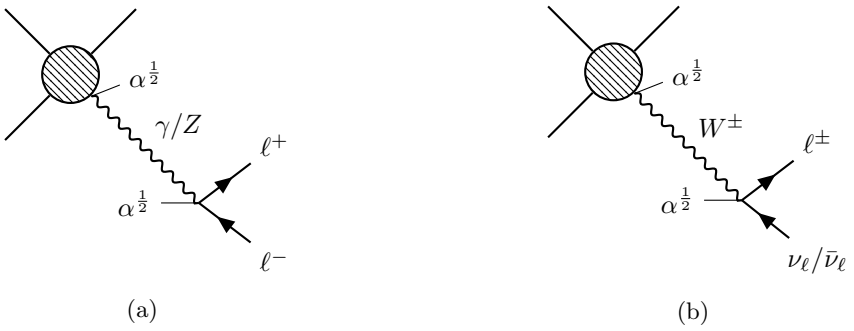


Figure 10.2.: Diagrams generating a final state lepton pair. Because weak gauge bosons are in general part of the process definition, we only have to consider the photon for the EW corrections. In that case the blob corresponds to the subdiagram already satisfying all the requirements set by the process definition (i.e. number of final state partons, photons, leptons etc.). The corresponding squared amplitude is of relative order $\alpha^2$ and therefore is part of the subleading EW corrections.

process definition itself. That is, the production of a state $X$ in association with a $Z$ or $W^\pm$ decaying into leptons will be considered as the process $X + Z/W^\pm$ and not a EW correction to inclusive $X$ production. Thus, also $Z$ and $W^\pm$ will only appear as virtual particles or as mediators between quark lines.

A similar argument can be made about the Higgs boson. Due to its central part in EW symmetry breaking, virtual Higgs bosons are usually also considered as part of the EW corrections, while on the other hand a real final state Higgs will be used to define the process itself, and is thus not to be considered as part of the EW corrections.

The Higgs couples to massive particles only. As long as the first five quark flavours and the leptons are considered massless, as it is conventionally done in the calculation of QCD corrections[2], the only massive particles are the weak gauge bosons $Z$ and $W^\pm$, and the top quark. This means that at the NLO EW level virtual Higgs bosons only appear when either of these particles is already present at LO QCD. For pure QCD processes like dijet production or photon processes this is not the case, and the insertion of a Higgs is an NNLO EW effect, because it will always be accompanied by the insertion of a $Z, W^\pm$ or $t$. In particular for diphoton and isolated photon production we therefore do not need to consider the Higgs.

We can summarise the new pieces we encounter in the NLO EW corrections with relative order $\alpha$ and $\alpha/\alpha_s$ at the matrix element level as follows:

- Genuine QED corrections with both real and virtual photons.
- Weak gauge bosons as virtual particles, either in loop diagrams or as mediators between quarks, but not as real radiation.
- Virtual Higgs bosons, but only if the QCD Born already contains massive particles, and again not as real radiation.

[2]Except for explicit mass-effect studies.

- Closed lepton loops, but no initial or final state leptons beyond the ones already present at the QCD Born level.

## 10.3. IR limits at NLO EW

Removing all real radiation weak gauge bosons from the calculation is not a problem from the perspective of IR singularity cancellation, because the corresponding loop amplitudes with virtual $Z$ and $W^{\pm}$ will be regulated in the IR due to their finite mass. Consequently the IR singularity structure of the NLO EW corrections is completely determined by the QED component, i.e. virtual photons and real radiation photons attached to quark lines.

For any contribution of $\mathcal{O}(\alpha_s^n \alpha^m)$ we can in principle encounter both IR QCD and QED limits. In the first case we will have a factorization onto an $\mathcal{O}\big(\alpha_s^{n-1}\alpha^m\big)$ reduced matrix element, in the latter onto an $\mathcal{O}\big(\alpha^n\alpha^{m-1}\big)$ reduced matrix element[3]. This reflects the twofold structure of the perturbative expansion we discussed before, with a given NLO contribution being connected to both a LO contribution of relative order $\alpha_s^{-1}$ and one with relative order $\alpha^{-1}$.

Since we are considering at most one additional real radiation particle at NLO EW, we do not need to worry about double unresolved mixed QCD/QED limits. For all single unresolved limits we encounter, standard NLO methods to deal with IR singularities can be applied. In NNLOJET it is straightforward[4] to extend the existing antenna subtraction method to also accommodate for the QED limits, as we shall se in section 10.4 below. Concerning the colour structure a photon exactly behaves as an abelian gluon, thus all limits we have to consider for the real radiation corrections are the photon either becoming soft or collinear to a (anti-)quark to which it directly coupled. Unlike an abelian gluon, a photon will also couple to the charged leptons, but the structure of the IR limits is exactly the same as for quarks, so that schematically we can write (compare eqs. (3.18) and (3.20))

$$M^0_{n+1}(\dots, i_f, j_\gamma, k_{\bar{f}}, \dots) \xrightarrow{\gamma\to 0} Q_f^2 S_{ijk} M^0_n(\dots, i_f, k_{\bar{f}}, \dots)\,, \tag{10.4a}$$

$$M^0_{n+1}(\dots, i_f, j_\gamma, \dots) \xrightarrow{\gamma||f} \frac{Q_f^2}{s_{ij}} P_{ij\to I}(z) M^0_n(\dots, I_f, \dots)\,, \tag{10.4b}$$

where $M^0_n$ and $M^0_{n+1}$ are colour-ordered tree level matrix elements with $n$ and $n+1$ final states, respectively. $S_{ijk}$ is the soft function and $P_{ij\to I}(z)$ the fermion-photon splitting function, which differs from the quark-gluon splitting function only by a different prefactor, from which we explicitly pulled out the charge factor $Q_f^2$ of the fermion-line the unresolved photon couples to. In the equations above $\bar{f}$ stands both for an anti-quark and an $\ell^+$. The $\gamma||\bar{f}$ limit can be obtained by swapping $f \leftrightarrow \bar{f}$ in (10.4b).

A special case of the collinear splittings we encounter in QCD is when two colour-adjacent quarks of the same flavour become collinear, i.e. a $g \to q\bar{q}$ splitting. This situation can occur both for final-final configurations with both quarks in the final state or initial-final configurations with one of the quarks crossed into the initial state. In principle we can have the same situation in QED, in form of a $\gamma \to q\bar{q}$ splitting, but one can argue that this does not contribute to

[3] Provided those levels exist, of course.
[4] There is a caveat to this which is related to the photon fragmentation, as we will discuss in section 10.6.

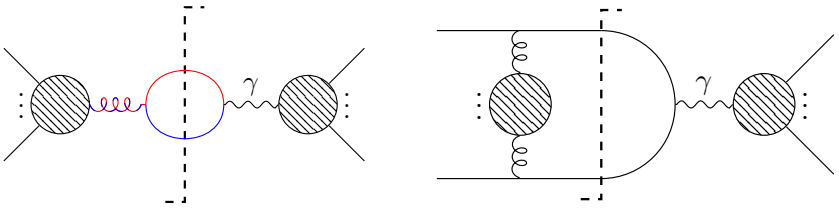


Figure 10.3.: Interferences between QCD and QED diagrams with $g \to q\bar{q}$ and $\gamma \to q\bar{q}$ splitting, respectively. Diagram (a) vanishes because of colour, diagram (b) is non-singular for $q||\bar{q}$.

the order we are considering (i.e. up to $\mathcal{O}(\alpha)$ and $\mathcal{O}\left(\alpha^2/\alpha_s\right)$ corrections over the QCD-Born). The photon splitting into the $q\bar{q}$ pair has to be internal and can couple only to another quark line, hence the diagram is $\mathcal{O}(\alpha/\alpha_s)$ relative to the corresponding pure QCD diagram. The squared amplitude is then $\mathcal{O}\left(\alpha^2/\alpha_s^2\right)$ relative to the QCD equivalent, and therefore not part of the level we are considering here. Notice, on the other hand, that the interference between the QED amplitude with $\gamma \to q\bar{q}$ splitting and the QCD amplitude with $g \to q\bar{q}$ splitting does contribute at the given level. They are, however, either vanishing because of colour conservation or exhibit at most integrable singularities in the $q||\bar{q}$ configuration (see figure 10.3). This can be understood from the fact that the only interferences not vanishing are the ones which have an s-channel $\times$ t-channel character[5]. Falling back to the nomenclature we introduced for the QCD matrix elements in section 6.1 for two external quark pairs those would be the D-types, see section 6.1.2.

## 10.4. Antenna subtraction for inclusive NLO EW corrections

In the case we treat the QED real radiation in an inclusive way, unresolved photons can be dealt with just as if they were abelian gluons. Following the factorisation properties we discussed in section 10.3, in the colour ordering the photon will always be sandwiched between two fermions of the same fermion line. Therefore the only antenna we need to correctly subtract all related limits, both soft and collinear, is the simple $A_3^0(i_f, j_\gamma, k_{\bar{f}})$ antenna. In the context of QCD it is defined as $(q, g, \bar{q})$ antenna [48], derived[6] from the decay $\gamma^* \to q\bar{q}$ with an additional gluon as real radiation [116]. It exhibits all the IR singular limits a gluon radiated from a quark line can participate in. Since there are no non-abelian couplings involved, i.e. the gluon couples directly to the quarks, we can simply replace it by a photon, provided we adapt the corresponding coupling factor. For the same reason the antenna can also be used if in addition we consider leptons instead of quarks.

While in the reduced matrix element we loose all information about the photon-momentum due to the momentum mapping, the charge factor $Q_f^2$ of the unresolved photon's coupling is retained and needs to be accounted for. This can be done by simply multiplying it to the antenna function, just as we did with the unresolved functions in the factorisation formulae

[5] Also $t \times u$ or $s \times u$ are possible.
[6] See section 3.5.2.

(10.4a) and (10.4b). In the following we will restrict ourselves to the discussion of quark-photon unresolved limits, the formulae, however, hold equally for lepton-photon limits once the charge factors are substituted accordingly.

Depending on whether the particles involved in the limit are crossed into the final or initial state we have to consider four different cases for the subtraction term, which we will present in the following. We base our discussion on the nomenclature introduced in section 3.5.3.

**The final-final configuration** In the case all three particles, the photon and the $q\bar{q}$-pair it radiates off, are in the final state the subtraction term is given by

$$\begin{aligned}\mathrm{d}\hat{\sigma}_{NLO}^{S,FF,q_i\gamma_j\bar{q}_k} = \mathcal{N}^R \sum_{perm.} \mathrm{d}\Phi_{n+1}(\{k\}_{n+1};p_1,p_2)\frac{1}{S_{n+1}} \\ \times Q_q^2 A_3^0(i_q,j_\gamma,k_{\bar{q}}) M_n^0(\dots,I_{q\gamma},K_{\gamma\bar{q}},\dots) J_n^{(m)}(\{\tilde{k}\}_n)\,, \end{aligned} \tag{10.5}$$

where we picked specifically photon $\gamma_j$ as the unresolved particle, i.e. there is no sum over $j$. It will account for the soft photon limit as well as the $q||\gamma$ and $\bar{q}||\gamma$ configurations. For the corresponding virtual subtraction term we find

$$\begin{aligned}\mathrm{d}\hat{\sigma}_{NLO}^{T,FF,q_i\gamma_j\bar{q}_k} = -\mathcal{N}^V \sum_{perm.} \mathrm{d}\Phi_{n}(\dots,I_q,K_{\bar{q}},\dots;p_1,p_2)\frac{1}{S_{n}} \\ \times Q_q^2 \mathbf{J}_2^{(1)}(I_q,K_{\bar{q}}) M_n^0(\dots;I_q,K_{\bar{q}};\dots) J_n^{(m)}(\{\tilde{k}\}_n)\,, \end{aligned} \tag{10.6}$$

with the integrated dipole (see also eq. (3.84))

$$\mathbf{J}_2^{(1)}(I_q,K_{\bar{q}}) = \mathcal{A}_3^{0,FF}(s_{IK})\,. \tag{10.7}$$

Since we are dealing with a final-final configuration, there is no mass factorisation contribution to the dipole and it is simply given by the integrated final-final antenna, as defined in eq. (3.80).

**The initial-final configuration: quark initiated** When the quark is crossed into the initial state we can use the initial-final version of the $A_3^0$ antenna to subtract all relevant limits, i.e. $\gamma \to 0$, $\bar{q}||\gamma$ and $q||\gamma$. The subtraction term reads

$$\begin{aligned}\mathrm{d}\hat{\sigma}_{NLO}^{S,IF,q_1\gamma_j\bar{q}_k} = \mathcal{N}^R \sum_{perm.} \mathrm{d}\Phi_{n+1}(\{k\}_{n+1};p_1,p_2)\frac{1}{S_{n+1}} \\ \times Q_q^2 A_3^0(1_q,j_\gamma,k_{\bar{q}}) M_n^0(\dots,K_{\gamma\bar{q}},\dots;\bar{1}_q,p_2) J_n^{(m)}(\{\tilde{k}\}_n)\,. \end{aligned} \tag{10.8}$$

The corresponding subtraction term for the anti-quark crossed into the initial state can readily be obtained by interchanging $q \leftrightarrow \bar{q}$ in above formula. The corresponding virtual subtraction term is given by

$$\mathrm{d}\hat{\sigma}_{NLO}^{T,IF,q_1\gamma_j\bar{q}_k} = -\mathcal{N}^V \int \frac{\mathrm{d}x}{x} \sum_{perm.} \mathrm{d}\Phi_n(\ldots, K_{\bar{q}}, \ldots; \bar{1}, p_2) \frac{1}{S_n} \times Q_q^2 \mathbf{J}_2^{(1)}(\bar{1}_q, K_{\bar{q}}; x) M_n^0(\ldots, K_{\bar{q}}, \ldots; \bar{1}_q, p_2) J_n^{(m)}(\{\tilde{k}\}_n)\,. \quad (10.9)$$

The integrated dipole (compare eq .(3.91)) now contains the mass factorisation kernel $\Gamma_{qq}^1$ in addition to the initial-final integrated antenna (eq. (3.89)):

$$\mathbf{J}_2^{(1)}(\bar{1}_q, K_{\bar{q}}; x) = \mathcal{A}_3^{0,IF}(s_{\bar{1}K}; x) - \Gamma_{qq}^1(x)\,. \quad (10.10)$$

**The initial-final configuration: photon initiated** Instead of the quark also the photon can be crossed into the initial state. In that case the only limit we have to consider is the (anti-)quark being collinear to the photon. We can use the initial-initial $A_3^0$ antenna together with an initial-initial momentum mapping to subtract this limit. This is done in order to avoid complications related to spurious IR limits which arise when using the D-type antennae one would usually take in such a situation [120]. The subtraction term (for $q||\gamma$) then looks like

$$\mathrm{d}\hat{\sigma}_{NLO}^{S,IF,q_i\gamma_1\bar{q}_k} = \mathcal{N}^R \sum_{perm.} \mathrm{d}\Phi_{n+1}(\{k\}_{n+1}; p_1, p_2) \frac{1}{S_{n+1}} \times Q_q^2 A_{3,\gamma\to q}^0(i_q, 1_\gamma, 2) M_n^0(\{\tilde{k}\}_n; \bar{1}_{\bar{q}}, \bar{2}) J_n^{(m)}(\{\tilde{k}\}_n)\,. \quad (10.11)$$

An important observation here is that the $q||\gamma$ limit changes the identity of the initial state particle in the reduced matrix element: the photon becomes an anti-quark. However, the contribution still has to be convoluted with the photonic PDF, just as the real radiation contribution. Otherwise there would be an inconsistency preventing the correct subtraction of the singularities. Notice that the identity of particle 2 does not matter here, as the two initial state particles never become collinear, thus we will never probe that limit of the antenna. In particular this also covers the case where 2 is the other end of the quark-line. Again the $\bar{q}||\gamma$ subtraction term is related by the swap $q \leftrightarrow \bar{q}$.

For the virtual subtraction term we find

$$\mathrm{d}\hat{\sigma}_{NLO}^{T,IF,q_i\gamma_1\bar{q}_k} = -\mathcal{N}^V \int \frac{\mathrm{d}x}{x} \sum_{perm.} \mathrm{d}\Phi_n(\{\tilde{k}\}_n; \bar{1}_{\bar{q}}, \bar{2}) \frac{1}{S_n} \times Q_q^2 \mathbf{J}_{2,\gamma\to q}^{(1)}(\bar{1}_{\bar{q}}, K_{\bar{q}}; x) M_n^0(\{\tilde{k}\}_n; \bar{1}_{\bar{q}}, \bar{2}) J_n^{(m)}(\{\tilde{k}\}_n)\,, \quad (10.12)$$

with the identity changing integrated dipole

$$\mathbf{J}_{2,\gamma\to q}^{(1)}(\bar{1}_{\bar{q}}, K_{\bar{q}}; x) = \mathbf{J}_{2,g\to q}^{(1)}(\bar{1}_{\bar{q}}, K_{\bar{q}}; x) = \mathcal{A}_{3,g\to q}^{0,II}(s_{\bar{1}K}) - \Gamma_{qg}^1(x)\,, \quad (10.13)$$

where we had to use the initial-initial integrated antenna (eq. (3.95)) because we used an initial-initial mapping in the un-integrated subtraction term. An important feature of the identity changing dipole is that the mass factorisation contribution completely cancels the poles of the integrated initial-final antenna,

$$\mathcal{P}oles\left[\mathbf{J}^{(1)}_{2,\gamma\to q}(\bar{1}_{\bar{q}}, j_{\bar{q}}; x)\right] = 0\,. \tag{10.14}$$

It has to be like that, because there is no contribution from a virtual correction against which the poles could cancel otherwise, due to the mismatch between the PDFs and the reduced matrix element.

**The initial-initial configuration** The last configuration we can encounter is when both quarks of the quark-line are crossed into the initial state. The final state photon can now either become soft or collinear to either of the initial state quarks. All three limits are correctly subtracted by an initial-initial $A^0_3$ antenna:

$$\begin{aligned}\mathrm{d}\hat{\sigma}^{S,II,q_1\gamma_j\bar{q}_2}_{NLO} = \mathcal{N}^R \sum_{perm.} \mathrm{d}\Phi_{n+1}(\{k\}_{n+1}; 1_q, 2_{\bar{q}}) \frac{1}{S_{n+1}} \\ \times Q_q^2 A^0_3(1_q, j_\gamma, 2_{\bar{q}}) M^0_n(\{\tilde{k}\}_n; \bar{1}_q, \bar{2}_{\bar{q}}) J^{(m)}_n(\{\tilde{k}\}_n)\,.\end{aligned} \tag{10.15}$$

The corresponding virtual subtraction reads

$$\begin{aligned}\mathrm{d}\hat{\sigma}^{T,II,q_1\gamma_j\bar{q}_2}_{NLO} = -\mathcal{N}^V \int \frac{\mathrm{d}x_1}{x_1}\frac{\mathrm{d}x_2}{x_2} \sum_{perm.} \mathrm{d}\Phi_n(\{k\}_n; \bar{1}_q, \bar{2}_{\bar{q}}) \frac{1}{S_n} \\ \times Q_q^2 \mathbf{J}^{(1)}_2(\bar{1}_q, \bar{2}_{\bar{q}}; x_1, x_2) M^0_n(\{\tilde{k}\}_n; \bar{1}_q, \bar{2}_{\bar{q}}) J^{(m)}_n(\{\tilde{k}\}_n)\,,\end{aligned} \tag{10.16}$$

with the integrated dipole (see eq. (3.98))

$$\mathbf{J}^{(1)}_2(\bar{1}_q, \bar{2}_{\bar{q}}; x_1, x_2) = \mathcal{A}^{0,II}_3(s_{\bar{1}\bar{2}}) - \Gamma^1_{qq}(x_1)\delta(1-x_2) - \Gamma^1_{qq}(x_2)\delta(1-x_1)\,. \tag{10.17}$$

In addition to the integrated initial-initial antenna (eq. (3.95)) we now have two mass factorisation kernels, one for each initial state quark.

## 10.5. Technical aspects of the calculation

### 10.5.1. Complex mass scheme for unstable particles

In QCD for all processes which do not explicitly involve the weak gauge bosons $Z$ and $W^\pm$, the Higgs or the top-quark already at LO, their respective masses and widths do not play a role when calculation higher order corrections. In most cases all quarks except for the top are considered massless and top-loops were excluded from the QCD matrix elements. However, if we consider EW corrections, the picture changes: Any particle of the set $Z, W^\pm, H, t$ can now appear in the virtual corrections, inducing a direct dependence on its properties.

To correctly account for the masses and widths of unstable particles in calculations, the complex-mass scheme (CMS) [219–221] has become the conventional choice. Here the masses $m_i$ of unstable particles are replaced by their complex counterpart $\mu_i$, defined by

$$\mu_i^2 = m_i^2 - i m_i \Gamma_i \,, \tag{10.18}$$

everywhere in the calculation, where $m_i$ and $\Gamma_i$ are given in the pole scheme (see section 2.3). The main motivation for the introduction of the CMS was to find a way to preserve gauge-invariance in the calculation. Choosing the masses of the weak gauge bosons complex will have a direct impact on relations between electroweak parameters, such as the tree-level relation for the weak mixing angle (eq. (2.20)). We will discuss this in more detail in the next section.

### 10.5.2. EW renormalisation schemes and the value of $\alpha$

In QCD, where only resolved tree-level final state photons can appear, we do not need to worry about electroweak renormalisation. Contrary to the running strong coupling $\alpha_s$, the electromagnetic coupling $\alpha$ is a mere multiplicative constant. Moreover the power of $\alpha$ is fixed for any order in QCD, hence it completely factorises from the results. This enables us to rescale any pure QCD calculation involving $n$ photons, performed with a coupling equal to $\alpha'$, to any other value $\alpha''$:

$$\mathrm{d}\sigma^{n\gamma}(\alpha'') = \left(\frac{\alpha''}{\alpha'}\right)^n \mathrm{d}\sigma^{n\gamma}(\alpha') \,. \tag{10.19}$$

We used this feature when comparing to the MCFM results for inclusive photon production in section 8.1.1.

Once we include NLO EW corrections, the situation is much more involved. Since the electroweak loop amplitudes need to be renormalised[7], we also have to ask the question which renormalisation condition we shall impose on $\alpha$. Conventionally we renormalise the coupling at some physical point, so that choosing a specific EW renormalisation scheme, or short just EW scheme, will then fix the numerical value of $\alpha$ in our calculation. Depending on the scale of the interaction under consideration, different schemes/values of $\alpha$ are appropriate. Roughly speaking EW interactions at some scale $\mu$ should in principle always be considered with the coupling set to equal to $\alpha(\mu)$. The important point is that all real radiation photons must couple with the exact same value of $\alpha$ as the virtual photons, in order to ensure correct cancellation of the QED IR singularities.

For EW interactions at LHC energies, one reasonable way to define the renormalized coupling is to set it to the value measured at $\mu = m_Z$, $\alpha(m_Z) = 1/127.952(9)$ [196]. This is usually

[7] Here we focus on the renormalisation of $\alpha$, in particular its numerical value as it is directly relevant for the way we set up our calculation. We essentially follow the discussion presented in [181]. Are more complete review on EW renormalisation can be found for example in [222, 223]. Remember that $\alpha = e^2/(4\pi)$ is related to the $SU(2) \times U(1)$ couplings $g$ and $g'$ through the weak mixing angle $\theta_W$, see eqs. (2.19).

| photon type | scheme | value for $\alpha$ [196] | id for external photons |
|---|---|---|---|
| final state on-shell / QCD-Born-photon | $\alpha(0)$ | 1/137.035999084(21) | 2002 |
| virtual and real radiation photons | $G_\mu$<br>$\alpha(m_Z)$ | 1/132.29(10)<br>1/127.952(9) | 22 |
| initial state photons | $G_\mu$<br>$\alpha(m_Z)$ | 1/132.29(10)<br>1/127.952(9) | -2002 |

Table 10.1.: EW schemes appropriate for different types of photons and corresponding values of the electromagnetic coupling constant $\alpha$, following the reasoning of [181], as well as the ids to be used for external photons during the channel registration, see section 11.3.2.

called the $\alpha(m_Z)$-scheme. Another way, which we will adopt as our default, is to relate the QED coupling to the Fermi constant $G_\mu$,

$$\alpha|_{G_\mu} = \frac{\sqrt{2}G_\mu}{\pi}\left|\mu_W^2 \sin^2\theta_W\right|, \tag{10.20}$$

where $G_\mu$ is measured through the $\mu$-lifetime. Its value is [196]

$$G_\mu = 1.1663787(6)\cdot 10^{-5}\ \text{GeV}^{-2}\,. \tag{10.21}$$

The weak mixing angle in turn is defined in terms of the weak gauge bosons' (complex) masses, using the tree-level relation (see eq. (2.20))

$$\sin^2\theta_W = 1-\cos^2\theta_W = 1-\frac{\mu_W^2}{\mu_Z^2}\,. \tag{10.22}$$

This scheme is naturally called the $G_\mu$-scheme.

The above schemes make sense for virtual photons in hard EW processes with virtualities close to the scale of the interaction, and for IR consistency reasons also for real radiation photons. For initial state photons, too, since they have virtuality associated with the factorization scale $\mu_F$, which conventionally is chosen as some high scale related to the process. For resolved final state photons (i.e. exactly the QCD-Born-photons), however, this is not necessarily the right choice of coupling. Since we are taking about real final state photons, they are on-shell, i.e. have virtuality zero. Thus they should naturally couple with $\alpha(0)$, the QED coupling at vanishing momentum transfer, which describes low-energy QED interactions. Identifying the renormalized coupling with $\alpha(0)\approx 1/137.036$ is what is called the $\alpha(0)$-scheme.

The best description of EW corrections at the LHC with external on-shell photons should therefore be achieved when choosing the most suitable EW-scheme for each photon coupling individually. With this we follow the reasoning presented in [181]. Sensible choices are summarized in table 10.1, where also the corresponding values of the electromagnetic coupling $\alpha$ are given.

## 10.6. Final state photons in NLO EW corrections

The presence of additional final state photons besides the QCD-Born ones will have an immediate effect on how the photon isolation is applied, but also how we define jet observables, which at first sight are two independent topics. In the following we will show that this is actually not the case and that the photon isolation and the treatment of jets can be regarded as two sides of the same coin. Eventually it all boils down to the seemingly trivial observation that real radiation photons are allowed to become unresolved and/or fail at the photon isolation stage.

### 10.6.1. General aspects regarding photon isolation

While for the calculation of QCD corrections the number of photons is fixed at all orders and part of the process definition, this is not the case for EW corrections. A candidate photon failing the isolation in a pure QCD calculation automatically leads to a rejection of the event. When extra real radiation photons are present, a number of candidate photons can fail the isolation without the event being discarded, as long as the number of passing photons is greater or equal to the number of QCD-Born-photons, defining the process.

There is another feature of real photon radiation we have to consider. The QCD-Born-photons are usually required to be sufficiently separated in order to get a clean experimental signal. This is achieved by imposing a cut on the photon-photon separation $\Delta R^{\gamma_1\gamma_2}$. It is therefore always clear which momentum in the calculation is assigned to the photon and should be considered in the photon isolation. As soon as real radiation photons are present, the situation becomes more complicated. Since they have to be allowed everywhere in the phase-space in order to ensure the correct cancellation of IR singularities, we cannot impose a cut on $\Delta R^{\gamma_i\gamma_j}$ for arbitrary pairs of candidate photons $\gamma_i$ and $\gamma_j$. The cut rather has to be applied to the two leading photons after the photon isolation has been performed, hence the order is important; For EW corrections it has to be a fiducial cut and not part of the photon definition, in QCD it does not matter.

As a consequence two candidate photons can in principle become arbitrarily close to each other. While this does not lead to any IR divergence, the question is raised how to treat such configurations in the photon isolation. The two photons can be treated as independent, however this does not correspond to what one would measure in an experiment. Given the finite resolution of the detector, two almost collinear photons will be detected as a single photon. It therefore is reasonable to combine two photons also in the theory prediction, as soon as they are closer than a certain threshold value, $\Delta R^{\gamma\gamma} < R^{\text{comb.}}$. In that case the two photons are replaced by a single photon with momentum

$$P_{\gamma_{12}} = P_{\gamma_1} + P_{\gamma_2}\,. \tag{10.23}$$

The combined photon then has to pass the photon isolation. A reasonable choice for the size of the combination threshold $R^{\text{comb.}}$ should be based on the resolution of the detector. We chose $R^{\text{comb.}} = 0.1$ as the default value, which roughly corresponds to the size of a detector cell.

For any $\Delta R^{\gamma\gamma} > R^{\text{comb.}}$ the two photons will be subject to their own photon isolation. Note that because the isolation cone radii are usually considerably greater than the combination

threshold, configurations with intersecting isolation cones are much more common in the calculation of EW corrections than in pure QCD. There they only occur for processes with at least two photons and enough additional final state particles, so that some recoil against the diphoton-system while others lie in the region affected by the isolation. In addition any fiducial cut on the separation of the QCD-Born-photons will limit the number of those configurations.

For fixed cone isolation with constant $E_{T,\text{fix}}^{\max}$ (i.e. independent of $p_T^\gamma$) overlapping cones are not a problem, but for any non-trivial isolation profiles intersections lead to an additional suppression of the cross section. In [160, 161] the effect of isolation cone intersections in diphoton production at NNLO QCD has been discussed. It was shown that they can lead to significant deviations between distributions derived either with smooth cone isolation and fixed cone isolation. In the paper the authors used hybrid isolation as a proxy for the fixed cone isolation, which was possible since they chose $R_d = 0.1 < 0.2 = \frac{1}{2}\Delta R^{\gamma_1\gamma_2}$, hence the inner cones did not intersect.

When considering EW correction with a combination threshold $R^{\text{comb.}}$ and an inner cone radius $R_d = 0.1$, an intersection between the inner cones of the hybrid isolation is indeed possible. Yet we expect the effect to be small, much smaller than when using standard smooth cone profiles. In particular we expect the hybrid isolation to be closer to fixed cone isolation than the standard smooth cone isolation.

### 10.6.2. Impact on the jet definition

Additional complications arise with the presence of real radiation photons. While we can choose a photon isolation such that the fragmentation component is completely suppressed for all isolated photons, the situation is slightly different for photons which are unresolved, in particular collinear to a final state quark. Those photons will by construction fail any isolation prescription tailored to remove the sensitivity on the fragmentation component. But as we discussed above, this will not necessarily lead to a rejection of the event, as long as enough isolated photons eventually remain. If we are inclusive in the species of this quark-photon collinear cluster, i.e. we do not care if it is rather a jet or more like a photon which just happens to have to much hadronic energy around it, then the collinear singularity can be treated with our conventional methods. In our case by constructing the appropriate subtraction term at the real level and integrate it over the unresolved phase-space.

The problem arises as soon as we do want to know, what kind of signature the collinear cluster has, is it an ordinary QCD-jet or something like a "photon-jet". Certainly, if the momentum of the collinear cluster is to very large extend carried by the quark, we want to register it as an ordinary jet. Whether or not the photon momentum should be clustered into the jet depends on how the jets are actually defined in the experiment. If, however, large part of the momentum is instead carried by the photon, then the cluster should probably not be counted as a QCD-jet. We therefore have to define an additional criterion, describing how much photonic energy we want to allow inside a proto-jet. In a sense, this is the opposite of a photon isolation. For this to work, we need to know how exactly the cluster's momentum is composed, quite similar to the situation we had for the fragmentation photons in section 4.2. And indeed, since the photon is not isolated (i.e. it failed the isolation criterion) its origin can be a fragmenting parton. Again, this would not be a problem when we are fully inclusive with respect to the type of the cluster,

but as soon as we apply our jet criterion we restrict the convolution variable $z$, previously defined as the photon momentum fraction, in the fragmentation component. This whole argument is very much alike to what we discussed in section 4.2 and to accommodate for this in the antenna subtraction formalism a treatment similar to what we presented in section 4.2.1 is required. But instead of only looking for a photon in some range $(z_{\text{cut}}, 1]$ we now are interested in the complement, too, i.e. the part of the inclusive cross section where we do not identify the photon-quark cluster as a photon, but rather as a jet. Obviously there will also be changes to the jet function $J_n^{(m)}(\{k\}_n; z)$, which will now apply our modified jet criterion. Of course it would be possible to always treat the collinear cluster as a jet. We are then also inclusive with respect to to its substructure and we would not need to include the fragmentation. This would, however, not agree with the experimental setups.

We can conclude from above argument that, as long as we do not include the fragmentation function to NLO accuracy, we cannot directly calculate the NLO corrections to any process exclusive in the number of jets, in particular not $\gamma + j$. Inclusive photon production, however, can be investigated with the tools at hand. How we can adopt the antenna subtraction formalism to work for the inclusive case will be subject of section 10.4.

### 10.6.3. Thoughts on democratic clustering

In the calculation of the QCD corrections and also of the NLO EW corrections to inclusive photon and diphoton production in chapters 12 and 13 the photon isolation and the jet algorithm were two completely independent aspects. While the jets were defined based on some kind of clustering algorithm, we used the hybrid or smooth cone criterion for the photon isolation. To define jet observables in the presence of EW corrections, in this approach we would have to perform several steps:

1. Apply the photon isolation to all candidate photons.

2. Perform the jet clustering, incorporating all photons which failed the photon isolation in a democratic way.

3. Apply the jet selection criterion to remove all jets which have too much photonic energy clustered into them.

Following the discussion above it is then clear that this separation between photon and jet definition is not optimal for the EW corrections. As we anyway have to cluster the photon democratically together with the partons in the modified jet algorithm, we might as well use this setup to isolate the photon, following the ideas discussed in section 4.1.2. That way we can define isolated photons and jets in a single step and based on only one variable $z$, i.e. the photon momentum fraction of the photon in the photon-jet cluster. At NLO it coincides with the convolution variable used in the fragmentation component. A proto-jet would then regarded as a photon, if $z > z_{\text{cut}}^{\text{iso}}$ for some $z_{\text{cut}}^{\text{iso}}$ close to 1, and as a jet if $z < z_{\text{cut}}^{\text{jet}}$ for some $z_{\text{cut}}^{\text{jet}} \leq z_{\text{cut}}^{\text{iso}}$. The precise values for the cuts would need to be matched to the jet and photon definition in experiment. Note that there is some freedom to this choice. It is therefore a potential source of

systematic uncertainty which has to be assessed with care. Still the advantages regarding the workflow outweigh the disadvantages.

## 10.7. Scales in mixed QCD+EW corrections

The theory uncertainty cited for a fixed order QCD calculation is conventionally defined though a variation of the renormalisation and factorisation scales. We used this intensively in chapters 7 and 8, where we independently varied $\mu_R$ and $\mu_F$ around some common central scale $\mu_0$ by factors of 0.5 and 2, discarding those configurations where $\mu_R/\mu_F = 0.25$ or 4. We called this the seven-point variation. The motivation to use this as a measure of the uncertainty is that in an all-orders result we expect the dependence on the unphysical scales to vanish altogether. The series truncated at order $k$ however, will depend on the scale choice,

$$0 = \frac{\mathrm{d}^2\sigma}{\mathrm{d}\ln\mu_R^2\,\mathrm{d}\ln\mu_F^2} = \underbrace{\frac{\mathrm{d}^2\sigma^k}{\mathrm{d}\ln\mu_R^2\,\mathrm{d}\ln\mu_F^2}}_{\neq 0} + \frac{\mathrm{d}^2\Delta^k}{\mathrm{d}\ln\mu_R^2\,\mathrm{d}\ln\mu_F^2}\,. \tag{10.24}$$

As we know that the missing higher order terms collected in $\Delta_k$ must exactly cancel this dependence, we can in principle estimate their size by varying the scales in $\sigma^k$, provided we assume that the coefficients[8] in the perturbative expansion are all of similar magnitude [224]. If the fixed order result changes a lot upon shifting $\mu_R$ and $\mu_F$, then the missing terms must be large enough to compensate for this. And if instead $\sigma^k$ is rather insensitive to variations of the scales, then $\Delta_k$ cannot be too large. A strong hint for good perturbative convergence is, when the scale variation envelope of a given order is smaller than and fully contained in that of the previous order. Of course this is not always a reliable estimate, in particular for low orders in which not all partonic channels or kinematical configurations might be accessible yet.

While this definition is unambiguous in the calculation of differential cross sections based on a fixed order expansion in a single coupling, it is much less clear when considering either ratios of cross sections, like we already briefly discussed in section 8.1.3, or when expanding in two couplings simultaneously, like it is the case in a mixed QCD+EW calculation. Here we will mainly focus on the latter situation.

The renormalisation scale dependence of the cross section enters exclusively through the couplings. Since we renormalise the QED coupling $\alpha$ at some physical point (see section 10.5.2), it is fixed and does not exhibit any scale dependence. On the other hand, the strong coupling $\alpha_s$ is conventionally renormalised in the $\overline{\mathrm{MS}}$ scheme, which does not have a physical renormalisation point, thus a $\mu_R$ dependence remains. This means that the renormalisation scale dependence of the EW corrections is entirely given by that of the strong coupling[9]. When we now calculate the EW corrections as a supplement to an existing NNLO QCD prediction, combining them additively, $\mathrm{d}\sigma_{\mathrm{QCD+EW}} = \mathrm{d}\sigma_{\mathrm{QCD}} + \delta_{\mathrm{EW}}$, the only reasonable option is to always choose the same $\mu_R$ in both calculations.

[8] By coefficients we mean the $c_n$ in the formal expansion $\sigma = \alpha^m \sum_n c_n \alpha^n$.
[9] Note that this in particular means that processes in which no $\alpha_s$ appears do not depend on $\mu_R$ at all.

The factorisation scale enters by solving the DGLAP equations for the PDFs up to a certain fixed order in the couplings. For the EW corrections they had to be modified to also accommodate for QED effects [212–214]. While in principle it is possible to choose independent scales for the QCD and QED factorisation, this is not customary, as it complicates the calculation unnecessarily. Thus also for the factorisation scale we choose the same in the QCD and EW parts.

In conclusion this means that when there is an existing NNLO QCD calculation with uncertainties estimated by means of a seven-point scale variation, and we want to add to this the corresponding NLO EW corrections, they should be evaluated with exactly the same scale choices and the two results added with the scales correlated, i.e.

$$\mathrm{d}\sigma_{\mathrm{QCD+EW}}(a\mu_R^0, b\mu_F^0) = \mathrm{d}\sigma_{\mathrm{QCD}}(a\mu_R^0, b\mu_F^0) + \delta_{\mathrm{EW}}(a\mu_R^0, b\mu_F^0)\,, \tag{10.25}$$

where $a, b \in \{0.5, 1, 2\}$ are the variation parameters of the seven-point prescription and $\mu_{R,F}^0$ the central scales.

Now when it comes to the interpretation of the scale variations as uncertainties, the important point is that the scale band of the pure QCD result captures the effect of missing higher orders in QCD only. By construction it cannot be an estimate of the impact missing EW effects might have. Therefore when we calculate the EW corrections to a given QCD process and then compare the mixed result to the pure QCD result and its scale uncertainty, this primarily gives us an idea of how big the EW corrections are compared to the missing higher orders in QCD. If the scale band for the mixed prediction lies well outside its pure QCD equivalent, then the inclusion of the EW corrections is certainly important, as we expect the effect of the next order in QCD to be smaller than this EW induced deviation. If in contrast it lies within the QCD uncertainty band, then the missing QCD corrections might very well be of similar size. In that case one might come to the conclusion that the EW effects only become relevant if one also pushes for the next order in $\alpha_s$.

However, one has to consider how the scale band is shifted by the EW corrections, too. If it is an overall flat and small change the distribution at hand can be regarded as robust under EW effects. On the other hand, if the shape of the distribution is altered non-trivially, this tells us that in some regions the EW effects are bigger and important, while in others they might be negligible compared to the next order in QCD.

In the following we will therefore introduce different kinds of ratios of cross sections and coefficients with which we try to assess different aspects of the EW corrections.

**Prescription A –** To compare to data we plot the ratio in the way which was the default for the figures in Part II, namely as a mere normalisation to the central scale value of a given prediction. The scales in the numerator are varied according to the seven-point prescription and the denominator is fixed at the central scale. As we also normalise the data accordingly, this gives us a means to directly compare the uncertainties of theory and experiment.

**Prescription B –** To get an overall idea of the relative size of the individual contributions to the cross section we plot the ratio of the EW coefficients (LO, NLO or specific channels) to

either QCD coefficients or the full QCD result at a certain order, using only the central scale values. Following the argument above the central scales should be the same in numerator and denominator. Symbolically

$$R^i = \frac{\delta^i_{\mathrm{EW}}(\mu_0)}{\mathrm{d}\sigma_{\mathrm{QCD}}(\mu_0)}\,, \tag{10.26}$$

where $i$ labels the type or order of the coefficient. Here we are not interested in how the contributions compare to any scale uncertainties, just in their size and distribution.

**Prescription C –** To understand how the relative size of the EW corrections depends on the concrete scale choice we plot the ratio of the full mixed result to the pure QCD result, correlating the scale choices in numerator and denominator. This way the scale dependence of the respective QCD contributions should exactly cancel, so that the residual dependence comes from the EW effects only. Symbolically

$$R = \frac{\mathrm{d}\sigma_{\mathrm{QCD}}(\mu) + \delta_{\mathrm{EW}}(\mu)}{\mathrm{d}\sigma_{\mathrm{QCD}}(\mu)} = 1 + \frac{\delta_{\mathrm{EW}}(\mu)}{\mathrm{d}\sigma_{\mathrm{QCD}}(\mu)}\,. \tag{10.27}$$

# 11. Implementation of NLO EW corrections

In NNLOJET NLO EW corrections to a given process `X` are implemented as an independent process `X_EW`. Both processes are clearly distinct; there is no overlap in their respective contributions. While `X` contains pure QCD corrections, corresponding to the leftmost branch of figure 10.1, the $\mathcal{O}\left(\alpha_s^n \alpha^{m+1}\right)$, $\mathcal{O}\left(\alpha_s^{n-1} \alpha^{m+1}\right)$ and $\mathcal{O}\left(\alpha_s^{n-2} \alpha^{m+2}\right)$ corrections are collected in `X_EW`. This includes potential interferences between QCD and EW amplitudes at the given order. The process `X_EW` is therefore, taken on its own, no consistent process, as it also lacks the $\mathcal{O}(\alpha_s^n \alpha^m)$ Born. Calculating the NLO EW corrections therefore always requires to also run at least part of `X` and the full NNLO QCD+NLO EW result is obtained by combining the results of `X` and `X_EW` in an additive way. Symbolically:

$$\texttt{X}\Big|_{\text{NNLO QCD+NLO EW}} = \texttt{X} + \texttt{X\_EW}\,. \tag{11.1}$$

It is implemented that way as it is the least invasive approach with respect to the existing NNLO QCD processes. The processes implemented at NNLO QCD are left untouched so that if one only wants to run the QCD corrections, one can do so without caring about the EW part. For the EW matrix elements, in particular for the EW virtual corrections, we heavily rely on the use of the OpenLoops2 [181] interface. In the following we will explain in detail how this is done, but first we have to explain a few key features of how the calculation in NNLOJET is set up and what changes, when we consider EW corrections.

## 11.1. PDFs, final state flavour sums and CKM factors

The number of individual crossings contributing to a certain process can quickly become quite large, especially if we consider inclusive production of a given final state. To reduce the number of channels we have to calculate we can make use of the fact that the partonic cross sections for some combinations of external quark flavours are actually identical, as long as we consider them as massless. In pure QCD, which is completely flavour blind, we can then just write down a generic partonic cross section $\mathrm{d}\hat{\sigma}$ with external quarks, without specifying their flavour. In

case we have initial state quarks $\mathrm{d}\hat{\sigma}$ then can be factored out when summing over the different quark PDFs, symbolically

$$\mathrm{d}\sigma_{qQ} \sim \sum_{ij} f_i f_j \otimes \mathrm{d}\hat{\sigma}_{ij} = \left(\sum_{ij} f_i f_j\right) \otimes \mathrm{d}\hat{\sigma}_{qQ}\,, \qquad (qQ\text{-initiated}) \tag{11.2a}$$

$$\mathrm{d}\sigma_{q\bar{q}} \sim \sum_{i} f_i \bar{f}_i \otimes \mathrm{d}\hat{\sigma}_{i\bar{i}} = \left(\sum_{i} f_i \bar{f}_i\right) \otimes \mathrm{d}\hat{\sigma}_{q\bar{q}}\,, \qquad (q\bar{q}\text{-initiated}) \tag{11.2b}$$

$$\mathrm{d}\sigma_{gq} \sim f_g \sum_{i} f_i \otimes \mathrm{d}\hat{\sigma}_{gi} = \left(f_g \sum_{i} f_i\right) \otimes \mathrm{d}\hat{\sigma}_{gq}\,, \qquad (gq\text{-initiated}) \tag{11.2c}$$

where $i, j = u, d, c, s, b$. If we have a $q\bar{q}$ pair in the final state coming from an genuine squared s-channel diagram[1], the summing the PDFs will obviously not help to include all possible flavours for that pair. Yet, we do not need to evaluate the corresponding partonic cross section five times for each flavour[2], but instead we can just evaluate it once and then multiply by $N_F$,

$$\mathrm{d}\sigma^{q\bar{q}+X} \sim \sum_{i} \mathrm{d}\hat{\sigma}^{i\bar{i}+X} = N_F \times \mathrm{d}\hat{\sigma}^{q\bar{q}+X}\,. \tag{11.3}$$

That way we can drastically reduce the number of independent evaluations needed. The argument also holds in the presence of photons or $Z$ bosons, with the only difference that now we have to distinguish between up-type and down-type flavours. Thus instead of defining generic quark partonic cross sections, we now have up- and down-type partonic cross sections, and in the final state flavour sum (11.3) we split $N_F$ into $N_d = 3$ and $N_u = 2$. For photonic processes the up- and down-type partonic cross sections are related by a simple rescaling of the quark charge factors, e.g. for one external photon $\mathrm{d}\hat{\sigma}_u = (Q_u^2/Q_d^2)\mathrm{d}\hat{\sigma}_d = 4\,\mathrm{d}\hat{\sigma}_d$.

The situation becomes more complicated as soon as we consider virtual $W^\pm$ bosons as part of the NLO EW corrections, due to their flavour changing coupling to quarks. For diphoton and inclusive photon production two general cases are of interest:

1. The $W^\pm$ couples to only one quark line.

2. The $W^\pm$ connects two distinct quark lines.

Let us first consider case one, where the $W$ couples to an external up-type quark line. The flavour dependence of the $q_i q_j W^\pm$ coupling is fully contained in the corresponding element of the CKM matrix, $V_{ij}$. As we can factor out the $V_{ij}$, we can discuss the dependence on the amplitude level. Consider the subdiagram

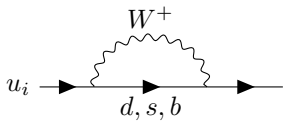


$$\sim \sum_{j=d,s,b} |V_{ij}|^2 A_j\,. \tag{11.4}$$

[1] For the D-type channels with an s×t or s×u interference the final state $q\bar{q}$ pair is in fact correlated to the initial state flavours.
[2] We do not consider external top quarks.

Here the $A_j$ are sub-amplitudes for the specific down-type flavours running in the loop and $u_i = u, c$. The rest of the full diagram, of which the above is supposed to be a part, we assume to be independent on the specific flavour. Since we treat all down-type flavours as massless, the subamplitudes $A_j$ are in-fact all the same,

$$A_s = A_d = A_b =: A_0 \,, \tag{11.5}$$

so we can write

$$\sum_{j=d,s,b} |V_{uj}|^2 A_j = A_0 \sum_{j=d,s,b} |V_{uj}|^2 = A_0 \,, \tag{11.6}$$

where we used the unitarity of the CKM matrix,

$$\sum_k V_{ik}^* V_{jk} = \delta_{ij} \,. \tag{11.7}$$

Thus, the dependence on the CKM factors drops out in the massless case. This observation still holds if we consider a diagonal CKM matrix, $V_{ij} = \delta_{ij}^{\mathrm{CKM}}$, which we do by default[3]. The situation is slightly different if the $W$ couples to an external down-type quark line. We consider the subdiagram

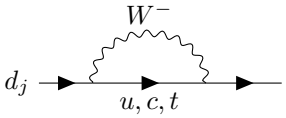


$$\sim \sum_{i=u,c,t} |V_{ij}|^2 A_i \,, \tag{11.8}$$

with $A_i$ now the subamplitudes for specific up-type flavours in the loop and $d_j = d, s, b$. We can define

$$A_u = A_c =: A_0 \,, \tag{11.9}$$

but because we should not treat the top-quark as massless $A_t \neq A_0$. Re-writing

$$\sum_{i=u,c,t} |V_{ij}|^2 A_i = A_0 \sum_{i=u,c,t} |V_{ij}|^2 + (A_t - A_0)|V_{tj}|^2 \tag{11.10a}$$

$$= A_0 + (A_t - A_0)|V_{tj}|^2 \tag{11.10b}$$

we find a very different situation for external $d, s$ on one side and $b$ on the other: While in the first case we can neglect the term $(A_t - A_0)|V_{tj}|^2$ due to the smallness of $|V_{td}|^2$ and $|V_{ts}|^2$ to

[3]The superscript CKM here indicates that the Kronecker-delta relates $u \leftrightarrow d$, $c \leftrightarrow s$ and $t \leftrightarrow b$.

approximate the amplitude with the massless case[4] (which is equivalent to assuming a diagonal CKM matrix), this cannot be done for external bottom-quarks. Here $|V_{tb}|^2 \approx 1$ and[5]

$$\sum_{i=u,c,t} |V_{ib}|^2 A_i \approx A_t \,. \tag{11.11}$$

This tells us that for the EW corrections we should consider the channels with external bottom quarks as different from generic down-type channels, unlike we did for the QCD corrections. Now whenever there is a down-type quark in the initial state we convolute the generic down-channel with the $d$- and $s$-PDFs, but take the $b$-channel separate. The same holds for $d\bar{d}$ in the final state: instead of multiplying by $N_d = 3$, coming from the sum over final state $d, s, b$, we now only multiply the generic down-channel by 2 and take the $b\bar{b}$ final state separate.

If now instead of forming a closed loop with the same quark line the $W^\pm$ connects two distinct external quark lines, the dependence on the CKM elements becomes more involved. For illustration we consider an amplitude with one up-type and one down-type quark-anti-quark pair in the final state and an arbitrary number of gluons and photons as further external states. Factoring out the CKM elements it can be written as

$$A_{u_i \bar{d}_k; \bar{u}_j d_l} = V_{ik} V_{jl}^* A_{4q}^{ik;jl} \,, \tag{11.12}$$

where $A_{4q}^{ik;jl}$ is a generic four quark amplitude without particular dependence on the flavours. The superscript just indicates the connection of the quark line within the amplitude: The quark with index $i$ connects to the anti-quark with index $k$, and the anti-quark with index $j$ to the quark with index $l$. The indices $k, l$ run over the down-type flavours $d, s, b$ and the indices $i, j$ over the up-type flavours $u, c$. We do not consider external top quarks. Note that we can obtain the same external state signature when instead we have a flavour-conserving mediator such as $\gamma$ or $Z$, with $u_i \bar{u}_j$ and $d_l \bar{d}_k$ vertices. Let us denote the corresponding amplitude

$$A'_{u_i \bar{u}_j; d_l \bar{d}_k} = \delta_{ij} \delta_{lk} A_{4q}'^{ij;kl} \,. \tag{11.13}$$

We will call it the neutral current (NC) amplitude in the following, in contrast to the charged current (CC) amplitude with $W^\pm$-exchange. The full amplitude contributing to the partonic channel is then

$$A_{u\bar{u}d\bar{d}} = V_{ik} V_{jl}^* A_{4q}^{ik;jl} + \delta_{ij} \delta_{lk} A'_{4q}{}^{ij;kl} \,, \tag{11.14}$$

and its square

$$|A_{u\bar{u}d\bar{d}}|^2 = M^C_{u_i \bar{d}_k; \bar{u}_j d_l} + M'^C_{u_i \bar{u}_j; d_l \bar{d}_k} + M^D_{u_i \bar{u}_j d_l \bar{d}_k} \,, \tag{11.15}$$

[4] Provided $(A_t - A_0) \ll |V_{td}|^{-2}, |V_{ts}|^{-2}$.
[5] For a diagonal CKM matrix the "≈" sign has to be replaced by an "=".

with[6]

$$M^{C}_{u_i\bar{d}_k;\bar{u}_j d_l} = |V_{ik}|^2 |V_{jl}|^2 M^{C}_{4q}\,, \tag{11.16a}$$

$$M'^{C}_{u_i\bar{d}_k;\bar{u}_j d_l} = \delta_{ij}\delta_{lk} M'^{C}_{4q}\,, \tag{11.16b}$$

$$M^{D}_{u_i\bar{u}_j d_l\bar{d}_k} = 2\,\mathrm{Re}\{\delta_{ij}\delta_{lk}V^*_{ik}V_{jl}\}M^{D}_{4q}\,. \tag{11.16c}$$

Here we labelled the genuine squares with a $C$ and the interference with a $D$ to highlight the similarity to the four-quark amplitudes in QCD, see section 6.1.2. While for the C-types the distinction between the two quark lines is preserved, for the D-types by construction it is not[7]

Now assume all four quarks remain in the final state and we want to sum up all the different contributions we get for the different flavours we can have. For the NC matrix elements we find

$$\sum_{i,j=u,c}\delta_{ij}\sum_{k,l=d,s,b}\delta_{lk}M'^{C}_{4q} = N_u N_d M'^{C}_{4q}\,, \tag{11.17}$$

exactly as in QCD for the gluon mediated four-quark channels. For the CC C-type matrix element (11.16a) we get

$$\sum_{i,j=u,c}\sum_{k,l=d,s,b}|V_{ik}|^2|V_{jl}|^2 M^{C}_{4q} = \sum_{i,j=u,c} M^{C}_{4q} = N_u^2 M^{C}_{4q}\,, \tag{11.18}$$

where we used the unitarity of the CKM matrix (eq. (11.7)). For the D-type we equivalently obtain

$$\begin{aligned}\sum_{i,j=u,c}\sum_{k,l=d,s,b}\mathrm{Re}\{\delta_{ij}\delta_{lk}V^*_{ik}V_{jl}\}M^{D}_{4q} &= \sum_{i,j=u,c}\delta_{ij}\sum_{k=d,s,b}\mathrm{Re}\{V^*_{ik}V_{jk}\}M^{D}_{4q}\\ &= \sum_{i,j=u,c}\delta_{ij}\,\mathrm{Re}\left\{\sum_{k=d,s,b}V^*_{ik}V_{jk}\right\}M^{D}_{4q} \underset{(11.7)}{=} \sum_{i,j=u,c}\delta_{ij}M^{D}_{4q} = N_u M^{D}_{4q}\,.\end{aligned} \tag{11.19}$$

It becomes more complicated as soon as we cross one or more of the quarks into the initial state. We then need to convolute the partonic cross section with the correct PDFs, as we did at the beginning of this section. Imagine for example crossing $\bar{d}_k$ into the initial state. For the sake of simplicity let the second initial state be a gluon. We can then write down for the NC C-type channels, summing over the final states and the different flavours in the pdf,

$$\mathrm{d}\sigma_d \sim f_g\sum_k\sum_{i,j,l} f_k\otimes\delta_{ij}\delta_{kl}\mathrm{d}\hat{\sigma}'^{C}_{4q} = f_g\sum_l f_l\otimes N_u\mathrm{d}\hat{\sigma}'^{C}_{4q}\,, \tag{11.20}$$

which is precisely the result given in eq. (11.2c). For the CC matrix element, however, we find

$$\mathrm{d}\sigma_d \sim f_g\sum_k\sum_{i,j,l} f_k\otimes|V_{ik}|^2|V_{jl}|^2\mathrm{d}\hat{\sigma}^{C}_{4q} = f_g\sum_{i,k}|V_{ik}|^2 f_k\otimes N_u\mathrm{d}\hat{\sigma}^{C}_{4q}\,. \tag{11.21}$$

[6] The indices $i, j, k, l$ label the flavour, i.e. we do not sum over them when forming the square.

[7] Remember that the D-types can be seen as interferences between different Mandelstam channels, thus the two quark lines are connected.

Here we could use the unitarity of the CKM matrix to remove the elements $|V_{jl}|^2$ by summing over $l$. For $|V_{ik}|^2$, however, that is not possible, as the summation over $k$ also affects the PDF $f_k$ and the summation over $i$ is incomplete: we do not consider the top as external state. The partonic cross section still factorises, but the PDFs now are weighted with the CKM factors. It is not hard to show that for the interference we obtain

$$\mathrm{d}\sigma_d \sim f_g \sum_k \sum_{i,j,l} f_k \otimes \mathrm{Re}\{\delta_{ij}\delta_{lk} V_{ik}^* V_{jl}\} \mathrm{d}\hat{\sigma}_{4q}^D = f_g \sum_{i,k} |V_{ik}|^2 f_k \otimes \mathrm{d}\hat{\sigma}_{4q}^D \,, \tag{11.22}$$

thus finding a equivalent pattern. Similar relations hold for the other crossings.

Note that if we consider a diagonal CKM matrix, for the CC channels this completely removes the bottom quark PDF from the convolution. When $V_{ik} = \delta_{ik}^{\mathrm{CKM}}$, then for example relation (11.21) above changes to

$$\mathrm{d}\sigma_d \sim f_g \sum_{i,k} \delta_{ik}^{\mathrm{CKM}} f_k \otimes N_u \mathrm{d}\hat{\sigma}_{4q}^C = f_g (f_d + f_s) \otimes N_u \mathrm{d}\hat{\sigma}_{4q}^C \,, \tag{11.23}$$

because $i = t$ is not included. This means that as long as a diagonal CKM matrix is assumed and final state top quarks explicitly excluded, there will never be a contribution form the bottom quark PDF in the charged-current four-quark matrix elements. The whole argument generalises to cases where we have a QCD×EW interference as discussed at the end of section 10.3, because we actually never used that the NC amplitude (11.13) is an EW amplitude. We only relied on the fact that it does not contain any flavour-changing couplings, which obviously holds for pure QCD amplitudes. There is also no problem with colour, because the interference is precisely of the $s \times t$-channel type depicted in figure 10.3b (see also figure 13.8 below).

## 11.2. Process auto-generation - part 2

As we already briefly discussed in section 5.2 we use a set of Maple scripts to generate new processes within NNLOJET. The process itself and the relevant ingredients are specified in the process `.map` file. In the following we will have a detailed look at one of those `.map` files and explain the different parts of the auto-generation. We take the `.map` file for the NLO EW corrections to inclusive photon production, `G_EW.map`, as an example, because it exhibits most of the features we can encounter in such a file. In some parts of the following we will anticipate discussions from chapter 13, in particular section 13.1, but we try to make this section as self-contained and conclusive as possible. The `G_EW.map` file looks like this:

```
Ofac:="ave*(4d0*pi*amz)**2*nc*8d0";
psymset:=[g,q,qb]:

dress1:={{q=u,qb=ub,nqqb=nup},{q=d,qb=db,nqqb=ndownred},{q=b,qb=bb,nqqb=1}}:

flag_EW   := true :
flag_frag := true :

# apply selector on final states
```

```
10 select_FS := [
11   min[G,1]
12 ] :
13
14 LO:=[
15 [B0g0GG,[qb,q,G,G],1]
16 ]:
17
18 R1:=[
19 [B1g0GG,[qb,g,q,G,G],(nc**2-1)/nc**2, {EW_real=0}],
20 [B1g0GG,[qb,g,q,G,G],(nc**2-1)/nc**2, {EW_real=1}],
21 [DG_EWR_OL,[qb,q,qb,q,G],1, {EW_real=0,OL_ew=2}],
22 [DG_EWR_OL,[db,d,ub,u,G],1, {EW_real=0,OL_ew=2,CC=1}]
23 ]:
24
25 V1:=[
26 [BG_EWV1_OL,[qb,g,q,G],1, {EW_virt=1,OL_qcd=1}],
27 [B0g1GG,[qb,q,G,G],(nc**2-1)/nc**2]
28 ]:
29
30 RR:=[
31 ]:
32
33 RV:=[
34 ]:
35
36 VV:=[
37 ]:
38
39 XX:=[LO,R1,V1,RR,RV,VV]:
40 nulllist:={}:
41
42 # need OpenLoops libraries:
43 #  ./openloops libinstall ppvj ppvj_ew compile_extra=1
```

In the following we will go through this piece of code line by line and explain its role for the auto-generation. Note that that there are more options and parameters one can set in a `.map` file, but those are usually very process specific and not relevant here, so we will not list them all.

L.1 An universal prefactor for the process, usually given by the couplings and overall colour factors of the Born level. `ave` is an initial state averaging factor which will be calculated for each channel.

L.2 Particles to be considered in the calculation of QCD symmetry factors.

L.4 Define the flavours with which the first (and only in this case) quark line is dressed. `nqqb` is the factor we get from summing over final state quark pairs. The $b$-quark is treated special for EW corrections, following the discussion in section 11.1. Since we separate the $b$-quark when summing over final state down-type quarks we get a factor of $N_d^{\text{red}} = N_d - 1 = 2$, hence the `ndownred`.

L.5-6 Flags to turn on parts of the auto-generation script specific for processes with EW corrections, `flag_EW`, and fragmentation, `flag_frag`.

L.10-12 Put constraints on the final state. Only channels meeting this requirement will be generated. Here we demand at least one final state photon.

L.15 Specifying the subleading (here $\mathcal{O}(\alpha^2)$) Born matrix element. The syntax is

```
[MEname,[particles],factor,{specs}]
```

where `MEname` is the identifier for this particular matrix element to be used in the code, `[particles]` a list of external states associated with the matrix element, `factor` can be used to assign a certain colour factor relative to `Ofac` to the matrix element, and `{specs}` some optional channel specific input needed for the auto-generation. For the EW corrections to inclusive photon production we can use the hardcoded diphoton matrix element `B0g0GG` $\widehat{=} B_{0g}^{0,2\gamma}$. The `factor` being equal to `1` indicates that this level comes with no extra colour factors, because we already considered them in the universal factor `Ofac` in L.1. We also do not need any extra specifications `{specs}` at this stage, unlike for the real and virtual contributions in L.19-22 and L.26-27, respectively. For some processes we might not have a subleading EW Born, in which case we leave the `LO:=[]:` block blank and define `Ofac` as the factor of a symbolic EW Born. We will encounter this situation for diphoton production. Multiple subleading Borns with different relative power of the couplings are currently not supported in the auto-generation due to the way the coupling factors of a given channel are constructed. For the process we consider here, diphoton and inclusive photon production, this is not an issue, because we have at most one subleading Born in those cases.

L.19 The real QCD radiation correction to the photon induced Born. Specifying `{EW_real=0}` fixes the number of final state photons to be exactly the one given in the `select_final state` block, i.e. one in this case. Consequently the second photon (`G`) in the list of external states `[qb,g,q,G,G]` will always be crossed into the initial state. Since we again use a hardcoded matrix element, `B1g0GG` $\widehat{=} B_{1g}^{0,2\gamma}$, we now have to specify the colour factor relative to the Born, $(N^2-1)/N^2 = C_F/N$.

L.20 Like L.19, but now we explicitly demand one extra final state photon, `{EW_real=1}`, in addition to the photon in the final state selector in L.11. This line therefore will only generate pure QCD initial states.

L.21 Here we register a special four-quark QCD×EW channel, which we will discuss in detail in section 13.1.4. We use OpenLoops2 to evaluate the matrix element, hence the suffix `_OL` in the `MEname`: Whenever the maple auto-generation scripts detect this suffix in a matrix element identifier, the routines needed to set up the OpenLoops2 interface will be triggered. Since the OpenLoops2 matrix element implicitly come with the correct colour factors, `factor` is always set to `1`. However, we need to specify either the power of the EW or QCD coupling, which can be done with the parameters `OL_ew` and `OL_qcd`. The power of the couplings together with the external states will uniquely determine the matrix

element. In addition in the virtual corrections this information is used to specify which kind of one-loop corrections OpenLoops2 shall consider: If we fix for example the power of $\alpha$ (i.e. set `OL_ew`) at the one-loop level only diagrams corresponding to one additional power in $\alpha_s$ are considered.

L.22 Like L.21, but here we consider a charged current (i.e. flavour changing) process (see section 13.1.4). This is achieved by setting `CC=1`. In order for this to work we have to specify the concrete flavour types `u,ub,d,db` instead of the generic quark identifiers `q,qb`.

L.26 The genuine EW one-loop corrections to the QCD-Born (specified through the external states). We use OpenLoops2 for the evaluation of the matrix elements. `OL_qcd=1` fixes the power of $\alpha_s$ to one, we will therefore only generate one-loop matrix elements which come with an extra power of $\alpha$. Similar to the `EW_real`, setting `EW_virt=1` will ensure that the correct crossings are generated. In particular this includes channels for which we do not have a matrix element, but which contain the integrated subtraction term and mass factorisation contributions which cancel certain initial state collinear limits. Those channels have to be included, even if they do not link to a matrix element. In addition `EW_virt=1` will make sure the correct OpenLoops2 routines for the evaluation of loop amplitudes are called (see section 11.3).

L.27 The QCD one-loop corrections to the diphoton Born matrix element, both in the $q\bar{q}$ and $\overset{(-)}{q}\gamma$ initiated configuration. Since we use a hardcoded matrix element, `B0g1GG` $\widehat{=} B_{0g}^{1,2\gamma}$, we have to explicitly give the relative colour factor, $(N^2-1)/N^2 = C_F/N$.

L.30-37 Since we only consider NLO EW, the NNLO parts `RR,RV,VV` remain empty.

L.39-43 Some technical inputs needed by the maple auto-generation scripts, which are universal and not specific for the process, and some comments.

## 11.3. OpenLoops2 interface - part 2

To run processes generated with OpenLoops2 amplitudes, NNLOJET has to be compiled with the option

```
make OLBASE=/path/to/OpenLoops2/
```

which will define the compiler flag `USE_OL`. Without this flag all calls to OpenLoops2 within the NNLOJET code will be ignored, as they are wrapped in FORTRAN preprocessor directive `\#ifdef` blocks:

```
#ifdef USE_OL
    openloops code
#endif
```

That way an OpenLoops2 installation is no prerequisite to compile NNLOJET, as long as one does not try to run a process with OpenLoops2 amplitudes. In that case the execution will stop with a corresponding error statement.

The OpenLoops2 interface is not limited to EW corrections only; in principle NNLOJET can be set up in such a way, that the tree and one-loop matrix elements (including loop-squared matrix elements) for any process can be taken from OpenLoops2, provided the corresponding OpenLoops2 libraries are installed. By default, however, processes are not generated using OpenLoops2 amplitudes. Thus, if one wants to link an existing process to OpenLoops2, the whole process has to be re-generated.

The NNLOJET-OpenLoops2 link itself is based on the native FORTRAN interface, described in appendix A of [181]. To function properly, the appropriate OpenLoops2 subroutines have to be called in different parts of the code and at different times during execution, which can be summarized as follows:

1. Pass basic parameters to OpenLoops2 and set up the calculation.
2. Register the relevant OpenLoops2 process ids.
3. During the actual integration, for each phase-space point: Pass the correct scale $\mu_R$ and the value of the running $\alpha_s$ to OpenLoops2, evaluate the amplitude.

In the following we will describe each step in detail, roughly following the actual workflow during execution.

### 11.3.1. Passing parameters to OpenLoops2

At the beginning of each run we need to pass some parameters and settings to OpenLoops2 in order to set up the calculation. This is done by the subroutine `initOL_param()` in the `Parameters` module. The renormalisation scale is initialized by setting the OL-parameter `mu`[8] to some arbitrary value, the same for the strong coupling `alphas`. Their correct values will be passed at a later stage for each phase-space-point individually. Since the renormalisation of the strong coupling constant $\alpha_s$ is handled by OpenLoops2 internally but its actual running is taken care of by LHAPDF, it is important to use the same number of active quark flavours in OpenLoops2 and LHAPDF. To ensure this we extract the number of flavours contributing to the running, $N_F^{\text{PDF}}$ from LHAPDF and pass it via the OL parameter `minnf_alphasrun`.

The renormalisation of the electromagnetic coupling $\alpha$ is also left to OpenLoops2. We only have to choose one of the three EW-schemes introduced in section 10.5.2 and pass the corresponding numerical input values, i.e. $\alpha(0)$ for the $\alpha(0)$-scheme, $G_\mu$ for the $G_\mu$-scheme and $\alpha(m_Z)$ for the $\alpha(m_Z)$-scheme. They can be accessed through the parameters `alpha_qed_0`, `alpha_qed_mz` and `gmu`. The program will then automatically compute the correct renormalisation counterterms, according to the scheme. External photons are handled such, that the amplitudes are first calculated and renormalized in the scheme chosen by the user. The coupling of on-shell final state photons and off-shell initial state photons is then rescaled, so that $\alpha^{\text{on-shell}} = \alpha(0)$ and $\alpha^{\text{off-shell}} = \alpha|_{G_\mu}$. Then a finite renormalisation of the rescaling factors is applied, such that the correct counterterm is chosen for each individual coupling. Couplings of real radiation final state photons are not rescaled, as they have to match those of the virtual photons. See

[8] `mu` is an auxiliary parameter to simultaneously set the renormalisation scale $\mu_R$ and the scale of dimensional regularisation $\mu_D$ to the same value.

sections 3.2 and 3.3 in [181] for a more detailed description. For some matrix elements, tree-level or without EW loops, and also the reduced matrix elements in the subtraction terms we use hardcoded amplitudes. Therefore we have to make sure that we choose matching values of the electromagnetic coupling for those amplitudes, but beyond that we do not need to worry about EW renormalisation.

The only EW-scheme currently supported when using NNLOJET with OpenLoops2 is the $G_\mu$-scheme, which is chosen by setting `ew_scheme` equal to 1. Since its input relies on complex masses of the weak gauge bosons (see eq. (10.20)), the only choice available for the mass-scheme is the CMS. Therefore we set `use_cms` to 1. If the user picks any other EW- or mass-scheme in the NNLOJET runcard, the execution of the program will be stopped with an appropriate error message.

When the CMS is selected, the runcard input values for mass and width of $Z$ and $W^\pm$, which are given in the on-shell mass scheme, are automatically converted in the pole scheme according to the conversion formulae given in eqs. (2.45). This is done during the call of the subroutine `init_param()` (before `initOL_param()` is called), which is part of the `Parameters` module, too. The input for the mass and width of the top-quark is by default taken in the pole scheme, while the Higgs mass and width is in the OS scheme[9] The masses and widths are passed to OpenLoops2 by setting the corresponding parameters `mass(pid)` and `width(pid)`, where pid is the PDG particle id.

At last some technical parameters are set, suppressing a large part of the OpenLoops2 terminal output,

```
1    call set_parameter("verbose",0)
```

and printing all OpenLoops2 parameters at the start of the run,

```
1    call set_parameter("parameters_verbose",1)
2    call parameters_flush()
3    call set_parameter("parameters_verbose",0)
```

The tolerance for internal phase-space-point checks increased,

```
1    call set_parameter("psp_tolerance ",1d-5)
```

which is necessary to suppress warnings when probing deep into IR singular regions.

If needed, the subroutine `initOL_param()` can easily be extended by additional parameters by simply adding more `call set\_parameter(...)` statements.

### 11.3.2. Registration of OpenLoops2 channel ids

Before starting the actual integration, the channels about to be computed by OpenLoops2 have to be registered using the

```
1    register_process("process, amptype")
```

function. Here `process` is a string describing the partonic channel in the format

```
1    p1 p2 -> k3 k4 ...
```

[9] Because of the extremely small width of the Higgs, OS and pole scheme values are identical for any practical purpose.

where the particles are passed in form of their respective ids following the PDG scheme [225]. `amptype` is an integer defining the type of amplitude: 1 for a tree-level amplitude, 11 for tree×one-loop interferences, and 12 for one-loop-squared amplitudes.

The process registration is handled by the subroutine `registerOLX()` in `registerOLX.f`, which is fully auto-generated by the maple scripts, including all relevant partonic channels. The subroutine needs to be called once at the start of the execution. It will then allocate an integer 1D array with length given by the total number of channels specified for the process[10], which will be used to store the process ids. After initializing the general OpenLoops2 parameters by calling `initOL_param()` (see previous section 11.3.1), several process specific parameters can be set. They have to be set in the `OL_param` block of the `X.map` file. In principle any OpenLoops2 parameter which can be addressed using the `set_parameter` subroutine can be modified here. Examples are physical parameters like the number of flavours to be considered in quark loops, `nf`, or technical settings concerning the OpenLoops2 stability system, `stability_mode`[11].

After that the actual partonic channels are registered. The registration is organized in blocks, describing the different levels of the calculation (LO,R,V etc.) as well as different contributions to a given level (EW loop insertion, QCD loop insertions, photon-induced, non-photon-induced etc.). At the beginning of each block either the EW or QCD coupling is fixed using the parameters `order_ew` or `order_qcd`, respectively. The correct value has to specified for each amplitude in the process `X.map` file. For tree level amplitudes giving the power of the EW coupling or QCD coupling is equivalent. At one-loop level, however, it specifies what kind of loops are calculated: if the power of the EW coupling is fixed, OpenLoops2 will calculate QCD loops, and vice-versa.

Depending on the block the `register_process` function will automatically be supplied with the correct `amptype` during auto-generation. If one wants to calculate loop induced processes (i.e. `amptype=12`), one has to set the `OL_loopind := true :` flag in the `X.map` file.

Following the discussion in section 10.5.2, external photons need to be treated differently depending on their type in order to ensure the right value for their associated coupling $\alpha$ is used. The correct ids to register photons are given in table 10.1.

### 11.3.3. Scale setting and amplitude evaluation

The evaluation of the OpenLoops2 matrix elements is directly included into the existing `sigX.f` files linking the matrix element source code. The calls of the OpenLoops2 subroutines `evaluate_tree`,`evaluate_loop` or `evaluate_loop2` replace the standard NNLOJET matrix element functions. Here the different OpenLoops2 subroutines have to be chosen according to the type of amplitude to be evaluated, tree, one-loop or loop-squared, respectively.

Before the actual calls, the `KinData_mod:fill_pOL` subroutine is called to translate the set of NNLOJET 4-momenta into the convention used by OpenLoops2[12]. After that the program loops over the active channels, and for each channel over the values set for the renormalisation scale by the scale variation. The scale is passed to OpenLoops2, as well as the current value of $\alpha_s$, which has been extracted from LHAPDF. We then call the actual matrix element evaluation.

[10] This number is calculated during auto-generation.
[11] We refer the reader to the OpenLoops2 manual [181] for discussion of the possible settings.
[12] In NNLOJET the energy is the fourth component, in OpenLoops2 it is the zeroth.

In the case of one-loop amplitudes we afterwards have to correct for the different conventions assumed in NNLOJET and OpenLoops2 for expanding the loop-factor $c_\Gamma$. It effectively amounts to a shift of the finite piece proportional to the $\epsilon^{-2}$ coefficient,

```
    if(ieorder.eq.0) then
        kinwt(i) = factor(i)*(loopME(0)-pi2/12d0*loopME(2))
    else
        kinwt(i) = factor(i)*loopME(abs(-ieorder))
    endif
```

Here `loopME[i]` is the $\epsilon^{-i}$ coefficient of the OpenLoops2 matrix element. `ieorder=-2, -1,0` counts the powers of $\epsilon$ in NNLOJET. `factor(i)` contains all symmetry, colour and final state sum factors associated to that specific channel. For the OpenLoops2 amplitudes the factors are stored in the auto-generated file `qcdnormOLX.f`, which contains the subroutine `getqcdnormOLX`. Colour factors have to be set manually in the `X.map` file, the symmetry and final state sum factors are auto-generated. For OpenLoops2 amplitudes the colour and symmetry factors are usually already included in the output we get from OpenLoops2. In most cases `getqcdnormOLX` will therefore just return `1d0` or a final state sum factor.

### 11.3.4. Subtraction terms

At the moment the OpenLoops2 link is set up to be used for the evaluation of the matrix elements only. The reduced matrix elements, which have to be colour-ordered, must be hardcoded because OpenLoops2 only provides full-colour matrix elements[13]. This is not a problem per se, as long as the colour decomposition of the full matrix element is known. The full-colour subtraction term can then be manually constructed using the subtraction bridge files in the `driver/process/X` directory, which link to the actual subtraction terms in the `src/process/X` directory. The following excerpt from an actual bridge file illustrates the construction:

```
      function qqbBGJR_OLSNLO(i1,i2,i3,i4,i5)
      implicit double precision (a-h,o-y)
      double precision nc, nf, nup, ndown, qnf
      parameter(nc=3d0)
      parameter(nf=5d0)
      parameter(nup=2d0)
      parameter(ndown=3d0)
      parameter(qnf=0.33333333333333333d0)

      wt = 0d0

      fac = subfac(1d0)
      wt = wt + fac*qqbB2g0GSNLO(i1,i2,i3,i4,i5)
      fac = subfac(1d0)

      fac = subfac(-1d0/nc**2)
      wt = wt + fac*qqbBt2g0GSNLO(i1,i2,i3,i4,i5)
      fac = subfac(1d0)

      qqbBGJR_OLSNLO = wt
```

[13] For some processes colour-decomposed versions are available, but it is not the default case.

```
21
22        return
23        end
```

This function constructs the full colour real subtraction term for OpenLoops2 version of the channel $q\bar{q} \to gg\gamma$, the colour decomposition of which is given in eq. (6.4). The functions `qqbB2g0GSNLO` and `qqbBt2g0GSNLO` in L.13 and L.17, respectively, are the subtraction terms for the individual colour-ordered matrix elements as they appear in eq. (6.4). To construct the full colour term we manually add the two terms, taking the relative colour factor $-1/N^2$ into account (L.16). Since the individual subtraction terms are originally coded to be used with the colour decomposed, analytical NNLOJET matrix elements, they come dressed with the overall colour factors of those matrix elements. The factors are specified in the `getqcdnormX` routine in `qcdnormX.f`. It is therefore important that this file is properly generated besides its OpenLoops2 equivalent `getqcdnormOLX`, which will contain different overall factors, as they are mostly absorbed into the result we receive from OpenLoops2.

# 12. NLO EW for diphoton production

Diphoton production at hadron colliders is of particular interest as it is a relevant background process for studies of the Higgs boson properties [41, 42]. At the same time it is an important channel in the search for both resonant and non-resonant NP signals [43, 44]. A good theoretical description of the SM process on the level of differential distributions is therefore absolutely necessary. While the NNLO QCD + NLO EW corrections have been calculated for massive vector boson pair production [186], for diphoton production the state of the art theoretical predictions are at the level of NNLO QCD only [147, 150, 151, 160, 161]. This, although the structure of the EW corrections are conceptually simple. In this chapter we will investigate which building blocks we have to consider. Will will then describe how these concrete contributions were implemented in NNLOJET and how they were validated. In the remainder of the chapter we will perform a full phenomenological study, based on the 8 TeV ATLAS measurement [29], extending the NNLO QCD calculation presented in [160, 161].

## 12.1. Structure

The sole leading order production channel for two final state photons at a hadron collider is $q\bar{q}$-annihilation, $q\bar{q} \to \gamma\gamma$, which in a sense is a pure QED process of $\mathcal{O}(\alpha^2)$. Since it is the Born process with simultaneously the highest power of $\alpha$ and $\alpha_s$ (zero in this case), there is no additional EW Born which has to be considered. The structure of the NLO EW corrections is therefore quite simple with all corrections being of $\mathcal{O}(\alpha^3)$, see figure 12.1. They can be split up in three distinct parts:

1. Radiative pure QED corrections to the $q\bar{q}$ channel.

2. Radiative weak corrections to the $q\bar{q}$ channel.

3. A new photon induced channel ${}^{(-)}_{q}\gamma \to {}^{(-)}_{q}\gamma\gamma$ opening up at NLO EW.

### 12.1.1. Radiative pure QED corrections to the $q\bar{q}$ channel

At the real level the only amplitude contributing to this part is $q\bar{q} \to \gamma\gamma\gamma$ (fig. 12.2a), while at the virtual level we can have an insertion of a virtual photon to the Born diagram (fig. 12.2b-12.2d). In pure QED we do not have any contributions from closed fermion triangles, as clockwise and counter clockwise fermion flow around the loop mutually cancel on the amplitude level.

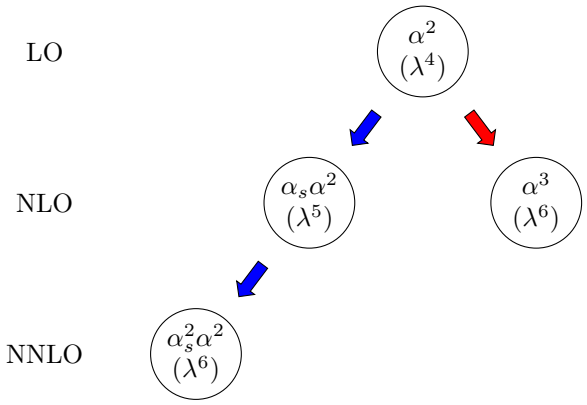


Figure 12.1.: Structure of the QCD and EW corrections to diphoton production. The $\lambda$s show the estimated size of the correction based on the comparison of the numerical size of the coupling constants.

#### IR structure and subtraction

Because both the real radiation matrix element $B_{0g}^{0,3\gamma}$ and the virtual correction matrix element $B_{0g}^{1,2\gamma}$ consist of only a single colour level we do not need to worry about constructing the full-colour subtraction term out of individual leading and subleading colour terms, even if we use OpenLoops2 as the source for the matrix elements. Since for diphoton production we demand at least two resolved photons, one of the final state photons in diagram 12.2a can become unresolved by either being soft or collinear to an initial state quark. These limits can be subtracted both at the same time by an $A_3^0$ antenna in the initial-initial configuration. The reduced matrix element is simply the Born-level $q\bar{q} \to \gamma\gamma$ matrix element, so that the subtraction term takes the form (compare eq. (10.15))

$$\mathrm{d}\hat{\sigma}_{q\bar{q}}^{S,II,\gamma} = \mathcal{N}^R \sum_i \mathrm{d}\Phi_3 \frac{1}{S_3} \times Q_q^2 A_3^0(1_q, \gamma_i, 2_{\bar{q}}) B_{0g}^{0,2\gamma}(\tilde{1}_q, \tilde{2}_{\bar{q}}, \tilde{\gamma}_1, \tilde{\gamma}_2) J_2^{(0)} \tag{12.1}$$

where $i$ runs over all three final state photons. Here $\mathcal{N}^R$ collects overall normalisation and colour factors as well as the couplings. $\mathrm{d}\Phi_3$ denotes the integral over the three particle phase-space and $S_3$ is the symmetry factor for identical particles in the final state; here $S_3 = 3! = 6$. The jet function $J_2^{(0)}$ is trivial in this case, in the sense that we do not want to (and also cannot due to the absence of final state partons) construct any jets. It can still be seen as a placeholder for the cuts and the photon isolation we apply to the event.

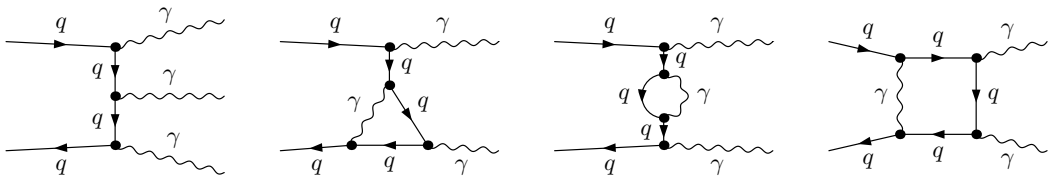


(a) (b) (c) (d)

Figure 12.2.: Example diagrams of the NLO QED corrections to diphoton production.

The corresponding virtual subtraction term (compare eq. (10.16)) contains the integrated $q\bar{q}$-antenna $\mathcal{A}_3^0$ as well as the mass factorisation contributions associated with the two initial state quarks. The latter cancel the initial state $\overset{(-)}{q}||\gamma$ singularities:

$$\mathrm{d}\hat{\sigma}_{q\bar{q}}^{T,II,\gamma} = -\mathcal{N}^V \int \frac{\mathrm{d}x_1}{x_1}\frac{\mathrm{d}x_2}{x_2}\mathrm{d}\Phi_2 \frac{1}{S_2} \times Q_q^2 \mathbf{J}_2^{(1)}(\bar{1}_q, \bar{2}_{\bar{q}}; x_1, x_2) B_{0g}^{0,2\gamma}(\bar{1}_q, \bar{2}_{\bar{q}}, \tilde{\gamma}_1, \tilde{\gamma}_2) J_2^{(0)}\,, \tag{12.2}$$

where (eq. (10.17))

$$\mathbf{J}_2^{(1)}(\bar{1}_q, \bar{2}_{\bar{q}}; x_1, x_2) = \mathcal{A}_{3,q\bar{q}}^{0,II}(s_{\bar{1}\bar{2}}) - \Gamma_{qq}^1(x_1)\delta(1-x_2) - \Gamma_{qq}^1(x_2)\delta(1-x_1)\,, \tag{12.3}$$

with the mass factorisation kernel defined as in appendix A of [48]. We again have to multiply the charge factor $Q_q^2$, in order to ensure the correct compensation of real and virtual subtraction terms.

### 12.1.2. Radiative weak corrections to the $q\bar{q}$ channel

Genuine weak corrections appear only at the virtual level, as additional weak bosons in the final state will in general lead to a different experimental signature and hence will be treated as a different process. $Z$ and $W^\pm$ can therefore only appear as virtual particles (fig. 12.3a,12.3b). The number of distinct 1-loop diagrams, is greater than in the pure QED, because of the trilinear and quartic gauge boson couplings (fig. 12.3c,12.3d). Again we do not have contributions from fermion triangles, but the reason is different than in pure QED. While for the vector component of the $qqZ$ coupling in diagrams such as 12.3e we again have a cancellation between fermion flows, for the axial component this cancellation does not occur. However, the contribution we get is proportional to $\epsilon_{\mu\nu\rho\sigma}p_1^\mu p_2^\nu p_3^\rho p_4^\sigma$, with $p_i$ the external momenta. This quantity vanishes because of 4-momentum conservation. The only dependence on the top mass and width therefore stem from the diagrams with flavour-changing $btW$-couplings (see section 11.1).

#### IR structure and subtraction

As already mentioned the finite mass of the particles in the loops ($Z, W^\pm$ and $t$) regulate their IR behaviour such that we do not have any IR divergences. All virtual weak radiation amplitudes are IR finite, and thus it is also not a problem to discard all real level diagrams with additional final state weak gauge bosons.

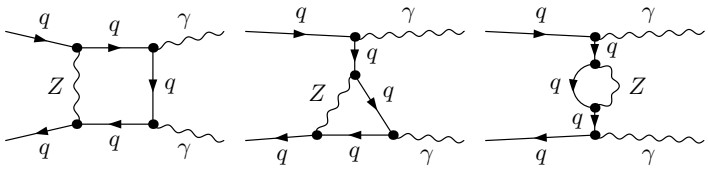


(a)

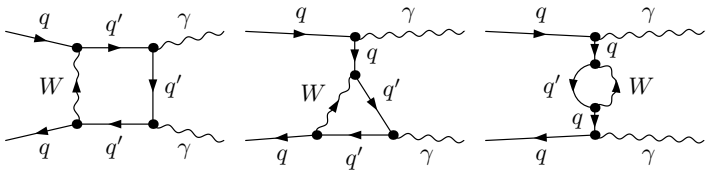


(b)

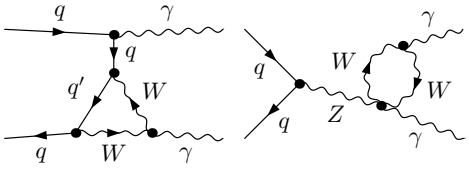


(c)

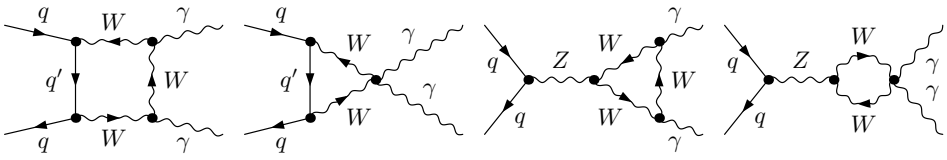


(d)

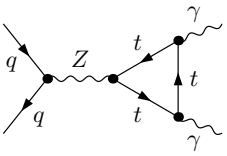


(e)

Figure 12.3.: Example diagrams of the NLO weak corrections to diphoton production. The triangle top-loop identically vanishes.

### 12.1.3. Photon induced channel

The photon induced channel opening up at the EW-R level is just a different crossing of the $2q3\gamma$ amplitude underlying the triphoton channel (see fig. 12.2a vs. 12.4), we therefore again only need to consider a single colour level. Note that there is no corresponding $1q3\gamma$ photon induced 1-loop matrix element.

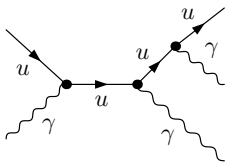


Figure 12.4.: Diagram for the photon induced channel opening at NLO EW.

#### IR structure and subtraction

The two final state photons must remain resolved, but the final state (anti-)quark can become collinear to the initial state photon. This is a special case of the initial-final photon initiated configuration we discussed in the third paragraph of section 10.4, where the particle associated to the initial state momentum 2 in the initial-initial A-type antenna is associated with the other end of the quark line, see eq. (10.11). The limit will effectively change the identity of the initial state photon in the reduced matrix element, $\gamma \to \bar{q}$, so that the rescaled initial state momentum $\bar{1}$ enters the reduced matrix element as if it was an anti-quark. The real subtraction then reads

$$\mathrm{d}\hat{\sigma}^{S,IF,\gamma}_{q\gamma} = \mathcal{N}^R \mathrm{d}\Phi_3 \frac{1}{S_3} \times Q_q^2 A^0_{3,\gamma\to q}(q, 1_\gamma, 2_q) B^{0,2\gamma}_{0g}(\bar{1}_{\bar{q}}, \bar{2}_q, \tilde{\gamma}_1, \tilde{\gamma}_2) J^{(0)}_2 \,. \tag{12.4}$$

The subtraction term for the configuration with an initial state anti-quark can readily obtained from above expression by interchanging $\bar{1}_{\bar{q}} \to \bar{2}_{\bar{q}}$ and $\bar{2}_q \to \bar{1}_q$ in the reduced matrix element and $2_q \to 2_{\bar{q}}$, $q \to \bar{q}$ in the antenna.

The virtual subtraction corresponding to the $q||\gamma$ limit is given by (see eq. (10.12))

$$\mathrm{d}\hat{\sigma}^{T,IF,\gamma}_{q\gamma} = -\mathcal{N}^V \int \frac{\mathrm{d}x}{x} \mathrm{d}\Phi_2 \frac{1}{S_2} \times Q_q^2 \mathbf{J}^{(1)}_{2,\gamma\to q}(\bar{1}_{\bar{q}}, \bar{2}_q; x) B^{0,2\gamma}_{0g}(\bar{1}_{\bar{q}}, \bar{2}_q, \tilde{\gamma}_1, \tilde{\gamma}_2) J^{(0)}_2 \,, \tag{12.5}$$

with the identity changing integrated dipole (see eq. (10.13))

$$\mathbf{J}^{(1)}_{2,\gamma\to q}(\bar{1}_{\bar{q}}, \bar{2}_q; x) = \mathcal{A}^{0,II}_{3,q\to g}(s_{\bar{1}\bar{2}}) - \Gamma^1_{qg}(x) \,. \tag{12.6}$$

The virtual subtraction corresponding to the $\bar{q}||\gamma$ limit can again be obtained by simply swapping $\bar{1}_q \to \bar{2}_q$ and $\bar{2}_{\bar{q}} \to \bar{1}_{\bar{q}}$ in the reduced matrix element. Note that because there is no photon induced 1-loop matrix element the poles of the integrated antenna $\mathcal{A}^0_3$ are completely cancelled by those of the mass factorisation kernel.

## 12.2. Implementation and Validation

The EW corrections to diphoton production have been implemented as the independent process `GG_EW`, containing only contributions to the real and virtual level, but no dedicated Born[1]. For the matrix elements we exclusively use OpenLoops2. Because all IR limits factor onto the QCD Born matrix element $B_{0g}^{0,2\gamma}$, the subtraction term can be constructed completely out of hardcoded pieces. Moreover, since all matrix elements only have a single colour level, the `driver` bridge files are trivial, i.e. no extra colour factors or combinations of subtraction terms are required.

### 12.2.1. Internal checks

Before proceeding to the validation of the our implementation in a direct comparison against the computational framework MATRIX [186], we performed some internal consistency checks, to make sure all IR limits are correctly accounted for. To this end we ran spike tests for all IR limits of the real-radiation matrix elements to confirm, that the subtraction terms subtract the divergences in the right way. On the side of the virtual corrections we checked that for a given phase-space-point all the poles of the virtual matrix elements are cancelled by the poles of the integrated subtraction terms.

### 12.2.2. Validation: setup

For the validation we collaborated directly with one of the authors [226] of MATRIX [186]. The setup for the validation follows the ATLAS 8 TeV diphoton study [29]. We apply the following fiducial cuts:

$$p_T^{\gamma_1} \geq 40 \text{ GeV}\,, \qquad p_T^{\gamma_2} \geq 30 \text{ GeV}\,, \qquad \Delta R^{\gamma_1\gamma_2} \geq 0.4 \tag{12.7}$$

to the two photons of the diphoton system. Of all photons present (i.e. two Born-level photons plus at most one additional real radiation photon) we choose the two with the highest transverse momentum, $p_T^{\gamma_1} > p_T^{\gamma_2} (> p_T^{\gamma_3})$. In addition the two leading photons must pass a cut on their rapidity,

$$|y^\gamma| \in [0, 1.37) \cup (1.56, 2.37)\,. \tag{12.8}$$

Should one of them violate this cut, the whole event is rejected. This setup slightly differs from the one we use for our phenomenology runs in section 12.3, where the infringing photon is removed from the list, the cut again applied to the leading two of the remaining photons, and the event kept, as long as in total enough photons survive.

[1] Since we do not have a subleading EW Born but the autogeneration relies on a LO coupling factor to construct all prefactors correctly, we have to specify a symbolic Born level prefactor $\sim \alpha^3/\alpha_s$.

To be registered as a photon in the first place in both the NNLOJET and the MATRIX calculation candidate photons must pass the smooth cone isolation criterion with parameters[2]

$$R = 0.4\,, \qquad \varepsilon_d = 0.1\,, \qquad n = 2\,. \tag{12.9}$$

Note that for simplicity we do not apply any photon combination in the case that two photons become relatively close to each other.

The validation uses the NNPDF3.1luxQED [218] PDF set provided by LHAPDF. LHAPDF also takes care of the running of the strong coupling constant.

The renormalisation scale $\mu_R$ and the factorisation scale $\mu_F$ are set equal to $m_{\gamma\gamma}$. We do not perform any variation of scales for the validation.

All particles except for the weak gauge bosons $Z, W^\pm$ and the top-quark are taken as massless. The massive particles, which only appear as virtual insertions and never as external states in our calculation, are treated in the complex-mass-scheme (CMS). It is defined in the pole scheme, thus the inputs for the $Z$ and $W^\pm$ mass and width, which are given in the on-shell scheme, are internally converted into the pole scheme according to (2.45). The numerical values in both the on-shell (where applicable) and the pole scheme are summarized in table 12.1. They correspond to the 2016 PDG [227].

Since the calculation is carried out in the $G_\mu$ scheme, the complex masses of the weak gauge bosons also enter the definition of the electroweak gauge coupling $\alpha|_{G_\mu}$, following (10.20). As discussed in section 10.5.2 we use $\alpha(0)$ for the coupling of final state Born-level photons. The electroweak input parameters for the $G_\mu$ scheme as well as related quantities are summarized in table 12.1.

| physics input | | | |
|---|---|---|---|
| quantity | value | input | derived quantities |
| $\sqrt{s}$ | 8000 GeV | ✓ | |
| $m_Z^{\text{os}}$ | 91.1876 GeV | ✓ | $m_Z^{\text{pole}} \approx 91.1535$ GeV |
| $\Gamma_Z^{\text{os}}$ | 2.4952 GeV | ✓ | $\Gamma_Z^{\text{pole}} \approx 2.4943$ GeV |
| $m_W^{\text{os}}$ | 80.385 GeV | ✓ | $m_W^{\text{pole}} \approx 80.358$ GeV |
| $\Gamma_W^{\text{os}}$ | 2.085 GeV | ✓ | $\Gamma_W^{\text{pole}} \approx 2.084$ GeV |
| $m_t^{\text{pole}}$ | 173.21 GeV | ✓ | |
| $\Gamma_t^{\text{pole}}$ | 1.41 GeV | ✓ | |
| schemes | | | |
| Mass scheme | CMS | | |
| EW scheme | $G_\mu$ | | $\sin^2\theta_w \approx 0.22289 - 0.00111i$ |
| $1/\alpha(0)$ | 137.035999139 | ✓ | |
| $G_\mu$ | $1.1663787 \cdot 10^{-5}$ | ✓ | $1/\alpha\|_{G_\mu} \approx 132.293$ |

Table 12.1.: Technical parameters and input values for the validation run. The masses and widths correspond to the 2016 PDG [227] values. In the rightmost column we also present some related quantities derived from the input values.

[2]We use the default functional form again:

$$E_{T,\text{dyn}}^{\max}(p_T^\gamma; r) = \varepsilon_d p_T^\gamma \left(\frac{1-\cos r}{1-\cos R}\right)^n$$

During the validation we also checked the limit of a vanishing top-mass (and width), which for diphoton production is equivalent to treating the bottom as a generic down-type quark in the matrix elements (for a diagonal CKM matrix)[3], while still convoluting with the correct bottom PDF. In NNLOJET we achieved this by explicitly replacing the bottom quark by a generic down quark in the OpenLoops2 process registration, while in MATRIX we set $m_t = 0.1$ GeV and $\Gamma_t = 0.001$ GeV. In the vanishing top-mass limit the $q\bar{q}$-channel contribution to the total cross section is increased by just 0.3%. The photon induced channel does not depend on the top parameters, thus we do not observe any deviations beyond statistical fluctuation.

### 12.2.3. Validation: results

We compare both the total cross section contributions of the individual coefficients, LO, NLO QCD, NLO EW, and the $m_{\gamma\gamma}$ distribution. The comparison of the QCD results, which for NNLOJET have previously been validated [160, 161] against MadGraph5 [228], serves as an additional check for the validation setup. As expected we find excellent agreement for the LO and the NLO coefficients (see table 12.2). We split the NLO EW coefficient in its $q\bar{q}$ and $\gamma$-induced sub-channels, in order to examine their individual impact. The results for the total cross section are summarized in table 12.2. We find good agreement, at a very high accuracy of $\mathcal{O}(0.01\%)$, both for the calculation with explicit $m_t$ dependence and the one with $m_t \to 0$. While NNLOJET and MATRIX both make use of OpenLoops2 as source for the matrix elements, the rest of the implementation, in particular the subtraction method, is completely independent. The matching results are therefore an important indication that the implementation within NNLOJET works as expected.

| contribution | $\sigma_{\text{NNLOJET}}$[fb] | $\sigma_{\text{MATRIX}}$[fb] | $\frac{\sigma_{\text{MATRIX}}}{\sigma_{\text{NNLOJET}}} - 1$ | deviation (st-dev.) |
|---|---|---|---|---|
| LO | 3379.943(59) | 3379.986(68) | $1.3 \cdot 10^{-5}$ | +0.5 |
| NLO QCD coeff | 5982.96(22) | 5982.850(99) | $-1.8 \cdot 10^{-5}$ | −0.5 |
| NLO EW coeff | 48.4498(41) | 48.4533(21) | $7.2 \cdot 10^{-5}$ | +0.8 |
| EW $q\bar{q}$ | 42.9375(41) | 42.9403(21) | $6.5 \cdot 10^{-5}$ | +0.6 |
| EW $\gamma$-ind. | 5.51235(24) | 5.51303(27) | $1.2 \cdot 10^{-4}$ | +1.9 |
| NLO EW coeff ($m_t = 0$) | 48.5799(48) | 48.5852(21) | $1.1 \cdot 10^{-4}$ | +1.0 |
| EW $q\bar{q}$ ($m_t = 0$) | 43.0676(48) | 43.0722(21) | $1.1 \cdot 10^{-4}$ | +0.9 |
| EW $\gamma$-ind. ($m_t = 0$) | 5.51238(19) | 5.51303(27) | $1.2 \cdot 10^{-4}$ | +2.0 |

Table 12.2.: Validation against MATRIX: total cross section

We can already make some interesting statements about these numbers. Compared to the LO contribution the NLO EW coefficient increases the cross section by only $\sim 1.4\%$, which is two orders of magnitude smaller than the effect of the NLO QCD corrections (+177%). This is actually much less than the one order of magnitude we got from the naive estimation based on the comparison of couplings. Moreover the photon induced channel contributes only slightly more than 10% to the total EW NLO coefficient. While it is true that the $q\bar{q}$ channel receives contributions from 1-loop diagrams and the photon induced channel does not, this cannot explain the big difference in size of the two contributions. Both the smallness of the

[3] Remember we treat all quarks except for the top as massless.

NLO EW contribution and the difference in size between the EW $q\bar{q}$ and $\gamma$-induced channel can actually be explained by considering the PDFs of the different initial state configurations appearing in EW and QCD corrections, respectively.

The $q\bar{q}$ channel comes with the same PDF convolution regardless of the type of correction, EW or QCD. Any difference in size between the two corrections can be attributed to genuine EW effects in the matrix elements[4]. Comparing the ratios of the NLO EW and NLO QCD coefficient in the $q\bar{q}$ channel to the LO cross section, we find

$$\text{QCD } q\bar{q} \text{ channel:} \qquad \delta = 1608.85(9) \text{ fb} \qquad \Rightarrow \qquad \frac{\delta}{\sigma_{\text{LO}}} = 47.600(3)\% \tag{12.10a}$$

$$\text{EW } q\bar{q} \text{ channel:} \qquad \delta = 42.9375(41) \text{ fb} \qquad \Rightarrow \qquad \frac{\delta}{\sigma_{\text{LO}}} = 1.27(1)\% \tag{12.10b}$$

Hence the NLO QCD corrections in the $q\bar{q}$ channel are approximately 37 times bigger than the corresponding NLO EW corrections. Given that $\alpha_s(m_Z)/\alpha(m_Z) \approx 15$, the naive estimate does not seem too bad.

The photon induced channel on the other hand has to be compared to the $qg$ channel opening at NLO QCD. Here also the effect of gluonic vs photonic PDF plays a role. Looking at the corresponding ratios to LO as above, we find

$$\text{QCD } qg \text{ channel:} \qquad \delta = 4374.10(9) \text{ fb} \qquad \Rightarrow \qquad \frac{\delta}{\sigma_{\text{LO}}} = 129.4(3)\% \tag{12.11a}$$

$$\text{EW } q\gamma \text{ channel:} \qquad \delta = 5.51235(24) \text{ fb} \qquad \Rightarrow \qquad \frac{\delta}{\sigma_{\text{LO}}} = 0.1631(8)\% \tag{12.11b}$$

This is a difference in size by a factor of $\sim 793$, i.e. roughly three orders of magnitude, and more than 50 times larger than we would expect from the naive estimate. But this factor of 50 is actually quite close to difference between the parton luminosities of a $q\gamma$ and a $qg$ initial state (cf. figure 10 in [213]). Thus, in explaining the relative smallness of the NLO EW corrections the size of the photonic PDF plays an important role.

Figure 12.6 shows the contribution of the $q\bar{q}$-channel differential in $m_{\gamma\gamma}$. The distribution is peaked around 80GeV, which is the threshold for contributions with Born-like kinematics: having only two photons in the final state forces them back to back in $p_T$, so that $p_T^{\gamma_1} = p_T^{\gamma_2} = p_T^{\gamma}$, and

$$m_{\gamma\gamma} = \sqrt{2p_T^{\gamma_1} p_T^{\gamma_2} (\cosh \Delta y_{\gamma\gamma} - \cos \Delta\phi_{\gamma\gamma})} \underset{\text{Born kin.}}{\to} p_T^{\gamma} \sqrt{2(1 + \cosh \Delta_{\gamma\gamma})} \geq 2p_T^{\gamma} \,, \tag{12.12}$$

which is obviously bounded from below by the fiducial cuts (here: $p_T^{\gamma_1} > 40$ GeV). The distribution then rapidly decreases and eventually becomes negative for values above $\sim 250$ GeV. In the region around the zero-crossing the Monte-Carlo error is comparatively large, which is related to numerical instabilities in the phase-space integration. Such an behaviour is expected and nothing to be worried about. At $m_{\gamma\gamma} = 2m_W$ we see a small resonance peak, which has its origin in diagrams like the ones depicted in figure 12.5. As for the total cross section we find excellent agreement between NNLOJET and MATRIX over the whole kinematical range. The comparatively large MC uncertainties in the very high $m_{\gamma\gamma}$ region, as well as close to the zero-

[4] Also fiducial cuts on the photons and the concrete observable definition play a role, as we shall see in section 12.3.

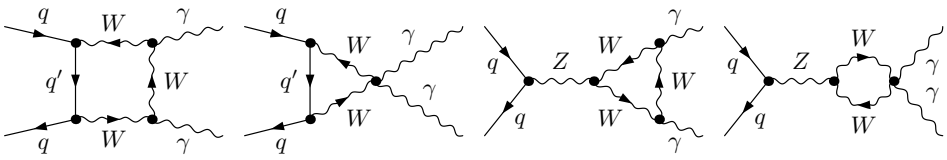


Figure 12.5.: Diagrams contributing to the $2m_W$ resonance.

crossing of the coefficient arise from limited statistics and therefore do not pose a problem per se. In the two lowest bins the contribution from the $q\bar{q}$ channel is identically vanishing, which is an artefact of the interplay between the observable definition and the cuts on the photons. Starting from the relation (12.12) we find a lower bound for $m_{\gamma\gamma}$,

$$m_{\gamma\gamma} \geq \sqrt{2p_T^{\gamma_1} p_T^{\gamma_2} (1 - \cos\Delta\phi_{\gamma\gamma})}\,. \tag{12.13}$$

As we will later show (section 12.3) the azimuthal distance has a strict lower bound $\Delta\phi_{\gamma\gamma} \geq \frac{2\pi}{3}$, thus we further find

$$m_{\gamma\gamma} \geq \sqrt{2p_T^{\gamma_1} p_T^{\gamma_2} \left(1 + \frac{1}{2}\right)} = \sqrt{3p_T^{\gamma_1} p_T^{\gamma_2}} \geq 60 \text{ GeV}\,, \tag{12.14}$$

where the last inequality comes from the fiducial cuts on the photon transverse momenta.

In figure 12.7 we show the contribution of the photon induced channel differential in $m_{\gamma\gamma}$. Again the distribution is peaked at 80GeV. Since there are no loop-diagrams contributing to this channel, the coefficient is positive throughout and does not show the $2m_W$ peak we saw before. Again good agreement between NNLOJET and MATRIX is given over the whole kinematical range. We observe a slight tendency in the tail, where the MATRIX numbers are larger, but the differences are still compatible within uncertainties.

Figure 12.8 shows the full NLO EW coefficient as a function of $m_{\gamma\gamma}$. Given the fact that the $q\bar{q}$-channel contribution is roughly one order of magnitude bigger than the one of the photon induced channel, it is not surprising to see that the NLO EW coefficient closely resembles the $q\bar{q}$-channel contribution.

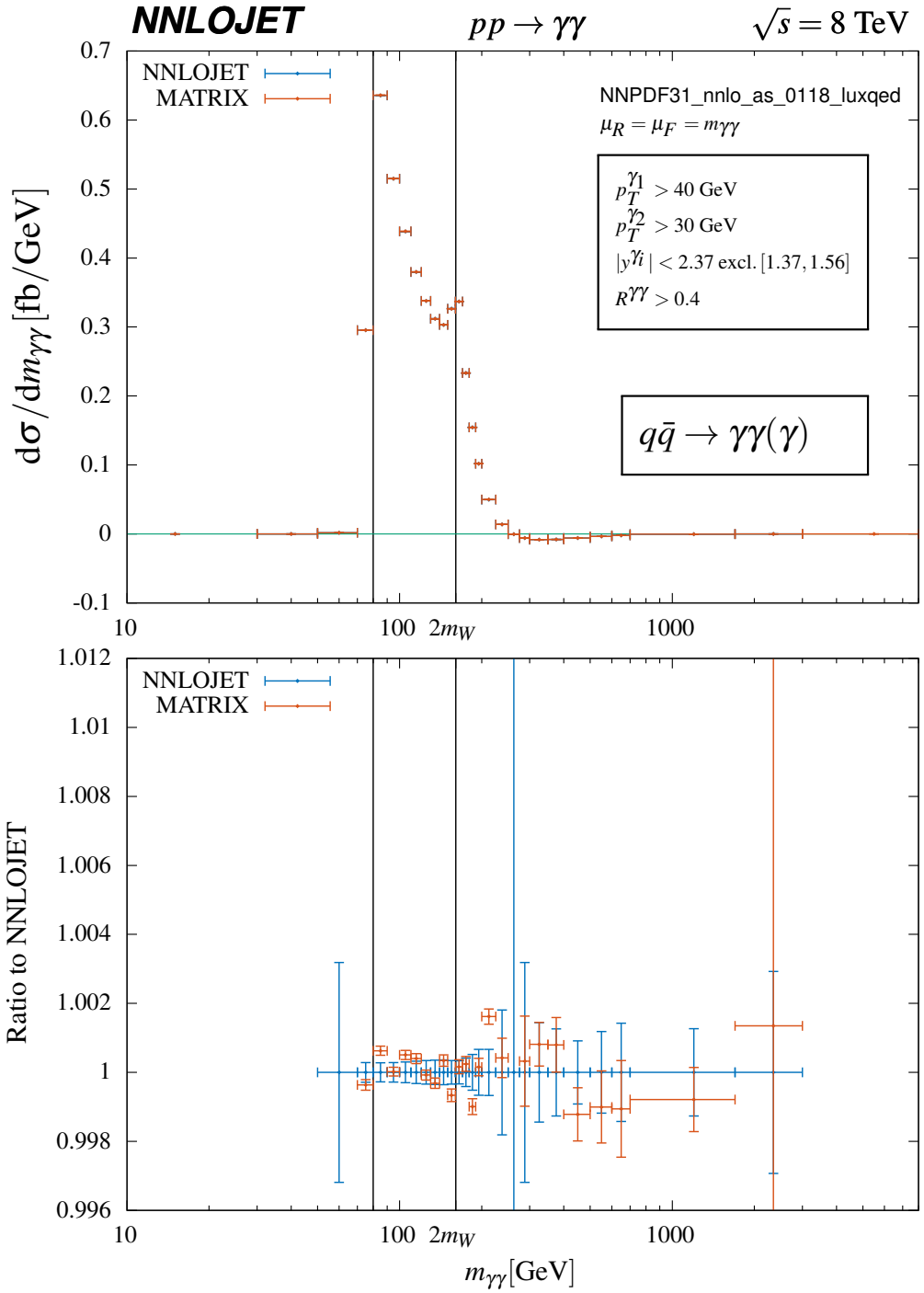


Figure 12.6.: Coefficient of the EW radiative corrections to the $q\bar{q}$ channel in diphoton production as calculated by MATRIX (red) and NNLOJET (blue). Top panel: contribution to the $m_{\gamma\gamma}$ distribution. Bottom panel: ratio to the NNLOJET result.

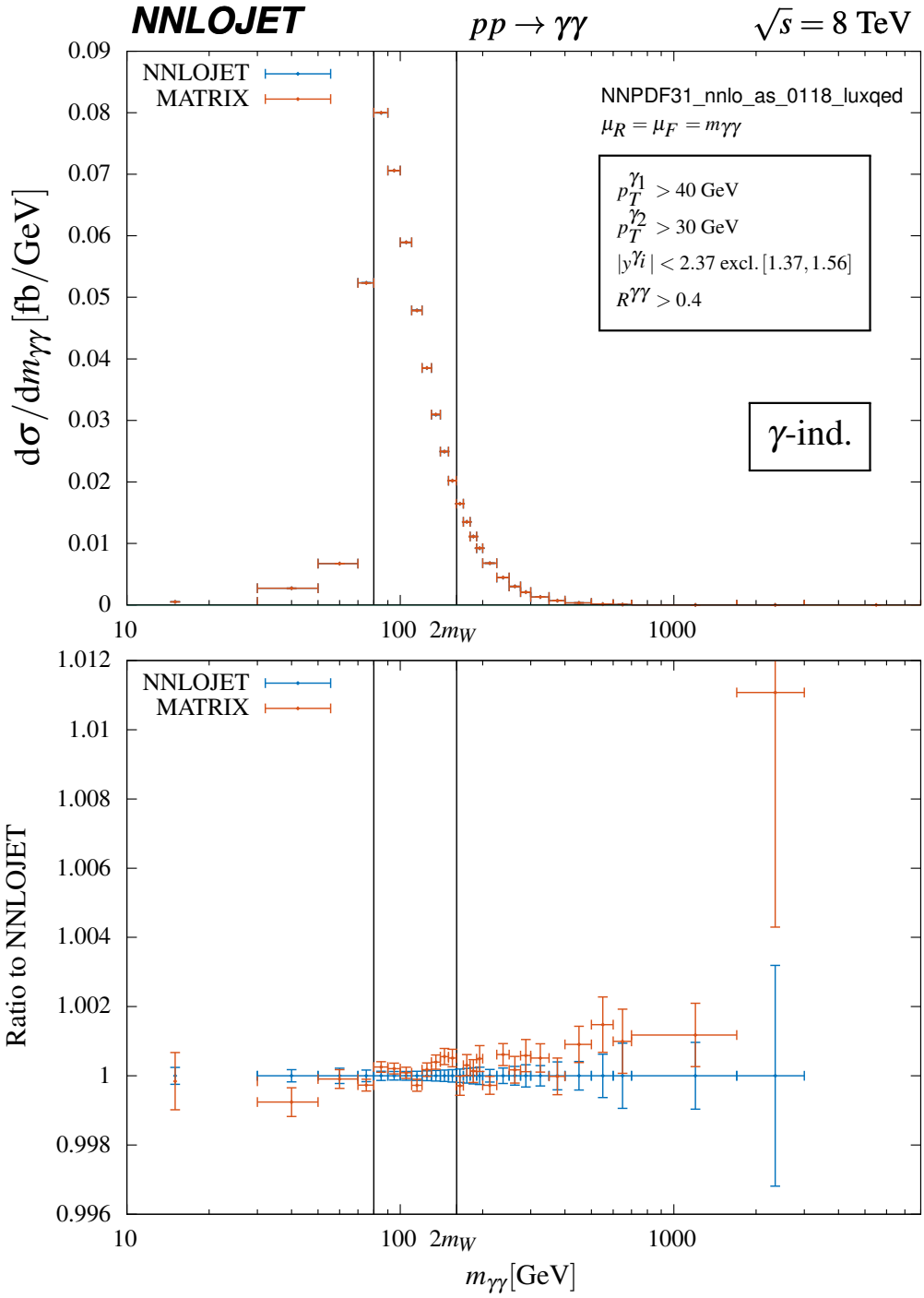


Figure 12.7.: Coefficient of the photon induced contribution of the NLO EW corrections to diphoton production as calculated by MATRIX (red) and NNLOJET (blue). Top panel: contribution to the $m_{\gamma\gamma}$ distribution. Bottom panel: ratio to the NNLOJET result.

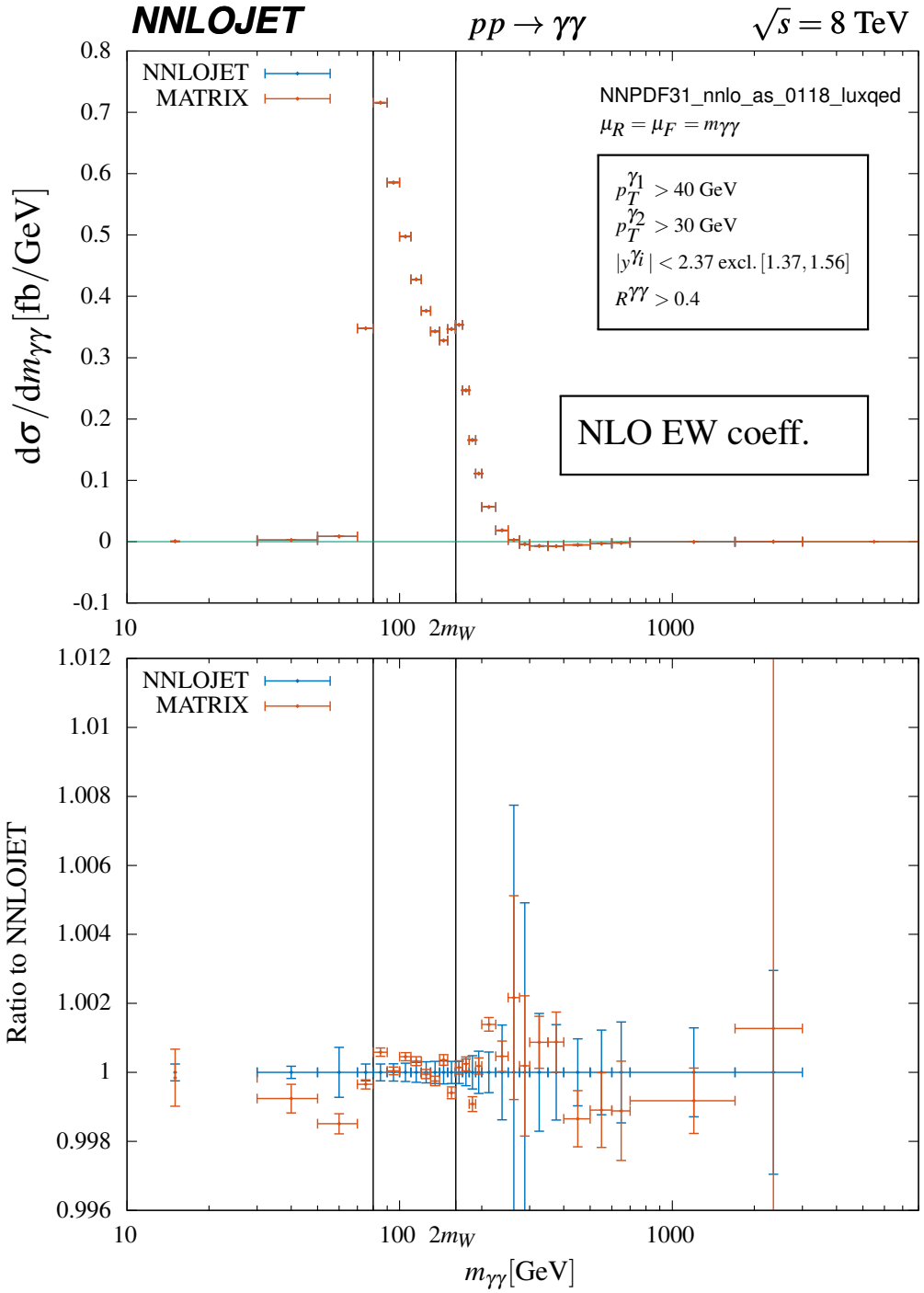


Figure 12.8.: Coefficient of the NLO EW corrections to diphoton production as calculated by MATRIX (red) and NNLOJET (blue). Top panel: contribution to the $m_{\gamma\gamma}$ distribution. Bottom panel: ratio to the NNLOJET result.

## 12.3. Phenomenology

### 12.3.1. Setup

The setup for our phenomenology study is based on the ATLAS 8 TeV diphoton study [29] and very similar to the setup for the validation in section 12.2 (see eq. (12.7)). It matches the setup used for the NNLO QCD calculation in [160, 161].

To be considered in the event photons must pass the matched hybrid isolation (see eq. (4.18))

$$E_{T,\text{hyb,matched}}^{\max}(p_T^\gamma; r; R_d) = E_T^{\text{thres}} \times \begin{cases} \left(\frac{1-\cos r}{1-\cos R}\right)^n, & (0 \le r < R_d) \\ 1\,, & (R_d \le r < R) \end{cases}, \tag{12.15}$$

with parameters

$$R = 0.4\,, \qquad R_d = 0.1\,, \qquad E_T^{\text{thres}} = 11\text{ GeV}\,, \qquad n = 1\,. \tag{12.16}$$

The parameters of the outer cone given in (12.16) correspond to what ATLAS describes as the particle level isolation supposed to closely match the actual isolation performed at the event level. In order to mimic the finite resolution of the detector we cluster all photons in our calculation with a distance smaller than $R = 0.1$ in the $\eta - \phi$ plane. Note that this only effects the contribution with real QED radiation. The photon list is then subject to the rapidity cut

$$|y^\gamma| \in [0, 1.37) \cup (1.56, 2.37) \tag{12.17}$$

for all photons. All photons failing the cut are removed from the list, but the event is kept, as long as at least two photons pass. The photons are then sorted by $p_T$ such that $p_T^{\gamma_1} > p_T^{\gamma_2} > \ldots$, before the fiducial cuts are applied to the event:

$$p_T^{\gamma_1} \ge 40\text{ GeV}\,, \qquad p_T^{\gamma_2} \ge 30\text{ GeV}\,, \qquad \Delta R^{\gamma_1\gamma_2} \ge 0.4\,. \tag{12.18}$$

We use the NNPDF3.1luxQED [218] PDF set calculate the EW corrections for each of the scale choices used in the calculation of the QCD corrections in [160, 161]: The renormalisation and factorisation scale are varied independently according to $\mu_R = a\mu$ and $\mu_F = b\mu$ with the pair

$$(a, b) \in \{(\tfrac{1}{2}, \tfrac{1}{2}), (\tfrac{1}{2}, 1), (1, \tfrac{1}{2}), (1, 1), (1, 2), (2, 1), (2, 2)\}\,.$$

This corresponds to the standard seven-point scale variation used to estimate the theoretical uncertainty. The study is performed for two different choices of the central scale $\mu$, the invariant mass of the diphoton system $m_{\gamma\gamma}$, which was also used for the validation in section 12.2, and the $p_T$-average $\langle p_T^\gamma \rangle$ of the diphoton system. The latter appears to be a more robust choice, at least when considering higher order QCD corrections.

As per default the calculation is performed in the complex-mass-scheme and the $G_\mu$-scheme, using the input parameters summarized in table 12.3. They correspond to the latest PDG [196] values[5].

| physics input | | | |
|---|---|---|---|
| quantity | value | input | derived quantities |
| $m_Z^{\text{os}}$ | 91.1876 GeV | ✓ | $m_Z^{\text{pole}} \approx 91.1535$ GeV |
| $\Gamma_Z^{\text{os}}$ | 2.4952 GeV | ✓ | $\Gamma_Z^{\text{pole}} \approx 2.4943$ GeV |
| $m_W^{\text{os}}$ | 80.379 GeV | ✓ | $m_W^{\text{pole}} \approx 80.352$ GeV |
| $\Gamma_W^{\text{os}}$ | 2.085 GeV | ✓ | $\Gamma_W^{\text{pole}} \approx 2.084$ GeV |
| $m_t^{\text{pole}}$ | 172.76 GeV | ✓ | |
| $\Gamma_t^{\text{pole}}$ | 1.42 GeV | ✓ | |
| schemes | | | |
| Mass scheme | CMS | | |
| EW scheme | $G_\mu$ | | $\sin^2\theta_w \approx 0.22298 - 0.00111i$ |
| $1/\alpha(0)$ | 137.035999139 | ✓ | |
| $G_\mu$ | $1.1663787 \cdot 10^{-5}$ | ✓ | $1/\alpha\vert_{G_\mu} \approx 132.244$ |

Table 12.3.: Technical parameters and input values for the phenomenology study. The masses and widths correspond to the latest PDG [196] values. In the rightmost column we also present some related quantities derived from the input values.

The corresponding NNLO QCD numbers were calculated in [160, 161]. Since these runs were performed in the five-flavour scheme, the top-mass does not enter, and also the other EW parameters, except for the coupling constant, do not play a role in the QCD calculation. The numerical value of the coupling slightly differs, $1/\alpha(0) = 137.035989$, but because for QCD corrections it is only a multiplicative constant we can simply rescale the results. This, however, is not really necessary here, since the effect will be well below MC accuracy.

A bigger impact comes from the choice of the PDFs: while for the EW runs we used NNPDF3.1luxQED, the QCD calculation used the counterpart without photon-content, i.e. NNPDF3.1. As we will discuss later, the actual magnitude of the NLO EW corrections, which is indeed small, is less important than how they modify the shape of the distributions. Since we do not expect the shape of the QCD distributions to be altered in any significant way when using NNPDF3.1luxQED instead of NNPDF3.1, the qualitative statements we make are not affected by this formal discrepancy.

The loop-induced $gg \to \gamma\gamma$ process is often considered as a special channel, being strongly enhanced by the gluon PDF. Here we consider it a natural part of the NNLO QCD coefficient. This corresponds to saying the $gg$ induced channel is included at its Born level.

[5] Apart from $\alpha(0)$, which is from the 2018 review [225]. The numerical impact of this inconsistency is negligible.

### 12.3.2. Results

ATLAS [29] measured the total fiducial cross section to be

$$\sigma_{\text{tot}} = 16.8 \pm 0.8 \text{ pb}\,, \tag{12.19}$$

which we compare to the result calculated at the (NNLO QCD)+(NLO EW) level:

$$\sigma_{\text{(NNLO QCD)+(NLO EW)}} = 15.5^{+1.1}_{-0.9} \text{ pb}\,, \qquad (\mu = m_{\gamma\gamma}) \tag{12.20a}$$

$$\sigma_{\text{(NNLO QCD)+(NLO EW)}} = 16.2^{+1.3}_{-1.1} \text{ pb}\,. \qquad (\mu = \langle p_T^\gamma \rangle) \tag{12.20b}$$

Both results underestimate the measured cross section, yet, with the given scale uncertainty of $^{+7\%}_{-6\%}$ ($^{+8\%}_{-7\%}$) for the calculation with $m_{\gamma\gamma}$ ($\langle p_T^\gamma \rangle$) as the central scale, they are compatible. As already observed in the pure QCD calculation [160, 161] the number obtained with $\mu = \langle p_T^\gamma \rangle$ is closer to the measurement. The EW corrections do not weaken or strengthen this statement in any particular way, as their impact is very small. Separating the theory result in its respective perturbative coefficients,

$$\sigma_{\text{(NNLO QCD)+(NLO EW)}} = \sigma_{\text{LO}} + \delta^{\text{QCD}}_{\text{NLO}} + \delta^{\text{QCD}}_{\text{NNLO}} + \delta^{\text{EW}}_{\text{NLO}}\,, \tag{12.21}$$

we find[6]

| | $\sigma_{\text{LO}}$ | $+\delta^{\text{QCD}}_{\text{NLO}}$ | $+\delta^{\text{QCD}}_{\text{NNLO}}$ | $+\delta^{\text{EW}}_{\text{NLO}}$ |
|---|---|---|---|---|
| $\mu = m_{\gamma\gamma}$ | $3400^{+204}_{-239}$ fb | $7449^{+851}_{-689}$ fb | $4604^{+519}_{-329}$ fb | $51.4^{+7.5}_{-7.3}$ fb |
| | (21.9%) | (50.0%) | (29.7%) | (0.33%) |
| $\mu = \langle p_T^\gamma \rangle$ | $3111^{+248}_{-290}$ fb | $8128^{+1066}_{-840}$ fb | $4942^{+820}_{-469}$ fb | $42.6^{+7.2}_{-7.0}$ fb |
| | (19.2%) | (50.1%) | (30.5%) | (0.26%) |

Thus we see that in both cases the EW corrections only contribute less than a third of a percent to the total result. Their impact is slightly enhanced when choosing $m_{\gamma\gamma}$ over $\langle p_T^\gamma \rangle$ as the central scale, while for the QCD corrections the opposite is true.

While the relevance for total cross section measurements might be negligible, it is still worth looking into differential distributions, as they might show non-trivial features which are washed out as the distributions are integrated, or simply because the effects appear in regions, which contribute only little to the total cross section. The observables measured by ATLAS, which we will discuss here are:

- The invariant mass of the diphoton system, $m_{\gamma\gamma}$, which can be used to search for resonances as signal of new particles or states decaying into photons.

- The absolute value of the cosine of the scattering angle in the diphoton centre-of-momentum frame, $\left|\theta^*_\eta\right|$, which is measured in terms of the rapidity difference of the two photons: $\left|\theta^*_\eta\right| = \tanh \frac{|\Delta\eta_{\gamma\gamma}|}{2}$. Its distribution is sensitive to the spin of the exchanged particle[7].

[6] Note that the stated uncertainties are scale uncertainties and therefore do not add in quadrature when summing up the coefficients.
[7] See discussion in the introduction of [34]

- The azimuthal distance of the two leading photons, $\Delta\phi_{\gamma\gamma}$. As an angular observable, it can be measured to very high accuracy. In the theory prediction, however, it is formally one order lower than $m_{\gamma\gamma}$ or $\left|\cos\theta^*_\eta\right|$, as in the $2 \to 2$ Born configuration, we are strictly forced to $\Delta\phi_{\gamma\gamma}|_{\text{Born}} = \pi$.
- The variable $\phi^*_\eta = \tan\left(\frac{\pi - \Delta\phi_{\gamma\gamma}}{2}\right) \sin\theta^*_\eta$, defined in [229] for dilepton systems, as a means to study the transverse momentum of the diphoton system solely based on angular variables for better resolution. Note that $\phi^*_\eta$ and $\Delta\phi_{\gamma\gamma}$ are closely related, and that we have $\phi^*_\eta|_{\text{Born}} = 0$, i.e. the distribution again is effectively one order lower.
- The transverse momentum of the diphoton system, $p_T^{\gamma\gamma} = |\vec{p}_T^{\,\gamma_1} + \vec{p}_T^{\,\gamma_2}|$. Note that $p_T^{\gamma\gamma}|_{\text{Born}} = 0$, as in the Born configuration the transverse momenta of the two photons exactly cancel each other. At NLO when we can have one additional real radiation particle, we have $p_T^{\gamma\gamma} = p_T^3$, where $p_T^3$ is the transverse momentum of the recoiling particle.
- The transverse momentum with respect to to the thrust axis $\hat{t}$, $a_T = \left|(\vec{p}_T^{\,\gamma_1} + \vec{p}_T^{\,\gamma_2}) \times \hat{t}\right|$ with $\hat{t} = (\vec{p}_T^{\,\gamma_1} - \vec{p}_T^{\,\gamma_2})/|\vec{p}_T^{\,\gamma_1} - \vec{p}_T^{\,\gamma_2}|$. The observable was defined in [230], again in the context of dilepton systems, in order to reduce the uncertainty coming from the measurements of the individual transverse momenta (i.e. $p_T^{\gamma_1}$ and $p_T^{\gamma_2}$ in our case). As $p_T^{\gamma\gamma}$, $a_T$ identically vanishes in the Born configuration, $a_T|_{\text{Born}} = 0$.

In order to better understand how the EW corrections behave differently from the QCD corrections, it is instructive to look at the ratio between the NLO QCD and EW coefficients. Since both allow for one additional final state particle, the overall geometric constraints on the observables are identical. Thus all qualitative differences in the shapes of distributions can be explained by the inherent differences between NLO EW and NLO QCD, with two caveats:

1. Extra QCD radiation will affect the photon isolation, while real QED radiation will not, apart from the photon combination we discussed earlier.
2. The above observables are always defined using the two leading photons, i.e. the two photons with the highest $p_T$. In NLO QCD it is inherently clear, which photons are considered. In NLO EW, as soon as we have a third photon in the final state, for different kinematical configurations different photons will be part of the observable definition. We will see later that this restricts some of the observables which are effectively LO to certain values, provided no further cuts are applied to the photon definition. There are cases, in which the definition of the observable becomes ambiguous (e.g. when $p_T^{\gamma_1} > p_T^{\gamma_2} = p_T^{\gamma_3}$). Those configurations, however, are a null set, so we do not need to worry about them.

In figure 12.9 we show the ratio of the NLO EW coefficient to the NLO QCD coefficient for all observables presented in the ATLAS study, both for $\mu = m_{\gamma\gamma}$ (left panels) and $\mu = \langle p_T^\gamma \rangle$ (right panels). To get an idea of the relative size of the NLO EW and NNLO QCD coefficients, we analogously present their ratio in 12.10. The effect on the full result (NNLO QCD + NLO EW), can best be seen in figure 12.11, where we present the ratio of the mixed QCD+EW result to the pure QCD distributions. The scale bands given in this figure are derived according to prescription B from section 10.7, i.e. the numerator and denominator use the same variation of the scales.

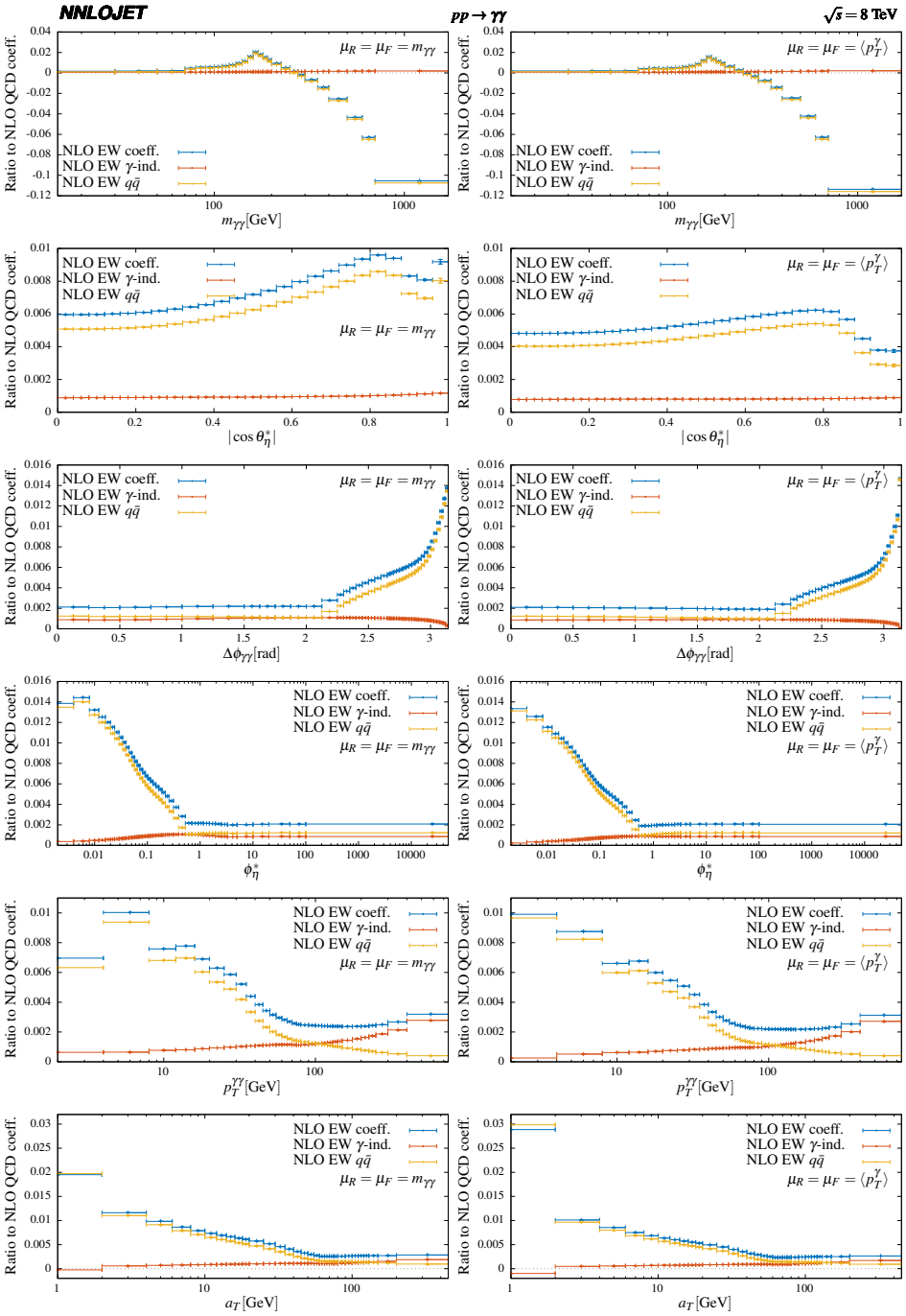


Figure 12.9.: Ratio of the NLO EW coefficient to the NLO QCD coefficient, for the different observables presented in [29] and [160, 161]. In blue we show the total NLO EW coefficient, in red and yellow its contributions from the photon-induced and the $q\bar{q}$ channel, respectively. We only show the central scales, with MC error, corresponding to prescription B from section 10.7. Left panels: $\mu = m_{\gamma\gamma}$, right panels: $\mu = \langle p_T^\gamma \rangle$.

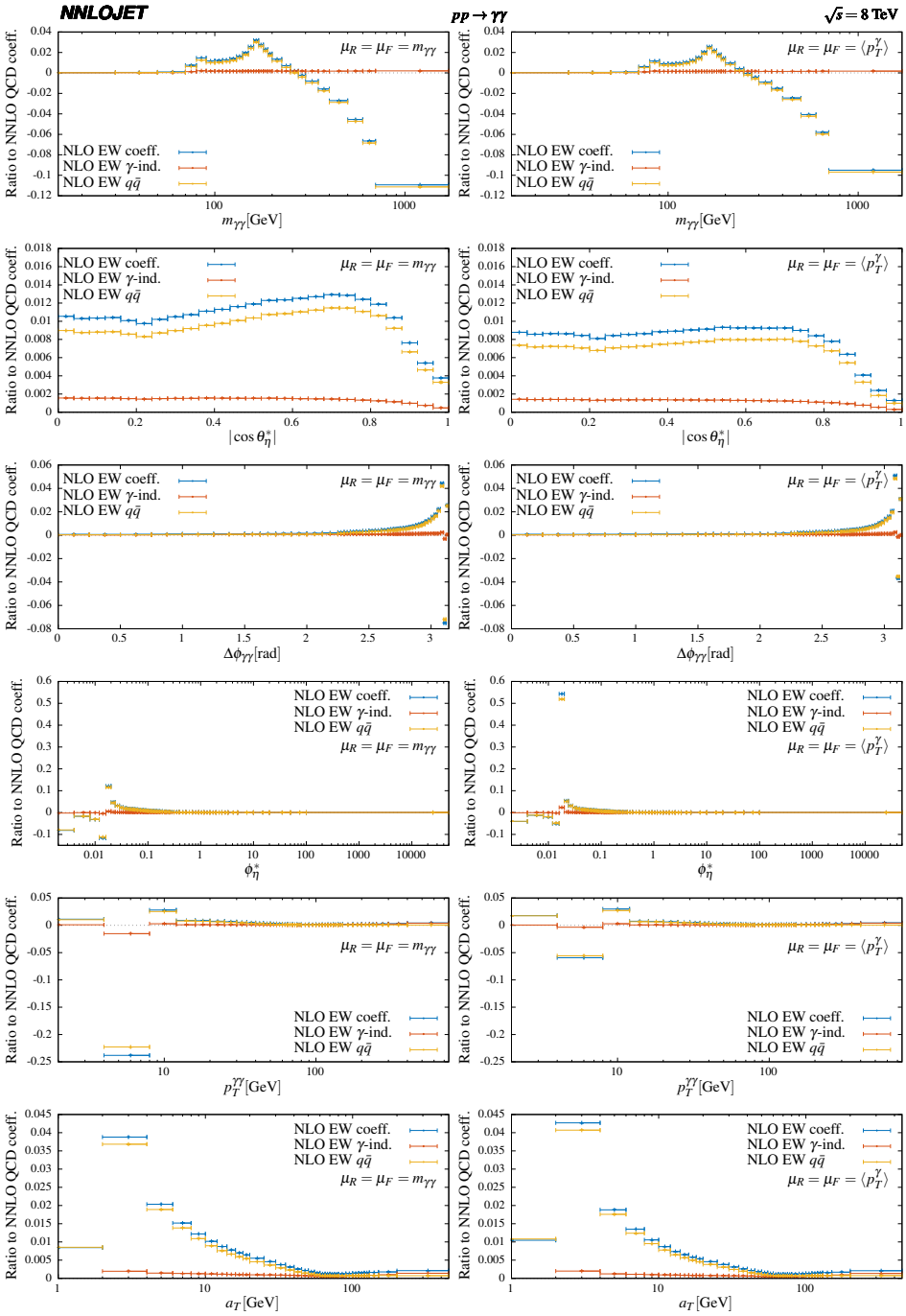


Figure 12.10.: Ratio of the NLO EW coefficient to the NNLO QCD coefficient, for the different observables presented in [29] and [160, 161]. In blue we show the total NLO EW coefficient, in red and yellow its contributions from the photon-induced and the $q\bar{q}$ channel, respectively. We only show the central scales, with MC error, corresponding to prescription B from section 10.7. Left panels: $\mu = m_{\gamma\gamma}$, right panels: $\mu = \langle p_T^\gamma \rangle$.

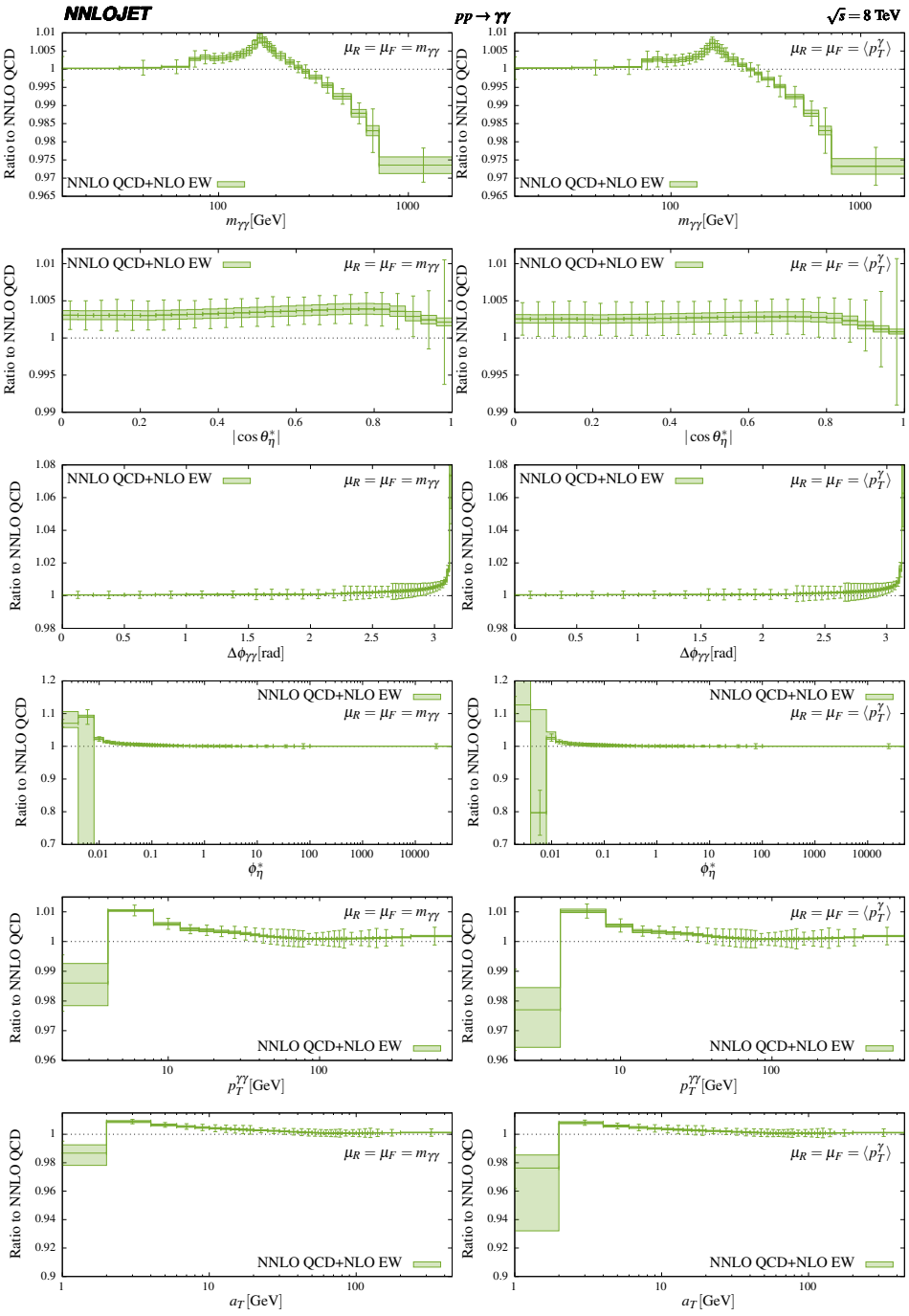


Figure 12.11.: Ratio of the full result (NNLO QCD+ NLO EW) to NNLO QCD, for the different observables presented in [29] and [160, 161]. The scales in numerator and denominator are correlated, corresponding to prescription C from section 10.7. On the central scale we show the MC error, which is dominated by the error on the NNLO QCD prediction. Left: $\mu = m_{\gamma\gamma}$, right: $\mu = \langle p_T^\gamma \rangle$.

**Invariant mass $m_{\gamma\gamma}$ -** The first thing one notices when looking at the NLO EW coeff. vs NLO QCD coeff. ratio of the $m_{\gamma\gamma}$ distribution in figure 12.9 is the peak at $m_{\gamma\gamma} = 2m_W$, which has already been noticed during the validation (see figures 12.8 and 12.6) and could be explained by certain weak 1-loop diagrams in the $q\bar{q}$-channel (see figure 12.5). For values of the invariant mass above $\sim 250$ GeV the NLO EW corrections become negative. This behaviour is dictated by the $q\bar{q}$-channel again. Given that the $m_{\gamma\gamma}$ distribution in figure 12.9 is non-trivial already at Born level, at least above the Born threshold of $m_{\gamma\gamma}^{\text{min,Born}} = 80\text{ GeV} = 2p_T^{\gamma_1,\text{min}}$ coming form the fiducial cuts on the photons, we do not see any effects from artificial PS boundaries. Comparing the two scale choices, $\mu = m_{\gamma\gamma}$ vs. $\mu = \langle p_T^\gamma \rangle$, we notice no qualitative differences. For the latter scale the resonance peak is slightly smaller ($\sim -18\%$) and the cross section suppression in the tail larger ($\sim -18\%$ in the last bin).

Given the flat NNLO/NLO QCD $k$-factor in the region above 80 GeV, and the fact that the NNLO QCD corrections are of similar size as the NLO QCD corrections (see [160, 161]), we see an almost identical picture in the ratio to the NNLO QCD coefficient, figure 12.10. The step we see at the Born-threshold stems from the enhanced cross section in the low $m_{\gamma\gamma}$ region due to the extra PS opening up at NNLO, and the observable being effectively one order lower in this region. Considering the magnitude of the EW corrections, we can confirm our observation made on the level of the total cross section, that the naive estimate based on the numerical size of the coupling constants, $\alpha_s^2 \approx \alpha$, does not hold for diphoton production, even in the tail of the distribution, where we see the largest effect. On the level of the full result (figure 12.11) this effects amounts to an $< \mathcal{O}(3\%)$ suppression of the cross section. The additional dependence on the scales we get from the inclusion of NLO EW corrections is modest and smaller than the MC uncertainty of the NNLO QCD corrections.

**Scattering angle $\left|\cos\theta_\eta^*\right|$ -** Besides $m_{\gamma\gamma}$ the cosine of the scattering angle is the only other observable the range of which is completely accessible already at LO[8]. For low values of the observable, which corresponds to values of $\theta_\eta^*$ close to $\pi/2$, the ratio of the NLO EW coefficient to the NLO QCD coefficient (figure 12.9) is basically flat, while it has a localised maximum for $\left|\cos\theta_\eta^*\right| \approx 0.8$. The ratio then drops again for values of the observable approaching 1. As for the $m_{\gamma\gamma}$ distribution the shape is dictated by the $q\bar{q}$-channel while the photon induced contribution is considerably smaller and absolutely flat. The shape distortion and the magnitude of the shift are more pronounced for $\mu = m_{\gamma\gamma}$ than for $\mu = \langle p_T^\gamma \rangle$. Still the overall effect is less significant than for the invariant mass, and the $\left|\cos\theta_\eta^*\right|$-distribution appears to be more robust under inclusion of NLO EW corrections.

The comparison with the NNLO QCD coefficient (figure 12.10) looks very much alike. The ratio is larger for all but the last three bins, while still of small overall magnitude. We again observe a drop of the ratio for $\left|\cos\theta_\eta^*\right| \to 1$, more pronounced than in the NLO EW coefficient to NLO QCD coefficient ratio. For the full result (figure 12.11) we observe an constant increment of the cross section by about 0.25% in all but the last bins where it is slightly smaller. We note

[8] The rapidity cuts on the photons limit the observable to $\left|\cos\theta_\eta^*\right| < \tanh(2.37) \approx 0.983$, which leads to an underestimated cross section in the last bin.

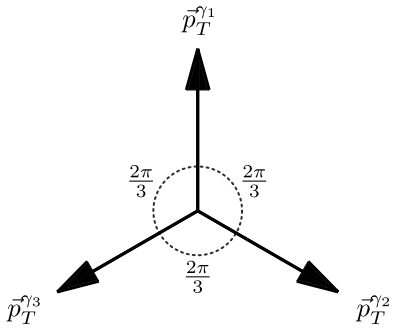


Figure 12.12.: Critical configuration in the three-particle final state. All particles have exactly the same $p_T$ and their mutual azimuthal distance is $\frac{2\pi}{3}$. If for any two-particle system $(i, j)$ in this configuration we either decrease the distance, $\Delta\phi_{ij} < \frac{2\pi}{3}$, or imbalance the transverse momenta, $p_T^i > p_T^j$, because of equation 12.22 the recoiling particle will *not* be the softest particle of the three.

however, that the shift is completely compatible with the MC error. Given the smallness of the effect and the trivial shape of the NLO EW corrections, it does not seem necessary to include them for this particular distribution

**Angular observables $\Delta\phi_{\gamma\gamma}$ and $\phi_\eta^*$ -** At NLO the distribution of both the azimuthal distance in the diphoton system and the directly related $\phi_\eta^*$ are effectively described to LO only, as their full range is only accessible with at least three particles in the final state. At NLO the distributions are therefore expected to be sensitive to constraints on the final state phase-space, in particular when these constraints interfere with the observable definition. In particular $\Delta\phi_{\gamma\gamma}$ is a prime example for the second caveat we mentioned earlier, where a third photon in the final state puts a limit on the possible values the observable can adopt, purely based on the interplay between certain geometrical configurations in the final state and the observable definition.

In a three-particle final state the total transverse momentum $\vec{p}_T^{\,ij}$ of any two-particle system $(i, j)$ is always balanced by the transverse momentum of the third particle taking the recoil,

$$\vec{p}_T^{\,ij} = -\vec{p}_T^{\,\text{recoil}}\,, \tag{12.22}$$

such that the total transverse momentum vanishes. This directly sets a hard lower bound on the angle between the particles $i$ and $j$, below which the transverse momentum of the recoiling particle necessarily needs to be greater than the transverse momentum of at least one of the particles $i$ or $j$ in order to fulfil above condition. The critical configuration is shown in figure 12.12. It is highly symmetric with all three particles having the same transverse momentum and the same mutual azimuthal distance $\Delta\phi = \frac{2\pi}{3}$. If we either decrease the angle between any two of the particles, $\Delta\phi_{ij} < \frac{2\pi}{3}$, or imbalance the transverse momenta, $p_T^i > p_T^j$, the transverse momentum condition (12.22) will force the recoiling particle to be harder than particle $i$, $j$ or both.

This has an immediate consequence on the observable definition in pure QCD vs. in presence of extra QED radiation: While in pure QCD we always will have exactly two photons, it will be those photons defining the diphoton system considered in the observables, irrespective of the transverse momentum of the recoiling particle. In NLO EW, more precisely in the radiative QED corrections to the $q\bar{q}$-channel, we can have three resolved photons in the final state. Since it is always the two leading photons (sorted by $p_T$) which are used to define the diphoton system, from the above argument it directly follows that these channels will only contribute in the region $\Delta\phi_{\gamma\gamma} \geq \frac{2\pi}{3} \approx 2.09$. For any angle smaller than that, the recoiling photon becomes harder than at least one of the photons taken as part of the system, thus leading to a re-ordering of the photons (in their $p_T$ sorting). This particular kinematical region is therefore inaccessible.

Note that this argument holds as long as there are no additional phase-space constraints in the definition of photons in the calculation. However, since we demand $|y^\gamma| \in [0, 1.37) \cup (1.56, 2.37)$, there can be situations where the recoiling photon is not registered as a photon, but the event still counted. In those situations the angle $\Delta\phi_{\gamma\gamma}$ can be arbitrary. We therefore expect a clear enhancement of the ratio to QCD for $\Delta\phi_{\gamma\gamma} \geq \frac{2\pi}{3}$, while the ratio should be flat for values lower than that. In the photon-induced case, with exactly two photons and a quark in the final state, we do not encounter such configurations, thus its ratio to QCD should be flat over the whole range.

This is exactly what we observe in figure 12.9, in identical ways for both central scale choices, $\mu = m_{\gamma\gamma}$ and $\mu = \langle p_T^\gamma \rangle$. Note that the photon induced contribution is suppressed close to the Born configuration ($\Delta\phi_{\gamma\gamma} = \pi$). Since $\phi_\eta^*$ is directly related to the azimuthal distance, the exact same argument is applicable. Without constraints in the photon definition we find a hard upper bound $\phi_\eta^{*\max} = \frac{1}{\sqrt{3}} \approx 0.577$, which is reached for $\theta_\eta^* = \frac{\pi}{2}$.

This behaviour we see for the NLO EW coefficient in comparison with the NLO QCD coefficient is a purely geometric effect. For any greater number of real radiation photons this effect will be washed-out, since the recoil can then be shared by several photons at once.

In pure QCD, having multiple real radiation particles, i.e. two at NNLO, leads to an higher population away from the Born configurations for both $\Delta\phi_{\gamma\gamma}$ and $\phi_\eta^*$. The ratio of the NLO EW coefficient to the NNLO QCD coefficient (figure 12.10) is practically zero for $\Delta\phi_{\gamma\gamma} \lesssim 2$ or $\phi_\eta^* \gtrsim 1$, respectively. For $\Delta\phi_{\gamma\gamma}$ close to the Born-configuration the same argument holds as for the NLO EW to NLO QCD ratio, with the ratio increasing even stronger. An exception is the last bin, the only one for which the QCD corrections are genuinely NNLO. Here the NNLO QCD coefficient is negative, thus the sign flip in the ratio.

For low values of $\phi_\eta^*$ we observe a more complicated behaviour of the ratio, which, however, is inherited from the NNLO QCD coefficient and is not a feature of the EW corrections.

Looking at the comparisons of the full predictions (figure 12.11), we see that indeed the only significant shifts arise in the geometrically enhanced regions. For $\Delta\phi_{\gamma\gamma}$ we find a enhancement in the cross section in the Born-configuration-bin by $\sim 7\%$ ($\sim 6\%$) for the scale choice $\mu = m_{\gamma\gamma}$ ($\mu = \langle p_T^\gamma \rangle$). Here we also see the strongest dependence on the scale chosen coherently for the numerator (NNLO QCD + NLO EW) and denominator (NNLO QCD) in order to calculate the ratio. Note that also the MC error, mainly coming from the NNLO QCD coefficient, is comparatively large in this bin. For $\phi_\eta^*$ we also observe an enhancement of the cross section

for $\phi_\eta^* \to 0$, with increased scale dependence of the EW corrections. In the lowest two bins, however, the shape is distorted by the behaviour of the NNLO QCD coefficient, which here is negative and competes with the NLO QCD coefficient.

**Transverse momentum observables $p_T^{\gamma\gamma}$ and $a_T$ -** Being completely accessible only from NLO onwards, i.e. for at least three final state particles, we expect similar geometric constraints also in the transverse momentum observables $p_T^{\gamma\gamma}$ and $a_T$. In figure 12.9 we see an enhanced ratio to the NLO QCD coefficient in the low $p_T^{\gamma\gamma}$ region, with origin in the $q\bar{q}$ channel, which is in turn suppressed at high $p_T^{\gamma\gamma}$. This can be understood from the observation that in the three photon final state the transverse momentum of the diphoton system is equal to the transverse momentum of the recoiling photon (equation (12.22)). For high values of $p_T^{\gamma\gamma}$ the individual transverse momenta of the two leading photons therefore have to be even greater,

$$p_T^{\gamma_1} > p_T^{\gamma_2} > p_T^{\gamma\gamma} = p_T^{\gamma_3} \,. \tag{12.23}$$

Otherwise, with the recoiling photon not being the softest, we would have a contradiction to the observable definition. In QCD we do not have this restriction. The diphoton system can be very collimated, so that we reach high values of $p_T^{\gamma\gamma}$ without the need of the individual photons being too hard[9]. The real QED radiation corrections are therefore expected to populate the lower $p_T^{\gamma\gamma}$ region, leading to the observed shape in the ratio. The (smaller) contribution of the photon induced channel again does not have this geometric constraint, and we actually observe quite the opposite behaviour, with an enhancement for high $p_T^{\gamma\gamma}$.

Comparing the scale choices, we see a nearly identical picture, except for the first two bins: while for $\mu = \langle p_T^\gamma \rangle$ the ratio to the NLO QCD coefficient monotonically rises for $p_T^{\gamma\gamma} \to 0$, for $\mu = m_{\gamma\gamma}$ we reach a maximum in the second bin.

Looking at $a_T$ we see a similar behaviour, with the ratio of NLO EW coefficient to NLO QCD coefficient being relatively small and flat for larger values and monotonically increasing with $a_T \to 0$ for values $a_T \lesssim 80$ GeV. Again the $q\bar{q}$-channel is the driving contribution. Given the more complicated nature of the observable, however, it is not straightforward to define a fixed bound, as we could for $p_T^{\gamma\gamma}$ or the angular observables. We observe no significant differences for the two different scale choices, except for the first bin, where the ratio for $\mu = \langle p_T^\gamma \rangle$ is about 50% bigger than for $\mu = m_{\gamma\gamma}$.

When considering the ratio to the NNLO QCD coefficient (figure 12.10), we find that for the $a_T$-distribution the behaviour we observed previously is pronounced, with the ratio basically vanishing above $a_T \approx 80$ GeV and increasing as $a_T \to 0$. For $p_T^{\gamma\gamma}$ the large NNLO QCD corrections in the first few bins dominate the ratio, such that the form of the NLO EW coefficient is washed out.

The small enhancement of the cross section in the low $p_T^{\gamma\gamma}$ and $a_T$ due to the NLO EW corrections can also be seen in the ratio of the full predictions (figure 12.11). The effect, however is small and there are no exposed bins in which the deviation becomes really noteworthy. The

[9] The fiducial cut $\Delta R^{\gamma\gamma} = \sqrt{(\Delta\phi^{\gamma\gamma})^2 + (\Delta\eta^{\gamma\gamma})^2} \geq 0.4$ implies the lower bound $p_T^{\gamma_{1,2}} > \frac{p_T^{\gamma\gamma}}{2\cos\frac{0.4}{2}} \approx 0.51 p_T^{\gamma\gamma}$.

first bins, in which the Born-configuration lives, appears to be affected the most, but here we also find large negative NNLO QCD corrections, which actually distort the ratio.

In order to see how the effect of the NLO EW corrections actually compares to the standard scale variation band at NNLO QCD[10], we plotted the exact same ratio as in figure 12.11, full NNLO QCD and NNLO QCD + NLO EW vs NNLO QCD, in figure 12.13, but this time using prescription A from section 10.7, i.e. with the scale variation carried out in the numerator only and the denominator fixed at the central scale.

The only observable where we see a non-negligible distortion in the shape compared to the NNLO scale band, due to the NLO EW correction is in the invariant mass distribution of the diphoton system, more precisely in its tail. All the other observables seem to be very robust under the inclusion of NLO EW, or show distortions in regions where the theoretical uncertainty is comparatively large to begin with.

It is important to notice that the NLO EW corrections are not sufficiently large to describe the discrepancy observed between the data, which we also show in figure 12.13, and the NNLO QCD fixed order prediction. Especially for the observables which are effectively one order lower ($\Delta\phi_{\gamma\gamma}, \phi^*_\eta, p_T^{\gamma\gamma}, a_T$) the measured shapes are very different from the theory numbers. While the inclusion of NNLO QCD corrections already improved the description of the data quite considerably[11] [160, 161], even higher order radiative corrections, included in form of a parton-shower as performed by ATLAS for their theory prediction using SHERPA, are desirable. Furthermore the fixed order predictions suffer from numerical instabilities arising from large logarithms in threshold regions defined by the fiducial cuts on the photon $p_T$. Those instabilities are smeared for a sufficiently wide binning [147, 160, 161], a full resummation of these logarithms, similar to what has been done in [231] for Drell-Yan, would certainly help to improve the theory predictions.

## 12.4. Summary

We investigated the NLO EW corrections to diphoton production and found their structure to be comparatively simple, because there is no subleading Born contribution besides the $q\bar{q} \to \gamma\gamma$ QCD-Born. We therefore only had to consider genuine EW radiative corrections to this channel, and a new photon induced channel, $\overset{(-)}{q}\gamma \to \overset{(-)}{q}\gamma\gamma$, opening up at the QED real level. No interferences between QCD-like and EW-like diagrams were present at this order.

We performed a phenomenology study based on the 8 TeV ATLAS measurement [29], using the matched hybrid isolation prescription established for fixed order QCD corrections to diphoton production in [160, 161] and [61]. The $q\bar{q}$-channel proved itself as the dominant contribution, both for the total cross section and in defining the shape of differential distributions. The smallness of the photon induced channel could be explained by the small photon PDF.

The shape of the EW corrections in differential distributions could be assigned to two main sources:

[10] It is known that for diphoton production that the standard NNLO scale variation is actually a poor measure of the uncertainty [147], underestimating it by a significant amount.

[11] Provided a careful choice of scales. In [160, 161] $\mu = \langle p_T^\gamma \rangle$ was shown to be superior to the conventional choice $\mu = m_{\gamma\gamma}$

1. Genuine EW effects due to EW diagrams, as in the $m_{\gamma\gamma}$ distribution.
2. Geometric constraints in the three photon final state. Those effects were in particular enhanced in the observables which were effectively one order lower.

Most of the distribution proved to be quite robust under the inclusion of EW corrections and, in comparison with the NNLO QCD uncertainty, higher order QCD effects and resummation of fiducial threshold effects are of greater importance to improve the theoretical predictions. Still, in particular for the tail of the $m_{\gamma\gamma}$ distribution one might want to consider NLO EW effects, once the experimental accuracy in that region is improved.

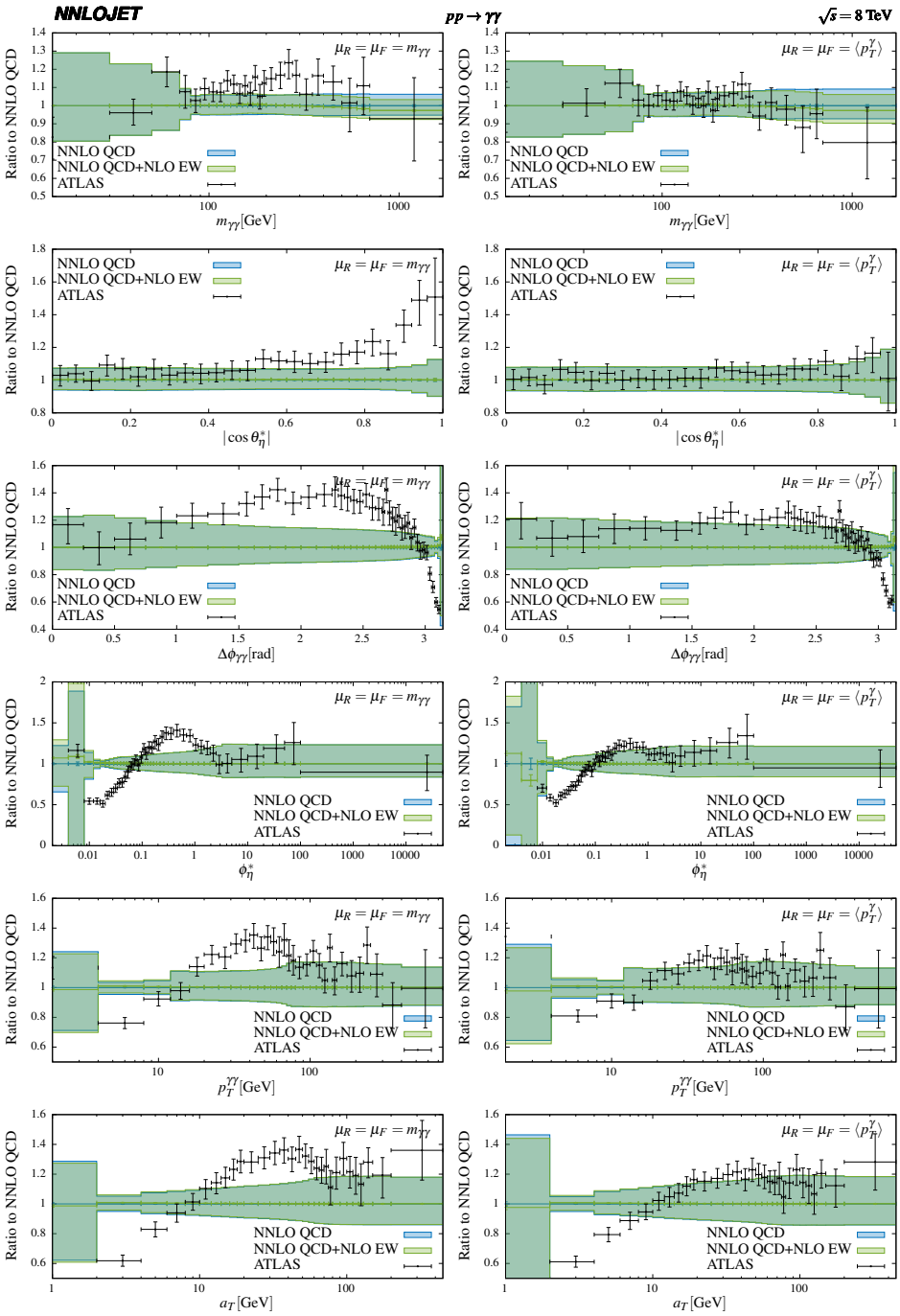


Figure 12.13.: Ratio of the full pure NNLO QCD and mixed NNLO QCD + NLO EW predictions to NNLO QCD. In this plot the scale band is derived in the standard way, prescription A from section 10.7, by varying the scales in the numerator only, while keeping the denominator fixed at the central scale choice. We also show the ATLAS data [29]. Left: $\mu = m_{\gamma\gamma}$, right: $\mu = \langle p_T^\gamma \rangle$.

# 13. NLO EW for inclusive photon production

After having calculated the NLO EW corrections for diphoton production we move our focus towards inclusive photon production to extend the study presented in section 8.1. It will be interesting to see how the full NLO EW corrections affect the tails of the distributions, given that within the current experimental uncertainties already the pure NNLO QCD corrections show a good agreement with the data, see also [24], while on the other hand the references [191, 192] found a significant impact of electroweak Sudakov logarithms for high $p_T^\gamma$.

## 13.1. Structure

The general structure of the corrections to inclusive photon production is depicted in figure 13.2. While for diphoton production all contributions to NLO EW were of the same order $\mathcal{O}(\alpha^3)$, we now find two different levels, a subleading Born of $\mathcal{O}(\alpha^2)$ and a NLO EW contribution $\mathcal{O}(\alpha_s\alpha^2)$. The subleading Born consists of different crossings of the $2q2\gamma$ squared amplitude, which are simply (see figure 13.1)

- the genuine diphoton channel $q\bar{q} \to \gamma\gamma$,
- and photon induced channels $\overset{(-)}{q}\gamma \to \overset{(-)}{q}\gamma$.

Note that the former only contributes to inclusive photon production, but not to the EW corrections to photon-plus-jet.

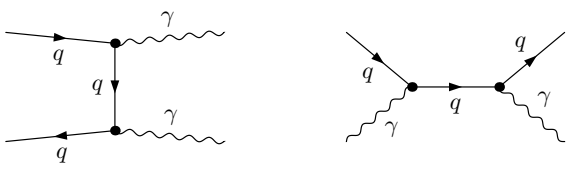


(a) diphoton channel (b) photon induced channel

Figure 13.1.: Example diagrams of the subleading Borns contributing to the NLO EW corrections of inclusive photon production.

Like for the $\mathcal{O}(\alpha_s\alpha^2)$ corrections it is not possible to unambiguously identify their respective contributions as EW corrections to the leading $\mathcal{O}(\alpha_s\alpha)$ Born or the subleading $\mathcal{O}(\alpha^2)$ Born, as through their IR factorisation properties matrix elements of $\mathcal{O}(\alpha_s\alpha^2)$ can factor on a reduced

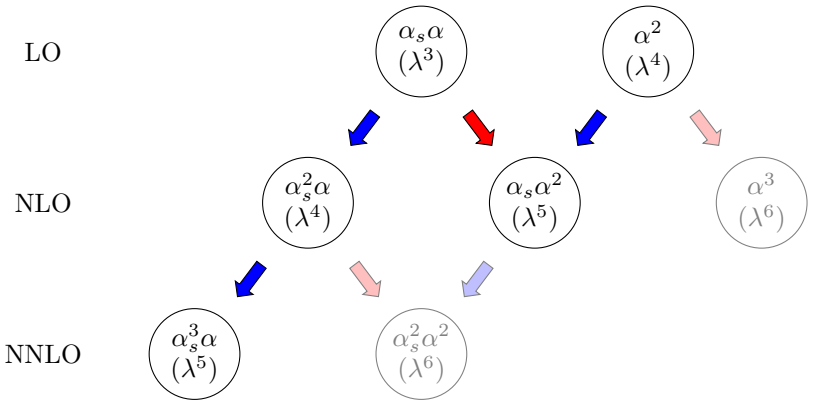


Figure 13.2.: Structure of the QCD and EW corrections to inclusive photon production. The $\lambda$s show the estimated size of the correction following the comparison of the numerical size of the coupling constants.

matrix element of either class. To ensure cancellation of IR singularities within one category the only way to make a reasonable distinction is through their respective initial states. In addition there are contributions which do not exhibit any IR divergent behaviour, be it because they are regulated by internal masses or because they are genuine interferences which only appear at the NLO EW level and for which no corresponding reduced matrix elements exist. In the following we will therefore distinguish between four different parts, which we will discuss in more detail later on:

- QCD initial states with two final state photons or QED loops. Those channels have both QCD-like and QED-like IR limits, thus they factorise either on the leading or subleading Born matrix elements. In the following we will call them *QED channels*.

- QCD initial states with one final state photon and genuine weak loops. Those channels are IR finite because they are regulated by the mass of the weak gauge bosons. In the following those will be called the *weak channels*.

- One-photon induced channels (one photon crossed into the initial state) with radiative QCD corrections, both real and virtual. The IR structure of those channels is exclusively QCD-like; they will all factor onto the subleading Born, the photon induced $\overset{(-)}{q}\gamma \to \overset{(-)}{q}\gamma$ to be precise.

- New $4q1\gamma$ interference channels, where in one diagram the quark lines are connected by a gluon and in the other by an EW gauge boson. Much like the C- and D-type matrix elements we encountered in the pure QCD corrections (see section 6.1.2), they appear first in the NLO real corrections. As we already discussed at the end of section 10.3 those channels are IR finite (if the single photon is required to remain resolved).

In principle there are also subleading NLO EW corrections of $\mathcal{O}(\alpha^3)$, but they are much suppressed compared to the other corrections, which is why will not include them in our calculation. Following the simple estimate based on the relative size of the couplings, they should be of the same size as the $\mathcal{O}(\alpha_s^2\alpha^2)$ corrections (both $\lambda^6$), which we consider as (NLO QCD)×(NLO EW), i.e. beyond the scope of simple NLO EW. We will still present a brief discussion about the channels contributing to $\mathcal{O}(\alpha^3)$ in section 13.1.5.

### 13.1.1. QCD initial states: QED channels

The pure QCD initial states we encounter at $\mathcal{O}(\alpha_s\alpha^2)$ are either $q\bar{q}$ annihilation or (anti-)quark-gluon scattering. For both classes of channels we will have two photons in the final state, accompanied by either a gluon (figure 13.3a) or a (anti-)quark (figure 13.3d), respectively:

- $q\bar{q} \to g\gamma\gamma$
- $\overset{(-)}{q}g \to \overset{(-)}{q}\gamma\gamma$

Unlike the real corrections we had for diphoton production we now encounter both QCD and QED IR limits, factoring either onto the subleading $\mathcal{O}(\alpha^2)$ or the $\mathcal{O}(\alpha_s\alpha)$ QCD Born. In the $q\bar{q}$ channel the QED like IR limits consist of one of the final state photons becoming unresolved, yielding a $q\bar{q} \to g\gamma$ reduced state. We can construct photonic real and virtual subtraction terms which, except for the reduced matrix element and the symmetry factors, will be identical to the ones defined in section 12.1.1 for the $q\bar{q} \to \gamma\gamma(\gamma)$ channels. This can be understood readily, as a single gluon must behave in an abelian fashion, so when it comes to the IR structure $q\bar{q} \to g\gamma(\gamma)$ and $q\bar{q} \to \gamma\gamma(\gamma)$ can be regarded as equivalent channels. While the soft limit will, after integration over the unresolved phase-space, cancel the explicit $\epsilon$ poles of the QED virtual corrections to $q\bar{q} \to g\gamma$ (figure 13.3c), the initial-final $\overset{(-)}{q}||\gamma$ limits is absorbed into the appropriate mass factorisation term. Instead of the photon also the gluon can become unresolved. From the above argument about the abelian behaviour of the gluon it follows that for those QCD like limits exactly the same subtraction terms can be used, provided one drops the quark charge factor, adjusts the symmetry factors and puts in the correct reduced matrix element, which in this case is the diphoton channel $q\bar{q} \to \gamma\gamma$. The soft gluon limit will cancel against the poles in the virtual QCD corrections to this channel (figure 13.3b), while the initial-final $\overset{(-)}{q}||g$ limits will again be absorbed into the mass factorisation.

If instead the gluon is crossed into the initial state ($\overset{(-)}{q}g \to \overset{(-)}{q}\gamma\gamma$), the only QCD like IR limit we can have is the final state (anti-)quark becoming collinear to the gluon. This limit will factor onto the diphoton channel due to its species changing properties, and will cancel against the appropriate part of the mass factorisation. Up to symmetry factors and the quark charge factor the corresponding subtraction terms are identical to the ones derived for the photon-induced diphoton channels in section 12.1.3.

As for the QED like limits, here we can have one of the photons becoming soft or collinear to either the final or initial state (anti-)quark. In all cases the reduced matrix element will be the QCD Born $\overset{(-)}{q}g \to \overset{(-)}{q}\gamma$. In the soft and final-final collinear limit the singularities cancel the poles of the virtual QED corrections to that channel (figure 13.3e). The initial state collinear

| channel | limit | type of limit | reduced ME | corresponding V |
|---|---|---|---|---|
| $q\bar{q} \to g\gamma\gamma$ | soft $\gamma$ | QED | $q\bar{q} \to g\gamma$ | $q\bar{q} \to g\gamma$ + virtual $\gamma$ |
| $q\bar{q} \to g\gamma\gamma$ | IF $\overset{(-)}{q}\|\|\gamma$ | QED | $q\bar{q} \to g\gamma$ | MF |
| $q\bar{q} \to g\gamma\gamma$ | soft $g$ | QCD | $q\bar{q} \to \gamma\gamma$ | $q\bar{q} \to \gamma\gamma$ + virtual $g$ |
| $q\bar{q} \to g\gamma\gamma$ | IF $\overset{(-)}{q}\|\|g$ | QCD | $q\bar{q} \to \gamma\gamma$ | MF |
| $\overset{(-)}{q}g \to \overset{(-)}{q}\gamma\gamma$ | soft $\gamma$ | QED | $\overset{(-)}{q}g \to \overset{(-)}{q}\gamma$ | $\overset{(-)}{q}g \to \overset{(-)}{q}\gamma$ + virtual $\gamma$ |
| $\overset{(-)}{q}g \to \overset{(-)}{q}\gamma\gamma$ | FF $\overset{(-)}{q}\|\|\gamma$ | QED | $\overset{(-)}{q}g \to \overset{(-)}{q}\gamma$ | $\overset{(-)}{q}g \to \overset{(-)}{q}\gamma$ + virtual $\gamma$ |
| $\overset{(-)}{q}g \to \overset{(-)}{q}\gamma\gamma$ | IF $\overset{(-)}{q}\|\|\gamma$ | QED | $\overset{(-)}{q}g \to \overset{(-)}{q}\gamma$ | MF |
| $\overset{(-)}{q}g \to \overset{(-)}{q}\gamma\gamma$ | IF $g\|\|\overset{(-)}{q}$ | QCD | $q\bar{q} \to \gamma\gamma$ | MF |

Table 13.1.: IR limits of the QCD initial state channels, their type (QED or QCD) and the corresponding reduced matrix elements. After integration over the unresolved phase-space the singularities cancel against the explicit $\epsilon$ poles of the virtual corrections given in the last column, or in case of the initial-final collinear singularities against the mass factorisation (MF) terms.

singularity is cancelled by the mass factorisation again. The corresponding subtraction terms utilize an initial-final $A_3^0$ antenna, which can take care of all three limits of the photon. For an initial state quark we find (see eq. (10.8))

$$\mathrm{d}\hat{\sigma}_{qg}^{S,IF,\gamma} = \mathcal{N}^R \sum_i \mathrm{d}\Phi_3 \frac{1}{S_3} \times Q_q^2 A_3^0(1_q, \gamma_i, q) B_{1g}^{0,\gamma}(\bar{1}_q, 2_g, \tilde{q}, \gamma) J_2^{(0)} \,. \tag{13.1}$$

The sum runs over the two final state photons, and the jet function is still trivial as we do not require any jet. The subtraction term for the configuration with an initial state anti-quark can readily obtained from above expression by interchanging $\bar{1}_q \to \tilde{\bar{q}}$ and $\tilde{q} \to \bar{1}_{\bar{q}}$ in the reduced matrix element and $1_q \to 1_{\bar{q}}$, $q \to \bar{q}$ in the antenna. The corresponding virtual subtraction term reads (see eq. (10.9))

$$\mathrm{d}\hat{\sigma}_{qg}^{T,IF,\gamma} = -\mathcal{N}^V \int \frac{\mathrm{d}x}{x} \mathrm{d}\Phi_2 \frac{1}{S_2} \times Q_q^2 \mathbf{J}_2^{(1)}(\bar{1}_q, \tilde{q}; x) B_{1g}^{0,\gamma}(\bar{1}_q, 2_g, \tilde{q}, \gamma) J_2^{(0)} \,, \tag{13.2}$$

with the identity preserving integrated dipole (see eq. (10.13))

$$\mathbf{J}_2^{(1)}(\bar{1}_q, \tilde{q}; x) = \mathcal{A}_3^{0,IF}(s_{\bar{1}\tilde{q}}; x) - \Gamma_{qq}^1(x) \,. \tag{13.3}$$

In table 13.1 we summarise the limits for the individual channels, onto what reduced matrix element they factor and which poles they cancel at the virtual level.

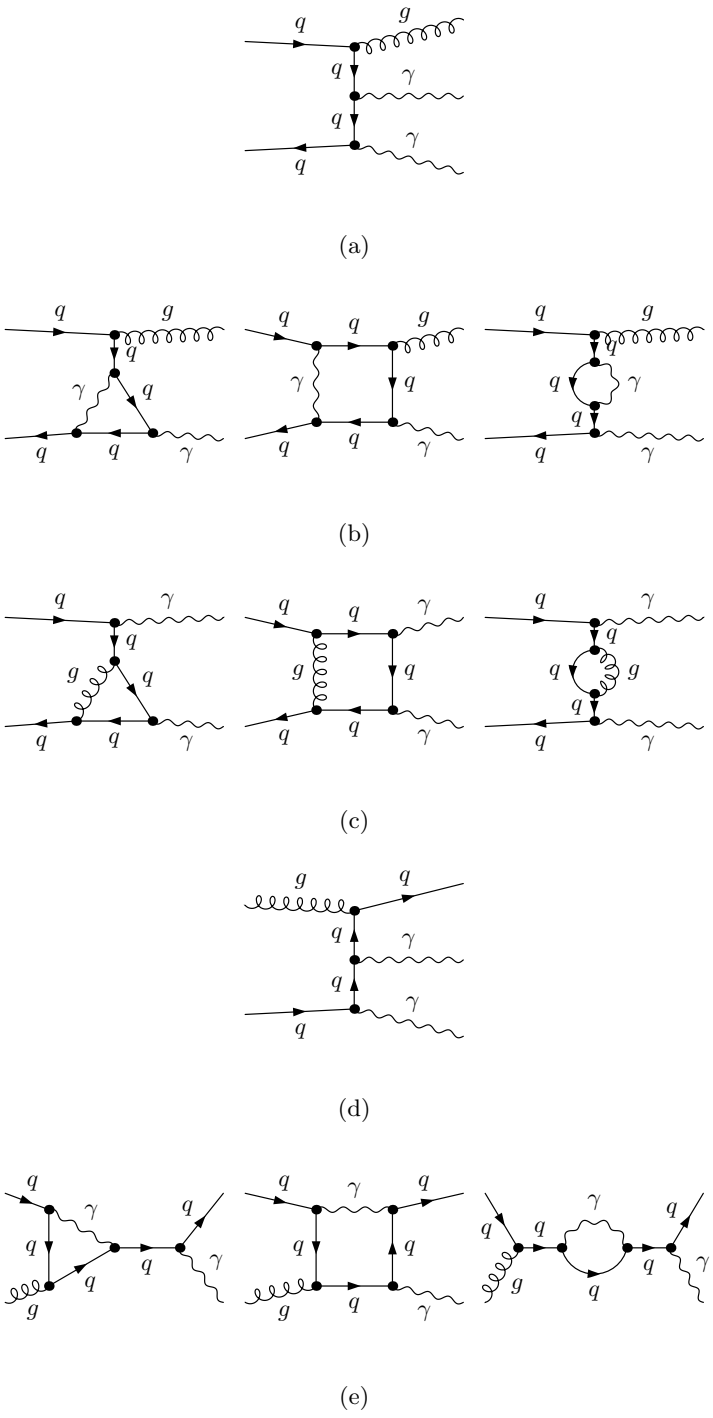


Figure 13.3.: Example diagrams of the $\mathcal{O}(\alpha_s\alpha^2)$ QCD induced, QED correction channels. The IR limits of (a) are partially compensated by the explicit poles of the virtual corrections in (b) and (c), depending on whether a photon or the gluon becomes unresolved, respectively. This also determines onto which Born the limit factors. As usual initial state collinear configurations are taken care of by the mass factorisation. The equivalent interplay takes place between diagrams (d) and (e).

### 13.1.2. QCD initial states: weak channels

Like for diphoton production we do not have any channels with final state weak gauge bosons and all the loop diagrams will be finite due to the gauge boson masses and again there will be no contributions from closed fermion triangles, this time because of colour conservation: At $\mathcal{O}(\alpha_s\alpha^2)$ the only way to draw a diagram with a fermion triangle is, when it internally is attached to an $Z$ and externally to exactly one photon and one gluon. The channels we have to consider are

- $q\bar{q} \to g\gamma$ + virtual $Z, W^\pm$
- $\overset{(-)}{q} g \to \overset{(-)}{q}\gamma$ + virtual $Z, W^\pm$

The corresponding one-loop diagrams (figures 13.4a, 13.4b) are essentially equivalent to those we had in the QED type virtual corrections (figures 13.3c,13.3e), neglecting for once the flavour changing nature of the $W^\pm$. The only genuinely new diagrams (figures 13.4c) come from the $\gamma WW$ triple gauge coupling. Note that it is also the aforementioned quark-$W$ coupling which introduces a dependence on the top mass, just like for the diphoton matrix elements, see section 12.1.2.

### 13.1.3. Photon induced channel

Having one photon crossed into the initial state, only one final state photon remains at the given order in $\alpha$. The second initial state particle can either be a gluon (figure 13.5a) or a (anti-)quark (figure 13.5b), so that we again find two classes for the real corrections:

- $\overset{(-)}{q}\gamma \to \overset{(-)}{q} g\gamma$
- $g\gamma \to q\bar{q}\gamma$

At $\mathcal{O}(\alpha_s\alpha^2)$ there are no $g\gamma$-induced one-loop diagrams, neither QCD like nor QED like. Consequently IR limits of the corresponding real channels must be absorbed into the mass factorisation contribution. And indeed, the only two limits we find are initial-final collinear singularities where one of the final state (anti-)quarks becomes collinear to either the initial state gluon (QCD limit) or the initial state photon (QED limit). The reduced matrix elements are either $\overset{(-)}{q}\gamma \to \overset{(-)}{q}\gamma$ or $g\overset{(-)}{q} \to \overset{(-)}{q}\gamma$. Since the single gluon behaves in an abelian fashion, both the QED and QCD limit are subtracted in the same way, provided one uses the appropriate symmetry and quark charge factors and reduced matrix element. The subtraction term can be constructed either by utilizing an initial-initial $A_3^0$ antenna, analogous to what we did in the photon induced channels in diphoton production 12.1.3, or with an initial final antenna, in which case the real subtraction term for limits involving the initial state photon reads

$$\mathrm{d}\hat{\sigma}^{S,IF,\gamma}_{g\gamma} = \mathcal{N}^R \mathrm{d}\Phi_3 \frac{1}{S_3} \times Q_q^2 A^0_{3,\gamma\to q}(\bar{q}, 1_\gamma, q) B^{0,\gamma}_{1g}(\bar{1}_q, 2_g, \tilde{q}, \gamma) J^{(0)}_2 + (q \leftrightarrow \bar{q})\,, \tag{13.4}$$

where the swap $(q \leftrightarrow \bar{q})$ ensures that both the $q||\gamma$ and $\bar{q}||\gamma$ limit are accounted for. The gluonic subtraction term is readily obtained by dropping the quark charge factor and by replacing the reduced matrix element, $B^{0,\gamma}_{1g} \to B^{0,2\gamma}_{0g}$.

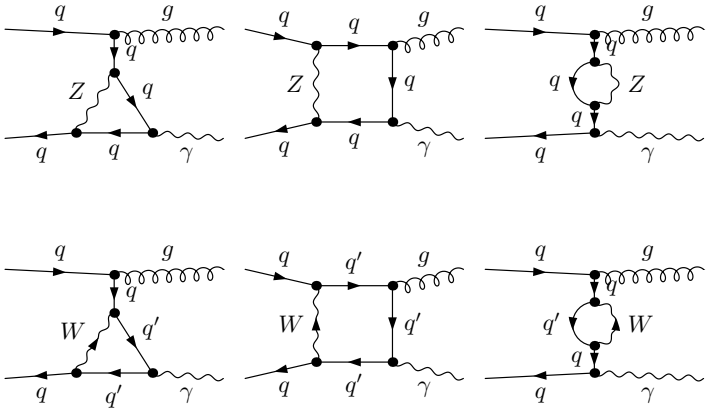


(a)

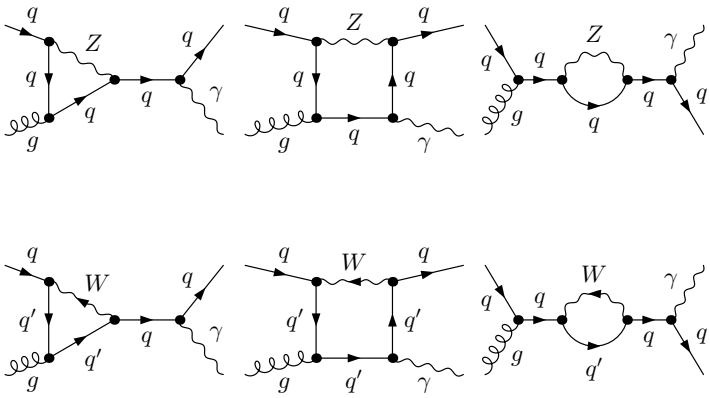


(b)

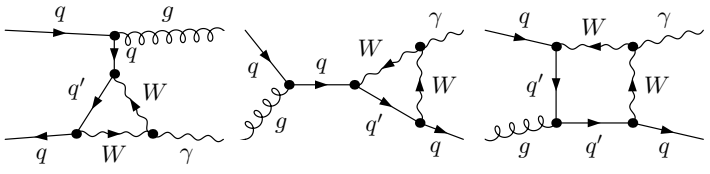


(c)

Figure 13.4.: Example diagrams of the $\mathcal{O}(\alpha_s\alpha^2)$ QCD induced, weak correction channels. The mass of the weak gauge bosons regulates the IR singularities of the loop diagrams.

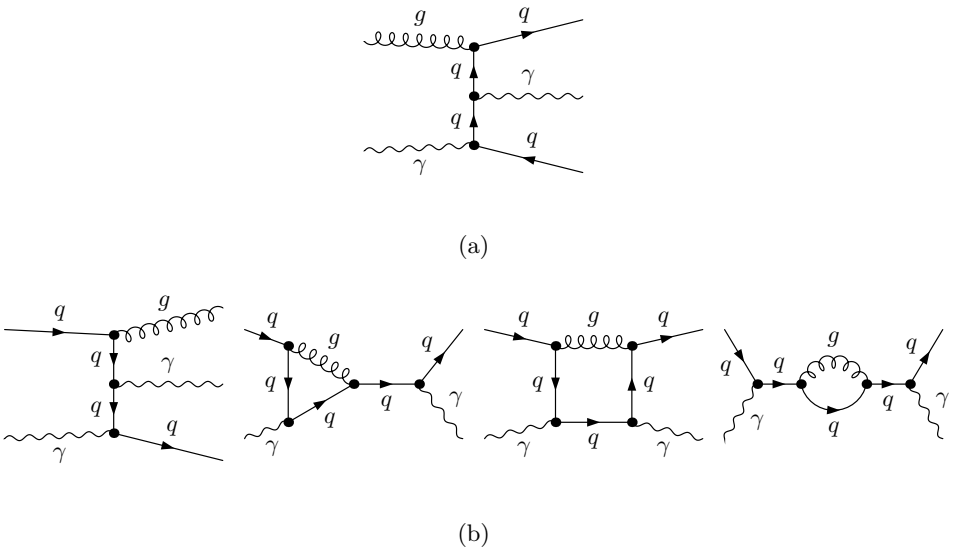


(a)

(b)

Figure 13.5.: Example diagrams of the $\mathcal{O}(\alpha_s\alpha^2)$ one-photon induced channels. In the IR limits they all factor onto the photon induced Born, figure 13.1b. The $g\gamma$-induced diagram (a) only has initial-final collinear singularities which are absorbed into the mass factorisation term. The final state IR QCD singularities of the $q\gamma$-induced real correction diagram ((b) left) are compensated by the explicit poles in the virtual corrections.

For the (photonic) virtual subtraction term we find

$$\mathrm{d}\hat{\sigma}^{T,IF,\gamma}_{g\gamma} = -\mathcal{N}^V \int \frac{\mathrm{d}x}{x}\mathrm{d}\Phi_2 \frac{1}{S_2} \times Q_q^2 \mathbf{J}^{(1)}_{2,\gamma\to q}(\bar{1}_q, \tilde{q}; x) B^{0,\gamma}_{1g}(\bar{1}_q, 2_g, \tilde{q}, \gamma) J^{(0)}_2 + (q \leftrightarrow \bar{q})\,, \tag{13.5}$$

with the identity changing integrated dipole

$$\mathbf{J}^{(1)}_{2,\gamma\to q}(\bar{1}_q, \tilde{q}; x) = \mathcal{A}^{0,IF}_{3,q\to g}(s_{\bar{1}\tilde{q}}) - \Gamma^1_{qg}(x)\,. \tag{13.6}$$

The gluonic virtual subtraction term is again directly related as explained above.

For the $\overset{(-)}{q}\gamma$-induced channels the situation is different, as now the final state gluon can participate in all kinds of QCD unresolved limits, which in this case include its soft limit and it becoming collinear to a final state (anti-)quark. In both cases the reduced state will be the photon induced subleading Born, $\overset{(-)}{q}\gamma \to \overset{(-)}{q}\gamma$. The singularities will be cancelled by the explicit poles of the virtual QCD corrections to that channel (see e.g. the one-loop diagrams in figure 13.5b). The QCD limit with the gluon becoming collinear to an initial state (anti-)quark is absorbed into the appropriate mass factorisation again. The QCD limits have subtraction terms equivalent to the ones we constructed for the QED limits in the $qg$-initiated channels in section 13.1.1 (eqs. (13.1), (13.2), (13.3)), provided we drop the quark charge factor and interchange the initial state gluon with one of the photons.

The only QED limit we have for the $\overset{(-)}{q}\gamma$-induced channels is the final state (anti-)quark becoming collinear to the initial state photon, which factors onto the $q\bar{q} \to g\gamma$ Born. The

| channel | limit | type of limit | reduced ME | corresponding V |
|---|---|---|---|---|
| $\overset{(-)}{q}\gamma \to \overset{(-)}{q}g\gamma$ | IF $\gamma \Vert \overset{(-)}{q}$ | QED | $q\bar{q} \to g\gamma$ | MF |
| $\overset{(-)}{q}\gamma \to \overset{(-)}{q}g\gamma$ | soft $g$ | QCD | $\overset{(-)}{q}\gamma \to \overset{(-)}{q}\gamma$ | $\overset{(-)}{q}\gamma \to \overset{(-)}{q}\gamma$ + virtual $g$ |
| $\overset{(-)}{q}\gamma \to \overset{(-)}{q}g\gamma$ | FF $\overset{(-)}{q} \Vert g$ | QCD | $\overset{(-)}{q}\gamma \to \overset{(-)}{q}\gamma$ | $\overset{(-)}{q}\gamma \to \overset{(-)}{q}\gamma$ + virtual $g$ |
| $\overset{(-)}{q}\gamma \to \overset{(-)}{q}g\gamma$ | IF $\overset{(-)}{q} \Vert g$ | QCD | $\overset{(-)}{q}\gamma \to \overset{(-)}{q}\gamma$ | MF |
| $g\gamma \to q\bar{q}\gamma$ | IF $\gamma \Vert \overset{(-)}{q}$ | QED | $g\overset{(-)}{q} \to \overset{(-)}{q}\gamma$ | MF |
| $g\gamma \to q\bar{q}\gamma$ | IF $g \Vert \overset{(-)}{q}$ | QCD | $\overset{(-)}{q}\gamma \to \overset{(-)}{q}\gamma$ | MF |

Table 13.2.: IR limits of the photon induced channels, their type (QED or QCD) and the corresponding reduced matrix elements. After integration over the unresolved phase-space the singularities cancel against the explicit $\epsilon$ poles of the virtual corrections given in the last column, or in case of the initial-final collinear singularities against the mass factorisation (MF) terms.

singularity is absorbed into the mass factorisation. The subtraction terms are just like in the photon induced channels in diphoton production (section 12.1.3), with the corresponding changes to the symmetry factors and to the reduced matrix element.

Table 13.2 summarises all the limits, together with the reduced state onto which they factor and their correspondence at the virtual level.

### 13.1.4. The D-type interference channels

At the $\mathcal{O}(\alpha_s\alpha^2)$ level we also encounter interferences between QCD-like and EW-like $4q1\gamma$ diagrams, because the two quark lines can be connected by either a gluon or a EW gauge boson, resulting in a $\mathcal{O}(\alpha_s\alpha^{1/2})$ or $\mathcal{O}(\alpha^{3/2})$ digram, respectively. Figures 13.6 and 13.7 show some example interferences.

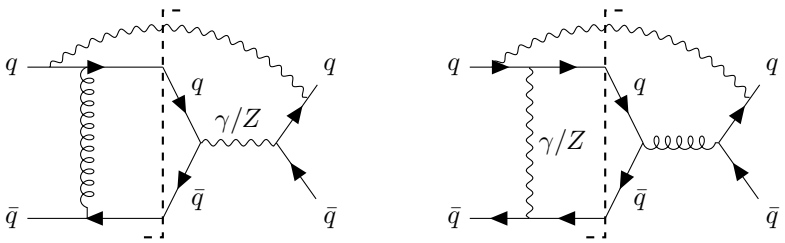


Figure 13.6.: NC $4q$ interference diagrams

Because of colour we are restricted to interferences which mix $s, t$ and $u$ channels. Those correspond to D-type matrix elements when using the terminology introduced in section 6.1.2. Schematically we can write, making the colour coefficients $c_{ij}$ explicit,

$$c_{q\bar{q}}c_{Q\bar{Q}}\mathcal{A}_C - c_{q\bar{Q}}c_{Q\bar{q}}\mathcal{A}_C \tag{13.7}$$

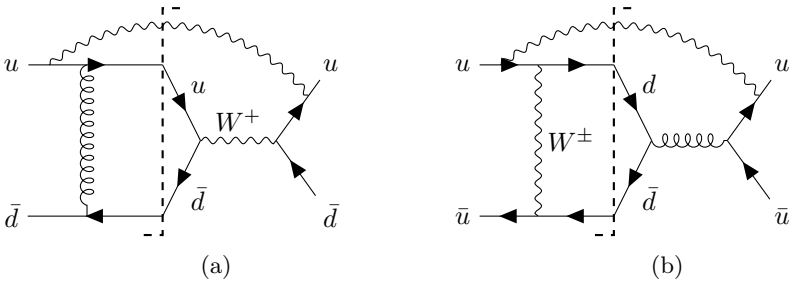


Figure 13.7.: CC $4q$ interference diagrams

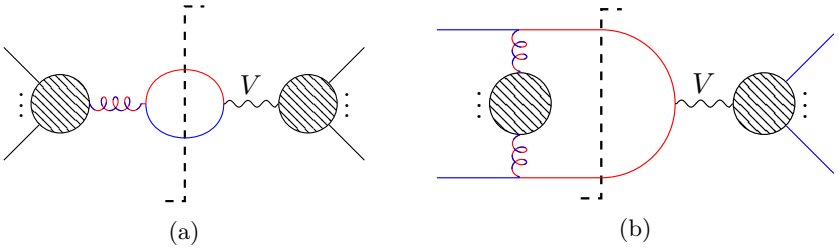


Figure 13.8.: The schematic colour flow in the C-type (a) and D-type (b) QCD×EW $4q$ interferences ($V = \gamma, Z, W^{\pm}$). In Diagram (a) colour conservation is violated, hence it vanishes.

for the amplitude anti-symmetrised over the anti-quark pair. $\mathcal{A}_C$ represents the C-type $2q2Q1\gamma$ amplitude. Here the colour coefficients are given by

$$c_{ij} = \begin{cases} \delta_{ij}\,, & \text{colourless mediator} \\ T^a_{ij}\,, & \text{coloured mediator} \end{cases}\,. \tag{13.8}$$

Interfering the QCD with the EW amplitude we get

$$\left(\delta_{q\bar{q}}\delta_{Q\bar{Q}}\right)\left(T^a_{\bar{Q}Q}T^a_{\bar{q}q}\right) = \left(\mathrm{Tr}[T^a]\right)^2 = 0 \tag{13.9}$$

for the C-type part, and

$$\left(\delta_{q\bar{q}}\delta_{Q\bar{Q}}\right)\left(T^a_{\bar{q}Q}T^a_{\bar{Q}q}\right) = \mathrm{Tr}[T^aT^a] = NC_F\,, \tag{13.10}$$

For the D-type interference part. The colour flow in C-type and D-type amplitudes is illustrated in figure 13.8.

Other than in QCD the EW D-types do not necessarily have identical quark flavours. We now have to distinguish between neutral current (NC) mediators ($\gamma, Z$), see figure 13.6, and charged current (CC) mediators ($W^{\pm}$), see figure 13.7. For the latter we always have two external up-type quarks (of the same generation) and two external down-type quarks (of the same generation), however, not all possible combinations will occur, since the QCD-diagram participating in the interference preserves flavour. Precisely which combinations we have to consider and how those depend on the CKM factors will be relevant for the convolution with the PDFs, see section 11.1.

As we can deduce from the discussion at the end of section 10.3 the only IR singular limits of those interference channels are related to the photon becoming unresolved. But since we explicitly require a final state photon, the contribution from the $4q$ channels to inclusive photon production is entirely IR finite.

### 13.1.5. Subleading corrections

Part of the subleading $\mathcal{O}(\alpha^3)$ corrections we already discussed in the context of the NLO EW corrections to diphoton production. In particular those are:

- Radiative QED corrections to $q\bar{q} \to \gamma\gamma$, with all the IR limits discussed in section 12.1.1.
- Radiative weak (virtual) corrections to $q\bar{q} \to \gamma\gamma$. Like for the diphoton case those channels are finite.
- The photon induced channel $\overset{(-)}{q}\gamma \to \overset{(-)}{q}\gamma\gamma$, but now there is a corresponding $\overset{(-)}{q}\gamma \to \overset{(-)}{q}\gamma$ QED loop amplitude (and its finite weak counterpart). Its poles will cancel the singularities related to one of the final state real photons becoming soft or collinear to the final state (anti-)quark, a limit which was not present in the diphoton case.

Genuine new crossings we encounter at this level are:

- The double-photon induced channel $\gamma\gamma \to q\bar{q}\gamma$ at the real level, which is very much suppressed due to its convolution with two photon PDFs. Since the single FS photon must be resolved, its only singular IR limits are those with one of the quarks going collinear to an IS photon, which is cancelled by the appropriate mass factorisation terms. There is no corresponding double-photon induced 1-loop amplitude.
- $4q$-channels, based on the electroweak gauge boson exchange diagrams we already encountered in section 13.1.4. But now they come in the form of genuine squared amplitudes. The ones with $Z$ or $W^{\pm}$ as mediators between the quark lines are finite, but the QED type matrix elements show an IR singularity structure much like the NLO QCD real correction C-type amplitudes (see section 6.1.2). The relevant limits are the $\gamma \to q\bar{q}$ splittings we already discussed in section 10.3. In fully inclusive processes without any final state jets they cancel against the poles of bubble diagrams on external photon propagators[1].

## 13.2. Implementation and Validation

The EW corrections to inclusive photon production have been implemented as the independent process `G_EW`. Its corresponding `.map` file for the generation of the process has been discussed in detail as an example in section 11.2. The subleading Born and its associated QCD corrections, both real and virtual, are based on matrix elements already implemented in analytic form for the QCD diphoton process, namely $B_{0g}^{0,2\gamma}$ (LO), $B_{1g}^{0,2\gamma}$ (R) and $B_{0g}^{1,2\gamma}$ (V). We use OpenLoops2 for the genuine electroweak one-loop amplitudes and for the $4q1\gamma$ interference channels. The

[1] If we require a final state jet, this statement no longer holds and we need to introduce the so-called photon-to-jet conversion function in order to absorb the infrared singularities associated to the splitting [232].

subtraction terms can be constructed completely out of already existing elements, as in the IR limits the NLO EW corrections factor either onto diphoton or photon-plus-jet matrix elements, which are available in analytic form. The `driver` bridge files are still trivial, i.e. no extra colour factors or combinations of subtraction terms are required, because the NLO EW matrix element only have a single colour level.

### 13.2.1. Internal checks

We performed the usual consistency checks for our implementation; the validity of the real subtraction terms was checked by performing the spike tests for all occurring limits. The cancellation of the poles between the integrated subtraction terms and the virtual matrix elements has been checked for several independent phase-space points.

### 13.2.2. Validation: setup

We validate the implementation of the EW corrections against MATRIX [186] again. As the EW corrections to inclusive photon production are not part of the public MATRIX code, we collaborated with one of the authors [226], in order to compare our results to those obtained with their code. We should remark that the validation is not yet fully completed, as we still observe a small discrepancy in certain channels. We will comment on this below. For the setup we choose a simplified version of that used for the 13 TeV inclusive photon study performed in section 8.1.2, based on the ATLAS measurement [22]. Photons are selected after they passed the smooth cone isolation criterion with parameters[2]

$$R = 0.4\,, \qquad \varepsilon_d = 0.1\,, \qquad n = 2\,. \tag{13.11}$$

For simplicity we do not apply any combination of photons close to each other. They are subject to the following cuts on their transverse momentum and rapidity:

$$p_T^\gamma \geq 125 \text{ GeV}\,, \qquad |y^\gamma| \in [0, 2.37)\,, \tag{13.12}$$

which are imposed as part of the photon selection, i.e. for inclusive photon production only one photon needs to pass for the event to be accepted. If multiple photons are present, the one highest in $p_T$ will be regarded as the leading photon.

We use the NNPDF3.1luxQED [218] PDF set and fix both the renormalisation scale $\mu_R$ and factorisation scale $\mu_F$ at 100 GeV, and do not perform any scale variations. We pick our default EW scheme, the $G_\mu$ scheme, with the coupling of the QCD Born photon set to $\alpha(0)$. The corresponding input is given in table 13.3, together with the input values for the masses of the weak gauge bosons $Z, W^\pm$. For the validation all other particles including the top-quark are

[2] Using the default form of the profile again:

$$E_{T,\text{dyn}}^{\max}(p_T^\gamma; r) = \varepsilon_d p_T^\gamma \left(\frac{1-\cos r}{1-\cos R}\right)^n$$

considered massless. On-shell masses are internally converted into the pole scheme according to the conversion formulae (2.45).

| physics input | | | |
|---|---|---|---|
| quantity | value | input | derived quantities |
| $\sqrt{s}$ | 13000 GeV | ✓ | |
| $m_Z^{\text{os}}$ | 91.1876 GeV | ✓ | $m_Z^{\text{pole}} \approx 91.1535$ GeV |
| $\Gamma_Z^{\text{os}}$ | 2.4952 GeV | ✓ | $\Gamma_Z^{\text{pole}} \approx 2.4943$ GeV |
| $m_W^{\text{os}}$ | 80.379 GeV | ✓ | $m_W^{\text{pole}} \approx 80.352$ GeV |
| $\Gamma_W^{\text{os}}$ | 2.084 GeV | ✓ | $\Gamma_W^{\text{pole}} \approx 2.084$ GeV |
| schemes | | | |
| Mass scheme | CMS | | |
| EW scheme | $G_\mu$ | | $\sin^2\theta_w \approx 0.22298 - 0.00111i$ |
| $1/\alpha(0)$ | 137.035999139 | ✓ | |
| $G_\mu$ | $1.1663787 \cdot 10^{-5}$ | ✓ | $1/\alpha\|_{G_\mu} \approx 132.244$ |

Table 13.3.: Technical parameters and input values for the validation run. The masses and widths correspond to the 2018 PDG [225] values used as default in NNLOJET. In the rightmost column we also present some related quantities derived from the input values.

### 13.2.3. Validation: results

We compare the NNLOJET and MATRIX numbers at the level of the total cross section. The contributions are separated according to the classification of channels we made above, only the QED channels and the weak channels had to be combined as they cannot be assessed individually when using OpenLoops2 amplitudes. We call their combination the QCD induced channels. Contrary to what this name might suggest, the $4q1\gamma$ interference channels are kept separate. As an additional check for the setup of the validation we also compared the QCD Born and the NLO QCD coefficient. The results are summarised in table 13.4.

| contribution | $\sigma_{\text{NNLOJET}}$[fb] | $\sigma_{\text{MATRIX}}$[fb] | $\frac{\sigma_{\text{MATRIX}}}{\sigma_{\text{NNLOJET}}} - 1$ | deviation (st-dev.) |
|---|---|---|---|---|
| LO QCD | 224266(83) | 224273(11) | $3.1 \cdot 10^{-5}$ | +0.1 |
| NLO QCD coeff | 182013(90) | 182005(18) | $-4.3 \cdot 10^{-5}$ | −0.1 |
| LO EW | 531.448(18) | 531.536(19) | $1.7 \cdot 10^{-4}$ | +3.3 |
| LO EW $\gamma$-ind | 222.083(10) | 222.126(11) | $1.9 \cdot 10^{-4}$ | +2.8 |
| LO EW $q\bar{q}$ | 309.365(15) | 309.410(15) | $1.5 \cdot 10^{-4}$ | +2.1 |
| NLO EW coeff | −2074.63(20) | −2120.97(20) | $2.2 \cdot 10^{-2}$ | −165 |
| NLO EW $\gamma$-ind. | 35.284(5) | 35.267(4) | $-4.9 \cdot 10^{-4}$ | −2.8 |
| NLO EW QCD-ind. | −2579.04(16) | −2625.33(19) | $1.8 \cdot 10^{-2}$ | −185 |
| NLO EW $4q1\gamma$ | 469.13(12) | 469.09(5) | $-8.7 \cdot 10^{-5}$ | −0.3 |

Table 13.4.: Validation against MATRIX: total cross section. The NLO EW numbers are the coefficients, i.e. without Born contributions. The QCD-induced channels contain both the QED-channels and the weak channels as introduced above. A discrepancy persists in the QCD-induced channels, the origin of which is currently investigated.

We find that the QCD results agree to very high precision, as expected. The EW contributions, however, exhibit some discrepancies between MATRIX and NNLOJET. The subleading Born

agrees only within $3.3\sigma$, which is not satisfactory and also unexpected, given that it is in large parts identical to the QCD Born of diphoton production, for which we found very good agreement in the previous chapter, see table 12.2. Given that the relative size of the deviation is clearly sub-per mille, it might actually be due to some technical differences in the two codes. The numerical impact is negligible by all means. A more serious deviation appears in the NLO EW coefficient, more precisely in the QCD induced channels, with $-185\sigma$, corresponding to 1.8%. Since the QCD channels turn out to be the dominant contribution to the NLO EW coefficient, this large discrepancy is directly passed on. A further decomposition in partonic sub-channels showed that the origin must lie within the $\overset{(-)}{q}g$-induced channels. We are currently investigating the issue. The root of all this must clearly be located before we can use our implementation to perform any fully reliable phenomenology studies. We can try to estimate the error we have to put up with, if we nonetheless make some first runs just to get an idea of the impact of the EW corrections.

We are looking at a $\mathcal{O}(3\%)$ discrepancy in the full EW contributions, i.e. subleading Born plus NLO EW coefficient. Given that the full NLO QCD cross section is $\sim 250$ times larger, we are actually dealing with a $\mathcal{O}(0.01\%)$ deviation for the (NLO QCD)+(NLO EW) result, which is completely absorbed by the (still very small) uncertainties on the QCD contributions. Consequently we should be able to already make some qualitative statements about the behaviour we get from the EW corrections. We will therefore present some first runs in the next section, always keeping in mind that we cannot trust the result entirely. Especially in the tails of the distributions where the cross section is very low the deviation can in principle be much bigger, without affecting the total EW coefficient to much.

## 13.3. Phenomenology

### 13.3.1. Setup

We construct the calculation of the NLO EW corrections to inclusive photon production as a supplement to the 13 TeV study performed in section 8.1.2, which was based on the ATLAS analysis [22] using 3.2 fb$^{-1}$ of the LHC Run-II data set. In the meantime an updated measurement with the full 36.1 fb$^{-1}$ data has been published [24], using exactly the same setup but extending the range in the transverse momentum of the photon. The measurement is performed in four different regions in rapidity

$$|y^\gamma| < 0.6, \quad 0.6 < |y^\gamma| < 1.37, \quad 1.56 < |y^\gamma| < 1.81, \quad 1.81 < |y^\gamma| < 2.37\,, \tag{13.13}$$

and differentially in transverse momentum, with a lower cut off $p_T^\gamma > 125$ GeV. No further cuts are applied. For the calculation of the EW corrections we use the same hybrid isolation setup as for the NNLO QCD prediction, defined in eq. (7.3),

$$E_{T,\text{hyb}}^{\max}(p_T^\gamma; r; R_d) = \begin{cases} \min\left(E_{T,\text{fix}}^{\max}(p_T^\gamma), \varepsilon_d p_T^\gamma \left(\frac{1-\cos r}{1-\cos R}\right)^n\right), & (0 \le r < R_d) \\ E_{T,\text{fix}}^{\max}(p_T^\gamma)\,, & (R_d \le r < R) \end{cases}, \tag{13.14}$$

with

$$E_{T,\text{fix}}^{\max}(p_T^\gamma) = \varepsilon p_T^\gamma + E_T^{\text{thres}} \,. \tag{13.15}$$

The parameters are given by (compare eqs. (8.5))

$$\begin{aligned} R_d &= 0.1\,, & \varepsilon_d &= 0.1\,, & n &= 2\,, \\ R &= 0.4\,, & E_T^{\text{thres}} &= 4.8\text{ GeV}\,, & \varepsilon &= 0.0042\,, \end{aligned} \tag{13.16}$$

where the outer cone parameters $R, E_T^{\text{thres}}, \varepsilon$ match the experimental isolation, as usual. Photons with a mutual distance of $R < 0.1$ in the $\eta - \phi$ plane are clustered before being passed to the isolation algorithm. We furthermore impose the photon level cut

$$|y^\gamma| \in [0, 1.37) \cup (1.56, 2.37)\,. \tag{13.17}$$

Candidate photons with rapidity outside of that range are not considered as resolved, but the event is kept provided enough photons remain. The $p_T$ cut mentioned above is defined as a fiducial cut on the leading photon, that is the photon with the largest transverse momentum. It is also the leading photon we consider in the histograms.

We use the NNPDF3.1luxQED [218] PDF set and estimate the uncertainty of the prediction by means of a seven-point scale variation. The central sale is set to $\mu_R = \mu_F = p_T^\gamma$. Like for the diphoton calculations there is a slight inconsistency in the choice of the PDFs, as the QCD prediction used the standard NNPDF3.1 set. We again do not expect significant effects from this.

As per default the calculation is performed in the complex-mass-scheme and the $G_\mu$-scheme, using the input parameters summarized in table 13.5. The QCD Born photon therefore comes with its on-shell coupling $\alpha(0)$. The NNLO QCD corrections on the other hand have been calculated setting the value to $\alpha|_{G_\mu} = 1/132.232$[3]. This had been done in order to partly compensate the effect of missing EW corrections. Now that we explicitly calculate the EW corrections, we should set the value of all final state resolved photons to $\alpha(0)$. Only this way the two calculations are actually compatible. For the NNLO QCD cross sections this amounts to a rescaling of about $-3.5\%$,

$$\mathrm{d}\hat{\sigma}_{QCD}^{\alpha(0)} = \frac{\alpha(0)}{\alpha|_{G_\mu}} \mathrm{d}\hat{\sigma}_{QCD}^{\alpha|_{G_\mu}} = \frac{1/137.035999139}{1/132.232} \mathrm{d}\hat{\sigma}_{QCD}^{\alpha|_{G_\mu}} \approx 0.964944\, \mathrm{d}\hat{\sigma}_{QCD}^{\alpha|_{G_\mu}}\,. \tag{13.18}$$

In the following when we talk about the QCD numbers, we will implicitly mean the rescaled ones.

[3] Note that the value for $\alpha|_{G_\mu}$ slightly changes with the updated definition we use in the EW corrections, see table 13.5.

| physics input | | | |
|---|---|---|---|
| quantity | value | input | derived quantities |
| $m_Z^{\text{os}}$ | 91.1876 GeV | ✓ | $m_Z^{\text{pole}} \approx 91.1535$ GeV |
| $\Gamma_Z^{\text{os}}$ | 2.4952 GeV | ✓ | $\Gamma_Z^{\text{pole}} \approx 2.4943$ GeV |
| $m_W^{\text{os}}$ | 80.379 GeV | ✓ | $m_W^{\text{pole}} \approx 80.352$ GeV |
| $\Gamma_W^{\text{os}}$ | 2.085 GeV | ✓ | $\Gamma_W^{\text{pole}} \approx 2.084$ GeV |
| $m_t^{\text{pole}}$ | 172.76 GeV | ✓ | |
| $\Gamma_t^{\text{pole}}$ | 1.42 GeV | ✓ | |
| schemes | | | |
| Mass scheme | CMS | | |
| EW scheme | $G_\mu$ | | $\sin^2\theta_w \approx 0.22298 - 0.00111i$ |
| $1/\alpha(0)$ | 137.035999139 | ✓ | |
| $G_\mu$ | $1.1663787 \cdot 10^{-5}$ | ✓ | $1/\alpha\vert_{G_\mu} \approx 132.244$ |

Table 13.5.: Technical parameters and input values for the phenomenology study. The masses and widths correspond to the latest PDG [196] values. In the rightmost column we also present some related quantities derived from the input values.

### 13.3.2. Results

Integrating the differential cross section provided by ATLAS [24] we obtain a total cross section for the inclusive cross section of

$$\sigma_{\text{tot}} = 406.7^{+5.5}_{-5.6}\ \text{pb} = 406.7^{+1.4\%}_{-1.4\%}\ \text{pb}\,. \tag{13.19}$$

which we have to compare to the predictions at NNLO QCD and (NNLO QCD)+(NLO EW),

$$\sigma_{(\text{NNLO QCD})} = 377.5^{+2.6}_{-9.5}\ \text{pb} = 377.5^{+0.7\%}_{-2.5\%}\ \text{pb}\,, \tag{13.20a}$$

$$\sigma_{(\text{NNLO QCD})+(\text{NLO EW})} = 376.5^{+2.5}_{-9.3}\ \text{pb} = 376.5^{+0.7\%}_{-2.5\%}\ \text{pb}\,, \tag{13.20b}$$

where the cited uncertainties come from the scale variation. Given the percent level uncertainties of both the measurement and the theory predictions we see a significant deviation of $\sigma_{\text{tot}}/\sigma_{\text{theo}} - 1$ of $\sim 7.2\%$ and $7.4\%$ for the pure QCD and the combined result, respectively. We note that without the rescaling of the QCD prediction the result would lie within $2.5\sigma$ of the measurement and is now shifted away from that. Unfortunately the inclusion of the NLO EW corrections does not compensate this decrease. In fact at the level of the total cross section the EW corrections are, within the given uncertainty, insignificant.

However, this is not true for the differential distributions. In figure 13.9 we show the ratio of the subleading EW Born and the NLO EW coefficient to the full NNLO QCD result as a function in the photon transverse momentum in the four rapidity bins given in eqs. (13.13), for the central scale choice $\mu_R = \mu_F = p_T^\gamma$. We also show the individual contributions of the photon induced and the QCD induced partonic channels. At NLO the latter contain both the QED channels and the weak channels like introduced in section 13.1, as they are inseparable when using the OpenLoops2 matrix elements. The D-type $4q1\gamma$ interference channels are presented separately. The regions of very high transverse momentum highlighted in grey are subject to a rapid decrease in both the QCD and EW cross section due to very limited statistics. We

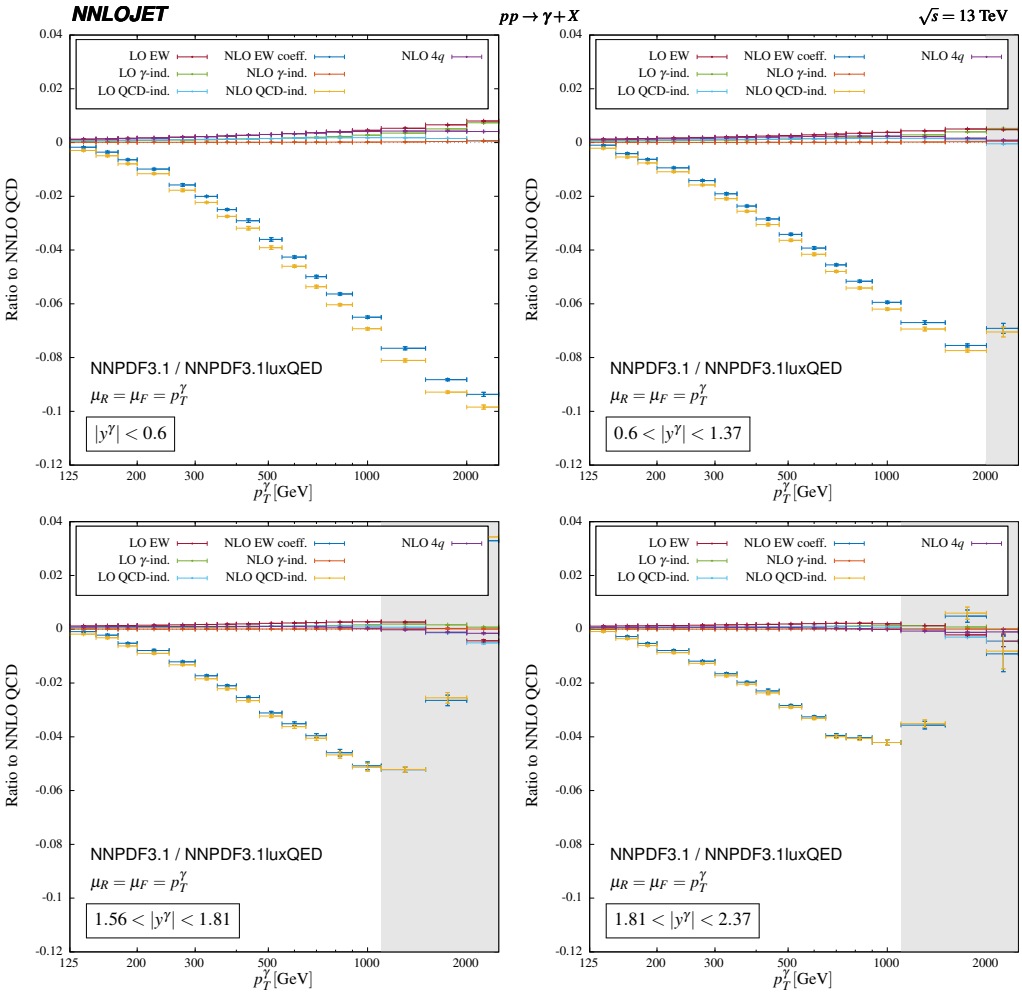


Figure 13.9.: Ratio of the subleading EW Born (LO EW, dark red) and the NLO EW coefficient (blue) to the full NNLO QCD predictions, for the same rapidity bins presented in figure 8.4 in section 8.1.2. We also show the individual contributions of the photon induced and the QCD induced partonic channels. The $4q1\gamma$ interferences are separated from the latter. We only show the central scales, with MC error, corresponding to prescription B in section 10.7. The bins highlighted in grey are subject to very low statistics and should be considered with care.

have seen effects of this when presenting the QCD results earlier in figure 8.4, where the scale uncertainty was drastically increased in those bins, in particular for the very forward rapidities. We conclude that more statistics is needed in this specific regions of the phase-space to make reliable statements about the corresponding cross section. We will therefore not consider them in the following discussion.

The first thing we observe for all four rapidity bins is that the negative contribution of the NLO QCD induced channels is dominating the corrections. All other contributions are consistently positive with an impact of well below 0.5%, except for the two last bins in the central rapidity region, where the subleading Born reaches up to $\sim 0.7\%$ and $\sim 0.8\%$, respectively, driven mainly by the photon induced channel. Numerically, however, the QCD induced NLO contribution is the only one which is relevant, in particular for the more forward rapidities. As we are considering a ratio, this does not mean that the other channels have a negligible contribution to the total cross section, too, as we in principle can already see from the validation run, see table 13.4. The point is that all but the QCD induced channels in their shape follow that of the NNLO QCD distribution. The QCD induced channels do not, with an enhancement of the their (negative) cross section in the high $p_T$. Hence the large effect in the ratio. Nonetheless is is true that the smallness of the photon PDF again suppresses the photon induced contributions (see in particular the NLO EW $\gamma$-ind. numbers in table 13.4).

The impact of the QCD induced channels increases with $p_T^\gamma$, from less than $-0.2\%$ just above threshold in the first $p_T^\gamma$ bin to approximately $-9.5\%/-7.5\%/-5\%/-4\%$ in the highest bin we consider in the first/second/third/fourth rapidity region. This is precisely the behaviour we expect form the Sudakov double logarithms [197] of the form $\alpha \log^2\left((p_T^\gamma)^2/m_i^2\right)$ with $m_i = m_W, m_Z$ present in the genuine weak virtual corrections to those channels. Their size has been estimated by means of a threshold resummation to next-to-next-to-leading logarithmic ($\mathrm{N^2LL}$) accuracy in [191], and in [192] the results have been presented in precisely the rapidity bins we are considering, however using a centre-of-mass energy of $\sqrt{s} = 8$ TeV. Unfortunately the explicit scales introduced in the calculation due to the masses of the weak gauge bosons and the top-quark prevent us from a straightforward rescaling of the cross sections to 13 TeV, but we can still make some qualitative statements. While we observe a concave shape[4] of the ratio in the low $p_T^\gamma$ bins, then changing to a convex form in the high $p_T^\gamma$, the resummation predicts an overall convex behaviour. The numerical difference, however, appears to be small, since both calculations predict basically no effect of the EW corrections close to the $p_T$ threshold and a negative $\mathcal{O}(10\%)$ shift for large transverse momenta. Our calculation sees a slightly smaller effect than [192], but then again a direct quantitative comparison is not possible. All things considered, the two predictions appear to be in line with each other.

The fact that the largest impact of the NLO EW corrections sits in the tail of the distributions explains, why the total cross section is basically unaffected; the by far greatest share of the total cross section comes from the region just about the fiducial threshold where the NLO EW

[4] In [192] the quantity $(\mathrm{d}\sigma_{ew} - \mathrm{d}\sigma)/\mathrm{d}\sigma$ is plotted, where $\mathrm{d}\sigma_{ew}$ is the cross section including both EW and QCD effects, while $\mathrm{d}\sigma$ only contains the latter. Given that we combine QCD and EW numbers additively, $\mathrm{d}\sigma_{ew} = \mathrm{d}\sigma + \delta_{ew}$, in our case this quantity actually corresponds to the ratio of the full EW coefficient to the NNLO QCD cross section, $\delta_{ew}/\mathrm{d}\sigma$. Since the contribution of the subleading Born in the ratio is small and basically flat, see figure 13.9, the comparison of the results in [192] with the ratio of the NLO EW coefficient to the NNLO QCD result, given as the blue points in figure 13.9, is justified.

corrections are negligible. At the point where they become relevant the differential contribution to the cross section is already decreased significantly.

To better assess how the scale dependence of the EW corrections enters the full result, we plot the ratio of (NNLO QCD)+(NLO EW) to NNLO QCD in figure 13.10 using prescription C form section 10.7, correlating the scales in the numerator and the denominator.

In line with what we observed previously, the effects are are largest in the tails of the distributions, where the scale uncertainty can become as large as $(+1, -2)\%$ for the highest bins in the two central rapidity regions. For the two forward rapidity bins, the picture is similar, but the uncertainty as depicted by the scale band is compatible with the Monte-Carlo error, which is dominated by the NNLO QCD numbers. We also see how the scale band and the Monte-Carlo errors appear to give unreliable results in the shaded regions with very limited statistics.

In order to compare to data we plot in figures 13.11 and 13.12 the ratio of NNLO QCD and (NNLO QCD)+(NLO EW) as well as the ATLAS data to the NNLO QCD result, using the standard scale variation prescription A from section 10.7. Unlike in the diphoton case (compare figure 12.13) we observe significant distortions in the shape of the scale uncertainty bands upon inclusion of the EW corrections. In the tails of the two central rapidity distributions the bands do not overlap, suggesting that especially in those regions the NLO EW effects are larger than the N$^3$LO QCD corrections. In the more forward rapidity regions the effects are not as large so that the scale bands still touch, but in the high $p_T^\gamma$ bins there is an obvious downward shift of the cross section. Thus, from the theory perspective the NLO EW corrections ought to be included when working at the precision determined by NNLO QCD.

Interestingly the scale uncertainty slightly shrinks when we also consider the NLO EW corrections, although we do not expect them to compensate the scale dependence of the NNLO QCD result. For the two central rapidity bins the uncertainty is now smaller than $(+1.1, -2.9)\%$ in all $p_T^\gamma$-bins (with sufficient statistics). For the pure NNLO QCD prediction on the other hand we find $(+3.0, -4.8)\%$, which is in particular inflated due to the broadening of the band in the high $p_T^\gamma$. For the two forward rapidity bins we find a reduction from $(+2.1, -4.7)\%$ to $(+1.8, -3.9)\%$ for the envelope of the uncertainties, ignoring the last three bins in $p_T^\gamma$.

Comparing to the 36.1 fb$^{-1}$ measurement by ATLAS [24] we make the same observation as for the total cross-section already, with the predictions underestimating the data almost everywhere. In the central rapidity region the data is subject to a basically constant shift compared to the NNLO QCD result by $5-10\%$, except for the last three bins, in which, however, the experimental statistical uncertainty grows significantly. The last data point (2000 GeV$-$2500 GeV) lies outside of the plot with a statistical error of more than 50%. Given the small uncertainties of both the data and the theory this shift is significant. Like already stated for the total cross section, the rescaling of $\alpha$ in the QCD corrections actually moves the result away from the data, a shift which is not compensated by the inclusion of the EW correction. In fact they rather seem to worsen the effect in the high $p_T^\gamma$, except for the last bins where we cannot make any reliable statements due to the large uncertainty. In figure 13.12 we show the 3.2 fb$^{-1}$ data instead, which we also used in the NNLO QCD study in section 8.1.2 (see figure 8.4). Here the situation appears to be better, but unfortunately the agreement vanishes with higher statistics.

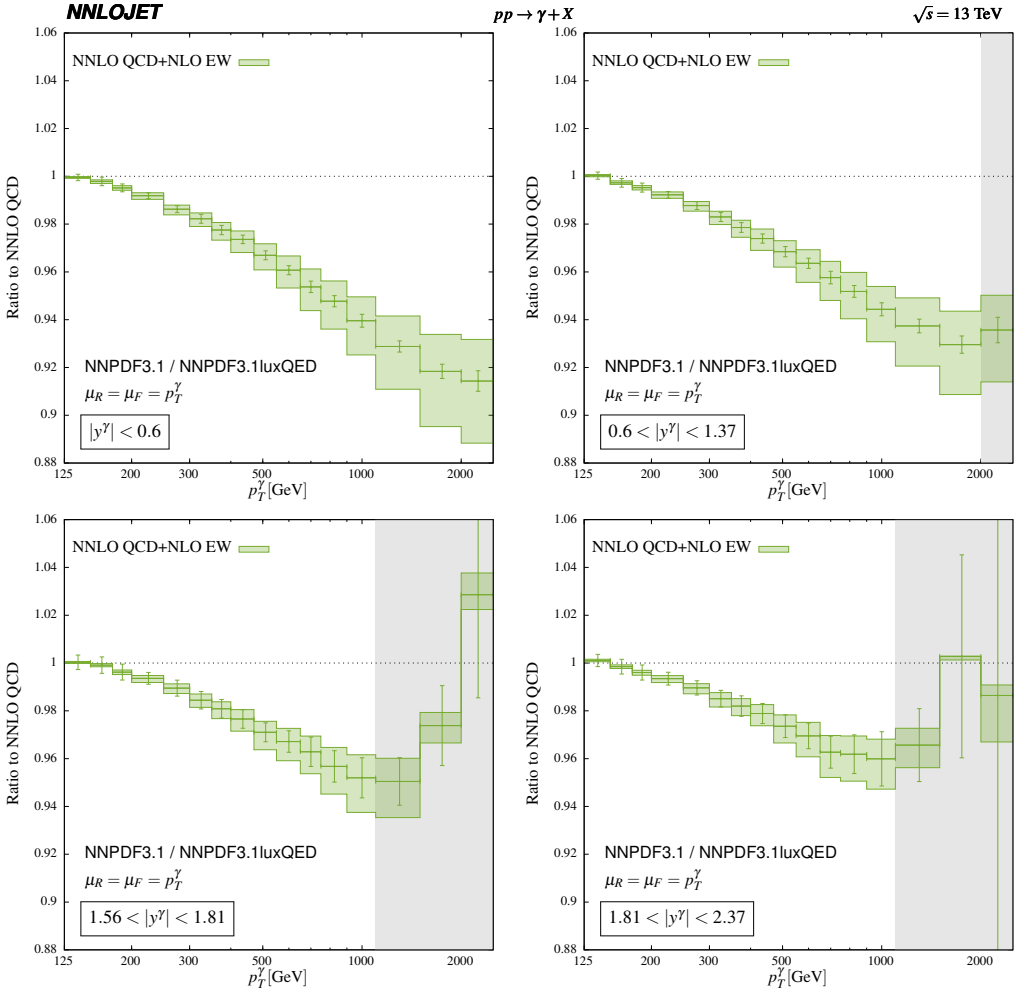


Figure 13.10.: Ratio of the full result (NNLO QCD+ NLO EW) to NNLO QCD, for the same rapidity bins presented in figure 8.4 in section 8.1.2. The scales in numerator and denominator are correlated, corresponding to prescription C from section 10.7. On the central scale we show the MC error, which is dominated by the error on the NNLO QCD prediction. The bin highlighted in grey are subject to very low statistics and should be considered with care.

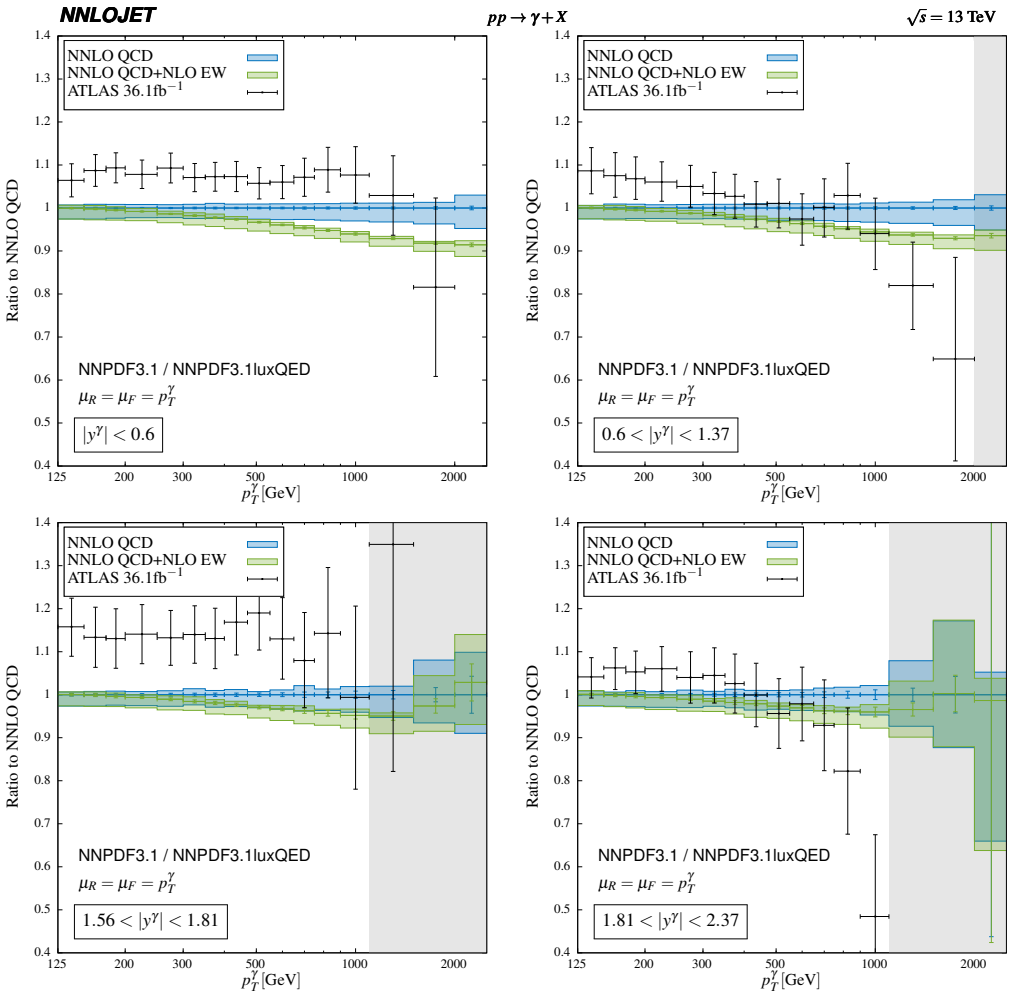


Figure 13.11.: Ratio of the full pure NNLO QCD and mixed NNLO QCD + NLO EW predictions to NNLO QCD. In this plot the scale band is derived in the standard way, prescription A from section 10.7, by varying the scales in the numerator only, while keeping the denominator fixed at the central scale choice. We also show the ATLAS data [24]. The bin highlighted in grey are subject to very low statistics and should be considered with care.

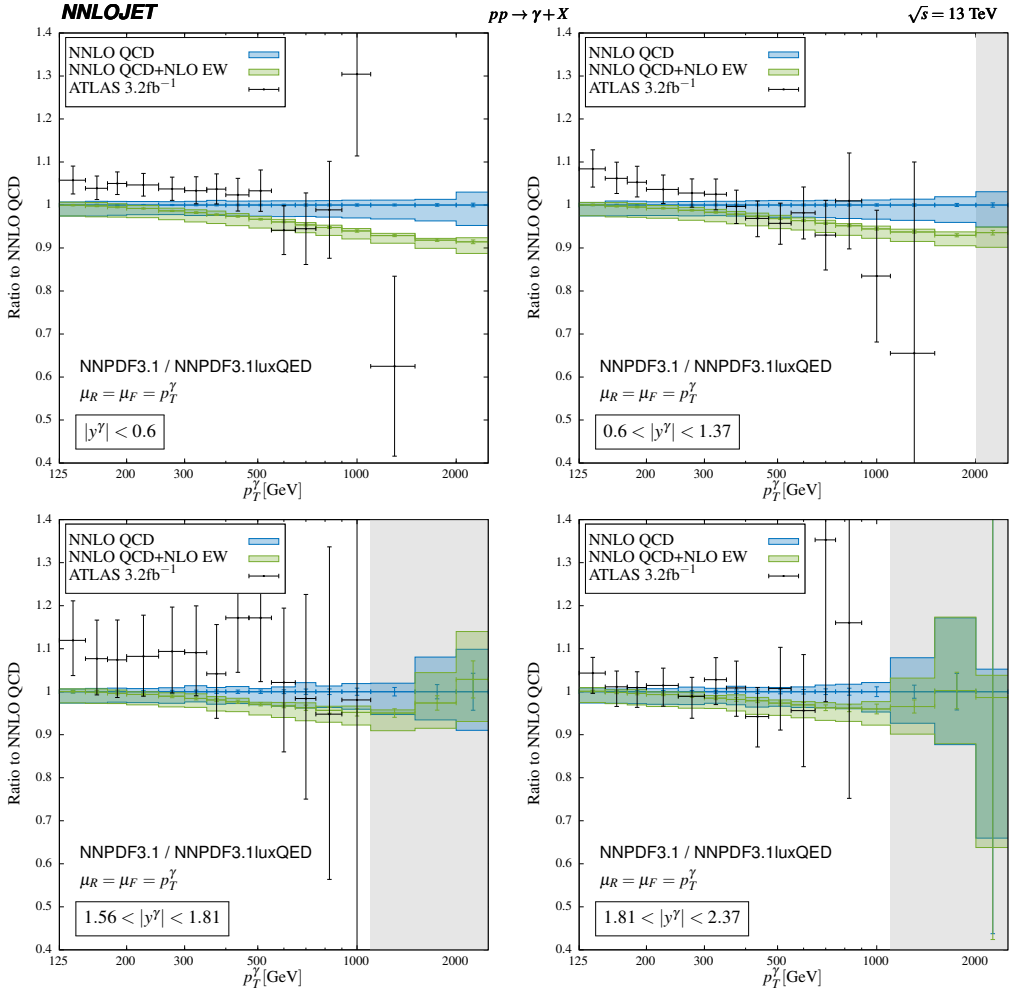


Figure 13.12.: Ratio of the full pure NNLO QCD and mixed NNLO QCD + NLO EW predictions to NNLO QCD. In this plot the scale band is derived in the standard way, prescription A from section 10.7, by varying the scales in the numerator only, while keeping the denominator fixed at the central scale choice. We also show the ATLAS data [22]. The bin highlighted in grey are subject to very low statistics and should be considered with care.

The slope we observed for the 3.2 fb$^{-1}$ data in the second rapidity bin in figure 8.4 and which again can be seen in figure 13.12 persists even with the full 36.1 fb$^{-1}$ statistics (figure 13.11). Interestingly here the inclusion of the EW corrections seems beneficial, as the shape is described better. There still is a slight underestimation of the data, but within uncertainties theory and experiment are compatible. In the highest measured $p_T^\gamma$ bin the statistical uncertainty is again quite large.

In the third panel the data again sits consistently above the predictions and is, at least in the bulk, barely compatible with them. Compared to the first two rapidity bins the experimental error is larger, which can be ascribed to the comparatively small range in the rapidity which is probed ($1.56 < |y^\gamma| < 1.81$) and the resulting limited statistics. The uncertainty is in particular larger than that of the theory results. As for the shape we cannot make any clear statements, as the shift we observe is, compared to the statistical error, insignificant. The same is true for the most forward distribution. Both the pure QCD and the full QCD+EW result agree with the data, which in turn is not accurate enough to resolve the effect of the EW corrections.

Overall we conclude that the inclusion of the EW corrections and the related choice of the electromagnetic coupling $\alpha$ for the isolated photon seem to induce a tension between the experimental measurement and the theory prediction, especially in the central rapidity region. Given that here we now reached $\mathcal{O}(\%)$ accuracy for both, to explain this discrepancy a careful evaluation of all the pieces contributing to the calculation might be in order. A recent study [233] on the impact of single inclusive jet and dijet production in global PDF fits, for example, hints at a larger gluon distribution for $x \gtrsim 0.1$ compared to what currently is reported by modern PDF sets, with an impact on differential cross sections with a magnitude and overall shape comparable to the discrepancy observed above. This could explain our observations, but a more detailed assessment is required to confirm this claim.

### 13.3.3. Summary

We supplemented the study performed on inclusive photon production at NNLO QCD accuracy presented in section 8.1.2, based on the 13 TeV ATLAS measurement [22], with the corresponding NLO EW corrections. To do so we investigated the structure of the corrections, which due to the presence of a subleading $\mathcal{O}(\alpha^2)$ Born is more complicated than for the diphoton production in the previous chapter. The IR limits of the new contributions at the NLO EW level could therefore be divided into QCD-like and QED-like singularities, for which we constructed the relevant antenna subtraction terms. In addition we found new QCD$\times$EW interference diagrams at the NLO EW real level, which, however, are IR finite.

We found the dominant contribution to the observed shifts in the shape of the $p_T^\gamma$ spectrum to come from the radiative EW corrections to the QCD induced partonic channels, following the behaviour expected from the study of EW Sudakov double logarithms [191, 192]. Compared to that the photon induced channels are again negligible, as is the subleading Born, at least in the tails.

To combine our result with the NNLO QCD corrections we had to rescale the latter to accommodate for the different choice of $\alpha$ made therein. Unfortunately this rescaling moved the prediction away from the data, which we took from the updated 36.1 fb$^{-1}$ ATLAS analysis [24].

This shift is not compensated by the EW corrections so that the discrepancy persists. We argued that this could be an effect of the PDFs, as a recent study [233] on global PDF fits suggests. A more careful evaluation of this statement is needed to give a definite answer on that point. Nevertheless, the observed incompatibility of the scale uncertainty bands of the pure NNLO QCD and the mixed QCD+EW result proves that with the high accuracy reached in both experiment and theory, the inclusion of EW corrections is definitely to be considered.

# 14. Summary and conclusion of part III

With the ever increasing precision required in the theory predictions in order to match the progress in the experimental measurements, the inclusion of NLO EW corrections besides the pure QCD perturbative expansion should be considered. This follows from a naive estimate regarding the relative size of the strong and electromagnetic coupling constants, $\alpha_s$ and $\alpha$, but also from studies on the explicit impact of EW Sudakov logarithms[191, 192].

We discussed the changes necessary to the organisation of the calculation when expanding both in the strong and the electromagnetic coupling simultaneously, compared to the pure QCD expansion. The new structures that can appear were discussed and we commented on their relevance for the calculation of EW corrections in particular to diphoton and inclusive photon production. Based on the observation that the corresponding additions to the IR structure are entirely QED-like and that the occurring limits fall in only a limited number of different classes, we constructed all relevant antenna subtraction terms for the NLO level.

After commenting on some technical aspects of the calculation, the mass and EW renormalisation schemes and, related to that, the right choice for the numerical value of $\alpha$, we briefly discussed how the treatment of final state photons has to be altered. Closely connected to this is the definition of jet observables, for which the inclusion of the photon fragmentation function is now mandatory. To get a handle on the substructure of photon-jet clusters the computation has to be modified in such a way that the distinction between photon isolation and the jet algorithm appears obstructive and we argue that one should move towards democratic clustering approaches instead, so that photon isolation and jet clustering can essentially be combined.

We then moved on to explain the actual implementation of the EW corrections in NNLOJET, focussing on the process auto-generation and the OpenLoops2 interface.

Our new tools have then been used to calculate the NLO EW corrections to diphoton production. We explained the relevant matrix element contributions and corresponding IR limits and subtraction terms. After a detailed validation of the process against MATRIX [186] we proceeded to extend the phenomenology study performed at NNLO QCD accuracy in [160, 161]. We found the impact of the corrections to fall short of our initial estimates and overall inferior compared to higher order QCD corrections and the resummation of fiducial threshold effects.

In the last chapter we repeated the exercise for inclusive photon production. After commenting on problems arising in the validation, which have not been resolved yet, we nevertheless calculated some EW numbers to supplement the 13 TeV ATLAS study presented in section 8.1.2 and [74], to get a first impression of their relative size. Here the effect of the EW corrections appears indeed larger and in line with previous approximations based on the resummation of EW Sudakov logarithms [191, 192].

We concluded that with the precision pushed down to the percent level in both experiment and theory, the inclusion of EW corrections should be an integral part of all further fixed order theory studies which aim for that precision.

# Appendix

# A. Spinor-helicity formalism

The traditional way to express scattering amplitudes is as functions of the momenta and polarisations of the external particles. This approach highlights the relation of the mathematical expression to the Feynman diagrams out of which the amplitude is constructed. For high multiplicity states the expressions quickly become large and unhandy, obscuring underlying structures, even for tree level amplitudes. The choice of momenta and polarisation vectors as the relevant quantities in the amplitude also brings some redundancy, as for example the polarisation and the momentum of an massless gauge boson are not independent, but rather satisfy the condition $\epsilon^{\pm}(p) \cdot p = 0$.

A much better way to write down the partial amplitudes we introduced in section 3.2 is in terms of spinor products, reflecting the helicites of the external particles. The amplitudes obtained in that way are called *helicity amplitudes* and the framework constructed around them is called the *spinor helicity formalism*. It was originally formulated for massless tree level amplitudes in pure Yang-Mills theories, but then has quickly been extended to also incorporate fermions (i.e. QCD) and to supersymmetric theories and even gravity. One-loop techniques have been developed, too. In the past thirty years the topic has been covered by some very instructive reviews, such as [92, 93, 234, 235]. Recently an effort has been made to consistently write down a formalism for massive particles as well, see for example [236].

The point about helicity amplitudes is, that, while their direct relation to the underlying Feynman diagrams is not obvious any more, they are comparatively compact objects reflecting the underlying symmetry inherent to the theory. Moreover it is possible to derive simple relations amongst different helicity amplitudes and recursion relations, enabling us to construct amplitudes for high multiplicity states, which would be a very tedious task in the traditional diagrammatic approach.

Here will just collect some basic results. For the details we refer the reader to the reviews listed above. The idea is to write both the four-momenta $p^{\mu}$ and polarisation vectors $\epsilon^{\mu}$ in terms of two two-component Weyl spinors[1] $\lambda_a$ and $\tilde{\lambda}_{\dot{a}}$, representing positive and negative chirality, respectively. We start by defining a matrix in spinor space

$$p_{a\dot{a}} = \sigma^{\mu}_{a\dot{a}} p_{\mu} = \lambda_a \tilde{\lambda}_{\dot{a}} \equiv |p\rangle_a \, |p]_{\dot{a}} \,, \tag{A.1}$$

[1] Some references build on Weyl spinors, some on Dirac spinors. The results are essentially equivalent.

where $\sigma^\mu = (1, \vec{\sigma})$ is the vector of Pauli matrices, and the second equation is valid for massless momenta, since then $p^2 = \det(p_{a\dot{a}}) = 0$, so the rank of the matrix is strictly smaller than two. Solving this expression for the momentum, we find

$$p_i^\mu = \frac{1}{2} \langle p_i | \sigma^\mu | p_i ] \equiv \frac{1}{2} \langle i | \sigma^\mu | i ] \,, \qquad\qquad p_{i\,\mu} = \frac{1}{2} [p_i | \bar{\sigma}_\mu | p_i \rangle \equiv \frac{1}{2} [i | \bar{\sigma}_\mu | i \rangle \,. \tag{A.2}$$

The polarisation vectors associated to a momentum $p_i$ can be written as

$$\left(\epsilon^+\right)^\mu (p_i) = \frac{1}{\sqrt{2}} \frac{\langle j | \sigma^\mu | i ]}{\langle j i \rangle} \,, \qquad\qquad \left(\epsilon^-\right)^\mu (p_i) = -\frac{1}{\sqrt{2}} \frac{[ j | \bar{\sigma}^\mu | i \rangle}{[ j i ]} \,, \tag{A.3}$$

where we defined an arbitrary reference momentum $q_j$ different from $p_i$. The momentum invariants can then easily be constructed in terms of spinor products,

$$s_{ij} = 2 p_i \cdot p_j = \langle i j \rangle [ j i ] \,, \tag{A.4}$$

where for real momenta the square and angle brackets are related by complex conjugation,

$$[ i j ] = \langle i j \rangle^* \,. \tag{A.5}$$

Moreover the spinor products are anti-symmetric objects,

$$\langle i j \rangle = - \langle j i \rangle \,, \qquad [ i j ] = - [ j i ] \qquad \Rightarrow \qquad \langle i i \rangle = [ i i ] = 0 \,. \tag{A.6}$$

Those will be the basic objects out of which the amplitudes can be constructed. In some cases, the expressions we find are very compact, even for an arbitrary number of legs. For example the $n$-gluon amplitudes, $n \geq 4$, with either all or all but one gluon having the same helicity identically vanish,

$$a_n^{\text{tree}}(1^\pm, 2^+, \ldots, n^+) = a_n^{\text{tree}}(1^\pm, 2^-, \ldots, n^-) = 0 \,, \tag{A.7}$$

while the so called *maximal helicity violating* (MHV) amplitudes[2], for which all but two gluons have positive helicity, take the simple form[3]

$$a_n^{\text{tree}}(1^+, 2^+, \ldots, I^-, \ldots, J^- \ldots, n^+) = i \frac{\langle I J \rangle^4}{\langle 12 \rangle \langle 23 \rangle \ldots \langle n1 \rangle} \,. \tag{A.8}$$

The corresponding amplitudes with all helicites swapped are sometimes called the $\overline{\text{MHV}}$ amplitudes. They are related through parity inversion ($P$), which acts on the spinor products as[4]

$$\langle i j \rangle \overset{P}{\leftrightarrow} [ j i ] \,. \tag{A.9}$$

[2] In case of pure gluon amplitudes they are called Parke-Taylor amplitudes [237].
[3] The amplitudes are conventionally defined with an all-outgoing momentum assignment.
[4] For each external quark pair he parity inverted amplitude gets an additional factor $-1$.

We can also write down the MHV amplitudes for amplitudes with a single quark pair, having an equally simple structure,

$$b_n^{\text{tree}}(\bar{q}^-, q^+, 3^+, \ldots, I^-, \ldots, n^+) = i\frac{\langle \bar{q}I\rangle^3\langle qI\rangle}{\langle \bar{q}q\rangle\langle q3\rangle\ldots\langle n\bar{q}\rangle}\,. \tag{A.10}$$

The MHV amplitudes for processes with two external quark pairs are slightly more complicated, but can still be written down in a compact form for an arbitrary number of gluons. They can be found for example in [95]. Amplitudes with external (charged) fermions are subject to charge conjugation ($C$), which exchanges the labels of the fermion line and can be seen as flipping the helicites. So for the MHV amplitude above we find

$$\begin{aligned} &b_n^{\text{tree}}(\bar{q}^-, q^+, 3^+, \ldots, I^-, \ldots, n^+) \\ &\qquad\xrightarrow{C} \quad b_n^{\text{tree}}(\bar{q}^+, q^-, 3^+, \ldots, I^-, \ldots, n^+) = i\frac{\langle qI\rangle^3\langle \bar{q}I\rangle}{\langle q\bar{q}\rangle\langle \bar{q}3\rangle\ldots\langle nq\rangle}\,. \end{aligned} \tag{A.11}$$

Parity inversion and charge conjugation are particularly useful to relate amplitudes for different helicity configurations. Together with the reflection symmetry,

$$a_n^{\text{tree}}(1,\ldots,n) = (-1)^n a_n^{\text{tree}}(n,\ldots,1)\,, \tag{A.12a}$$

$$b_n^{\text{tree}}(1_{\bar{q}}^+, 2_q^-, 3, \ldots, n) = (-1)^n b_n^{\text{tree}}(n, \ldots, 3, 2_{\bar{q}}^+, 1_q^-)\,, \tag{A.12b}$$

this enables us to drastically reduce the number of independent helicity amplitudes. Note that the reflection symmetry also holds for non-MHV (N-MHV) amplitudes. Those are in general less simple, but for both the pure gluon and the two-quark amplitudes we need to have at least six external particles for them to appear; in all other cases the amplitudes are either MHV or $\overline{\text{MHV}}$.

# B. Helicity amplitudes for $\gamma + X/j$ up to NNLO QCD

This appendix serves as a source for the individual matrix elements used in NNLOJET for inclusive photon and photon-plus-jet production. We will discuss how the matrix elements and their colour decomposition can be derived by squaring or interfering the corresponding amplitudes and applying the rules collected in eqs. (3.10). For all amplitudes and matrix elements which have been coded manually, we show how they relate to the expressions in the references they are taken from.

## B.1. Notation and conventions

Before discussing the individual amplitudes and how they merge into the matrix elements described in section 6.1, we need to fix some conventions and notations. The naming of the amplitudes is done according to the following scheme:

- The **full un-squared amplitudes** are written as curly, capital $\mathcal{A}$s with subscripts corresponding to their type defined, by the number of external quark pairs, e.g. $\mathcal{A}_B, \mathcal{A}_C$. If not mentioned otherwise, the amplitude is assumed to represent one helicity configuration.
- **Colour stripped amplitudes** are written in small letters, corresponding to their type, e.g. $b, c$.
- **partial amplitudes with internal colour structure** (i.e. not fully colour stripped) are written as curly capital letters, corresponding to their type, e.g. $\mathcal{B}$,$\mathcal{C}$. This kind of amplitudes only occurs at loop level, where even after decomposition according to the external (i.e. tree-level) colour structure an internal colour dependence of the partial amplitudes might persist.
- The **full matrix elements**, summed over helicites, are written as capital As with subscripts corresponding to their type, e.g. $A_B, A_C$.
- The **colour stripped matrix elements** are written in capital letters, corresponding to their type, e.g. $B, C$.

Strings and traces of $SU(3)$ generators are written with the shorthand notation (see eqs. (3.9))

$$(T^{a_1}T^{a_2}\dots T^{a_n})q\bar{q} \equiv (a_1 a_2 \dots a_n)_{q\bar{q}}\,, \tag{B.1a}$$

$$\mathrm{Tr}[T^{a_1}T^{a_2}\dots T^{a_n}] \equiv [a_1 a_2 \dots a_n]\,. \tag{B.1b}$$

The generators are normalised such that $[ab] = \delta^{ab}$, i.e. $T_F = 1$. We will use a very concise notation for summing over permutations of generators. For example (compare eq. (B.5))

$$\sum_{S_n(1,\ldots,n)} (1\ldots n)_{q\bar{q}} b^{\text{tree}}_{(n+2)}(\bar{q}, 1, \ldots, n, q) \tag{B.2}$$

is short for

$$\sum_{\sigma\in S_n} (\sigma(1)\ldots\sigma(n))_{q\bar{q}} b^{\text{tree}}_{(n+2)}(\bar{q}, \sigma(1), \ldots, \sigma(n), q)\,. \tag{B.3}$$

All one-loop amplitudes we need come with an universal combination of $\Gamma$ functions as prefactor, which we denote

$$c_\Gamma = e^{\gamma\epsilon}\frac{\Gamma(1+\epsilon)\Gamma^2(1-\epsilon)}{\Gamma(1-2\epsilon)} = 1 - \frac{\pi^2}{12}\epsilon^2 + \mathcal{O}\big(\epsilon^3\big)\,. \tag{B.4}$$

The references often use slightly different definitions, which usually correspond to absorbing additional factors of $4\pi$. Where necessary, we will explicitly point out the differences.

## B.2. Trading gluons for photons and tree level amplitude relations

The photonic partial amplitudes can be derived from the pure QCD amplitudes following a simple recipe, by simply choosing one of the gluons in the amplitude and replace its associated $SU(3)$ generator with $\sqrt{2}$ times the identity matrix $\mathbb{1}$. The extra $\sqrt{2}$ comes from the normalisation of the generators. Additionally the power of the strong coupling constant $g$ is decreased by one and a factor of the electromagnetic coupling $e$ added. For tree level amplitudes where the photon couples to an external quark $q$, we also need to add the charge factor $Q_q$ of that quark. The one loop case is more involved, as we will se at the end of this section.

As already discussed in section 6.1 the only relevant tree level amplitudes for inclusive photon and photon-plus-jet production are those with one or two external quark pairs, the B-type and C/D-type amplitudes, respectively. Using the procedure above, it is possible to write an $m$-photon colour stripped amplitude in terms of a sum of colour stripped amplitudes with $m-1$ photons and an additional gluon. The pure QCD $2qng$ amplitude has the following structure [94, 95]:

$$\mathcal{A}^{\text{tree}}_{(n+2),B}(\bar{q}, 1, \ldots, n, q) = g^n \sum_{S_n(1,\ldots,n)} (1\ldots n)_{q\bar{q}} b^{\text{tree}}_{(n+2)}(\bar{q}, 1, \ldots, n, q)\,, \tag{B.5}$$

where the sum runs over all permutations of the $n$ gluons and $b^{\text{tree}}_{(n+2)}$ is the colour stripped partial amplitude. W.l.o.g. we can replace gluon $n$ following the above steps to obtain

$$\begin{aligned}&\mathcal{A}^{1\gamma,\text{tree}}_{(n+2),B}(\bar{q},1,\ldots,n-1,q,\gamma)\\&\qquad=\sqrt{2}g^{(n-1)}eQ_q\sum_{S_{(n-1)}(1,\ldots,n-1)}(1\ldots n-1)_{q\bar{q}}b^{1\gamma,\text{tree}}_{(n+2)}(\bar{q},1,\ldots,n-1,q,\gamma)\,,\end{aligned}\tag{B.6}$$

where

$$\begin{aligned}b^{1\gamma,\text{tree}}_{(n+2)}(\bar{q},1,\ldots,n-1,q,\gamma)=\;&b^{\text{tree}}_{(n+2)}(\bar{q},1,\ldots,n-1,\gamma,q)\\&+b^{\text{tree}}_{(n+2)}(\bar{q},1,\ldots,n-2,\gamma,n-1,q)\\&+\ldots\\&+b^{\text{tree}}_{(n+2)}(\bar{q},\gamma,1,\ldots,n-1,q)\,.\end{aligned}\tag{B.7}$$

Eq. (B.11) is a so-called photon decoupling equation, as it decouples the gluon which we permute, gluon $n$ in this example, from any other gluon; the pieces related to the $3g$- and $4g$-vertices will exactly cancel in the sum, so that the gluon is left with the $U(1)$ like coupling to quarks, only. For that reason we call it an abelian gluon. Apart from the coupling factor it has the same properties as a photon[1]. The photonic amplitude we defined with eq. (B.7) is precisely one of the kind we encounter in the subleading colour pure QCD matrix elements, as discussed at the end of section 3.2. Note that above equation can easily be generalised to $m$-photon amplitudes by repeated use of the recipe, such that $(r=n-m)$

$$\begin{aligned}b^{m\gamma,\text{tree}}_{(n+2)}(\bar{q},1,\ldots,r,q,\gamma_1,\ldots,\gamma_m)=\;&b^{(m-1)\gamma,\text{tree}}_{(n+2)}(\bar{q},1,\ldots,r,\gamma_m,q,\gamma_1,\ldots,\gamma_{m-1})\\&+b^{(m-1)\gamma,\text{tree}}_{(n+2)}(\bar{q},1,\ldots,r-1,\gamma_m,r,q,\gamma_1,\ldots,\gamma_{m-1})\\&+\ldots\\&+b^{(m-1)\gamma,\text{tree}}_{(n+2)}(\bar{q},\gamma_m,1,\ldots,r,q,\gamma_1,\ldots,\gamma_{m-1})\,.\end{aligned}\tag{B.8}$$

We will use this feature explicitly when constructing the tree level B-type 1-photon amplitudes. It is particularly useful, when the multiplicity of gluons is low. As the number of coloured particles is increased, colour decomposing the matrix element becomes more and more tedious and the expressions relating photonic and gluon amplitudes grow significantly. Since the gluon amplitudes exhibit more IR singular limits, those limits which are not present in the photon amplitudes must mutually cancel in the sum. While analytically this is not a problem, cancellations of many large numbers in a numerical expression can lead to instabilities and performance penalties. In more complicated cases it is therefore advisable to code the amplitudes directly, or at least simplify the photon decoupling equations analytically first.

In principle it is possible to find decoupling equations like the one above also for amplitudes with two external quark pairs. In the general case those are, however, more complicated. Since

[1] This feature does not persist in theories beyond QCD. In the EW theory the photon couples to the charged leptons and the $W^{\pm}$ bosons, which an abelian gluon does not.

we will code the 4-quark 1-photon amplitudes we need directly, we will not present the decoupling equations here. For MHV amplitudes they can be found in [95].

It is interesting to note that for all-gluon A-type tree amplitudes [92, 93] the photon decoupling equation take a particularly simple form. Starting form the $n$-gluon amplitude

$$\mathcal{A}_{n,A}^{\text{tree}}(1,\ldots,n) = g^{n-2} \sum_{S_n/\mathbb{Z}_n(1,\ldots,n)} [1\ldots n] a_n^{\text{tree}}(1,\ldots,n)\,, \tag{B.9}$$

we derive the corresponding 1-photon amplitude

$$\mathcal{A}_{n,A}^{1\gamma,\text{tree}}(1,\ldots,n-1,\gamma) = \sum_{S_{n-1}/\mathbb{Z}_{n-1}(1,\ldots,n-1)} [1\ldots n-1] a_n^{1\gamma,\text{tree}}(1,\ldots,n-1,\gamma)\,. \tag{B.10}$$

The sum now runs over all non-cyclic permutations of the gluons, because of the cyclic symmetry of the trace. Since the photon does not couple to gluons, the photonic amplitude must vanish, which implies

$$\begin{aligned} a_n^{1\gamma,\text{tree}}(1,\ldots,n-1,\gamma) = \quad & a_n^{\text{tree}}(1,\ldots,n-1,\gamma) \\ & + a_n^{\text{tree}}(1,\ldots,n-2,\gamma,n-1) \\ & + \ldots \\ & + a_n^{\text{tree}}(1,\gamma,2,\ldots,n-1) = 0\,. \end{aligned} \tag{B.11}$$

which is the original photon decoupling equation.

For one-loop amplitudes turning gluons into photons is more involved. The difficulties are related to two new features which are absent at tree level:

- A more complicated colour structure of the amplitude. While e.g. the tree level A- and B-type amplitudes had a single colour structure, a single trace or string of the $SU(3)$ generators, at one-loop level we have multiple structures consisting of products of traces and strings. Formally terms proportional to a trace of a single generator appear, but since such traces vanish, $\text{Tr}[T^a] \equiv [a] = 0$, the corresponding partial amplitude does not contribute. If we now replace gluon $a$ by a photon, $[a] \to \sqrt{2}[\mathbb{1}] = \sqrt{2}N \neq 0$, so the formerly neglected partial amplitude needs to be considered.

- Closed quark loops. When the gluon we replace with the photon couples to an internal closed quark loop, corresponding to a partial amplitude coming with a factor $N_F$, we should not replace the associated strong coupling $g$ with $eQ_q$, but rather with $eN_F^q$, where $N_F^q = \sum_q Q_q$, with the sum over all flavours in the loop.

When these points are taken into account, one can derive the photonic amplitudes and matrix elements from the pure QCD ones. For B-type one-loop amplitudes with a single photon the procedure is described in appendix IV of [94]. We used the method to obtain the B-type $2q1g1\gamma$ and the A-type $3g1\gamma$ one-loop amplitudes. Amplitudes with higher final state multiplicities have been coded directly using expressions given in the literature.

## B.3. Leading order - Born contribution

At LO we only have the B-type Born contribution. Following the discussion about the photon decoupling in section B.2 it is instructive to start from the pure QCD amplitudes in order to derive relations between jet an photonic amplitudes. The colour decomposition of the $2q2g$ amplitude reads

$$\mathcal{A}^{\text{tree}}_{4,B}(\bar{q},1,2,q) = g^2 \sum_{S_2(1,2)} (12)_{q\bar{q}} b^{\text{tree}}_4(\bar{q},1,2,q)\,. \tag{B.12}$$

Squaring the amplitude and and carrying out the colour algebra yields

$$A^{\text{tree}}_{4,B} = \sum_{\text{hel}} \left|\mathcal{A}^{\text{tree}}_{4,B}\right|^2 = g^4 N^2 C_F \left( \sum_{S_2(1,2)} B^0_{2g,12} - \frac{1}{N^2} \tilde{B}^0_{2g} \right) \tag{B.13}$$

with

$$B^0_{2g,ij} = \sum_{\text{hel}} \left|b^{\text{tree}}_{4,ij}\right|^2, \tag{B.14a}$$

$$\tilde{B}^0_{2g} = \sum_{\text{hel}} \left| \sum_{S_2(1,2)} b^{\text{tree}}_{4,12} \right|^2 = \sum_{\text{hel}} \left| b^{1\gamma,\text{tree}}_4 \right|^2 = \sum_{\text{hel}} \left| b^{2\gamma,\text{tree}}_4 \right|^2, \tag{B.14b}$$

where we introduce the shorthand notations $B^0_{2g,ij} = B^0_{2g}(\bar{q},i,j,q)$ and $b^{\text{tree}}_{4,ij} = b^{\text{tree}}_4(\bar{q},i,j,q)$. In (B.14b) we used the photon decoupling equation (B.7),

$$\begin{aligned}
\sum_{S_2(1,2)} b^{\text{tree}}_{4,12} &= b^{\text{tree}}_4(\bar{q},1,2,q) + b^{\text{tree}}_4(\bar{q},2,1,q) && \text{(B.15a)}\\
&= b^{1\gamma,\text{tree}}_4(\bar{q},1,q,2_\gamma) && \text{(B.15b)}\\
&= b^{1\gamma,\text{tree}}_4(\bar{q},2,q,1_\gamma) && \text{(B.15c)}\\
&= b^{2\gamma,\text{tree}}_4(\bar{q},q,1_\gamma,2_\gamma) && \text{(B.15d)}\\
&= b^{2\gamma,\text{tree}}_4(\bar{q},q,2_\gamma,1_\gamma)\,. && \text{(B.15e)}
\end{aligned}$$

Trading gluon 2 for a photon in the jet amplitude (B.12) we obtain the 1-photon amplitude

$$\mathcal{A}^{1\gamma,\text{tree}}_{4,B}(\bar{q},1,q,\gamma) = \sqrt{2} g e Q_q (1)_{q\bar{q}} b^{1\gamma,\text{tree}}_4(\bar{q},1,q,\gamma)\,. \tag{B.16}$$

Carrying out the simple colour algebra we get the result given in eq. (6.1),

$$A^{1\gamma,\text{tree}}_{4,B} = \sum_{\text{hel}} \left|\mathcal{A}^{1\gamma,\text{tree}}_{4,B}\right|^2 = \underbrace{4g^2e^2NC_F}_{\mathcal{N}^B} B^{0,\gamma}_{1g}\,, \tag{B.17}$$

with

$$B_{1g}^{0,\gamma} = \frac{1}{2} Q_q^2 \sum_{\text{hel}} \left| b_4^{1\gamma,\text{tree}} \right|^2 . \tag{B.18}$$

The factor 1/2 has no physical meaning and is just pulled out for convenience related to the coding of the matrix elements. Trading also the remaining gluon for a photon, we arrive at the 2-photon amplitude

$$\mathcal{A}_{4,B}^{2\gamma,\text{tree}}(\bar{q}, q, \gamma, \gamma) = 2e^2 Q_q^2 \delta_{q\bar{q}} b_4^{2\gamma,\text{tree}}(\bar{q}, q, \gamma, \gamma) , \tag{B.19}$$

for which we directly can write down the square,

$$A_{4,B}^{2\gamma,\text{tree}} = \sum_{\text{hel}} \left| \mathcal{A}_{4,B}^{2\gamma,\text{tree}} \right|^2 = 8e^4 N B_{0g}^{0,2\gamma} , \tag{B.20}$$

with

$$B_{0g}^{0,2\gamma} = \frac{1}{2} Q_q^4 \sum_{\text{hel}} \left| b_4^{2\gamma,\text{tree}} \right|^2 . \tag{B.21}$$

We thus find the following relation between the colour stripped matrix elements:

$$\tilde{B}_{2g}^{0} = \frac{2}{Q_q^2} B_{1g}^{0,\gamma} = \frac{2}{Q_q^4} B_{1g}^{0,2\gamma} . \tag{B.22}$$

For two-quark amplitudes with up to three gluons/photons, we can only have MHV configurations[2] , all others vanish. The helicity amplitude for the $2q2g$ tree level amplitude is a well known result and is given by (see eq. (A.10))

$$b_4^{\text{tree}}(\bar{q}^+, 1, 2, q^-) = i \frac{\langle \bar{q} I \rangle \langle q I \rangle^3}{\langle q\bar{q} \rangle \langle \bar{q}1 \rangle \langle 12 \rangle \langle 2q \rangle} , \tag{B.23}$$

where $I$ is the gluon with negative helicity. All other helicity configurations can be derived through parity inversion and charge conjugation. We use eq. (B.22) construct all photonic matrix elements out of the pure QCD matrix elements, based on the helicity amplitude above. Since the amplitudes and matrix elements are very simple and the IR structure not too involved, we do not expect a big stability penalty from the cancellation of large numbers in unresolved regions of the QCD matrix elements.

[2] I.e. $(++--\cdots-)$ or inverted, where the quark and anti-quark need to have opposite helicity.

## B.4. Next-to-leading order - real contribution

### B.4.1. B-type matrix element

For the B-type we start with the jet $2q3g$ amplitude again. It reads [92, 93]

$$\mathcal{A}_{5,B}^{\text{tree}}(\bar{q},1,2,3,q) = g^3 \sum_{S_3(1,2,3)} (123)_{q\bar{q}} b_5^{\text{tree}}(\bar{q},1,2,3,q)\,. \tag{B.24}$$

For the corresponding squared matrix element we find

$$A_{5,B}^{\text{tree}} = \sum_{\text{hel}} \left|\mathcal{A}_{5,B}^{\text{tree}}\right|^2 = g^6 N^3 C_F \left( \sum_{S_3(1,2,3)} B_{3g,123}^0 - \frac{1}{N^2} \sum_{S_3(1,2,3)} \tilde{B}_{3g,12\tilde{3}}^0 + \frac{N^2+1}{N^4} \tilde{\tilde{B}}_{3g}^0 \right), \tag{B.25}$$

with

$$B_{3g,ijk}^0 = \sum_{\text{hel}} \left|b_{5,ijk}^{\text{tree}}\right|^2, \tag{B.26a}$$

$$\tilde{B}_{3g,ij\tilde{k}}^0 = \sum_{\text{hel}} \left|b_{5,ij\tilde{k}}^{\text{tree}} + b_{5,i\tilde{k}j}^{\text{tree}} + b_{5,\tilde{k}ij}^{\text{tree}}\right|^2 = \sum_{\text{hel}} \left|b_{5,ij}^{\gamma,\text{tree}}\right|^2, \tag{B.26b}$$

$$\tilde{\tilde{B}}_{3g}^0 = \sum_{\text{hel}} \left| \sum_{S_3(1,2,3)} b_{5,123}^{\text{tree}} \right|^2 = \sum_{\text{hel}} \left| \sum_{S_3(1,2)} b_{5,12}^{1\gamma,\text{tree}} \right|^2 = \sum_{\text{hel}} \left|b_5^{2\gamma,\text{tree}}\right|^2, \tag{B.26c}$$

where we made use of the photon decoupling (B.7) again. Note that by construction it does not matter which gluon we take as the photon, as we permute over all possible orderings. In particular the 2-photon colour stripped amplitude coincides with the 3-photon colour stripped amplitude, $b_5^{2\gamma,\text{tree}} = b_5^{3\gamma,\text{tree}}$, as a single gluon will always behave in an abelian fashion. Consequently both the 2- and 3-photon matrix elements exhibit a high degree of symmetry with respect to to interchanging their photon/gluon momenta.

Abelianising gluon 3 in the jet amplitude (B.24) we find the 1-photon amplitude,

$$\mathcal{A}_{5,B}^{1\gamma,\text{tree}}(\bar{q},1,2,q,\gamma) = \sqrt{2} g^2 e Q_q \sum_{S_2(1,2)} (12)_{q\bar{q}} b_5^{1\gamma,\text{tree}}(\bar{q},1,2,q,\gamma)\,, \tag{B.27}$$

from which we obtain the result from eq. (6.4),

$$A_{5,B}^{1\gamma,\text{tree}} = \sum_{\text{hel}} \left|\mathcal{A}_{5,B}^{1\gamma,\text{tree}}\right|^2 = \underbrace{4 g^4 e^2 N^2 C_F}_{\mathcal{N}^R} \left( \sum_{S_2(1,2)} B_{2g,12}^{0,1\gamma} - \frac{1}{N^2} \tilde{B}_{2g}^{0,\gamma} \right), \tag{B.28}$$

with

$$B^{0,\gamma}_{2g,ij} = \frac{1}{2} Q_q^2 \sum_{\text{hel}} \left| b^{1\gamma,\text{tree}}_{5,ij} \right|^2 , \tag{B.29a}$$

$$\tilde{B}^{0,\gamma}_{2g} = \frac{1}{2} Q_q^2 \sum_{\text{hel}} \left| \sum_{S_2(1,2)} b^{1\gamma,\text{tree}}_{5,12} \right|^2 = \frac{1}{2} Q_q^2 \sum_{\text{hel}} \left| b^{2\gamma,\text{tree}}_{5} \right|^2 . \tag{B.29b}$$

This is very similar to the dijet matrix element (B.13), which is not very surprising, as the colour structure is essentially the same. The diphoton amplitude, with $2 \to \gamma$, is given by

$$\mathcal{A}^{2\gamma,\text{tree}}_{5,B}(\bar{q}, 1, q, \gamma, \gamma) = 2ge^2 Q_q^2 (1)_{q\bar{q}} b^{2\gamma,\text{tree}}_5(\bar{q}, 1, q, \gamma, \gamma) , \tag{B.30}$$

and its square reads

$$A^{2\gamma,\text{tree}}_{5,B} = \sum_{\text{hel}} \left| \mathcal{A}^{2\gamma,\text{tree}}_{5,B} \right|^2 = 8g^2 e^4 N C_F B^{0,2\gamma}_{1g} , \tag{B.31}$$

with

$$B^{0,2\gamma}_{1g} = \frac{1}{2} Q_q^4 \sum_{\text{hel}} \left| b^{2\gamma,\text{tree}}_5 \right|^2 . \tag{B.32}$$

We find the relations

$$\tilde{B}^{0}_{3g,ij\tilde{k}} = \frac{2}{Q_q^2} B^{0,\gamma}_{2g,ij} , \tag{B.33a}$$

$$\tilde{\tilde{B}}^{0}_{3g} = \frac{2}{Q_q^2} \tilde{B}^{0,\gamma}_{2g} = \frac{2}{Q_q^4} B^{0,2\gamma}_{1g} . \tag{B.33b}$$

As for the Born level amplitudes we only have MHV configurations for the two-quark real radiation amplitudes. The pure QCD tree level amplitudes are given by (see eq. (A.10))

$$b^{\text{tree}}_5(\bar{q}^+, 1, 2, 3, q^-) = i \frac{\langle \bar{q} I \rangle \langle q I \rangle^3}{\langle q\bar{q} \rangle \langle \bar{q} 1 \rangle \langle 12 \rangle \langle 23 \rangle \langle 3q \rangle} , \tag{B.34}$$

where $I$ is the negative helicity gluon again, and all other MHV helicity configurations are related through parity and charge conjugation. As for the Born level contribution we derive all photonic real radiation matrix elements with the help of the relations (B.33).

### B.4.2. C/D-type matrix element

The C-type $2q2Q1\gamma$ tree level amplitude is given by

$$\begin{aligned} \mathcal{A}^{1\gamma,\text{tree}}_{5,C}(\bar{q}, \bar{Q}, Q, q, \gamma) = \sqrt{2} g^2 e \Big[ & \delta_{q\bar{Q}} \delta_{Q\bar{q}} \Big( Q_q c^{1\gamma,\text{tree}}_{5,q} + Q_Q c^{1\gamma,\text{tree}}_{5,Q} \Big) \\ & - \frac{1}{N} \delta_{q\bar{q}} \delta_{Q\bar{Q}} \Big( Q_q \tilde{c}^{1\gamma,\text{tree}}_{5,q} + Q_Q \tilde{c}^{1\gamma,\text{tree}}_{5,Q} \Big) \Big] , \end{aligned} \tag{B.35}$$

where the subscripts $q$ or $Q$ indicate to which quark line the photon couples, which is also reflected in the quark charge factors $Q_q$ and $Q_Q$. The colour stripped amplitudes obey some useful tree level relations,

$$\begin{aligned} c_5^{1\gamma,\text{tree}}(\bar{q},\bar{Q},Q,q,\gamma) &\equiv \tilde{c}_{5,q}^{1\gamma,\text{tree}}(\bar{q},\bar{Q},Q,q,\gamma) && \text{(B.36a)}\\ &= c_{5,q}^{1\gamma,\text{tree}}(\bar{q},\bar{Q},Q,q,\gamma) && \text{(B.36b)}\\ &= \tilde{c}_{5,Q}^{1\gamma,\text{tree}}(\bar{Q},\bar{q},q,Q,\gamma) && \text{(B.36c)}\\ &= c_{5,Q}^{1\gamma,\text{tree}}(\bar{Q},\bar{q},q,Q,\gamma)\,, && \text{(B.36d)} \end{aligned}$$

The precise form of $c_5^{1\gamma,\text{tree}}$ for all helicity configurations is given in [238]. We can use the relations above to simplify the amplitude,

$$\mathcal{A}_{5,C}^{1\gamma,\text{tree}}(\bar{q},\bar{Q},Q,q,\gamma) = \sqrt{2}g^2 e\left(\delta_{q\bar{Q}}\delta_{Q\bar{q}} - \frac{1}{N}\delta_{q\bar{q}}\delta_{Q\bar{Q}}\right) c_{5,\gamma}^{1\gamma,\text{tree}}(\bar{q},\bar{Q},Q,q,\gamma) \tag{B.37}$$

with

$$c_{5,\gamma}^{1\gamma,\text{tree}}(\bar{q},\bar{Q},Q,q,\gamma) \equiv Q_q c_5^{1\gamma,\text{tree}}(\bar{q},\bar{Q},Q,q,\gamma) + Q_Q c_5^{1\gamma,\text{tree}}(\bar{Q},\bar{q},q,Q,\gamma)\,. \tag{B.38}$$

Here the colour structure is internal, i.e completely determined by fierzing over the internal gluon line connecting the two quark lines,

$$T^a_{\bar{q}q}T^a_{Q\bar{Q}} = \delta_{\bar{q}\bar{Q}}\delta_{qQ} - \frac{1}{N}\delta_{\bar{q}q}\delta_{Q\bar{Q}}\,. \tag{B.39}$$

Squaring the above amplitude we find the result given in eq. (6.6)

$$A_{5,C}^{1\gamma,\text{tree}} = \sum_{\text{hel}}\left|\mathcal{A}_{5,C}^{1\gamma,\text{tree}}\right|^2 = \underbrace{4g^4e^2N^2C_F}_{\mathcal{N}^R}\left(\frac{1}{N}C_{0g}^{0,\gamma}\right) \tag{B.40}$$

with

$$C_{0g}^{0,\gamma} = \frac{1}{2}\sum_{\text{hel}}\left|c_{5,\gamma}^{1\gamma,\text{tree}}\right|^2. \tag{B.41}$$

In case of identically flavoured quarks we have to anti-symmetrise the amplitude over the anti-quarks,

$$\mathcal{A}_{5,C+D}^{1\gamma,\text{tree}}(\bar{q},\bar{Q},Q,q,\gamma) = \mathcal{A}_{5,C}^{1\gamma,\text{tree}}(\bar{q},\bar{Q},Q,q,\gamma) - \mathcal{A}_{5,C}^{1\gamma,\text{tree}}(\bar{Q},\bar{q},Q,q,\gamma)\,. \tag{B.42}$$

The interference term we obtain from the square of the amplitude (see eqs. (6.8) and (6.9)) is then given by

$$A_{5,D}^{1\gamma,\text{tree}} = -2\sum_{\substack{\text{hel}\\(h_q=h_Q)}}\text{Re}\left\{\mathcal{A}_{5,C}^{1\gamma,\text{tree}\,\dagger}(\bar{q},\bar{Q})\mathcal{A}_{5,C}^{1\gamma,\text{tree}}(\bar{Q},\bar{q})\right\} = \underbrace{4g^4e^2N^2C_F}_{\mathcal{N}^R}\left(\frac{1}{N^2}D_{0g}^{0,\gamma}\right), \tag{B.43}$$

| expression in thesis | counterpart in literature | ref. |
|---|---|---|
| $c_{5,q}^{1\gamma,\text{tree}}$ | $u_2^{(0)}$ | [238] |
| $\tilde{c}_{5,q}^{1\gamma,\text{tree}}$ | $u_1^{(0)}$ | [238] |
| $c_{5,Q}^{1\gamma,\text{tree}}$ | $d_2^{(0)}$ | [238] |
| $\tilde{c}_{5,Q}^{1\gamma,\text{tree}}$ | $d_1^{(0)}$ | [238] |

Table B.1.: References for the colour stripped amplitudes used in the C and D-type virtual corrections

where

$$D_{0g}^{0,\gamma} = \sum_{\substack{\text{hel} \\ (h_q = h_Q)}} \text{Re}\left\{ c_{5,\gamma}^{1\gamma,\text{tree}\,\dagger}(\bar{q},\bar{Q}) c_{5,\gamma}^{1\gamma,\text{tree}}(\bar{Q},\bar{q}) \right\}. \tag{B.44}$$

We used a shorthand notation for the momentum assignment, $(\bar{q},\bar{Q},Q,q,\gamma) \equiv (\bar{q},\bar{Q})$ and $(\bar{Q},\bar{q},Q,q,\gamma) \equiv (\bar{Q},\bar{q})$. In table B.1 we list the references for the colour stripped amplitudes, and the expressions they relate to.

## B.5. Next-to-leading order - virtual contribution

The B-type $2q1g1\gamma$ one-loop amplitudes have been derived using the method to convert gluons into photons in one-loop amplitudes described in appendix IV of [94], and the explicit helicity amplitudes given in appendix II of the same reference. The unrenormalised[3] full amplitude is given by

$$\bar{\mathcal{A}}_{4,B}^{1\gamma,1-\text{loop}}(\bar{q},1,q,\gamma) = \frac{c_\Gamma}{(4\pi)^2}\sqrt{2}g^3 e Q_q N(1)_{q\bar{q}} \bar{\mathcal{B}}_4^{1\gamma,1-\text{loop}}, \tag{B.45}$$

where the loop factor[4] $c_\Gamma$ is given in eq. (B.4). Unlike for the tree amplitudes, the partial amplitude now has an internal colour structure and can be decomposed further into the colour stripped amplitudes,

$$-i\bar{\mathcal{B}}_4^{1\gamma,1-\text{loop}} = b_4^{1\gamma,1-\text{loop}} + \frac{1}{N^2}\tilde{b}_4^{1\gamma,1-\text{loop}}. \tag{B.46}$$

[3] Indicated by a bar above the corresponding quantity.

[4] The reference uses a slightly different definition of the factor, $c_\Gamma^{\text{ref}} = (4\pi)^{-2}e^{\ln(4\pi)-\gamma}c_\Gamma$. In NNLOJET the exponential is absorbed in the overall normalisation and the factor $(4\pi)^{-2}$ is made explicit in eq. (B.45).

Note that for the unrenormalised amplitude there are no coefficients of $N_F$ or $N_F^q = \sum_q Q_q$, since the diagrams with internal quark loops cancel in this case. Interfering the loop amplitude with the corresponding tree (eq. (B.16)) we find

$$\begin{aligned}\bar{A}_{4,B}^{1\gamma,1-\text{loop}} &= 2\sum_{\text{hel}} \text{Re}\left\{\mathcal{A}_{4,B}^{1\gamma,\text{tree}\,\dagger}\bar{\mathcal{A}}_{4,B}^{1\gamma,1-\text{loop}}\right\} \\ &= \frac{1}{2\pi^2} g^4 e^2 N^2 C_F \left(\bar{B}_{1g}^{1,\gamma} - \frac{1}{N^2}\tilde{\bar{B}}_{1g}^{1,\gamma}\right) \end{aligned} \tag{B.47}$$

with

$$\bar{B}_{1g}^{1,\gamma} \equiv c_\Gamma \bar{B}_{1g}^{1,\gamma'} = \frac{c_\Gamma}{2} Q_q^2 \sum_{\text{hel}} \text{Re}\left\{i b_4^{1\gamma,\text{tree}\,\dagger} b_4^{1\gamma,1-\text{loop}}\right\}, \tag{B.48a}$$

$$\tilde{\bar{B}}_{1g}^{1,\gamma} \equiv c_\Gamma \tilde{\bar{B}}_{1g}^{1,\gamma'} = -\frac{c_\Gamma}{2} Q_q^2 \sum_{\text{hel}} \text{Re}\left\{i b_4^{1\gamma,\text{tree}\,\dagger} \tilde{b}_4^{1\gamma,1-\text{loop}}\right\}. \tag{B.48b}$$

Since both the loop factor $c_\Gamma$ and the one-loop colour stripped amplitudes depend on $\epsilon$, we have to expand those expressions to obtain the correct pole coefficients. If we symbolically define $B'$ such that $B = c_\Gamma B'$, we can write

$$B = c_\Gamma B' = \left(1 - \frac{\pi^2}{12}\epsilon^2\right)\left(B'\big|_{\text{finite}} + \frac{1}{\epsilon}B'\big|_{\epsilon^{-1}} + \frac{1}{\epsilon^2}B'\big|_{\epsilon^{-2}}\right) + \mathcal{O}(\epsilon) \tag{B.49a}$$

$$= \left(B'\big|_{\text{finite}} - \frac{\pi^2}{12}B'\big|_{\epsilon^{-2}}\right) + \frac{1}{\epsilon}B'\big|_{\epsilon^{-1}} + \frac{1}{\epsilon^2}B'\big|_{\epsilon^{-2}} + \mathcal{O}(\epsilon). \tag{B.49b}$$

Thus we find that the finite part is shifted proportional to the $\epsilon^{-2}$ coefficient, while the pole coefficients remain unchanged.

The amplitudes given in [94] are calculated in the four-dimensional-helicity (FDH) regularisation scheme[5] and not renormalised. For our purposes we therefore need to renormalise the amplitudes (in the $\overline{\text{MS}}$ scheme) and convert them to the t'Hooft-Veltman (HV) scheme, in which we are working. This can be achieved at amplitude level by simply subtracting corrections proportional to the tree level amplitude (B.16),

$$\bar{\mathcal{A}}_{4,B}^{1\gamma,1-\text{loop}} \quad \to \quad \mathcal{A}_{4,B}^{1\gamma,1-\text{loop}} = \bar{\mathcal{A}}_{4,B}^{1\gamma,1-\text{loop}} - \left(\alpha_3^{\text{UV}} + \alpha^{\text{FDH}\to\text{HV}}\right)\mathcal{A}_{4,B}^{1\gamma,\text{tree}}. \tag{B.50}$$

The $\overline{\text{MS}}$ renormalisation correction factor $\alpha_m^{\text{UV}}$, which stems from the coupling constant counterterm, only depends on the number $m$ of external QCD legs (here: three) and is otherwise universal. It reads[6]

$$\alpha_m^{\text{UV}} = \frac{c_\Gamma}{(4\pi)^2} g^2 \frac{m-2}{2}\frac{\beta_0}{\epsilon} \tag{B.51a}$$

$$= \frac{g^2 N}{(4\pi)^2}\frac{m-2}{2}\frac{1}{\epsilon}\frac{\beta_0}{N} + \mathcal{O}(\epsilon), \tag{B.51b}$$

[5] The amplitudes are often derived using supersymmetry techniques, therefore a supersymmetry-preserving regularisation scheme is chosen. For physical applications, however, a scheme like the t'Hooft-Veltman scheme is better suited.

[6] See for example eq. (5.1) in [239].

with the first term of the QCD beta function,

$$\beta_0 = \frac{11}{3}N - \frac{2}{3}N_F\,. \tag{B.52}$$

The regularisation scheme correction factor $\alpha^{\text{FDH}\to\text{HV}}$ only depends on the number $n_q$ of external quarks (here: two) and is given by[7]

$$\alpha^{\text{FDH}\to\text{HV}} = \frac{c_\Gamma}{(4\pi)^2} g^2 N \left(\frac{4+n_q}{12} - \frac{n_q}{4N^2}\right) \tag{B.53a}$$

$$= \frac{g^2 N}{(4\pi)^2}\left(\frac{4+n_q}{12} - \frac{n_q}{4N^2}\right) + \mathcal{O}(\epsilon^2)\,. \tag{B.53b}$$

It is easy to see that a shift of this kind will at the level of the matrix element result in shifts proportional to the tree matrix element $B_{1g}^{0,\gamma}$. Furthermore note that while the FDH→HV correction will only affect the finite part of $B_{1g}^{1,\gamma}$ and $\tilde{B}_{1g}^{1,\gamma}$, the renormalisation correction will shift the $\epsilon^{-1}$ coefficient of $B_{1g}^{1,\gamma}$ and also introduce a new colour level $N_F/N$, the coefficient of which we denote $\hat{B}_{1g}^{1,\gamma}$. The full one-loop matrix element then reads (see eq. (6.10))

$$\begin{aligned} A_{4,B}^{1\gamma,1-\text{loop}} &= 2\sum_{\text{hel}} \text{Re}\left\{\mathcal{A}_{4,B}^{1\gamma,\text{tree}\,\dagger}\,\mathcal{A}_{4,B}^{1\gamma,1-\text{loop}}\right\} \\ &= \underbrace{\frac{1}{2\pi^2} g^4 e^2 N^2 C_F}_{\mathcal{N}^V}\left(B_{1g}^{1,\gamma} + \frac{N_F}{N}\hat{B}_{1g}^{1,\gamma} - \frac{1}{N^2}\tilde{B}_{1g}^{1,\gamma}\right), \end{aligned} \tag{B.54}$$

which is exactly the result given in eq. (6.10). The colour stripped matrix elements $B_{1g}^{1,\gamma}$, $\hat{B}_{1g}^{1,\gamma}$ and $\tilde{B}_{1g}^{1,\gamma}$ are given in table B.2, where we used that the pole coefficients of $\bar{B}_{1g}^{1,\gamma}$ and $\tilde{\bar{B}}_{1g}^{1,\gamma}$ are proportional to the tree level matrix element $B_{1g}^{0,\gamma}$,

$$\bar{B}_{1g}^{1,\gamma}\big|_{\epsilon^{-1}} = -\underbrace{\left(\mathcal{P}_{q\gamma}^1 + \mathcal{P}_{\bar{q}\gamma}^1 + \frac{3}{2}\right)}_{a_{-1}} B_{1g}^{0,\gamma}\,, \qquad \bar{B}_{1g}^{1,\gamma}\big|_{\epsilon^{-2}} = -2B_{1g}^{0,\gamma}\,, \tag{B.55a}$$

$$\tilde{\bar{B}}_{1g}^{1,\gamma}\big|_{\epsilon^{-1}} = \underbrace{\left(\mathcal{P}_{\bar{q}q}^1 + \frac{3}{2}\right)}_{\tilde{a}_{-1}} B_{1g}^{0,\gamma}\,, \qquad \tilde{\bar{B}}_{1g}^{1,\gamma}\big|_{\epsilon^{-2}} = B_{1g}^{0,\gamma}\,. \tag{B.55b}$$

Here we defined the quantity $\mathcal{P}_{kl}^1 = \ln\left(\frac{\mu^2}{-s_{kl}}\right)$. In table B.3 we list the references for the colour stripped amplitudes, and to what expressions therein they relate.

[7] See for example eq. (5.5) and the following paragraph in [94] or eq. (2.19) in [239]

| | $\epsilon^0$ | $\epsilon^{-1}$ | $\epsilon^{-2}$ |
|---|---|---|---|
| $B_{1g}^{1,\gamma}$ | $\bar{B}_{1g}^{1,\gamma'}\big\|_{\text{finite}} + \left(\frac{\pi^2}{6} - \frac{1}{2}\right) B_{1g}^{0,\gamma}$ | $-\left(a_{-1} + \frac{11}{6}\right) B_{1g}^{0,\gamma}$ | $-2B_{1g}^{0,\gamma}$ |
| $\tilde{B}_{1g}^{1,\gamma}$ | $\tilde{\bar{B}}_{1g}^{1,\gamma'}\big\|_{\text{finite}} + \left(\frac{\pi^2}{12} - \frac{1}{2}\right) B_{1g}^{0,\gamma}$ | $\tilde{a}_{-1} B_{1g}^{0,\gamma}$ | $B_{1g}^{0,\gamma}$ |
| $\hat{B}_{1g}^{1,\gamma}$ | 0 | $\frac{1}{3} B_{1g}^{0,\gamma}$ | 0 |

Table B.2.: Pole structure of the B-type virtual matrix elements. The coefficients $a_{-1}$ and $\tilde{a}_{-1}$ are defined in eqs. (B.55).

| expression in thesis | counterpart in literature | ref. |
|---|---|---|
| $ic_\Gamma (4\pi)^{-2} b_4^{1\gamma,1-\text{loop}}(\bar{q}, q, 1, \gamma)$ | $-A_4^L(\bar{q}, \gamma, q, 1)$ | [94] |
| $ic_\Gamma (4\pi)^{-2} \tilde{b}_4^{1\gamma,1-\text{loop}}(\bar{q}, q, 1, \gamma)$ | $A_4^L(\bar{q}, q, 1, \gamma) - A_4^{\text{SUSY}}(\bar{q}, q, 1, \gamma) + (1 \leftrightarrow \gamma)$ | [94] |

Table B.3.: References for the colour stripped amplitudes used in the B-type virtual corrections.

## B.6. Next-to-next-to-leading order - double real contribution

### B.6.1. B-type matrix element

Starting from the B-type $2q4g$ jet amplitude again [95],

$$\mathcal{A}_{6,B}^{\text{tree}}(\bar{q}, 1, 2, 3, 4, q) = g^4 \sum_{S_3(1,2,3,4)} (1234)_{q\bar{q}} b_6^{\text{tree}}(\bar{q}, 1, 2, 3, 4, q)\,, \tag{B.56}$$

we arrive, after quite some colour algebra, at the full B-type double real dijet matrix element

$$\begin{aligned} A_{6,B}^{\text{tree}} = \sum_{\text{hel}} \left|\mathcal{A}_{6,B}^{\text{tree}}\right|^2 = g^8 N^4 C_F \Bigg( & \sum_{S_4(1,2,3,4)} B_{4g,1234}^0 \\ & - \frac{1}{N^2} \sum_{S_4(1,2,3,4)} \left( \tilde{B}_{4g,123\tilde{4}}^0 + R_{4g,1234}^0 \right) \\ & + \frac{1}{N^4} \sum_{S_4/\mathbb{Z}_4(1,2,3,4)} \tilde{\tilde{B}}_{4g,12\tilde{3}\tilde{4}}^0 + \frac{N^4 - 3N^2 - 1}{N^6} \tilde{\tilde{B}}_{4g}^0 \Bigg)\,, \end{aligned} \tag{B.57}$$

with

$$B^0_{4g,ijkl} = \sum_{\text{hel}} \left| b^{\text{tree}}_{6,ijkl} \right|^2 , \tag{B.58a}$$

$$\tilde{B}^0_{4g,ijk\tilde{l}} = \sum_{\text{hel}} \left| b^{\text{tree}}_{6,ijk\tilde{l}} + b^{\text{tree}}_{6,ij\tilde{l}k} + b^{\text{tree}}_{6,i\tilde{l}jk} + b^{\text{tree}}_{6,\tilde{l}ijk} \right|^2 = \sum_{\text{hel}} \left| b^{1\gamma,\text{tree}}_{6,ijk} \right|^2 , \tag{B.58b}$$

$$\tilde{\tilde{B}}^0_{4g,ij\tilde{k}\tilde{l}} = \sum_{\text{hel}} \left| b^{1\gamma,\text{tree}}_{6,ij\tilde{k}} + b^{1\gamma,\text{tree}}_{6,i\tilde{k}j} + b^{1\gamma,\text{tree}}_{6,\tilde{k}ij} \right|^2 = \sum_{\text{hel}} \left| b^{2\gamma,\text{tree}}_{6,ij} \right|^2 , \tag{B.58c}$$

$$\tilde{\tilde{B}}^0_{4g} = \sum_{\text{hel}} \left| \sum_{S_4(1,2,3,4)} b^{\text{tree}}_{6,1234} \right|^2 = \sum_{\text{hel}} \left| \sum_{S_3(1,2,3)} b^{1\gamma,\text{tree}}_{6,123} \right|^2 = \sum_{\text{hel}} \left| \sum_{S_2(1,2)} b^{2\gamma,\text{tree}}_{6,12} \right|^2 . \tag{B.58d}$$

The $R$-term is a new object we encounter the first time when we have at least six coloured external states. It cannot be written as a square of an amplitude, but is rather given as an interference,

$$\begin{aligned} R^0_{4g,ijkl} = \text{Re} \Big\{ & b^{0,\dagger}_{6,ijkl} \\ & \times \left( b^0_{6,jilk} + b^0_{6,jlik} + b^0_{6,jlki} + b^0_{6,kilj} + b^0_{6,kjli} + b^0_{6,likj} + b^0_{6,ljik} + b^0_{6,lkji} \right) \Big\} . \end{aligned} \tag{B.59}$$

Trading gluon 4 for a photon in the jet amplitude (B.56), we arrive at the 1-photon amplitude

$$\mathcal{A}^{1\gamma,\text{tree}}_{6,B}(\bar{q},1,2,3,q,\gamma) = \sqrt{2} g^3 e Q_q \sum_{S_3(1,2,3)} (123)_{q\bar{q}} b^{1\gamma,\text{tree}}_6(\bar{q},1,2,3,q,\gamma) . \tag{B.60}$$

Its square is the result given in eq. (6.13),

$$\begin{aligned} A^{1\gamma,\text{tree}}_{6,B} = \sum_{\text{hel}} \left| \mathcal{A}^{1\gamma,\text{tree}}_{6,B} \right|^2 = \\ \underbrace{4 g^6 e^2 N^3 C_F}_{\mathcal{N}^{RR}} \left( \sum_{S_3(1,2,3)} B^{0,\gamma}_{3g,123} - \frac{1}{N^2} \sum_{S_3(1,2,3)} \tilde{B}^{0,\gamma}_{3g,123} + \frac{N^2+1}{N^4} \tilde{\tilde{B}}^{0,\gamma}_{3g} \right) \end{aligned} \tag{B.61}$$

with

$$B^{0,\gamma}_{3g,ijk} = \frac{1}{2} Q_q^2 \sum_{\text{hel}} \left| b^{1\gamma,\text{tree}}_{6,ijk} \right|^2 , \tag{B.62a}$$

$$\tilde{B}^{0,\gamma}_{3g,ij\tilde{k}} = \frac{1}{2} Q_q^2 \sum_{\text{hel}} \left| b^{1\gamma,\text{tree}}_{6,ij\tilde{k}} + b^{1\gamma,\text{tree}}_{6,i\tilde{k}j} + b^{1\gamma,\text{tree}}_{6,\tilde{k}ij} \right|^2 = \frac{1}{2} Q_q^2 \sum_{\text{hel}} \left| b^{2\gamma,\text{tree}}_{6,ij} \right|^2 , \tag{B.62b}$$

$$\tilde{\tilde{B}}^{0,\gamma}_{3g} = \frac{1}{2} Q_q^2 \sum_{\text{hel}} \left| \sum_{S_3(1,2,3)} b^{1\gamma,\text{tree}}_{6,123} \right|^2 = \frac{1}{2} Q_q^2 \sum_{\text{hel}} \left| \sum_{S_2(1,2)} b^{2\gamma,\text{tree}}_{6,12} \right|^2 . \tag{B.62c}$$

| expression in thesis | counterpart in literature | ref. | |
|---|---|---|---|
| $b_6^{1\gamma,\text{tree}}(\bar{q},1,2,3,q,\gamma)$ | $A_6(\bar{q},q,1,2,3,\gamma)$ | [95] | MHV - eq. (2.9) in reference<br>N-MHV - eqs. (3.1),(3.2),(3.3) |

Table B.4.: References for the colour stripped amplitude used in the B-type double real corrections.

Trading also gluon 3 for a photon, we obtain the diphoton amplitude

$$\mathcal{A}_{6,B}^{2\gamma,\text{tree}}(\bar{q},1,2,q,\gamma,\gamma) = 2g^2e^2Q_q^2\sum_{S_2(1,2)}(12)_{q\bar{q}}b_6^{2\gamma,\text{tree}}(\bar{q},1,2,q,\gamma,\gamma)\,. \tag{B.63}$$

Squaring this amplitude yields the full B-type diphoton double real matrix element

$$A_{5,6}^{2\gamma,\text{tree}} = \sum_{\text{hel}}\left|\mathcal{A}_{6,B}^{2\gamma,\text{tree}}\right|^2 = 4g^2e^4N^2C_F\left(\sum_{S_2(1,2)}B_{2g,12}^{0,2\gamma} - \frac{1}{N^2}\tilde{B}_{2g}^{0,2\gamma}\right), \tag{B.64}$$

with

$$B_{2g,ij}^{0,2\gamma} = \frac{1}{2}Q_q^2\sum_{\text{hel}}\left|b_{6,ij}^{2\gamma,\text{tree}}\right|^2, \tag{B.65a}$$

$$\tilde{B}_{2g}^{0,2\gamma} = \frac{1}{2}Q_q^2\sum_{\text{hel}}\left|\sum_{S_2(1,2)}b_{6,12}^{2\gamma,\text{tree}}\right|^2. \tag{B.65b}$$

We find the following relations between the jet, 1- and 2-photon colour stripped matrix elements:

$$\tilde{B}_{4g,ijk\tilde{l}}^{0} = \frac{2}{Q_q^2}B_{3g,ijk}^{0,\gamma}\,, \tag{B.66a}$$

$$\tilde{\tilde{B}}_{4g,ij\tilde{k}\tilde{l}}^{0} = \frac{2}{Q_q^2}\tilde{B}_{3g,ij\tilde{k}}^{0,\gamma} = \frac{2}{Q_q^4}B_{2g,ij}^{0,2\gamma}\,, \tag{B.66b}$$

$$\tilde{\tilde{B}}_{4g}^{0} = \frac{2}{Q_q^2}\tilde{\tilde{B}}_{3g}^{0,\gamma} = \frac{2}{Q_q^4}\tilde{B}_{2g}^{0,2\gamma}\,. \tag{B.66c}$$

To increase the numerical stability and boost performance, the 1-photon amplitudes are coded directly from [95], instead of summing the pure QCD amplitudes. The reference for the colour stripped amplitude and the corresponding expression therein is presented in table B.4.

### B.6.2. C/D-type matrix element

The $2q2Q1g1\gamma$ C-type double real radiation tree level amplitude is given by [95]

$$\begin{aligned}\mathcal{A}_{6,C}^{1\gamma,\text{tree}}(\bar{q},1,\bar{Q},Q,q,\gamma) = \\ \sqrt{2}g^3 e\Big[&(1)_{\bar{q}Q}\delta_{\bar{Q}q}\Big(Q_q c_{6,10,q}^{1\gamma,\text{tree}} + Q_Q c_{6,10,Q}^{1\gamma,\text{tree}}\Big) \\ &+ \delta_{\bar{q}Q}(1)_{\bar{Q}q}Q_q c_{6,01,q}^{1\gamma,\text{tree}} + Q_Q c_{6,01,Q}^{1\gamma,\text{tree}}) \\ &- \frac{1}{N}(1)_{\bar{q}q}\delta_{\bar{Q}Q}\Big(Q_q \tilde{c}_{6,10,q}^{1\gamma,\text{tree}} + Q_Q \tilde{c}_{6,10,Q}^{1\gamma,\text{tree}}\Big) \\ &- \frac{1}{N}\delta_{\bar{q}q}(1)_{\bar{Q}Q}\Big(Q_q \tilde{c}_{6,01,q}^{1\gamma,\text{tree}} + Q_Q \tilde{c}_{6,01,Q}^{1\gamma,\text{tree}}\Big)\Big]. \end{aligned} \tag{B.67}$$

The labels 10 and 01 describe which colour line the additional gluon is attached to, which can also be seen by looking at the explicit colour factors. Defining the photonic colour stripped amplitudes[8]

$$c_{6,kl,\gamma}^{1\gamma,\text{tree}} \equiv Q_q c_{6,kl,q}^{1\gamma,\text{tree}} + Q_Q c_{6,kl,Q}^{1\gamma,\text{tree}}\,, \tag{B.68a}$$

$$\tilde{c}_{6,kl,\gamma}^{1\gamma,\text{tree}} \equiv Q_q \tilde{c}_{6,kl,q}^{1\gamma,\text{tree}} + Q_Q \tilde{c}_{6,kl,Q}^{1\gamma,\text{tree}}\,, \tag{B.68b}$$

we can rewrite the full amplitude as

$$\begin{aligned}\mathcal{A}_{6,C}^{1\gamma,\text{tree}} = \sqrt{2}g^3 e\Big[&(1)_{\bar{q}Q}\delta_{\bar{Q}q}c_{6,10,\gamma}^{1\gamma,\text{tree}} + \delta_{\bar{q}Q}(1)_{\bar{Q}q}c_{6,01,\gamma}^{1\gamma,\text{tree}} \\ &- \frac{1}{N}(1)_{\bar{q}q}\delta_{\bar{Q}Q}\tilde{c}_{6,10,\gamma}^{1\gamma,\text{tree}} - \frac{1}{N}\delta_{\bar{q}q}(1)_{\bar{Q}Q}\tilde{c}_{6,01,\gamma}^{1\gamma,\text{tree}}\Big]. \end{aligned} \tag{B.69}$$

Squaring the amplitude we find the result given in eq. (6.14),

$$A_{6,C}^{1\gamma,\text{tree}} = \sum_{\text{hel}} \left|\mathcal{A}_{6,C}^{1\gamma,\text{tree}}\right|^2 = \underbrace{4g^6e^2N^3C_F}_{\mathcal{N}^{RR}}\left(\frac{1}{N}C_{1g}^{0,\gamma} + \frac{1}{N^3}\tilde{C}_{1g}^{0,\gamma}\right) \tag{B.70}$$

with

$$C_{1g}^{0,\gamma} = \frac{1}{2}\sum_{\text{hel}}\left(\left|c_{6,10,\gamma}^{1\gamma,\text{tree}}\right|^2 + \left|c_{6,01,\gamma}^{1\gamma,\text{tree}}\right|^2\right), \tag{B.71a}$$

$$\tilde{C}_{1g}^{0,\gamma} = \frac{1}{2}\sum_{\text{hel}}\left(\left|\tilde{c}_{6,10,\gamma}^{1\gamma,\text{tree}}\right|^2 + \left|\tilde{c}_{6,01,\gamma}^{1\gamma,\text{tree}}\right|^2 - 2\left|\tilde{c}_{6,10,\gamma}^{1\gamma,\text{tree}} + \tilde{c}_{6,01,\gamma}^{1\gamma,\text{tree}}\right|^2\right), \tag{B.71b}$$

where for the SLC matrix element we used the photonic LC-SLC relation

$$c_{6,10,\gamma}^{1\gamma,\text{tree}} + c_{6,01,\gamma}^{1\gamma,\text{tree}} = \tilde{c}_{6,10,\gamma}^{1\gamma,\text{tree}} + \tilde{c}_{6,01,\gamma}^{1\gamma,\text{tree}}\,. \tag{B.72}$$

[8] The labels 10 and 01 correspond to the summation labels $k, l$ in eq. (2.14) of [95]. In the same reference the explicit form of the photonic amplitudes is given for all helicity structures, see eqs. (2.15), (3.5), (3.6) and (3.13) in the reference.

In case of identically flavoured quarks we have to anti-symmetrise the amplitude over the anti-quarks again,

$$\mathcal{A}^{1\gamma,\text{tree}}_{6,C+D}(\bar{q},g,\bar{Q},Q,q,\gamma) = \mathcal{A}^{1\gamma,\text{tree}}_{6,C}(\bar{q},g,\bar{Q},Q,q,\gamma) - \mathcal{A}^{1\gamma,\text{tree}}_{6,C}(\bar{Q},g,\bar{q},Q,q,\gamma)\,, \tag{B.73}$$

So that the interference term is given by (see eqs. (6.16) and (6.17))

$$A^{1\gamma,\text{tree}}_{6,D} = -2 \sum_{\substack{\text{hel}\\(h_q=h_Q)}} \text{Re}\left\{\mathcal{A}^{1\gamma,\text{tree}\,\dagger}_{6,C}(\bar{q},g,\bar{Q},Q,q,\gamma)\mathcal{A}^{1\gamma,\text{tree}}_{6,C}(\bar{Q},g,\bar{q},Q,q,\gamma)\right\} \tag{B.74a}$$

$$= 4g^6e^2VN^2\left(-\frac{1}{N^2}D^{0,\gamma}_{1g} + \frac{1}{N^4}\tilde{D}^{0,\gamma}_{1g}\right) \tag{B.74b}$$

where

$$\begin{aligned} D^{0,\gamma}_{1g} = \sum_{\substack{\text{hel}\\(h_q=h_Q)}} \text{Re}\Big\{ &\big(c_{10}(\bar{q},\bar{Q}) + c_{01}(\bar{q},\bar{Q})\big)^\dagger\big(c_{10}(\bar{Q},\bar{q}) + c_{01}(\bar{Q},\bar{q})\big) \\ &- \tilde{c}_{01}(\bar{q},\bar{Q})^\dagger c_{10}(\bar{Q},\bar{q}) - \tilde{c}_{10}(\bar{q},\bar{Q})^\dagger c_{01}(\bar{Q},\bar{q}) \\ &- \tilde{c}_{01}(\bar{Q},\bar{q})^\dagger c_{10}(\bar{q},\bar{Q}) - \tilde{c}_{10}(\bar{Q},\bar{q})^\dagger c_{01}(\bar{q},\bar{Q})\Big\}\,, \end{aligned} \tag{B.75}$$

$$\tilde{D}^{0,\gamma}_{1g} = -\sum_{\substack{\text{hel}\\(h_q=h_Q)}} \text{Re}\left\{\big(c_{10}(\bar{q},\bar{Q}) + c_{01}(\bar{q},\bar{Q})\big)^\dagger\big(c_{10}(\bar{Q},\bar{q}) + c_{01}(\bar{Q},\bar{q})\big)\right\} \tag{B.76a}$$

$$= -\sum_{\substack{\text{hel}\\(h_q=h_Q)}} \text{Re}\left\{\big(\tilde{c}_{10}(\bar{q},\bar{Q}) + \tilde{c}_{01}(\bar{q},\bar{Q})\big)^\dagger\big(\tilde{c}_{10}(\bar{Q},\bar{q}) + \tilde{c}_{01}(\bar{Q},\bar{q})\big)\right\}. \tag{B.76b}$$

In eqs. (B.75) and (B.76) we used the shorthand notation

$$c_{10} \equiv c^{1\gamma,\text{tree}}_{6,10,\gamma}\,, \qquad\qquad \tilde{c}_{10} \equiv \tilde{c}^{1\gamma,\text{tree}}_{6,10,\gamma}\,.$$

In table B.5 we list the references for the colour stripped amplitudes, and the corresponding expressions in therein.

| expression in thesis | counterpart in literature | ref. | comments |
|---|---|---|---|
| $c^{1\gamma,\text{tree}}_{6,10,\gamma}(\bar{q},1,\bar{Q},Q,q,\gamma)$ | $A^{\text{tree}}_6(\bar{q},q;\bar{Q},Q;1;\emptyset;\gamma)$<br>$A^{\text{tree}}_6(\bar{q},q;\bar{Q},Q;\emptyset;1;\gamma)$ | [95] | MHV - eq. (2.15) in reference<br>N-MHV - eqs. (3.5),(3.6),(3.13) |
| $c^{1\gamma,\text{tree}}_{6,01,\gamma}(\bar{q},1,\bar{Q},Q,q,\gamma)$ | $A^{\text{tree}}_6(\bar{q},q;\bar{Q},Q;\emptyset;1;\gamma)$<br>$A^{\text{tree}}_6(\bar{q},q;\bar{Q},Q;1;\emptyset;\gamma)$ | [95] | MHV - eq. (2.15) in reference<br>N-MHV - eqs. (3.5),(3.6),(3.13) |
| $\tilde{c}^{1\gamma,\text{tree}}_{6,10,\gamma}(\bar{q},1,\bar{Q},Q,q,\gamma)$ | $B^{\text{tree}}_6(\bar{q},q;\bar{Q},Q;1;\emptyset;\gamma)$ | [95] | MHV - eq. (2.15) in reference<br>N-MHV - eqs. (3.5),(3.6),(3.13) |
| $\tilde{c}^{1\gamma,\text{tree}}_{6,01,\gamma}(\bar{q},1,\bar{Q},Q,q,\gamma)$ | $B^{\text{tree}}_6(\bar{q},q;\bar{Q},Q;\emptyset;1;\gamma)$ | [95] | MHV - eq. (2.15) in reference<br>N-MHV - eqs. (3.5),(3.6),(3.13) |

Table B.5.: References for the colour stripped amplitudes used in the C and D-type double real corrections.

## B.7. Next-to-next-to-leading order - real virtual contribution

### B.7.1. B-type matrix element

The one-loop $2q2g1\gamma$ amplitude is given in [94] and [238, 239]. Here we follow the construction in the latter references. In its unrenormalised form it reads[9]

$$\bar{\mathcal{A}}^{1\gamma,1-\text{loop}}_{5,B}(\bar{q},1,2,q,\gamma) = \frac{c_\Gamma}{(4\pi)^2}\sqrt{2}g^4 eQ_q N\left[\sum_{S_2(1,2)}(12)_{q\bar{q}}\bar{\mathcal{B}}^{1\gamma,1-\text{loop}}_{5,12} + [12]\delta_{q\bar{q}}\bar{\mathcal{B}}^{1\gamma,1-\text{loop}}_{5,\text{tr}}\right], \quad \text{(B.77)}$$

where

$$-i\bar{\mathcal{B}}^{1\gamma,1-\text{loop}}_{5,ij} = b^{1\gamma,l}_{ij} + \frac{1}{N^2}b^{1\gamma,s}_{ij} + \frac{N^q_F}{Q_q N}b^{1\gamma,\text{int}} + \frac{N_F}{N}b^{1\gamma,\text{ext}}_{ij}\,, \quad \text{(B.78a)}$$

$$-i\bar{\mathcal{B}}^{1\gamma,1-\text{loop}}_{5,\text{tr}} = \frac{1}{N}b^{1\gamma}_{\text{tr}} - 2\frac{N^q_F}{Q_q N^2}b^{1\gamma,\text{int}}\,. \quad \text{(B.78b)}$$

[9] The difference between the loop factor used here and the one in the reference is $c^{\text{ref}}_\Gamma = e^{\ln(4\pi)-\gamma}c_\Gamma$. In NNLOJET the exponential is absorbed in the overall normalisation.

Note that the internal quark charge factor $N_F^q = \sum_i Q_i$ comes with an inverse power of the external quark charge factor $Q_q$, compensating the $Q_q$ we absorbed into the overall factor. Interfering the loop amplitude with the corresponding tree amplitude $\mathcal{A}_{5,B}^{1\gamma,\text{tree}}$ (B.27) we find

$$\bar{A}_{5,B}^{1\gamma,1-\text{loop}} = 2\sum_{\text{hel}} \text{Re}\left\{\mathcal{A}_{5,B}^{1\gamma,\text{tree}\,\dagger}\bar{\mathcal{A}}_{5,B}^{1\gamma,1-\text{loop}}\right\} \tag{B.79a}$$

$$= \frac{1}{2\pi^2} g^6 e^2 N^3 C_F \left( \sum_{S_2(1,2)} \bar{B}_{2g,12}^{1,\gamma} - \frac{1}{N^2} \sum_{S_2(1,2)} \tilde{\bar{B}}_{2g,12}^{1,\gamma} - \frac{1}{N^2}\tilde{\bar{B}}_{2g}^{1,\gamma} + \frac{1}{N^4}\tilde{\tilde{\bar{B}}}_{2g}^{1,\gamma} \right.$$
$$\left. + \frac{N_F}{N} \sum_{S_2(1,2)} \hat{\bar{B}}_{2g,12}^{1,\gamma} + \frac{N_F}{N^3}\hat{\tilde{\bar{B}}}_{2g}^{1,\gamma} + \frac{N_F^q}{N}\left(1-\frac{4}{N^2}\right)\check{\bar{B}}_{2g}^{1,\gamma} \right), \tag{B.79b}$$

with

$$\bar{B}_{2g,ij}^{1,\gamma} \equiv c_\Gamma \bar{B}_{2g,ij}^{1,\gamma'} = \frac{c_\Gamma}{2} Q_q^2 \sum_{\text{hel}} \text{Re}\left\{ i b_{5,ij}^{1\gamma,\text{tree}\,\dagger} b_{ij}^{1\gamma,l} \right\}, \tag{B.80a}$$

$$\tilde{\bar{B}}_{2g,ij}^{1,\gamma} \equiv c_\Gamma \tilde{\bar{B}}_{2g,ij}^{1,\gamma'} = -\frac{c_\Gamma}{2} Q_q^2 \sum_{\text{hel}} \text{Re}\left\{ i b_{5,ij}^{1\gamma,\text{tree}\,\dagger} b_{ij}^{1\gamma,s} \right\}, \tag{B.80b}$$

$$\tilde{\tilde{\bar{B}}}_{2g}^{1,\gamma} \equiv c_\Gamma \tilde{\tilde{\bar{B}}}_{2g}^{1,\gamma'} = \frac{c_\Gamma}{2} Q_q^2 \sum_{\text{hel}} \text{Re}\left\{ i b_{5,\underline{ij}}^{1\gamma,\text{tree}\,\dagger} b_{\underline{ij}}^{1\gamma,l} - i b_{5,\underline{ij}}^{1\gamma,\text{tree}\,\dagger} b_{\text{tr}}^{1\gamma} \right\}, \tag{B.80c}$$

$$\check{\tilde{\bar{B}}}_{2g}^{1,\gamma} \equiv c_\Gamma \check{\tilde{\bar{B}}}_{2g}^{1,\gamma'} = -\frac{c_\Gamma}{2} Q_q^2 \sum_{\text{hel}} \text{Re}\left\{ i b_{5,\underline{ij}}^{1\gamma,\text{tree}\,\dagger} b_{\underline{ij}}^{1\gamma,s} \right\}, \tag{B.80d}$$

$$\hat{\bar{B}}_{2g,ij}^{1,\gamma} \equiv c_\Gamma \hat{\bar{B}}_{2g,ij}^{1,\gamma'} = \frac{c_\Gamma}{2} Q_q^2 \sum_{\text{hel}} \text{Re}\left\{ i b_{5,ij}^{1\gamma,\text{tree}\,\dagger} b_{ij}^{1\gamma,\text{ext}} \right\}, \tag{B.80e}$$

$$\hat{\tilde{\bar{B}}}_{2g}^{1,\gamma} \equiv c_\Gamma \hat{\tilde{\bar{B}}}_{2g}^{1,\gamma'} = \frac{c_\Gamma}{2} Q_q^2 \sum_{\text{hel}} \text{Re}\left\{ i b_{5,\underline{ij}}^{1\gamma,\text{tree}\,\dagger} b_{\underline{ij}}^{1\gamma,\text{ext}} \right\} \equiv 0, \tag{B.80f}$$

$$\check{\bar{B}}_{2g}^{1,\gamma} \equiv c_\Gamma \check{\bar{B}}_{2g}^{1,\gamma'} = \frac{c_\Gamma}{2} \sum_{\text{hel}} \text{Re}\left\{ i b_{5,\underline{ij}}^{1\gamma,\text{tree}\,\dagger} b^{1\gamma,\text{int}} \right\}. \tag{B.80g}$$

Here $\underline{ij}$ means that one has to sum over both orderings of the indices, e.g.

$$b_{5,\underline{ij}}^{1\gamma,\text{tree}\,\dagger} b_{\underline{ij}}^{1\gamma,l} = \left(b_{5,ij}^{1\gamma,\text{tree}} + b_{5,ji}^{1\gamma,\text{tree}}\right)^\dagger \left(b_{ij}^{1\gamma,l} + b_{ji}^{1\gamma,l}\right). \tag{B.81}$$

Note that for the unrenormalised matrix element, the subleading $N_F$ contribution $\hat{\tilde{\bar{B}}}_{2g}^{1,\gamma}$ vanishes because $b_{ij}^{1\gamma,\text{ext}} = -b_{ji}^{1\gamma,\text{ext}}$, so $b_{\underline{ij}}^{1\gamma,\text{ext}} = 0$. Expanding $c_\Gamma$ and the primed amplitudes in $\epsilon$, like we did for the virtual amplitudes (see eq. (B.49), we can rewrite the above matrix elements as

$$B = c_\Gamma B' = \left(B'\big|_{\text{finite}} - \frac{\pi^2}{12} B'\big|_{\epsilon^{-2}}\right) + \frac{1}{\epsilon} B'\big|_{\epsilon^{-1}} + \frac{1}{\epsilon^2} B'\big|_{\epsilon^{-2}} + \mathcal{O}(\epsilon) \tag{B.82}$$

To get the renormalised matrix elements, shifted to the 't Hooft-Veltman scheme, we again have to subtract the appropriate correction factors from the one-loop amplitude:

$$\bar{\mathcal{A}}_{5,B}^{1\gamma,1-\text{loop}} \quad \to \quad \mathcal{A}_{5,B}^{1\gamma,1-\text{loop}} = \bar{\mathcal{A}}_{5,B}^{1\gamma,1-\text{loop}} - \left(\alpha_4^{\text{UV}} + \alpha^{\text{FDH}\to\text{HV}}\right)\mathcal{A}_{5,B}^{1\gamma,\text{tree}}, \tag{B.83}$$

where (see eq. (B.51))

$$\alpha_4^{\mathrm{UV}} = \frac{g^2 N}{(4\pi)^2}\frac{1}{\epsilon}\left(\frac{11}{3} - \frac{2}{3}\frac{N_F}{N}\right) + \mathcal{O}(\epsilon)\,, \tag{B.84}$$

and (see eq. (B.53))

$$\alpha^{\mathrm{FDH}\to\mathrm{HV}} = \frac{g^2 N}{(4\pi)^2}\left(\frac{1}{2} - \frac{1}{2N^2}\right) + \mathcal{O}(\epsilon^2)\,. \tag{B.85}$$

Taking all the shifts and corrections into account, we arrive at the full renormalised matrix element as given in eq. (6.19),

$$A_{5,B}^{1\gamma,1-\mathrm{loop}} = 2\sum_{\mathrm{hel}} \mathrm{Re}\left\{\mathcal{A}_{5,B}^{1\gamma,\mathrm{tree}\,\dagger}\mathcal{A}_{5,B}^{1\gamma,1-\mathrm{loop}}\right\} \tag{B.86a}$$

$$= \underbrace{\frac{1}{2\pi^2}g^6 e^2 N^3 C_F}_{\mathcal{N}^{RV}}\left(\sum_{S_2(1,2)} B_{2g,12}^{1,\gamma} - \frac{1}{N^2}\sum_{S_2(1,2)}\tilde{B}_{2g,12}^{1,\gamma} - \frac{1}{N^2}\tilde{\tilde{B}}_{2g}^{1,\gamma} + \frac{1}{N^4}\tilde{\tilde{\tilde{B}}}_{2g}^{1,\gamma}\right.$$
$$\left. + \frac{N_F}{N}\sum_{S_2(1,2)}\hat{B}_{2g,12}^{1,\gamma} + \frac{N_F}{N^3}\hat{\tilde{B}}_{2g}^{1,\gamma} + \frac{N_F^q}{N}\left(1 - \frac{4}{N^2}\right)\check{B}_{2g}^{1,\gamma}\right)\,. \tag{B.86b}$$

The colour stripped matrix elements are given in table B.6. We used that the poles of the unrenormalised colour stripped matrix elements are given by

$$\bar{B}_{2g,ij}^{1,\gamma}\big|_{\epsilon^{-2}} = -3B_{2g,ij}^{0,\gamma}\,, \tag{B.87a}$$

$$\tilde{\bar{B}}_{2g,ij}^{1,\gamma}\big|_{\epsilon^{-2}} = -B_{2g,ij}^{0,\gamma}\,, \tag{B.87b}$$

$$\tilde{\tilde{B}}_{2g}^{1,\gamma}\big|_{\epsilon^{-2}} = -3\tilde{B}_{2g}^{0,\gamma}\,, \tag{B.87c}$$

$$\tilde{\tilde{\tilde{B}}}_{2g}^{1,\gamma}\big|_{\epsilon^{-2}} = -\tilde{B}_{2g}^{0,\gamma}\,, \tag{B.87d}$$

and

$$\bar{B}_{2g,ij}^{1,\gamma}\big|_{\epsilon^{-2}} = -\left(\mathcal{P}_{qi}^1 + \mathcal{P}_{\bar{q}j}^1 + \mathcal{P}_{ij}^1 + \frac{3}{2}\right)B_{2g,ij}^{0,\gamma} = -a_{-1,ij}B_{2g,ij}^{0,\gamma}\,, \tag{B.88a}$$

$$\tilde{\bar{B}}_{2g,ij}^{1,\gamma}\big|_{\epsilon^{-2}} = -\left(\mathcal{P}_{\bar{q}q}^1 + \frac{3}{2}\right)B_{2g,ij}^{0,\gamma} = -\tilde{a}_{-1}B_{2g,ij}^{0,\gamma}\,, \tag{B.88b}$$

$$\tilde{\tilde{B}}_{2g}^{1,\gamma}\big|_{\epsilon^{-2}} = -\left(\mathcal{P}_{q1}^1 + \mathcal{P}_{q2}^1 + \mathcal{P}_{\bar{q}1}^1 + \mathcal{P}_{\bar{q}2}^1 - \mathcal{P}_{\bar{q}q}^1 + \frac{3}{2}\right)\tilde{B}_{2g}^{0,\gamma} = -\tilde{\tilde{a}}_{-1}\tilde{B}_{2g,ij}^{0,\gamma}\,, \tag{B.88c}$$

$$\tilde{\tilde{\tilde{B}}}_{2g}^{1,\gamma}\big|_{\epsilon^{-2}} = -\left(\mathcal{P}_{\bar{q}q}^1 + \frac{3}{2}\right)\tilde{B}_{2g}^{0,\gamma} = -\tilde{a}_{-1}\tilde{B}_{2g,ij}^{0,\gamma}\,, \tag{B.88d}$$

| | $\epsilon^0$ | $\epsilon^{-1}$ | $\epsilon^{-2}$ |
|---|---|---|---|
| $B^{1,\gamma}_{2g,ij}$ | $\bar{B}^{1,\gamma'}_{2g,ij}\big\vert_{\text{finite}} + \left(\frac{\pi^2}{4} - \frac{1}{2}\right) B^{0,\gamma}_{2g,ij}$ | $-\left(a_{-1,ij} + \frac{11}{3}\right) B^{0,\gamma}_{2g,ij}$ | $-3B^{0,\gamma}_{2g,ij}$ |
| $\tilde{B}^{1,\gamma}_{2g,ij}$ | $\tilde{\bar{B}}^{1,\gamma'}_{2g,ij}\big\vert_{\text{finite}} + \left(\frac{\pi^2}{12} - \frac{1}{2}\right) B^{0,\gamma}_{2g,ij}$ | $-\tilde{a}_{-1} B^{0,\gamma}_{2g,ij}$ | $-B^{0,\gamma}_{2g,ij}$ |
| $\tilde{\tilde{B}}^{1,\gamma}_{2g}$ | $\tilde{\tilde{\bar{B}}}^{1,\gamma'}_{2g}\big\vert_{\text{finite}} + \left(\frac{\pi^2}{4} - \frac{1}{2}\right) \tilde{B}^{0,\gamma}_{2g}$ | $-\left(\tilde{\tilde{a}}_{-1} + \frac{11}{3}\right) \tilde{B}^{0,\gamma}_{2g}$ | $-3\tilde{B}^{0,\gamma}_{2g}$ |
| $\tilde{\tilde{B}}^{1,\gamma}_{2g}$ | $\tilde{\tilde{\bar{B}}}^{1,\gamma'}_{2g}\big\vert_{\text{finite}} + \left(\frac{\pi^2}{12} - \frac{1}{2}\right) \tilde{B}^{0,\gamma}_{2g}$ | $-\tilde{a}_{-1} \tilde{B}^{0,\gamma}_{2g}$ | $-\tilde{B}^{0,\gamma}_{2g}$ |
| $\hat{B}^{1,\gamma}_{2g,ij}$ | $\hat{\bar{B}}^{1,\gamma'}_{2g,ij}\big\vert_{\text{finite}}$ | $\frac{2}{3} B^{0,\gamma}_{2g,ij}$ | $0$ |
| $\hat{\tilde{B}}^{1,\gamma}_{2g}$ | $0$ | $\frac{2}{3} \tilde{B}^{0,\gamma}_{2g}$ | $0$ |
| $\check{B}^{1,\gamma}_{2g}$ | $\check{\bar{B}}^{1,\gamma'}_{2g}\big\vert_{\text{finite}}$ | $0$ | $0$ |

Table B.6.: Pole structure of the B-type real-virtual matrix elements. The coefficients $a_{-1,ij}$, $\tilde{a}_{-1}$ and $\tilde{\tilde{a}}_{-1}$ are defined in eqs. (B.88).

where again $\mathcal{P}^1_{kl} = \ln\left(\frac{\mu^2}{-s_{kl}}\right)$. The other matrix elements do not have explicit poles in $\epsilon$. In table B.7 we list the references for the partial and colour stripped amplitudes, and to what expressions therein they relate.

## B.7.2. C/D-type matrix element

We take the $2q2Q1\gamma$ one-loop amplitude from [238]. It reads[10]

$$\begin{aligned}\bar{\mathcal{A}}^{1\gamma,1-\text{loop}}_{5,C}(\bar{q},\bar{Q},Q,q,\gamma) = \\ \frac{c_\Gamma}{(4\pi)^2}\sqrt{2}g^4 eN\Big[\delta_{q\bar{Q}}\delta_{Q\bar{q}}\Big(Q_q\bar{\mathcal{C}}^{1\gamma,1-\text{loop}}_{5,q} + Q_Q\bar{\mathcal{C}}^{1\gamma,1-\text{loop}}_{5,Q}\Big) \\ - \frac{1}{N}\delta_{q\bar{q}}\delta_{Q\bar{Q}}\Big(Q_q\tilde{\bar{\mathcal{C}}}^{1\gamma,1-\text{loop}}_{5,q} + Q_Q\tilde{\bar{\mathcal{C}}}^{1\gamma,1-\text{loop}}_{5,Q}\Big)\Big]. \end{aligned} \tag{B.89}$$

The partial amplitudes have an internal colour structure and can be decomposed further,

$$-i\bar{\mathcal{C}}^{1\gamma,1-\text{loop}}_{5,q} = c^{1\gamma,l}_5 + \frac{1}{N^2}c^{1\gamma,s}_5 + \frac{N_F}{N}c^{1\gamma,N_F}_5\,, \tag{B.90a}$$

$$-i\tilde{\bar{\mathcal{C}}}^{1\gamma,1-\text{loop}}_{5,q} = \tilde{c}^{1\gamma,l}_5 + \frac{1}{N^2}\tilde{c}^{1\gamma,s}_5 - \frac{N_F}{N}c^{1\gamma,N_F}_5\,. \tag{B.90b}$$

The remaining two partial amplitudes are related to those above via

$$\bar{\mathcal{C}}^{1\gamma,1-\text{loop}}_{5,Q}(\bar{q},\bar{Q},Q,q,\gamma) = \bar{\mathcal{C}}^{1\gamma,1-\text{loop}}_{5,q}(\bar{Q},\bar{q},q,Q,\gamma)\,, \tag{B.91a}$$

$$\tilde{\bar{\mathcal{C}}}^{1\gamma,1-\text{loop}}_{5,Q}(\bar{q},\bar{Q},Q,q,\gamma) = \tilde{\bar{\mathcal{C}}}^{1\gamma,1-\text{loop}}_{5,q}(\bar{Q},\bar{q},q,Q,\gamma)\,. \tag{B.91b}$$

[10] The difference between the loop factor used here and the one in the reference is $c^{\text{ref}}_\Gamma = e^{\ln(4\pi)-\gamma}c_\Gamma$. In NNLOJET the exponential is absorbed in the overall normalisation.

| expression in thesis | counterpart in literature | ref. | comments |
|---|---|---|---|
| $c_\Gamma N \mathcal{B}^{1\gamma,1-\text{loop}}_{5,12}$ | $b^{1\gamma,(1)}_{12}$ | [238, 239] | |
| $c_\Gamma N \mathcal{B}^{1\gamma,1-\text{loop}}_{5,\text{tr}}$ | $b^{1\gamma,(1)}_{\text{tr}}$ | [238, 239] | |
| $b^{1\gamma,l}_{12}$ | $\mathcal{B}^{1\gamma,l}_{12}$ | [239] | |
| $b^{1\gamma,s}_{12}$ | $\mathcal{B}^{1\gamma,s}_{12}$ | [239] | |
| $b^{1\gamma,\text{int}}$ | $\mathcal{B}^{1\gamma,\text{int}}_{12}$ | [238] | Corresponds to $-B^{N_F}$ in [239]. For the construction we use that $B^{N_F}$ is symmetric under interchange of same-helicity bosons. |
| $b^{1\gamma,\text{ext}}$ | $\mathcal{B}^{1\gamma,\text{ext}}$ | [238] | In (5.86) of [239] this bit is merged with $B^{N_F}$. |
| $b^{1\gamma}_{\text{tr}}$ | $\mathcal{B}^{1\gamma}_{\text{tr}}$ | [239] | |

Table B.7.: References for the partial and colour stripped amplitudes used in the B-type real virtual corrections.

Interfering with the corresponding tree amplitude $\mathcal{A}^{1\gamma,\text{tree}}_{5,C}$ (B.35) we get

$$\bar{A}^{1\gamma,1-\text{loop}}_{5,C} = 2\sum_{\text{hel}} \text{Re}\left\{\mathcal{A}^{1\gamma,\text{tree}\,\dagger}_{5,C}\bar{\mathcal{A}}^{1\gamma,1-\text{loop}}_{5,C}\right\} \tag{B.92a}$$

$$= \frac{1}{2\pi^2} g^6 e^2 N^3 C_F \left(\frac{1}{N}\bar{C}^{1,\gamma}_{0g} + \frac{1}{N^3}\tilde{\bar{C}}^{1,\gamma}_{0g} + \frac{N_F}{N^2}\hat{\bar{C}}^{1,\gamma}_{0g}\right) \tag{B.92b}$$

with

$$\bar{C}^{1,\gamma}_{0g} \equiv c_\Gamma \bar{C}^{1,\gamma'}_{0g} = \frac{c_\Gamma}{2}\sum_{\text{hel}} \text{Re}\left\{i c^{1\gamma,\text{tree}\,\dagger}_{5,\gamma} c^{1\gamma,l}_{5,\gamma}\right\}, \tag{B.93a}$$

$$\tilde{\bar{C}}^{1,\gamma}_{0g} \equiv c_\Gamma \tilde{\bar{C}}^{1,\gamma'}_{0g} = \frac{c_\Gamma}{2}\sum_{\text{hel}} \text{Re}\left\{i c^{1\gamma,\text{tree}\,\dagger}_{5,\gamma} c^{1\gamma,s}_{5,\gamma}\right\}, \tag{B.93b}$$

$$\hat{\bar{C}}^{1,\gamma}_{0g} \equiv c_\Gamma \hat{\bar{C}}^{1,\gamma'}_{0g} = \frac{c_\Gamma}{2}\sum_{\text{hel}} \text{Re}\left\{i c^{1\gamma,\text{tree}\,\dagger}_{5,\gamma} c^{1\gamma,N_F}_{5,\gamma}\right\}, \tag{B.93c}$$

where $c^{1\gamma,\text{tree}}_{5,\gamma}$ is defined as in eq. (B.38) and the one-loop analogues as

$$c^{1\gamma,l}_{5,\gamma}(\bar{q},\bar{Q},Q,q,\gamma) \equiv Q_q c^{1\gamma,l}_5(\bar{q},\bar{Q},Q,q,\gamma) + Q_Q c^{1\gamma,l}_5(\bar{Q},\bar{q},q,Q,\gamma), \tag{B.94a}$$

$$c^{1\gamma,s}_{5,\gamma}(\bar{q},\bar{Q},Q,q,\gamma) \equiv Q_q c^{1\gamma,s}_5(\bar{q},\bar{Q},Q,q,\gamma) + Q_Q c^{1\gamma,s}_5(\bar{Q},\bar{q},q,Q,\gamma), \tag{B.94b}$$

$$c^{1\gamma,N_F}_{5,\gamma}(\bar{q},\bar{Q},Q,q,\gamma) \equiv Q_q c^{1\gamma,N_F}_5(\bar{q},\bar{Q},Q,q,\gamma) + Q_Q c^{1\gamma,N_F}_5(\bar{Q},\bar{q},q,Q,\gamma). \tag{B.94c}$$

Note that the subleading amplitudes $\tilde{\tilde{\mathcal{C}}}^{1\gamma,1-\text{loop}}_{5,q}$ and $\tilde{\tilde{\mathcal{C}}}^{1\gamma,1-\text{loop}}_{5,Q}$ do not contribute, which can be attributed to the way the colour structures of the tree and one-loop amplitudes interfere in this particular case.

We again have to expand the colour stripped matrix elements in $\epsilon$ according to (see eq. (B.49)),

$$C = c_\Gamma C' = \left(C'\big|_{\text{finite}} - \frac{\pi^2}{12} C'\big|_{\epsilon^{-2}}\right) + \frac{1}{\epsilon} C'\big|_{\epsilon^{-1}} + \frac{1}{\epsilon^2} C'\big|_{\epsilon^{-2}} + \mathcal{O}(\epsilon)\,, \tag{B.95}$$

renormalise them and apply the FDH→HV shift,

$$\bar{\mathcal{A}}^{1\gamma,1-\text{loop}}_{5,C} \quad \to \quad \mathcal{A}^{1\gamma,1-\text{loop}}_{5,C} = \bar{\mathcal{A}}^{1\gamma,1-\text{loop}}_{5,C} - \left(\alpha_4^{\text{UV}} + \alpha^{\text{FDH}\to\text{HV}}\right)\mathcal{A}^{1\gamma,\text{tree}}_{5,C}\,, \tag{B.96}$$

where the renormalisation factor is the same as for the B-types, as it only depends on the number of external QCD legs (see eq. (B.51)),

$$\alpha_4^{\text{UV}} = \frac{g^2 N}{(4\pi)^2}\frac{1}{\epsilon}\left(\frac{11}{3} - \frac{2}{3}\frac{N_F}{N}\right) + \mathcal{O}(\epsilon)\,, \tag{B.97}$$

and the scheme conversion factor for four-quark amplitudes is given by ($n_q = 4$ in eq. (B.53)[11])

$$\alpha^{\text{FDH}\to\text{HV}} = \frac{g^2 N}{(4\pi)^2}\left(\frac{2}{3} - \frac{1}{N^2}\right) + \mathcal{O}(\epsilon^2)\,. \tag{B.98}$$

We eventually obtain the result given in eq. (6.21),

$$A^{1\gamma,1-\text{loop}}_{5,C} = 2\sum_{\text{hel}} \text{Re}\left\{\mathcal{A}^{1\gamma,\text{tree}\,\dagger}_{5,C}\mathcal{A}^{1\gamma,1-\text{loop}}_{5,C}\right\} \tag{B.99a}$$

$$= \underbrace{\frac{1}{2\pi^2} g^6 e^2 N^3 C_F}_{\mathcal{N}^{RV}} \left(\frac{1}{N} C^{1,\gamma}_{0g} + \frac{1}{N^3}\tilde{C}^{1,\gamma}_{0g} + \frac{N_F}{N^2}\hat{C}^{1,\gamma}_{0g}\right). \tag{B.99b}$$

The colour stripped matrix elements are given in table B.8. We again explicitly write out the poles of the colour stripped unrenormalised matrix elements,

$$\bar{C}^{1,\gamma}_{0g}\big|_{\epsilon^{-2}} = -2C^{0,\gamma}_{0g}\,, \tag{B.100a}$$

$$\tilde{\bar{C}}^{1,\gamma}_{0g}\big|_{\epsilon^{-2}} = 2C^{0,\gamma}_{0g}\,, \tag{B.100b}$$

$$\hat{\bar{C}}^{1,\gamma}_{0g}\big|_{\epsilon^{-2}} = 0\,, \tag{B.100c}$$

[11] See for example eq. (6.5) in [240].

| | $\epsilon^0$ | $\epsilon^{-1}$ | $\epsilon^{-2}$ |
|---|---|---|---|
| $C_{0g}^{1,\gamma}$ | $\bar{C}_{0g}^{1,\gamma\,\prime}\big\|_{\text{finite}} + \left(\frac{\pi^2}{6} - \frac{2}{3}\right) C_{0g}^{0,\gamma}$ | $-\left(a_{-1,c} + \frac{11}{3}\right) C_{0g}^{0,\gamma}$ | $-2C_{0g}^{0,\gamma}$ |
| $\tilde{C}_{0g}^{1,\gamma}$ | $\tilde{\bar{C}}_{0g}^{1,\gamma\,\prime}\big\|_{\text{finite}} - \left(\frac{\pi^2}{6} - 1\right) C_{0g}^{0,\gamma}$ | $\tilde{a}_{-1,c} C_{0g}^{0,\gamma}$ | $2C_{0g}^{0,\gamma}$ |
| $\hat{C}_{0g}^{1,\gamma}$ | $\hat{\bar{C}}_{0g}^{1,\gamma\,\prime}\big\|_{\text{finite}}$ | $0$ | $0$ |

Table B.8.: Pole structure of the C-type real-virtual matrix elements. The coefficients $a_{-1,c}$ and $\tilde{a}_{-1,c}$ are defined in eqs. (B.101). The $\epsilon^{-1}$ coefficient of $\hat{\bar{C}}_{0g}^{1,\gamma}$ is cancelled exactly by the renormalisation correction.

and

$$\bar{C}_{0g}^{1,\gamma}\big|_{\epsilon^{-1}} = -\left(\mathcal{P}^1_{\bar{q}Q} + \mathcal{P}^1_{q\bar{Q}} - \frac{2}{3}\right) C_{0g}^{0,\gamma} = -a_{-1,c} C_{0g}^{0,\gamma}\,, \tag{B.101a}$$

$$\tilde{\bar{C}}_{0g}^{1,\gamma}\big|_{\epsilon^{-1}} = \left(\mathcal{P}^1_{\bar{q}q} + \mathcal{P}^1_{\bar{Q}Q} - 2\mathcal{P}^1_{\bar{q}\bar{Q}} - 2\mathcal{P}^1_{qQ} + 2\mathcal{P}^1_{\bar{q}Q} + 2\mathcal{P}^1_{q\bar{Q}} + 3\right) C_{0g}^{0,\gamma} = \tilde{a}_{-1,c} C_{0g}^{0,\gamma}\,, \tag{B.101b}$$

$$\hat{\bar{C}}_{0g}^{1,\gamma}\big|_{\epsilon^{-1}} = -\frac{2}{3} C_{0g}^{0,\gamma}\,, \tag{B.101c}$$

with $\mathcal{P}^1_{kl} = \ln\left(\frac{\mu^2}{-s_{kl}}\right)$. Note that the renormalisation actually removes the $\epsilon^{-1}$ coefficient present in the unrenormalised $\hat{\bar{C}}_{0g}^{1,\gamma}$. In table B.10 we list the references for the partial and colour stripped amplitudes, and to what expressions therein they relate.

In case of identically flavoured quarks we have to anti-symmetrise both the tree and the one-loop amplitude over the anti-quarks before interfering them (compare eq. (B.42)):

$$\mathcal{A}^{1\gamma,\text{tree}}_{5,C+D}(\bar{q},\bar{Q},Q,q,\gamma) = \mathcal{A}^{1\gamma,\text{tree}}_{5,C}(\bar{q},\bar{Q},Q,q,\gamma) - \mathcal{A}^{1\gamma,\text{tree}}_{5,C}(\bar{Q},\bar{q},Q,q,\gamma)\,, \tag{B.102}$$

$$\mathcal{A}^{1\gamma,1-\text{loop}}_{5,C+D}(\bar{q},\bar{Q},Q,q,\gamma) = \mathcal{A}^{1\gamma,1-\text{loop}}_{5,C}(\bar{q},\bar{Q},Q,q,\gamma) - \mathcal{A}^{1\gamma,1-\text{loop}}_{5,C}(\bar{Q},\bar{q},Q,q,\gamma)\,. \tag{B.103}$$

We can directly work with the renormalised amplitudes in the t'Hooft-Veltman scheme for which we explained the derivation above. The expansion in $\epsilon$ (eq. (B.95)) shows the same effect on the D-type amplitudes as on the C-types. For the tree×one-loop interference we find the result given in eq. (6.25),

$$\begin{aligned} A^{1\gamma,1-\text{loop}}_{5,D} = -2 \sum_{\substack{\text{hel}\\(h_q = h_Q)}} \text{Re}\Big\{ & \mathcal{A}^{1\gamma,\text{tree}\,\dagger}_{5,C}(\bar{q},\bar{Q}) \mathcal{A}^{1\gamma,1-\text{loop}}_{5,C}(\bar{Q},\bar{q}) \\ & + \mathcal{A}^{1\gamma,\text{tree}\,\dagger}_{5,C}(\bar{Q},\bar{q}) \mathcal{A}^{1\gamma,1-\text{loop}}_{5,C}(\bar{q},\bar{Q}) \Big\} \end{aligned} \tag{B.104a}$$

$$= \underbrace{\frac{1}{2\pi^2} g^6 e^2 N^3 C_F}_{\mathcal{N}^{RV}} \left( \frac{1}{N^2} D_{0g}^{1,\gamma} + \frac{1}{N^4} \tilde{D}_{0g}^{1,\gamma} + \frac{N_F}{N^3} \hat{D}_{0g}^{1,\gamma} \right). \tag{B.104b}$$

| | $\epsilon^0$ | $\epsilon^{-1}$ | $\epsilon^{-2}$ |
|---|---|---|---|
| $D_{0g}^{1,\gamma}$ | $\bar{D}_{0g}^{1,\gamma'}\Big\vert_{\text{finite}} - \left(\frac{\pi^2}{6} - \frac{2}{3}\right) D_{0g}^{0,\gamma}$ | $\left(a_{-1,d} + \frac{11}{3}\right) D_{0g}^{0,\gamma}$ | $2D_{0g}^{0,\gamma}$ |
| $\tilde{D}_{0g}^{1,\gamma}$ | $\tilde{\bar{D}}_{0g}^{1,\gamma'}\Big\vert_{\text{finite}} + \left(\frac{\pi^2}{6} - 1\right) D_{0g}^{0,\gamma}$ | $-\tilde{a}_{-1,d} D_{0g}^{0,\gamma}$ | $-2D_{0g}^{0,\gamma}$ |
| $\hat{D}_{0g}^{1,\gamma}$ | $\hat{\bar{D}}_{0g}^{1,\gamma'}\Big\vert_{\text{finite}}$ | $0$ | $0$ |

Table B.9.: Pole structure of the D-type real-virtual matrix elements. The coefficients $a_{-1,d}$ and $\tilde{a}_{-1,d}$ are defined in eqs. (B.108). The $\epsilon^{-1}$ coefficient of $\hat{\bar{D}}_{0g}^{1,\gamma}$ is cancelled exactly by the renormalisation correction.

The colour stripped matrix elements are given in table B.9, where we defined

$$\bar{D}_{0g}^{1,\gamma'} = -\frac{1}{2}\sum_{\text{hel}} \text{Re}\left\{ ic_{5,\gamma}^{1\gamma,\text{tree}\dagger}(\bar{q},\bar{Q}) \tilde{c}_{5,\gamma}^{1\gamma,l}(\bar{Q},\bar{q}) + \left(\bar{q} \leftrightarrow \bar{Q}\right)\right\}, \tag{B.105a}$$

$$\tilde{\bar{D}}_{0g}^{1,\gamma'} = -\frac{1}{2}\sum_{\text{hel}} \text{Re}\left\{ ic_{5,\gamma}^{1\gamma,\text{tree}\dagger}(\bar{q},\bar{Q}) \tilde{c}_{5,\gamma}^{1\gamma,s}(\bar{Q},\bar{q}) + \left(\bar{q} \leftrightarrow \bar{Q}\right)\right\}, \tag{B.105b}$$

$$\hat{\bar{D}}_{0g}^{1,\gamma'} = \frac{1}{2}\sum_{\text{hel}} \text{Re}\left\{ ic_{5,\gamma}^{1\gamma,\text{tree}\dagger}(\bar{q},\bar{Q}) c_{5,\gamma}^{1\gamma,N_F}(\bar{Q},\bar{q}) + \left(\bar{q} \leftrightarrow \bar{Q}\right)\right\}. \tag{B.105c}$$

Here $c_{5,\gamma}^{1\gamma,N_F}$ is as in (B.94c), and

$$\tilde{c}_{5,\gamma}^{1\gamma,l}(\bar{q},\bar{Q},Q,q,\gamma) \equiv Q_q \tilde{c}_5^{1\gamma,l}(\bar{q},\bar{Q},Q,q,\gamma) + Q_Q \tilde{c}_5^{1\gamma,l}(\bar{Q},\bar{q},q,Q,\gamma), \tag{B.106a}$$

$$\tilde{c}_{5,\gamma}^{1\gamma,s}(\bar{q},\bar{Q},Q,q,\gamma) \equiv Q_q \tilde{c}_5^{1\gamma,s}(\bar{q},\bar{Q},Q,q,\gamma) + Q_Q \tilde{c}_5^{1\gamma,s}(\bar{Q},\bar{q},q,Q,\gamma). \tag{B.106b}$$

Note that we only get contributions from the subleading partial amplitudes $\tilde{\tilde{c}}_{5,q}^{1\gamma,1-\text{loop}}$ and $\tilde{\tilde{c}}_{5,Q}^{1\gamma,1-\text{loop}}$, which again is related to the particular colour structure in the interference. The poles of the matrix elements defined in eqs.(B.105a)-(B.105c) are given by

$$\bar{D}_{0g}^{1,\gamma}\big\vert_{\epsilon^{-2}} = 2D_{0g}^{0,\gamma}, \tag{B.107a}$$

$$\tilde{\bar{D}}_{0g}^{1,\gamma}\big\vert_{\epsilon^{-2}} = -2D_{0g}^{0,\gamma}, \tag{B.107b}$$

$$\hat{\bar{D}}_{0g}^{1,\gamma}\big\vert_{\epsilon^{-2}} = 0, \tag{B.107c}$$

and

$$\bar{D}_{0g}^{1,\gamma}\big\vert_{\epsilon^{-1}} = -\left(\mathcal{P}_{\bar{q}\bar{Q}}^1 + \mathcal{P}_{qQ}^1 - \frac{2}{3}\right) D_{0g}^{0,\gamma} = a_{-1,d} D_{0g}^{0,\gamma}, \tag{B.108a}$$

$$\tilde{\bar{D}}_{0g}^{1,\gamma}\big\vert_{\epsilon^{-1}} = \left(\mathcal{P}_{\bar{q}q}^1 + \mathcal{P}_{\bar{Q}Q}^1 - \mathcal{P}_{\bar{q}\bar{Q}}^1 - \mathcal{P}_{qQ}^1 + \mathcal{P}_{\bar{q}Q}^1 + \mathcal{P}_{q\bar{Q}}^1 + 3\right) D_{0g}^{0,\gamma} = -\tilde{a}_{-1,d} D_{0g}^{0,\gamma}, \tag{B.108b}$$

$$\hat{\bar{D}}_{0g}^{1,\gamma}\big\vert_{\epsilon^{-1}} = \frac{2}{3} D_{0g}^{0,\gamma}, \tag{B.108c}$$

with $\mathcal{P}_{kl}^1 = \ln\left(\frac{\mu^2}{-s_{kl}}\right)$. As for $\hat{C}_{0g}^{1,\gamma}$ the $\epsilon^{-1}$ coefficient of $\hat{\bar{D}}_{0g}^{1,\gamma}$ is exactly cancelled by the renormalisation.

| expression in thesis | counterpart in literature | ref. | comments |
|---|---|---|---|
| $c_\Gamma N \bar{\mathcal{C}}^{1\gamma,1-\text{loop}}_{5,q}$ | $u_2^{(1)}$ | [238] | |
| $c_\Gamma N \tilde{\bar{\mathcal{C}}}^{1\gamma,1-\text{loop}}_{5,q}$ | $u_1^1$ | [238] | Factor of $N$ missing in reference. |
| $c_\Gamma N \bar{\mathcal{C}}^{1\gamma,1-\text{loop}}_{5,Q}$ | $d_2^{(1)}$ | [238] | |
| $c_\Gamma N \tilde{\bar{\mathcal{C}}}^{1\gamma,1-\text{loop}}_{5,Q}$ | $d_1^1$ | [238] | |
| $c_5^{1\gamma,l}$ | $u_2^l$ | [238] | |
| $c_5^{1\gamma,s}$ | $u_2^s$ | [238] | |
| $\tilde{c}_5^{1\gamma,l}$ | $u_1^l$ | [238] | |
| $\tilde{c}_5^{1\gamma,l}$ | $u_1^s$ | [238] | |

Table B.10.: References for the partial and colour stripped amplitudes used in the C and D-type real virtual corrections

## B.8. Next-to-next-to-leading order - double virtual contribution

### B.8.1. A-type matrix element

The $3g1\gamma$ one-loop amplitude we need for the loop-squared contribution to the double virtual correction can be derived from the $4g$ one-loop amplitude which is given in appendix II of [94]. Other references useful for the derivation are [241] (section 5) and [242] (section 3.1). We start from the unrenormalised all gluon amplitude,

$$\bar{\mathcal{A}}^{1-\text{loop}}_{4,A}(1,2,3,4) = \frac{c_\Gamma}{(4\pi)^2} g^4 \left[ \sum_{S_4/\mathbb{Z}_3(1,2,3,4)} N[1234]\bar{\mathcal{A}}^{1-\text{loop}}_{4;1}(1,2,3,4) + \sum_{S_4/\mathbb{Z}_2^3(1,2,3,4)} [12][34]N_c\bar{\mathcal{A}}^{1-\text{loop}}_{4;2}(1,2,3,4) \right], \tag{B.109}$$

where the sums are over those permutations which lead to distinct trace structures. Replacing w.l.o.g. gluon 4 by a photon, we find

$$\bar{\mathcal{A}}^{1\gamma,1-\text{loop}}_{4,A}(1,2,3,\gamma) = \frac{c_\Gamma}{(4\pi)^2}\sqrt{2}g^3 e N_F^q \sum_{S_3/\mathbb{Z}_3(1,2,3)} [123]\bar{\mathcal{A}}^{1\gamma,1-\text{loop}}_{4,123}, \tag{B.110}$$

where

$$\bar{\mathcal{A}}^{1\gamma,1-\text{loop}}_{4,ijk} = \bar{\mathcal{A}}^{1-\text{loop}}_{4;1(\text{fermion})}(i,j,k,\gamma) + \bar{\mathcal{A}}^{1-\text{loop}}_{4;1(\text{fermion})}(i,j,\gamma,k) + \bar{\mathcal{A}}^{1-\text{loop}}_{4;1(\text{fermion})}(i,\gamma,j,k)\,. \tag{B.111}$$

Here we defined

$$\bar{\mathcal{A}}^{1-\text{loop}}_{4;1(\text{fermion})} = N\frac{\partial}{\partial N_F}\bar{\mathcal{A}}^{1-\text{loop}}_{4;1}\,, \tag{B.112}$$

i.e. the part of the all gluon amplitude which corresponds to diagrams with an internal quark loop, which is the only object the photon can couple to in this case. One can check that in fact all other parts of the leading colour pure gluon amplitude mutually cancel in the sum above. Note that in the photonic amplitude (B.110) we therefore replaced $g \to eN_F^q$ instead of $g \to eQ_q$. The second line of eq. (B.109) does not contribute, because a trace over a single $SU(3)$ generator vanishes.

To proceed we can make use of the tree level photon decoupling equation for all gluon amplitudes (B.11), which tells us

$$\mathcal{A}^{\text{tree}}_{4,ijk} = \mathcal{A}^{\text{tree}}_4(i,j,k,\gamma) + \mathcal{A}^{\text{tree}}_4(i,j,\gamma,k) + \mathcal{A}^{\text{tree}}_4(i,\gamma,j,k) = 0\,. \tag{B.113}$$

But then the photonic amplitude must be finite, as the coefficients of the one-loop $\epsilon$ poles are proportional to the tree level amplitude[12], but there is no $3g1\gamma$ tee level amplitude. It follows that the one-loop amplitude neither receives corrections from the renormalisation or the regularisation scheme change, as both are shifts proportional to the tree level amplitude, nor does the finite piece change when expanding the loop factor $c_\Gamma$, as the corresponding shift is proportional to the $\epsilon^{-2}$ coefficient (see eq. (B.4)).

One can show that $\mathcal{A}^{\text{tree}}_{4,ijk}$ is completely symmetric with respect to permutations of the gluons, thus we arrive at the final expression for the (renormalised) $3g1\gamma$ one-loop amplitude,

$$\mathcal{A}^{1\gamma,1-\text{loop}}_{4,A}(1,2,3,\gamma) = \frac{c_\Gamma}{(4\pi)^2}\sqrt{2}g^3 eN_F^q([123]+[132])\mathcal{A}^{1\gamma,1-\text{loop}}_4\,. \tag{B.114}$$

The partial amplitude $\mathcal{A}^{1\gamma,1-\text{loop}}_4$ does not have an internal colour structure, so we can write

$$\mathcal{A}^{1\gamma,1-\text{loop}}_4 \equiv i a^{1\gamma,1-\text{loop}}_4\,. \tag{B.115}$$

Squaring the amplitude we obtain the result given in eq. (6.27),

$$A^{1\gamma,2-\text{loop}}_{4,A} = \sum_{\text{hel}}\left|\mathcal{A}^{1\gamma,1-\text{loop}}_{4,A}\right|^2 = \underbrace{\frac{1}{16\pi^4}g^6e^2N^3C_F}_{\mathcal{N}^V V}\frac{\left(N_F^q\right)^2}{N}\left(1-\frac{4}{N^2}\right)A^{2,\gamma}_{3g}\,, \tag{B.116}$$

with

$$A^{2,\gamma}_{3g} = \frac{1}{4}\sum_{\text{hel}}\left|a^{1\gamma,1-\text{loop}}_4\right|^2. \tag{B.117}$$

[12] The amplitudes in the sum are not always in the same helicity configuration, but the combination of the three is always such that the coefficients of the poles are the same. In fact the $N_F$ piece of the $4g$ amplitude does not have any $\epsilon^{-2}$ poles to begin with, and for two of the four independent helicity configurations the $\epsilon^{-1}$ pole vanishes, too.

| expression in thesis | counterpart in literature | ref. | comments |
|---|---|---|---|
| $-c_\Gamma(4\pi)^{-2}\bar{\mathcal{A}}^{1-\text{loop}}_{4;1(\text{fermion})}(1,2,3,4)$ | $-A_4^f(1,2,3,4) - A_4^s(1,2,3,4)$ | [94] | Only finite piece required. |

Table B.11.: References for the colour stripped amplitude used in the A-type double virtual corrections.

In table B.11 we list the reference for the partial amplitude and to what expression therein it relates.

### B.8.2. B-type matrix element

The B-type $2q1g1\gamma$ double virtual amplitudes were taken from [243–245]. The full matrix element including the loop-squared contribution as given in eq. (6.28) has been generated directly with the FORM code which has also been used to generate the amplitudes and formulae in [245]. As therein they have been discussed in quite some detail, we will not repeat the derivation here.

The automatised generation of the genuine two-loop×tree interferences and of the one-loop squared matrix elements provided the one-loop×tree interferences we discussed in section B.5 as a by-product. In NNLOJET both versions are implemented. Their agreement served as an additional check of the hand-coded matrix elements.

# Acknowledgements

Physics isn't a one-man show and during the last almost four years I worked with and spoke to many people without whom this thesis would never have come into existence. I apologise in advance to anyone I might forget in the following.

First and foremost my gratitude goes to Thomas Gehrmann for supervising me during this project. His insights into the field helped me out more than once. I would like to thank Nigel Glover for inviting me to stay at the IPPP in Durham for a few months during the first year of my PhD. It was a great experience. Many thanks also go to Xuan Chen, James Currie, Jan Niehues, Alexander Huss, Robin Schürmann, Duncan Walker and James Whitehead for all the physics discussions, and a special "Thank you" to Alexander Huss for helping me out with all the bug hunting. Further thanks go to Ana Rosario Cueto Gomez and Juan Terron Cuadrado from the ATLAS group for the productive collaboration, and to Alexander Huss and Robin Schürmann again for proofreading parts of this thesis. Of course I should mention all the other, former and present, members of the physics institute and people I became friends with, who made my stay in Zürich so nice: Agnieszka, Alexander, Anne, Daniel, Dominik, Elia, Fede, Ignacio, Javi, Jean-Nicolas, Jonathan, JY, Katie, Luca, Martina, Matteo, Matthias, Nacho, Nerina, Sara, Simone, Tomáš. Thanks for the many boardgame nights and the shared experiences during our ski trips!

Last but not least I want to express my deep gratitude towards my family, that gave me great support, and to Anka, of course, who made the countless hours on Swiss and German trains worth every minute.

# Bibliography


[1] A. Einstein. "Über einen die Erzeugung und Verwandlung des Lichtes betreffenden heuristischen Gesichtspunkt". In: *Annalen der Physik* 322.6 (1905), pp. 132–148. DOI: 10.1002/andp.19053220607. eprint: https://onlinelibrary.wiley.com/doi/pdf/10.1002/andp.19053220607.

[2] Max Planck. "Ueber das Gesetz der Energieverteilung im Normalspectrum". In: *Annalen der Physik* 309.3 (1901), pp. 553–563. DOI: 10.1002/andp.19013090310. eprint: https://onlinelibrary.wiley.com/doi/pdf/10.1002/andp.19013090310.

[3] Paul Adrien Maurice Dirac and Niels Henrik David Bohr. "The quantum theory of the emission and absorption of radiation". In: *Proceedings of the Royal Society of London. Series A, Containing Papers of a Mathematical and Physical Character* 114.767 (1927), pp. 243–265. DOI: 10.1098/rspa.1927.0039. eprint: https://royalsocietypublishing.org/doi/pdf/10.1098/rspa.1927.0039.

[4] Enrico Fermi. "Quantum Theory of Radiation". In: *Rev. Mod. Phys.* 4 (1 Jan. 1932), pp. 87–132. DOI: 10.1103/RevModPhys.4.87.

[5] W. Vogelsang and A. Vogt. "Constraints on the proton's gluon distribution from prompt photon production". In: *Nucl. Phys.* B453 (1995), pp. 334–354. DOI: 10.1016/0550-3213(95)00424-Q. arXiv: hep-ph/9505404 [hep-ph].

[6] P. N. Harriman et al. "Parton Distributions Extracted From Data on Deep Inelastic Lepton Scattering, Prompt Photon Production and the Drell-Yan Process". In: *Phys. Rev.* D42 (1990), pp. 798–810. DOI: 10.1103/PhysRevD.42.798.

[7] David d'Enterria and Juan Rojo. "Quantitative constraints on the gluon distribution function in the proton from collider isolated-photon data". In: *Nucl. Phys.* B860 (2012), pp. 311–338. DOI: 10.1016/j.nuclphysb.2012.03.003. arXiv: 1202.1762 [hep-ph].

[8] L. Carminati et al. "Sensitivity of the LHC isolated-gamma+jet data to the parton distribution functions of the proton". In: *EPL* 101.6 (2013), p. 61002. DOI: 10.1209/0295-5075/101/61002. arXiv: 1212.5511 [hep-ph].

[9] John M. Campbell et al. "Direct photon production and PDF fits reloaded". In: *Eur. Phys. J.* C78.6 (2018), p. 470. DOI: 10.1140/epjc/s10052-018-5944-4. arXiv: 1802.03021 [hep-ph].

[10] F. Halzen and D. M. Scott. "Testing QCD in the Hadroproduction of Real and Virtual Photons". In: *Phys. Rev. Lett.* 40 (1978), p. 1117. DOI: 10.1103/PhysRevLett.40.1117.

[11] R. Rückl, Stanley J. Brodsky, and J. F. Gunion. "The Production of Real Photons at Large Transverse Momentum in $pp$ Collisions". In: *Phys. Rev.* D18 (1978), pp. 2469–2483. DOI: 10.1103/PhysRevD.18.2469.

[12] J. M. Lindert et al. "Precise predictions for V + jets dark matter backgrounds". In: *The European Physical Journal C* 77.12 (Dec. 2017). ISSN: 1434-6052. DOI: 10.1140/epjc/s10052-017-5389-1. arXiv: 1705.04664 [hep-ph].

[13] M. Diakonou et al. "Direct Production of High $p_T$ Single Photons at the CERN Intersecting Storage Rings". In: *Phys. Lett.* 87B (1979), pp. 292–296. DOI: 10.1016/0370-2693(79)90985-7.

[14] E. Anassontzis et al. "High $p_T$ Direct Photon Production in pp Collisions". In: *Z. Phys.* C13 (1982), pp. 277–289. DOI: 10.1007/BF01572345.

[15] A. L. S. Angelis et al. "Direct Photon Production at the CERN ISR". In: *Nucl. Phys.* B327 (1989), pp. 541–568. DOI: 10.1016/0550-3213(89)90305-2.

[16] C. Albajar et al. "Direct Photon Production at the CERN $p\bar{p}$ Collider". In: *Phys. Lett.* B209 (1988), pp. 385–396. DOI: 10.1016/0370-2693(88)90968-9.

[17] J. Alitti et al. "A Measurement of the direct photon production cross-section at the CERN $p\bar{p}$ collider". In: *Phys. Lett.* B263 (1991), pp. 544–550. DOI: 10.1016/0370-2693(91)90503-I.

[18] T. Aaltonen et al. "Measurement of the inclusive-isolated prompt-photon cross section in $p\bar{p}$ collisions using the full CDF data set". In: *Phys. Rev.* D96 (2017), p. 092003. DOI: 10.1103/PhysRevD.96.092003. arXiv: 1703.00599 [hep-ex].

[19] V. M. Abazov et al. "Measurement of the isolated photon cross section in $p\bar{p}$ collisions at $\sqrt{s} = 1.96$ TeV". In: *Phys. Lett.* B639 (2006). [Erratum: Phys. Lett.B658,285(2008)], pp. 151–158. DOI: 10.1016/j.physletb.2007.06.047,10.1016/j.physletb.2006.04.048. arXiv: hep-ex/0511054 [hep-ex].

[20] Georges Aad et al. "Measurement of the inclusive isolated prompt photon cross-section in $pp$ collisions at $\sqrt{s} = 7$ TeV using 35 pb$^{-1}$ of ATLAS data". In: *Phys. Lett.* B706 (2011), pp. 150–167. DOI: 10.1016/j.physletb.2011.11.010. arXiv: 1108.0253 [hep-ex].

[21] G. Aad et al. "Measurement of the inclusive isolated prompt photon cross section in $pp$ collisions at $\sqrt{s} = 8$TeV with the ATLAS detector". In: *Journal of High Energy Physics* 2016.8 (Aug. 2016). ISSN: 1029-8479. DOI: 10.1007/jhep08(2016)005. arXiv: 1605.03495 [hep-ex].

[22] M. Aaboud et al. "Measurement of the cross section for inclusive isolated-photon production in $pp$ collisions at $\sqrt{s} = 13$TeV using the ATLAS detector". In: *Physics Letters B* 770 (July 2017), pp. 473–493. ISSN: 0370-2693. DOI: 10.1016/j.physletb.2017.04.072. arXiv: 1701.06882 [hep-ex].

[23] M. Aaboud et al. "Measurement of the ratio of cross sections for inclusive isolated-photon production in $pp$ collisions at $\sqrt{s} = 13$ and 8TeV with the ATLAS detector". In: *Journal of High Energy Physics* 2019.4 (Apr. 2019). ISSN: 1029-8479. DOI: 10.1007/jhep04(2019)093. arXiv: 1901.10075 [hep-ex].

[24] G. Aad et al. "Measurement of the inclusive isolated-photon cross section in $pp$ collisions at $\sqrt{s} = 13$TeV using 36fb$^{-1}$ of ATLAS data". In: *Journal of High Energy Physics* 2019.10 (Oct. 2019). ISSN: 1029-8479. DOI: 10.1007/jhep10(2019)203. arXiv: 1908.02746 [hep-ex].

[25] Serguei Chatrchyan et al. "Measurement of the Differential Cross Section for Isolated Prompt Photon Production in pp Collisions at 7 TeV". In: *Phys. Rev.* D84 (2011), p. 052011. DOI: 10.1103/PhysRevD.84.052011. arXiv: 1108.2044 [hep-ex].

[26] A. M. Sirunyan et al. "Measurement of differential cross sections for inclusive isolated-photon and photon+jet production in proton-proton collisions at $\sqrt{s} = 13$TeV". In: *The European Physical Journal C* 79.1 (Jan. 2019). ISSN: 1434-6052. DOI: 10.1140/epjc/s10052-018-6482-9. arXiv: 1807.00782 [hep-ex].

[27] A. M. Sirunyan et al. "Measurements of triple-differential cross sections for inclusive isolated-photon+jet events in $pp$ collisions at $\sqrt{s} = 8$TeV". In: *The European Physical Journal C* 79.11 (Nov. 2019). ISSN: 1434-6052. DOI: 10.1140/epjc/s10052-019-7451-7. arXiv: 1907.08155 [hep-ex].

[28] S. Acharya et al. "Measurement of the inclusive isolated photon production cross section in pp collisions at $\sqrt{s} = 7$ TeV". In: *The European Physical Journal C* 79.11 (Nov. 2019). ISSN: 1434-6052. DOI: 10.1140/epjc/s10052-019-7389-9. arXiv: 1906.01371 [nucl-ex].

[29] M. Aaboud et al. "Measurements of integrated and differential cross sections for isolated photon pair production in $pp$ collisions at $\sqrt{s} = 8$TeV with the ATLAS detector". In: *Physical Review D* 95.11 (June 2017). ISSN: 2470-0029. DOI: 10.1103/physrevd.95.112005. arXiv: 1704.03839 [hep-ex].

[30] V. M. Abazov et al. "Measurement of the Differential Cross-Section for the Production of an Isolated Photon with Associated Jet in $p\bar{p}$ Collisions at $\sqrt{s} = 1.96$-TeV". In: *Phys. Lett.* B666 (2008), pp. 435–445. DOI: 10.1016/j.physletb.2008.06.076. arXiv: 0804.1107 [hep-ex].

[31] Victor Mukhamedovich Abazov et al. "Measurement of the differential cross section of photon plus jet production in $p\bar{p}$ collisions at $\sqrt{s} = 1.96$ TeV". In: *Phys. Rev.* D88 (2013), p. 072008. DOI: 10.1103/PhysRevD.88.072008. arXiv: 1308.2708 [hep-ex].

[32] Georges Aad et al. "Dynamics of isolated-photon plus jet production in pp collisions at $\sqrt{(s)} = 7$ TeV with the ATLAS detector". In: *Nucl. Phys.* B875 (2013), pp. 483–535. DOI: 10.1016/j.nuclphysb.2013.07.025. arXiv: 1307.6795 [hep-ex].

[33] Morad Aaboud et al. "High-$E_{\mathrm{T}}$ isolated-photon plus jets production in $pp$ collisions at $\sqrt{s} = 8$ TeV with the ATLAS detector". In: *Nucl. Phys.* B918 (2017), pp. 257–316. DOI: 10.1016/j.nuclphysb.2017.03.006. arXiv: 1611.06586 [hep-ex].

[34] M. Aaboud et al. "Measurement of the cross section for isolated-photon plus jet production in $pp$ collisions at $\sqrt{s} = 13$TeV using the ATLAS detector". In: *Physics Letters B* 780 (May 2018), pp. 578–602. ISSN: 0370-2693. DOI: 10.1016/j.physletb.2018.03.035. arXiv: 1801.00112 [hep-ex].

[35] Serguei Chatrchyan et al. "Rapidity distributions in exclusive Z + jet and $\gamma$ + jet events in $pp$ collisions at $\sqrt{s} = 7$ TeV". In: *Phys. Rev.* D88.11 (2013), p. 112009. DOI: 10.1103/PhysRevD.88.112009. arXiv: 1310.3082 [hep-ex].

[36] Serguei Chatrchyan et al. "Measurement of the triple-differential cross section for photon+jets production in proton-proton collisions at $\sqrt{s}$=7 TeV". In: *JHEP* 06 (2014), p. 009. DOI: 10.1007/JHEP06(2014)009. arXiv: 1311.6141 [hep-ex].

[37] V. Khachatryan et al. "Comparison of the $Z/\gamma^*$ + jets to $\gamma$ + jets cross sections in $pp$ collisions at $\sqrt{s}$ = 8TeV". In: *Journal of High Energy Physics* 2015.10 (Oct. 2015). [Erratum: JHEP04,010(2016)]. ISSN: 1029-8479. DOI: 10.1007/jhep10(2015)128. arXiv: 1505.06520 [hep-ex].

[38] G. Aad et al. "Measurement of isolated-photon plus two-jet production in $pp$ collisions at $\sqrt{s} = 13$ TeV with the ATLAS detector". In: *Journal of High Energy Physics* 2020.3 (Mar. 2020). ISSN: 1029-8479. DOI: 10.1007/jhep03(2020)179. arXiv: 1912.09866 [hep-ex]. URL: http://dx.doi.org/10.1007/JHEP03(2020)179.

[39] G. Aad et al. "Observation of a new particle in the search for the Standard Model Higgs boson with the ATLAS detector at the LHC". In: *Physics Letters B* 716.1 (Sept. 2012), pp. 1–29. ISSN: 0370-2693. DOI: 10.1016/j.physletb.2012.08.020. arXiv: 1207.7214 [hep-ex].

[40] S. Chatrchyan et al. "Observation of a new boson at a mass of 125 GeV with the CMS experiment at the LHC". In: *Physics Letters B* 716.1 (Sept. 2012), pp. 30–61. ISSN: 0370-2693. DOI: 10.1016/j.physletb.2012.08.021. arXiv: 1207.7235 [hep-ex].

[41] M. Aaboud et al. "Measurements of Higgs boson properties in the diphoton decay channel with 36 fb$^{-1}$ of $pp$ collision data at $\sqrt{s} = 13$ TeV with the ATLAS detector". In: *Physical Review D* 98.5 (Sept. 2018). ISSN: 2470-0029. DOI: 10.1103/physrevd.98.052005. arXiv: 1802.04146 [hep-ex].

[42] A.M. Sirunyan et al. "A measurement of the Higgs boson mass in the diphoton decay channel". In: *Physics Letters B* 805 (June 2020), p. 135425. ISSN: 0370-2693. DOI: 10.1016/j.physletb.2020.135425. arXiv: 2002.06398 [hep-ex].

[43] M. Aaboud et al. "Search for new phenomena in high-mass diphoton final states using 37 fb$^{-1}$ of proton-proton collisions collected at $\sqrt{s} = 13$ TeV with the ATLAS detector". In: *Physics Letters B* 775 (Dec. 2017), pp. 105–125. ISSN: 0370-2693. DOI: 10.1016/j.physletb.2017.10.039. arXiv: 1707.04147 [hep-ex].

[44] A. M. Sirunyan et al. "Search for physics beyond the standard model in high-mass diphoton events from proton-proton collisions at $\sqrt{s} = 13$ TeV". In: *Physical Review D* 98.9 (Nov. 2018). ISSN: 2470-0029. DOI: 10.1103/physrevd.98.092001. arXiv: 1809.00327 [hep-ex].

[45] Stefano Catani and Bryan R Webber. "Infrared safe but infinite: soft-gluon divergences inside the physical region". In: *Journal of High Energy Physics* 1997.10 (Oct. 1997), pp. 005–005. ISSN: 1029-8479. DOI: 10.1088/1126-6708/1997/10/005. arXiv: hep-ph/9710333 [hep-ph].

[46] Aude Gehrmann-De Ridder, Thomas Gehrmann, and E.W. Nigel Glover. "Antenna subtraction at NNLO". In: *Journal of High Energy Physics* 2005.09 (Sept. 2005), pp. 056–056. ISSN: 1029-8479. DOI: 10.1088/1126-6708/2005/09/056. arXiv: hep-ph/0505111 [hep-ph].

[47] Alejandro Daleo, Thomas Gehrmann, and Daniel Maître. "Antenna subtraction with hadronic initial states". In: *Journal of High Energy Physics* 2007.04 (Apr. 2007), pp. 016–016. ISSN: 1029-8479. DOI: 10.1088/1126-6708/2007/04/016. arXiv: hep-ph/0612257 [hep-ph].

[48] James Currie, E. W. N. Glover, and Steven Wells. "Infrared structure at NNLO using antenna subtraction". In: *Journal of High Energy Physics* 2013.4 (Apr. 2013). ISSN: 1029-8479. DOI: 10.1007/jhep04(2013)066. arXiv: 1301.4693 [hep-ph].

[49] M. Czakon. "A novel subtraction scheme for double-real radiation at NNLO". In: *Physics Letters B* 693.3 (Oct. 2010), pp. 259–268. ISSN: 0370-2693. DOI: 10.1016/j.physletb.2010.08.036. arXiv: 1005.0274 [hep-ph].

[50] M. Czakon. "Double-real radiation in hadronic top quark pair production as a proof of a certain concept". In: *Nuclear Physics B* 849.2 (Aug. 2011), pp. 250–295. ISSN: 0550-3213. DOI: 10.1016/j.nuclphysb.2011.03.020. arXiv: 1101.0642 [hep-ph].

[51] Radja Boughezal, Kirill Melnikov, and Frank Petriello. "Subtraction scheme for next-to-next-to-leading order computations". In: *Physical Review D* 85.3 (Feb. 2012). ISSN: 1550-2368. DOI: 10.1103/physrevd.85.034025. arXiv: 1111.7041 [hep-ph].

[52] Stefano Catani and Massimiliano Grazzini. "Next-to-Next-to-Leading-Order Subtraction Formalism in Hadron Collisions and its Application to Higgs-Boson Production at the Large Hadron Collider". In: *Physical Review Letters* 98.22 (May 2007). ISSN: 1079-7114. DOI: 10.1103/physrevlett.98.222002. arXiv: hep-ph/0703012 [hep-ph].

[53] Radja Boughezal, Xiaohui Liu, and Frank Petriello. "N-jettiness soft function at next-to-next-to-leading order". In: *Physical Review D* 91.9 (May 2015). ISSN: 1550-2368. DOI: 10.1103/physrevd.91.094035. arXiv: 1504.02540 [hep-ph]. URL: http://dx.doi.org/10.1103/PhysRevD.91.094035.

[54] Radja Boughezal et al. "$W$-boson production in association with a jet at next-to-next-to-leading order in perturbative QCD". In: *Phys. Rev. Lett.* 115.6 (2015), p. 062002. DOI: 10.1103/PhysRevLett.115.062002. arXiv: 1504.02131 [hep-ph].

[55] Jonathan Gaunt et al. "N-jettiness Subtractions for NNLO QCD Calculations". In: *JHEP* 09 (2015), p. 058. DOI: 10.1007/JHEP09(2015)058. arXiv: 1505.04794 [hep-ph].

[56] Vittorio Del Duca et al. "Higgs boson decay into b-quarks at NNLO accuracy". In: *Journal of High Energy Physics* 2015.4 (Apr. 2015). ISSN: 1029-8479. DOI: 10.1007/jhep04(2015)036. arXiv: 1501.07226 [hep-ph].

[57] Fabrizio Caola, Kirill Melnikov, and Raoul Röntsch. "Nested soft-collinear subtractions in NNLO QCD computations". In: *The European Physical Journal C* 77.4 (Apr. 2017). ISSN: 1434-6052. DOI: 10.1140/epjc/s10052-017-4774-0. arXiv: 1702.01352 [hep-ph].

[58] L. Magnea et al. "Local analytic sector subtraction at NNLO". In: *JHEP* 12 (2018). [Erratum: JHEP 06, 013 (2019)], p. 107. DOI: 10.1007/JHEP12(2018)107. arXiv: 1806.09570 [hep-ph].

[59] Lorenzo Magnea et al. "Factorisation and Subtraction beyond NLO". In: *JHEP* 12 (2018), p. 062. DOI: 10.1007/JHEP12(2018)062. arXiv: 1809.05444 [hep-ph].

[60] Matteo Cacciari et al. "Fully Differential Vector-Boson-Fusion Higgs Production at Next-to-Next-to-Leading Order". In: *Phys. Rev. Lett.* 115.8 (2015). [Erratum: Phys.Rev.Lett. 120, 139901 (2018)], p. 082002. DOI: 10.1103/PhysRevLett.115.082002. arXiv: 1506.02660 [hep-ph].

[61] S. Amoroso et al. *Les Houches 2019: Physics at TeV Colliders: Standard Model Working Group Report*. 2020. arXiv: 2003.01700 [hep-ph].

[62] A. Gehrmann-De Ridder et al. "EERAD3: Event shapes and jet rates in electron-positron annihilation at order $\alpha_s^3$". In: *Comput. Phys. Commun.* 185 (2014), p. 3331. DOI: 10.1016/j.cpc.2014.07.024. arXiv: 1402.4140 [hep-ph].

[63] T. Gehrmann et al. "NNLO QCD corrections to event orientation in $e^+e^-$ annihilation". In: *Phys. Lett. B* 775 (2017), pp. 185–189. DOI: 10.1016/j.physletb.2017.10.069. arXiv: 1709.01097 [hep-ph].

[64] James Currie et al. "NNLO QCD corrections to jet production in deep inelastic scattering". In: *JHEP* 07 (2017), p. 018. DOI: 10.1007/JHEP07(2017)018. arXiv: 1703.05977 [hep-ph].

[65] J. Niehues and D.M. Walker. "NNLO QCD Corrections to Jet Production in Charged Current Deep Inelastic Scattering". In: *Phys. Lett. B* 788 (2019), pp. 243–248. DOI: 10.1016/j.physletb.2018.11.025. arXiv: 1807.02529 [hep-ph].

[66] J Currie, E.W.N. Glover, and J Pires. "Next-to-Next-to Leading Order QCD Predictions for Single Jet Inclusive Production at the LHC". In: *Phys. Rev. Lett.* 118.7 (2017), p. 072002. DOI: 10.1103/PhysRevLett.118.072002. arXiv: 1611.01460 [hep-ph].

[67] James Currie et al. "Precise predictions for dijet production at the LHC". In: *Phys. Rev. Lett.* 119.15 (2017), p. 152001. DOI: 10.1103/PhysRevLett.119.152001. arXiv: 1705.10271 [hep-ph].

[68] A. Gehrmann-De Ridder et al. "Precise QCD Predictions for the Production of a $Z$ Boson in Association with a Hadronic Jet". In: *Physical Review Letters* 117.2 (July 2016). ISSN: 1079-7114. DOI: 10.1103/physrevlett.117.022001. arXiv: 1507.02850 [hep-ph].

[69] Aude Gehrmann-De Ridder et al. "The NNLO QCD corrections to Z boson production at large transverse momentum". In: *JHEP* 07 (2016), p. 133. DOI: 10.1007/JHEP07(2016)133. arXiv: 1605.04295 [hep-ph].

[70] A. Gehrmann-De Ridder et al. "Next-to-Next-to-Leading-Order QCD Corrections to the Transverse Momentum Distribution of Weak Gauge Bosons". In: *Phys. Rev. Lett.* 120.12 (2018), p. 122001. DOI: 10.1103/PhysRevLett.120.122001. arXiv: 1712.07543 [hep-ph].

[71] X. Chen et al. "NNLO QCD corrections to Higgs boson production at large transverse momentum". In: *JHEP* 10 (2016), p. 066. DOI: 10.1007/JHEP10(2016)066. arXiv: 1607.08817 [hep-ph].

[72] R. Gauld et al. "Associated production of a Higgs boson decaying into bottom quarks and a weak vector boson decaying leptonically at NNLO in QCD". In: *JHEP* 10 (2019), p. 002. DOI: 10.1007/JHEP10(2019)002. arXiv: 1907.05836 [hep-ph].

[73] J. Cruz-Martinez et al. "Second-order QCD effects in Higgs boson production through vector boson fusion". In: *Phys. Lett. B* 781 (2018), pp. 672–677. DOI: 10.1016/j.physletb.2018.04.046. arXiv: 1802.02445 [hep-ph].

[74] Xuan Chen et al. "Isolated photon and photon+jet production at NNLO QCD accuracy". In: *Journal of High Energy Physics* 2020.4 (Apr. 2020). ISSN: 1029-8479. DOI: 10.1007/jhep04(2020)166. arXiv: 1904.01044 [hep-ph].

[75] O. W. Greenberg. "Spin and Unitary-Spin Independence in a Paraquark Model of Baryons and Mesons". In: *Phys. Rev. Lett.* 13 (20 Nov. 1964), pp. 598–602. DOI: 10.1103/PhysRevLett.13.598. URL: https://link.aps.org/doi/10.1103/PhysRevLett.13.598.

[76] M. Y. Han and Y. Nambu. "Three-Triplet Model with Double SU(3) Symmetry". In: *Phys. Rev.* 139 (4B Aug. 1965), B1006–B1010. DOI: 10.1103/PhysRev.139.B1006. URL: https://link.aps.org/doi/10.1103/PhysRev.139.B1006.

[77] Michael E Peskin and Daniel V Schroeder. *An introduction to quantum field theory*. Boulder, CO: Westview, 1995. URL: https://cds.cern.ch/record/257493.

[78] Nicola Cabibbo. "Unitary Symmetry and Leptonic Decays". In: *Phys. Rev. Lett.* 10 (1963), pp. 531–533. DOI: 10.1103/PhysRevLett.10.531.

[79] Makoto Kobayashi and Toshihide Maskawa. "CP Violation in the Renormalizable Theory of Weak Interaction". In: *Prog. Theor. Phys.* 49 (1973), pp. 652–657. DOI: 10.1143/PTP.49.652.

[80] Ziro Maki, Masami Nakagawa, and Shoichi Sakata. "Remarks on the unified model of elementary particles". In: *Prog. Theor. Phys.* 28 (1962), pp. 870–880. DOI: 10.1143/PTP.28.870.

[81] Matthew D. Schwartz. *Quantum Field Theory and the Standard Model*. Cambridge University Press, Mar. 2014. ISBN: 978-1-107-03473-0.

[82] Gerard 't Hooft. "Renormalizable Lagrangians for Massive Yang-Mills Fields". In: *Nucl. Phys. B* 35 (1971). Ed. by J.C. Taylor, pp. 167–188. DOI: 10.1016/0550-3213(71)90139-8.

[83] Gerard 't Hooft and M.J.G. Veltman. "Combinatorics of gauge fields". In: *Nucl. Phys. B* 50 (1972), pp. 318–353. DOI: 10.1016/S0550-3213(72)80021-X.

[84] B.W. Lee and Jean Zinn-Justin. "Spontaneously Broken Gauge Symmetries Part 1: Preliminaries". In: *Phys. Rev. D* 5 (1972), pp. 3121–3137. DOI: 10.1103/PhysRevD.5.3121.

[85] B.W. Lee and Jean Zinn-Justin. "Spontaneously Broken Gauge Symmetries Part 2: Perturbation Theory and Renormalization". In: *Phys. Rev. D* 5 (1972). [Erratum: Phys.Rev.D 8, 4654 (1973)], pp. 3137–3155. DOI: 10.1103/PhysRevD.5.3137.

[86] B.W. Lee and Jean Zinn-Justin. "Spontaneously Broken Gauge Symmetries Part 3: Equivalence". In: *Phys. Rev. D* 5 (1972), pp. 3155–3160. DOI: 10.1103/PhysRevD.5.3155.

[87] B.W. Lee and Jean Zinn-Justin. "Spontaneously Broken Gauge Symmetries Part 4: General Gauge Formulation". In: *Phys. Rev. D* 7 (1973), pp. 1049–1056. DOI: 10.1103/PhysRevD.7.1049.

[88] M. Bohm, Ansgar Denner, and H. Joos. *Gauge theories of the strong and electroweak interaction*. 2001. ISBN: 978-3-519-23045-8, 978-3-322-80162-3, 978-3-322-80160-9.

[89] Alexander Huss. "Mixed QCD-electroweak $\mathcal{O}(\alpha_s\alpha)$ corrections to Drell-Yan processes in the resonance region". PhD thesis. Albert-Ludwigs-Universität Freiburg, 2014. URL: https://nbn-resolving.org/urn:nbn:de:bsz:25-opus-100226.

[90] John C. Collins, Davison E. Soper, and George Sterman. *Factorization of Hard Processes in QCD*. 2004. arXiv: hep-ph/0409313 [hep-ph].

[91] R.Keith Ellis, W.James Stirling, and B.R. Webber. *QCD and collider physics*. Vol. 8. Cambridge University Press, Feb. 2011. ISBN: 978-0-511-82328-2, 978-0-521-54589-1.

[92] Michelangelo L. Mangano and Stephen J. Parke. "Multi-parton amplitudes in gauge theories". In: *Physics Reports* 200.6 (Feb. 1991), pp. 301–367. ISSN: 0370-1573. DOI: 10.1016/0370-1573(91)90091-y. arXiv: hep-th/0509223 [hep-th].

[93] Lance J. Dixon. *Calculating Scattering Amplitudes Efficiently*. 1996. arXiv: hep-ph/9601359 [hep-ph].

[94] Zvi Bern, Lance Dixon, and David A. Kosower. "One-loop corrections to two-quark three-gluon amplitudes". In: *Nuclear Physics B* 437.2 (Mar. 1995), pp. 259–304. ISSN: 0550-3213. DOI: 10.1016/0550-3213(94)00542-m. arXiv: hep-ph/9409393 [hep-ph].

[95] Vittorio Del Duca, William B. Kilgore, and Fabio Maltoni. "Multi-photon amplitudes for next-to-leading order QCD". In: *Nuclear Physics B* 574.3 (May 2000), pp. 851–873. ISSN: 0550-3213. DOI: 10.1016/s0550-3213(99)90663-6. arXiv: hep-ph/9910253 [hep-ph].

[96] Aude Gehrmann-De Ridder et al. "Infrared structure of $e^+e^- \to 3$ jets at NNLO". In: *Journal of High Energy Physics* 2007.11 (Nov. 2007), pp. 058–058. ISSN: 1029-8479. DOI: 10.1088/1126-6708/2007/11/058. arXiv: 0710.0346 [hep-ph].

[97] T. Kinoshita. "Mass singularities of Feynman amplitudes". In: *J. Math. Phys.* 3 (1962), pp. 650–677. DOI: 10.1063/1.1724268.

[98] T.D. Lee and M. Nauenberg. "Degenerate Systems and Mass Singularities". In: *Phys. Rev.* 133 (1964). Ed. by G. Feinberg, B1549–B1562. DOI: 10.1103/PhysRev.133.B1549.

[99] R.Keith Ellis, G. Marchesini, and B.R. Webber. "Soft Radiation in Parton Parton Scattering". In: *Nucl. Phys. B* 286 (1987). [Erratum: Nucl.Phys.B 294, 1180 (1987)], p. 643. DOI: 10.1016/0550-3213(87)90456-1. URL: https://inspirehep.net/literature/233672.

[100] Guido Altarelli and G. Parisi. "Asymptotic Freedom in Parton Language". In: *Nucl. Phys. B* 126 (1977), pp. 298–318. DOI: 10.1016/0550-3213(77)90384-4. URL: http://www.sciencedirect.com/science/article/pii/0550321377903844.

[101] Stefano Catani and Massimiliano Grazzini. "Infrared factorization of tree-level QCD amplitudes at the next-to-next-to-leading order and beyond". In: *Nuclear Physics B* 570.1-2 (Mar. 2000), pp. 287–325. ISSN: 0550-3213. DOI: 10.1016/s0550-3213(99)00778-6. arXiv: hep-ph/9908523 [hep-ph].

[102] Zvi Bern, Vittorio Del Duca, and Carl R. Schmidt. "The infrared behavior of one-loop gluon amplitudes at next-to-next-to-leading order". In: *Physics Letters B* 445.1-2 (Dec. 1998), pp. 168–177. ISSN: 0370-2693. DOI: 10.1016/s0370-2693(98)01495-6. arXiv: hep-ph/9810409 [hep-ph].

[103] Zvi Bern et al. "Infrared behavior of one-loop QCD amplitudes at next-to-next-to-leading order". In: *Physical Review D* 60.11 (Oct. 1999). ISSN: 1089-4918. DOI: 10.1103/physrevd.60.116001. arXiv: hep-ph/9903516 [hep-ph].

[104] Frits A. Berends and W.T. Giele. "Multiple Soft Gluon Radiation in Parton Processes". In: *Nucl. Phys. B* 313 (1989), pp. 595–633. DOI: 10.1016/0550-3213(89)90398-2.

[105] J.M. Campbell and E.W.N. Glover. "Double unresolved approximations to multiparton scattering amplitudes". In: *Nuclear Physics B* 527.1-2 (Aug. 1998), pp. 264–288. ISSN: 0550-3213. DOI: 10.1016/s0550-3213(98)00295-8. arXiv: hep-ph/9710255 [hep-ph].

[106] Stefano Catani. "The singular behaviour of QCD amplitudes at two-loop order". In: *Physics Letters B* 427.1-2 (May 1998), pp. 161–171. ISSN: 0370-2693. DOI: 10.1016/s0370-2693(98)00332-3. arXiv: hep-ph/9802439 [hep-ph].

[107] Aude Gehrmann-De Ridder, E. W. N. Glover, and Joao Pires. "Real-virtual corrections for gluon scattering at NNLO". In: *Journal of High Energy Physics* 2012.2 (Feb. 2012). ISSN: 1029-8479. DOI: 10.1007/jhep02(2012)141. arXiv: 1112.3613 [hep-ph].

[108] V.N. Gribov and L.N. Lipatov. "Deep inelastic e p scattering in perturbation theory". In: *Sov. J. Nucl. Phys.* 15 (1972), pp. 438–450.

[109] Yuri L. Dokshitzer. "Calculation of the Structure Functions for Deep Inelastic Scattering and $e^+e^-$ Annihilation by Perturbation Theory in Quantum Chromodynamics." In: *Sov. Phys. JETP* 46 (1977), pp. 641–653.

[110] S. Catani and M.H. Seymour. "A general algorithm for calculating jet cross sections in NLO QCD". In: *Nuclear Physics B* 485.1-2 (Feb. 1997), pp. 291–419. ISSN: 0550-3213. DOI: 10.1016/s0550-3213(96)00589-5. arXiv: hep-ph/9605323 [hep-ph].

[111] A. Gehrmann-De Ridder, T. Gehrmann, and E.W.N. Glover. "Gluon–gluon antenna functions from Higgs boson decay". In: *Physics Letters B* 612.1-2 (Apr. 2005), pp. 49–60. ISSN: 0370-2693. DOI: 10.1016/j.physletb.2005.03.003. arXiv: hep-ph/0502110 [hep-ph].

[112] A. Gehrmann-De Ridder, T. Gehrmann, and E.W.N. Glover. "Quark–gluon antenna functions from neutralino decay". In: *Physics Letters B* 612.1-2 (Apr. 2005), pp. 36–48. ISSN: 0370-2693. DOI: 10.1016/j.physletb.2005.02.039. arXiv: hep-ph/0501291 [hep-ph].

[113] Alejandro Daleo et al. "Antenna subtraction at NNLO with hadronic initial states: initial-final configurations". In: *Journal of High Energy Physics* 2010.1 (Jan. 2010). ISSN: 1029-8479. DOI: 10.1007/jhep01(2010)118. arXiv: 0912.0374 [hep-ph].

[114] Thomas Gehrmann and Pier Francesco Monni. "Antenna subtraction at NNLO with hadronic initial states: real-virtual initial-initial configurations". In: *Journal of High Energy Physics* 2011.12 (Dec. 2011). ISSN: 1029-8479. DOI: 10.1007/jhep12(2011)049. arXiv: 1107.4037 [hep-ph].

[115] A. Gehrmann-De Ridder, T. Gehrmann, and M. Ritzmann. "Antenna subtraction at NNLO with hadronic initial states: double real initial-initial configurations". In: *Journal of High Energy Physics* 2012.10 (Oct. 2012). ISSN: 1029-8479. DOI: 10.1007/jhep10(2012)047. arXiv: 1207.5779 [hep-ph].

[116] A. Gehrmann-De Ridder, T. Gehrmann, and E.W.N. Glover. "Infrared structure of $e^+e^- \to 2$ jets at NNLO". In: *Nuclear Physics B* 691.1-2 (July 2004), pp. 195–222. ISSN: 0550-3213. DOI: 10.1016/j.nuclphysb.2004.05.017. arXiv: hep-ph/0403057 [hep-ph].

[117] David A. Kosower. "Antenna factorization of gauge-theory amplitudes". In: *Physical Review D* 57.9 (May 1998), pp. 5410–5416. ISSN: 1089-4918. DOI: 10.1103/physrevd.57.5410. arXiv: hep-ph/9710213 [hep-ph].

[118] David A. Kosower. "Multiple singular emission in gauge theories". In: *Physical Review D* 67.11 (June 2003). ISSN: 1089-4918. DOI: 10.1103/physrevd.67.116003. arXiv: hep-ph/0212097 [hep-ph].

[119] Thomas Anthony Morgan. "Precision $Z$ Boson Phenomenology at the LHC". PhD thesis. Durham University, 2016. URL: http://etheses.dur.ac.uk/11773/.

[120] James Richard Currie. "Antenna Subtraction for NNLO Calculations at the LHC". PhD thesis. Durham University, 2012. URL: http://etheses.dur.ac.uk/4942/.

[121] Joao Pires and E.W.N. Glover. "Double real radiation corrections to gluon scattering at NNLO". In: *Nuclear Physics B - Proceedings Supplements* 205-206 (Aug. 2010), pp. 176–181. ISSN: 0920-5632. DOI: 10.1016/j.nuclphysbps.2010.08.039. arXiv: 1006.1849 [hep-ph].

[122] Yakov I. Azimov et al. "Similarity of Parton and Hadron Spectra in QCD Jets". In: *Z. Phys. C* 27 (1985), pp. 65–72. DOI: 10.1007/BF01642482.

[123] John E. Huth et al. "Toward a standardization of jet definitions". In: *1990 DPF Summer Study on High-energy Physics: Research Directions for the Decade (Snowmass 90)*. Dec. 1990, pp. 0134–136.

[124] Gavin P. Salam. "Towards jetography". In: *The European Physical Journal C* 67.3-4 (May 2010), pp. 637–686. ISSN: 1434-6052. DOI: 10.1140/epjc/s10052-010-1314-6. arXiv: 0906.1833 [hep-ph].

[125] Matteo Cacciari, Gavin P Salam, and Gregory Soyez. "The anti-ktjet clustering algorithm". In: *Journal of High Energy Physics* 2008.04 (Apr. 2008), pp. 063–063. ISSN: 1029-8479. DOI: 10.1088/1126-6708/2008/04/063. arXiv: 0802.1189 [hep-ph].

[126] S. Catani et al. "Longitudinally invariant $K_t$ clustering algorithms for hadron hadron collisions". In: *Nucl. Phys. B* 406 (1993), pp. 187–224. DOI: 10.1016/0550-3213(93)90166-M.

[127] Stephen D. Ellis and Davison E. Soper. "Successive combination jet algorithm for hadron collisions". In: *Physical Review D* 48.7 (Oct. 1993), pp. 3160–3166. ISSN: 0556-2821. DOI: 10.1103/physrevd.48.3160. arXiv: hep-ph/9305266 [hep-ph].

[128] Yu.L Dokshitzer et al. "Better jet clustering algorithms". In: *Journal of High Energy Physics* 1997.08 (Aug. 1997), pp. 001–001. ISSN: 1029-8479. DOI: 10.1088/1126-6708/1997/08/001. arXiv: hep-ph/9707323 [hep-ph].

[129] M. Wobisch and T. Wengler. "Hadronization corrections to jet cross-sections in deep inelastic scattering". In: *Workshop on Monte Carlo Generators for HERA Physics (Plenary Starting Meeting)*. Apr. 1998, pp. 270–279. arXiv: hep-ph/9907280.

[130] Vardan Khachatryan et al. "Performance of Photon Reconstruction and Identification with the CMS Detector in Proton-Proton Collisions at sqrt(s) = 8 TeV". In: *JINST* 10.08 (2015), P08010. DOI: 10.1088/1748-0221/10/08/P08010. arXiv: 1502.02702 [physics.ins-det].

[131] Gregor Geßner. "Photon identification with the ATLAS detector". In: *PoS* EPS-HEP2017 (2017). Ed. by Paolo Checchia et al., p. 760. DOI: 10.22323/1.314.0760.

[132] Morad Aaboud et al. "Measurement of the photon identification efficiencies with the ATLAS detector using LHC Run 2 data collected in 2015 and 2016". In: *Eur. Phys. J. C* 79.3 (2019), p. 205. DOI: 10.1140/epjc/s10052-019-6650-6. arXiv: 1810.05087 [hep-ex].

[133] Mathias Weber. "Unfolding at CMS". In: *PHYSTAT 2011*. Geneva: CERN, 2011, pp. 292–296. DOI: 10.5170/CERN-2011-006.292.

[134] Silvia Biondi. "Experience with using unfolding procedures in ATLAS". In: *EPJ Web Conf.* 137 (2017). Ed. by Y. Foka, N. Brambilla, and V. Kovalenko, p. 11002. DOI: 10.1051/epjconf/201713711002.

[135] K. Koller, T.F. Walsh, and P.M. Zerwas. "Testing QCD: Direct Photons in $e^+e^-$ Collisions". In: *Z. Phys. C* 2 (1979), p. 197. DOI: 10.1007/BF01474661.

[136] E. Laermann et al. "Direct Photons in $e^+e^-$ Annihilation". In: *Nucl. Phys. B* 207 (1982), pp. 205–232. DOI: 10.1016/0550-3213(82)90162-6.

[137] Stefano Catani et al. "Cross section of isolated prompt photons in hadron-hadron collisions". In: *Journal of High Energy Physics* 2002.05 (May 2002), pp. 028–028. ISSN: 1029-8479. DOI: 10.1088/1126-6708/2002/05/028. arXiv: hep-ph/0204023 [hep-ph].

[138] D. Buskulic et al. "First measurement of the quark to photon fragmentation function". In: *Z. Phys. C* 69 (1996), pp. 365–378. DOI: 10.1007/BF02907417.

[139] K. Ackerstaff et al. "Measurement of the quark to photon fragmentation function through the inclusive production of prompt photons in hadronic $Z^0$ decays". In: *The European Physical Journal C* 2.1 (Mar. 1998), pp. 39–48. ISSN: 1434-6052. DOI: 10.1007/s100520050122. arXiv: hep-ex/9708020 [hep-ex].

[140] S. Catani et al. "Isolating prompt photons with narrow cones". In: *Journal of High Energy Physics* 2013.9 (Sept. 2013). ISSN: 1029-8479. DOI: 10.1007/jhep09(2013)007. arXiv: 1306.6498 [hep-ph].

[141] S. Abachi et al. "Isolated photon cross-section in the central and forward rapidity regions in $p\bar{p}$ collisions at $\sqrt{s} = 1.8$ TeV". In: *Physical Review Letters* 77.25 (Dec. 1996), pp. 5011–5015. ISSN: 1079-7114. DOI: 10.1103/physrevlett.77.5011. arXiv: hep-ex/9603006 [hep-ex].

[142] B. Abbott et al. "The isolated photon cross-section in $p\bar{p}$ collisions at $\sqrt{s} = 1.8$ TeV". In: *Physical Review Letters* 84.13 (Mar. 2000), pp. 2786–2791. ISSN: 1079-7114. DOI: 10.1103/physrevlett.84.2786. arXiv: hep-ex/9912017 [hep-ex].

[143] V. Abazov et al. "The Ratio of the Isolated Photon Cross Sections at $\sqrt{s} = 630$ GeV and 1800 GeV". In: *Physical Review Letters* 87.25 (Nov. 2001). ISSN: 1079-7114. DOI: 10.1103/physrevlett.87.251805. arXiv: hep-ex/0106026 [hep-ex].

[144] Stefano Frixione. "Isolated photons in perturbative QCD". In: *Physics Letters B* 429.3-4 (June 1998), pp. 369–374. ISSN: 0370-2693. DOI: 10.1016/s0370-2693(98)00454-7. arXiv: hep-ph/9801442 [hep-ph].

[145] J. Butterworth et al. *Les Houches 2013: Physics at TeV Colliders: Standard Model Working Group Report*. 2014. arXiv: 1405.1067 [hep-ph].

[146] S. Badger et al. *Les Houches 2015: Physics at TeV Colliders Standard Model Working Group Report*. 2016. arXiv: 1605.04692 [hep-ph].

[147] Stefano Catani et al. "Diphoton production at the LHC: a QCD study up to NNLO". In: *Journal of High Energy Physics* 2018.4 (Apr. 2018). ISSN: 1029-8479. DOI: 10.1007/jhep04(2018)142. arXiv: 1802.02095 [hep-ph].

[148] John M. Campbell, R. Keith Ellis, and Ciaran Williams. "Direct Photon Production at Next-to–Next-to-Leading Order". In: *Physical Review Letters* 118.22 (May 2017). ISSN: 1079-7114. DOI: 10.1103/physrevlett.118.222001. arXiv: 1612.04333 [hep-ph].

[149] John M. Campbell, R. Keith Ellis, and Ciaran Williams. "Driving missing data at the LHC: NNLO predictions for the ratio of $\gamma + j$ and $Z + j$". In: *Physical Review D* 96.1 (July 2017). ISSN: 2470-0029. DOI: 10.1103/physrevd.96.014037. arXiv: 1703.10109 [hep-ph]. URL: http://dx.doi.org/10.1103/PhysRevD.96.014037.

[150] Stefano Catani et al. "Diphoton production at hadron colliders: a fully-differential QCD calculation at NNLO". In: *Phys. Rev. Lett.* 108 (2012). [Erratum: Phys.Rev.Lett. 117, 089901 (2016)], p. 072001. DOI: 10.1103/PhysRevLett.108.072001. arXiv: 1110.2375 [hep-ph].

[151] John M. Campbell et al. "Predictions for diphoton production at the LHC through NNLO in QCD". In: *Journal of High Energy Physics* 2016.7 (July 2016). ISSN: 1029-8479. DOI: 10.1007/jhep07(2016)148. arXiv: 1603.02663 [hep-ph].

[152] T. Binoth et al. *The SM and NLO multileg working group: Summary report*. 2010. arXiv: 1003.1241 [hep-ph].

[153] J. Alcaraz Maestre et al. *The SM and NLO Multileg and SM MC Working Groups: Summary Report*. 2012. arXiv: 1203.6803 [hep-ph].

[154] Christopher Frye et al. "Precision diboson observables for the LHC". In: *Journal of High Energy Physics* 2016.3 (Mar. 2016). ISSN: 1029-8479. DOI: 10.1007/jhep03(2016)171. arXiv: 1510.08451 [hep-ph].

[155] Marcel Balsiger, Thomas Becher, and Ding Yu Shao. "Non-global logarithms in jet and isolation cone cross sections". In: *Journal of High Energy Physics* 2018.8 (Aug. 2018). ISSN: 1029-8479. DOI: 10.1007/jhep08(2018)104. arXiv: 1803.07045 [hep-ph].

[156] Frank Siegert. "A practical guide to event generation for prompt photon production with Sherpa". In: *Journal of Physics G: Nuclear and Particle Physics* 44.4 (Mar. 2017), p. 044007. ISSN: 1361-6471. DOI: 10.1088/1361-6471/aa5f29. arXiv: 1611.07226 [hep-ph].

[157] T Gleisberg et al. "Event generation with SHERPA 1.1". In: *Journal of High Energy Physics* 2009.02 (Feb. 2009), pp. 007–007. ISSN: 1029-8479. DOI: 10.1088/1126-6708/2009/02/007. arXiv: 0811.4622 [hep-ph].

[158] Stefan Höche et al. "QCD matrix elements + parton showers. The NLO case". In: *Journal of High Energy Physics* 2013.4 (Apr. 2013). ISSN: 1029-8479. DOI: 10.1007/jhep04(2013)027. arXiv: 1207.5030 [hep-ph].

[159] X. Chen et al. "Isolated photon and photon+jet production at NNLO QCD accuracy and the ratio $R^{\gamma}_{13/8}$". In: *54th Rencontres de Moriond on QCD and High Energy Interactions*. ARISF, May 2019, pp. 185–188. arXiv: 1905.08577 [hep-ph].

[160] Thomas Gehrmann, E.W. Nigel Glover, Alexander Huss, and James Whitehead. *Scale and isolation sensitivity of diphoton distributions at the LHC*. In preparation. 2020.

[161] James Whitehead. "The Production of Pairs of Isolated Photons at Higher Orders in QCD". PhD thesis. Durham University, 2020.

[162] E.W. Nigel Glover and A.G. Morgan. "Measuring the photon fragmentation function at LEP". In: *Z. Phys. C* 62 (1994), pp. 311–322. DOI: 10.1007/BF01560245.

[163] Zachary Hall and Jesse Thaler. "Photon isolation and jet substructure". In: *Journal of High Energy Physics* 2018.9 (Sept. 2018). ISSN: 1029-8479. DOI: 10.1007/jhep09(2018)164. arXiv: 1805.11622 [hep-ph].

[164] Andrew J. Larkoski et al. "Soft drop". In: *Journal of High Energy Physics* 2014.5 (May 2014). ISSN: 1029-8479. DOI: 10.1007/jhep05(2014)146. arXiv: 1402.2657 [hep-ph].

[165] T. Binoth et al. "A full next-to-leading order study of direct photon pair production in hadronic collisions". In: *The European Physical Journal C* 16.2 (Aug. 2000), pp. 311–330. ISSN: 1434-6052. DOI: 10.1007/s100520050024. arXiv: hep-ph/9911340 [hep-ph].

[166] T. Binoth et al. "A next-to-leading order study of pion-pair production and comparison with E706 data". In: *The European Physical Journal C* 24.2 (June 2002), pp. 245–260. ISSN: 1434-6052. DOI: 10.1007/s100520200921. arXiv: hep-ph/0111043 [hep-ph].

[167] T. Binoth et al. "A Next-to-leading order study of photon pion and pion pair hadro production in the light of the Higgs boson search at the LHC". In: *Eur. Phys. J. direct* 4.1 (2002), p. 7. DOI: 10.1007/s1010502c0007. arXiv: hep-ph/0203064.

[168] P. Aurenche et al. "Recent critical study of photon production in hadronic collisions". In: *Physical Review D* 73.9 (May 2006). ISSN: 1550-2368. DOI: 10.1103/physrevd.73.094007. arXiv: hep-ph/0602133 [hep-ph].

[169] Z. Belghobsi et al. "Photon-jet correlations and constraints on fragmentation functions". In: *Physical Review D* 79.11 (June 2009). ISSN: 1550-2368. DOI: 10.1103/physrevd.79.114024. arXiv: 0903.4834 [hep-ph].

[170] L. Bourhis, M. Fontannaz, and J.P. Guillet. "Quark and gluon fragmentation functions into photons". In: *The European Physical Journal C* 2.3 (Apr. 1998), pp. 529–537. ISSN: 1434-6052. DOI: 10.1007/s100529800708. arXiv: hep-ph/9704447 [hep-ph].

[171] S. Catani and M.H. Seymour. "The dipole formalism for the calculation of QCD jet cross sections at next-to-leading order". In: *Physics Letters B* 378.1-4 (June 1996), pp. 287–301. ISSN: 0370-2693. DOI: 10.1016/0370-2693(96)00425-x. arXiv: hep-ph/9602277 [hep-ph].

[172] W.T. Giele and E.W. Nigel Glover. "Higher order corrections to jet cross-sections in e+ e- annihilation". In: *Phys. Rev. D* 46 (1992), pp. 1980–2010. DOI: 10.1103/PhysRevD.46.1980.

[173] W.T. Giele, E.W. Nigel Glover, and David A. Kosower. "Higher order corrections to jet cross-sections in hadron colliders". In: *Nucl. Phys. B* 403 (1993), pp. 633–670. DOI: 10.1016/0550-3213(93)90365-V. arXiv: hep-ph/9302225.

[174] M. Furman. "Study of a Nonleading QCD Correction to Hadron Calorimeter Reactions". In: *Nucl. Phys. B* 197 (1982), pp. 413–445. DOI: 10.1016/0550-3213(82)90452-7.

[175] A. Gehrmann-De Ridder and E.W.N. Glover. "A complete $\mathcal{O}(\alpha\alpha_s)$ calculation of the Photon + 1 Jet rate in $e^+e^-$ annihilation". In: *Nuclear Physics B* 517.1-3 (Apr. 1998), pp. 269–323. ISSN: 0550-3213. DOI: 10.1016/s0550-3213(97)00818-3. arXiv: hep-ph/9707224 [hep-ph].

[176] Duncan Martin Walker. "Higher Order QCD Corrections to Electroweak Boson Production at Colliders". PhD thesis. Durham University, 2019. URL: http://etheses.dur.ac.uk/13284/.

[177] Jan Niehues. "Higher-Order QCD Corrections to Jet Production in Deep Inelastic Scattering". PhD thesis. University of Zurich, Sept. 2017. URL: https://doi.org/10.5167/uzh-144060.

[178] Juan Manuel Cruz-Martinez. "Next-to-Next-to-Leading Order QCD Corrections to Higgs Boson Production in Association with two Jets in Vector Boson Fusion". PhD thesis. Durham University, 2018. URL: http://etheses.dur.ac.uk/12806/.

[179] G.Peter Lepage. "VEGAS: AN ADAPTIVE MULTIDIMENSIONAL INTEGRATION PROGRAM". In: (Mar. 1980).

[180] Andy Buckley et al. "LHAPDF6: parton density access in the LHC precision era". In: *The European Physical Journal C* 75.3 (Mar. 2015). ISSN: 1434-6052. DOI: 10.1140/epjc/s10052-015-3318-8. arXiv: 1412.7420 [hep-ph].

[181] Federico Buccioni et al. "OpenLoops 2". In: *The European Physical Journal C* 79.10 (Oct. 2019). ISSN: 1434-6052. DOI: 10.1140/epjc/s10052-019-7306-2. arXiv: 1907.13071 [hep-ph].

[182] A. Gehrmann-De Ridder et al. "NNLO QCD corrections for Drell-Yan $p_T^Z$ and $\phi^*$ observables at the LHC". In: *JHEP* 11 (2016). [Erratum: JHEP 10, 126 (2018)], p. 094. DOI: 10.1007/JHEP11(2016)094. arXiv: 1610.01843 [hep-ph].

[183] A. Gehrmann-De Ridder et al. "Vector Boson Production in Association with a Jet at Forward Rapidities". In: *Eur. Phys. J. C* 79.6 (2019), p. 526. DOI: 10.1140/epjc/s10052-019-7010-2. arXiv: 1901.11041 [hep-ph].

[184] F. Cascioli, P. Maierhöfer, and S. Pozzorini. "Scattering Amplitudes with Open Loops". In: *Physical Review Letters* 108.11 (Mar. 2012). ISSN: 1079-7114. DOI: 10.1103/physrevlett.108.111601. arXiv: 1111.5206 [hep-ph].

[185] R. Kleiss, W.James Stirling, and S.D. Ellis. "A New Monte Carlo Treatment of Multiparticle Phase Space at High-energies". In: *Comput. Phys. Commun.* 40 (1986), p. 359. DOI: 10.1016/0010-4655(86)90119-0.

[186] Massimiliano Grazzini, Stefan Kallweit, and Marius Wiesemann. "Fully differential NNLO computations with MATRIX". In: *The European Physical Journal C* 78.7 (June 2018). ISSN: 1434-6052. DOI: 10.1140/epjc/s10052-018-5771-7. arXiv: 1711.06631 [hep-ph].

[187] A. Gehrmann-De Ridder and E.W.N. Glover. "Final state photon production at LEP". In: *The European Physical Journal C* 7.1 (Feb. 1999), pp. 29–48. ISSN: 1434-6052. DOI: 10.1007/s100529800958. arXiv: hep-ph/9806316 [hep-ph].

[188] Richard D. Ball et al. "Parton distributions from high-precision collider data". In: *Eur. Phys. J. C* 77.10 (2017), p. 663. DOI: 10.1140/epjc/s10052-017-5199-5. arXiv: 1706.00428 [hep-ph].

[189] Sayipjamal Dulat et al. "New parton distribution functions from a global analysis of quantum chromodynamics". In: *Physical Review D* 93.3 (Feb. 2016). ISSN: 2470-0029. DOI: 10.1103/physrevd.93.033006. arXiv: 1506.07443 [hep-ph].

[190] J. M. Campbell and C. Williams, private communication.

[191] Thomas Becher and Xavier Garcia i Tormo. "Electroweak Sudakov effects in W, Z and $\gamma$ production at large transverse momentum". In: *Physical Review D* 88.1 (July 2013). ISSN: 1550-2368. DOI: 10.1103/physrevd.88.013009. arXiv: 1305.4202 [hep-ph].

[192] Thomas Becher and Xavier Garcia i Tormo. "Addendum: Electroweak Sudakov effects in W, Z and $\gamma$ production at large transverse momentum". In: *Physical Review D* 92.7 (Oct. 2015). ISSN: 1550-2368. DOI: 10.1103/physrevd.92.073011. arXiv: 1509.01961 [hep-ph].

[193] Claude Duhr, Falko Dulat, and Bernhard Mistlberger. "Charged Current Drell-Yan Production at N3LO". In: (July 2020). arXiv: 2007.13313 [hep-ph].

[194] A. Gehrmann-De Ridder, T. Gehrmann, and E. Poulsen. "Measuring the photon fragmentation function at HERA". In: *The European Physical Journal C* 47.2 (June 2006), pp. 395–411. ISSN: 1434-6052. DOI: 10.1140/epjc/s2006-02574-x. arXiv: hep-ph/0604030 [hep-ph].

[195] Tom Kaufmann, Asmita Mukherjee, and Werner Vogelsang. "Access to photon fragmentation functions in hadronic jet production". In: *Physical Review D* 93.11 (June 2016). ISSN: 2470-0029. DOI: 10.1103/physrevd.93.114021. arXiv: 1604.07175 [hep-ph].

[196] P.A. Zyla et al. "Review of Particle Physics". In: *Prog. Theor. Exp. Phys.* 2020.8 (Aug. 2020). 083C01. ISSN: 2050-3911. DOI: 10.1093/ptep/ptaa104. URL: http://pdg.lbl.gov/2020.

[197] V.V. Sudakov. "Vertex parts at very high-energies in quantum electrodynamics". In: *Sov. Phys. JETP* 3 (1956), pp. 65–71.

[198] V. S. Fadin et al. "Resummation of double logarithms in electroweak high energy processes". In: *Physical Review D* 61.9 (Mar. 2000). ISSN: 1089-4918. DOI: 10.1103/physrevd.61.094002. arXiv: hep-ph/9910338 [hep-ph].

[199] A. Denner and S. Pozzorini. "One-loop leading logarithms in electroweak radiative corrections". In: *The European Physical Journal C* 18.3 (Jan. 2001), pp. 461–480. ISSN: 1434-6052. DOI: 10.1007/s100520100551. arXiv: hep-ph/0010201 [hep-ph].

[200] E. Accomando, A. Denner, and A. Kaiser. "Logarithmic electroweak corrections to gauge-boson pair production at the LHC". In: *Nuclear Physics B* 706.1-2 (Jan. 2005), pp. 325–371. ISSN: 0550-3213. DOI: 10.1016/j.nuclphysb.2004.11.019. arXiv: hep-ph/0409247 [hep-ph].

[201] Simone Alioli et al. "Precision Probes of QCD at High Energies". In: *JHEP* 07 (2017), p. 097. DOI: 10.1007/JHEP07(2017)097. arXiv: 1706.03068 [hep-ph].

[202] Marco Farina et al. "Energy helps accuracy: electroweak precision tests at hadron colliders". In: *Phys. Lett. B* 772 (2017), pp. 210–215. DOI: 10.1016/j.physletb.2017.06.043. arXiv: 1609.08157 [hep-ph].

[203] Admir Greljo and David Marzocca. "High-$p_T$ dilepton tails and flavor physics". In: *Eur. Phys. J. C* 77.8 (2017), p. 548. DOI: 10.1140/epjc/s10052-017-5119-8. arXiv: 1704.09015 [hep-ph].

[204] Kalanand Mishra et al. *Electroweak Corrections at High Energies*. 2013. arXiv: 1308.1430 [hep-ph].

[205] Stefan Dittmaier, Alexander Huss, and Christian Speckner. "Weak radiative corrections to dijet production at hadron colliders". In: *Journal of High Energy Physics* 2012.11 (Nov. 2012). ISSN: 1029-8479. DOI: 10.1007/jhep11(2012)095. arXiv: 1210.0438 [hep-ph].

[206] Stefan Dittmaier, Alexander Huss, and Christian Schwinn. "Dominant mixed QCD-electroweak $\mathcal{O}(\alpha_S\alpha)$ corrections to Drell–Yan processes in the resonance region". In: *Nuclear Physics B* 904 (Mar. 2016), pp. 216–252. ISSN: 0550-3213. DOI: 10.1016/j.nuclphysb.2016.01.006. arXiv: 1511.08016 [hep-ph].

[207] R. Frederix et al. "The complete NLO corrections to dijet hadroproduction". In: *Journal of High Energy Physics* 2017.4 (Apr. 2017). ISSN: 1029-8479. DOI: 10.1007/jhep04(2017)076. arXiv: 1612.06548 [hep-ph].

[208] S. Kallweit et al. "NLO QCD+EW predictions for $2\ell 2\nu$ diboson signatures at the LHC". In: *Journal of High Energy Physics* 2017.11 (Nov. 2017). ISSN: 1029-8479. DOI: 10.1007/jhep11(2017)120. arXiv: 1705.00598 [hep-ph].

[209] Rikkert Frederix, Davide Pagani, and Marco Zaro. "Large NLO corrections in $t\bar{t}W^{\pm}$ and $t\bar{t}t\bar{t}$ hadroproduction from supposedly subleading EW contributions". In: *Journal of High Energy Physics* 2018.2 (Feb. 2018). ISSN: 1029-8479. DOI: 10.1007/jhep02(2018)031. arXiv: 1711.02116 [hep-ph].

[210] M. Grazzini et al. "NNLO QCD + NLO EW with Matrix+OpenLoops: precise predictions for vector-boson pair production". In: *Journal of High Energy Physics* 2020.2 (Feb. 2020). ISSN: 1029-8479. DOI: 10.1007/jhep02(2020)087. arXiv: 1912.00068 [hep-ph].

[211] Maximilian Delto et al. "Mixed QCD⊗QED corrections to on-shell Z boson production at the LHC". In: *Journal of High Energy Physics* 2020.1 (Jan. 2020). ISSN: 1029-8479. DOI: 10.1007/jhep01(2020)043. arXiv: 1909.08428 [hep-ph].

[212] A. D. Martin et al. "Parton distributions incorporating QED contributions". In: *The European Physical Journal C* 39.2 (Feb. 2005), pp. 155–161. ISSN: 1434-6052. DOI: 10.1140/epjc/s2004-02088-7. arXiv: hep-ph/0411040 [hep-ph].

[213] Valerio Bertone et al. "On the impact of lepton PDFs". In: *Journal of High Energy Physics* 2015.11 (Nov. 2015). ISSN: 1029-8479. DOI: 10.1007/jhep11(2015)194. arXiv: 1508.07002 [hep-ph].

[214] Daniel de Florian, Germán F. R. Sborlini, and Germán Rodrigo. "QED corrections to the Altarelli–Parisi splitting functions". In: *The European Physical Journal C* 76.5 (May 2016). ISSN: 1434-6052. DOI: 10.1140/epjc/s10052-016-4131-8. arXiv: 1512.00612 [hep-ph].

[215] A. D. Martin and M. G. Ryskin. "The photon PDF of the proton". In: *The European Physical Journal C* 74.9 (Sept. 2014). ISSN: 1434-6052. DOI: 10.1140/epjc/s10052-014-3040-y. arXiv: 1406.2118 [hep-ph].

[216] Aneesh Manohar et al. "How Bright is the Proton? A Precise Determination of the Photon Parton Distribution Function". In: *Physical Review Letters* 117.24 (Dec. 2016). ISSN: 1079-7114. DOI: 10.1103/physrevlett.117.242002. arXiv: 1607.04266 [hep-ph].

[217] Aneesh V. Manohar et al. "The photon content of the proton". In: *Journal of High Energy Physics* 2017.12 (Dec. 2017). ISSN: 1029-8479. DOI: 10.1007/jhep12(2017)046. arXiv: 1708.01256 [hep-ph].

[218] Valerio Bertone et al. "Illuminating the photon content of the proton within a global PDF analysis". In: *SciPost Physics* 5.1 (July 2018). ISSN: 2542-4653. DOI: 10.21468/scipostphys.5.1.008. arXiv: 1712.07053 [hep-ph].

[219] A. Denner et al. "Predictions for all processes $e^+e^- \to$fermions+$\gamma$". In: *Nuclear Physics B* 560.1-3 (Nov. 1999), pp. 33–65. ISSN: 0550-3213. DOI: 10.1016/s0550-3213(99)00437-x. arXiv: hep-ph/9904472 [hep-ph].

[220] A. Denner et al. "Electroweak corrections to charged-current fermion processes: Technical details and further results". In: *Nuclear Physics B* 724.1-2 (Sept. 2005), pp. 247–294. ISSN: 0550-3213. DOI: 10.1016/j.nuclphysb.2005.06.033. arXiv: hep-ph/0505042 [hep-ph].

[221] A. Denner and S. Dittmaier. "The complex-mass scheme for perturbative calculations with unstable particles". In: *Nuclear Physics B - Proceedings Supplements* 160 (Oct. 2006), pp. 22–26. ISSN: 0920-5632. DOI: 10.1016/j.nuclphysbps.2006.09.025. arXiv: hep-ph/0605312 [hep-ph].

[222] Ansgar Denner. "Techniques for calculation of electroweak radiative corrections at the one loop level and results for W physics at LEP-200". In: *Fortsch. Phys.* 41 (1993), pp. 307–420. DOI: 10.1002/prop.2190410402. arXiv: 0709.1075 [hep-ph].

[223] W. Hollik. *Electroweak Theory*. 1996. arXiv: hep-ph/9602380 [hep-ph].

[224] Matteo Cacciari and Nicolas Houdeau. "Meaningful characterisation of perturbative theoretical uncertainties". In: *JHEP* 09 (2011), p. 039. DOI: 10.1007/JHEP09(2011)039. arXiv: 1105.5152 [hep-ph].

[225] M. Tanabashi et al. "Review of Particle Physics". In: *Phys. Rev. D* 98.3 (2018), p. 030001. DOI: 10.1103/PhysRevD.98.030001. URL: http://pdg.lbl.gov/2018.

[226] Stefan Kallweit, private communication.

[227] C. Patrignani et al. "Review of Particle Physics". In: *Chin. Phys. C* 40.10 (2016), p. 100001. DOI: 10.1088/1674-1137/40/10/100001. URL: http://pdg.lbl.gov/2016.

[228] J. Alwall et al. "The automated computation of tree-level and next-to-leading order differential cross sections, and their matching to parton shower simulations". In: *Journal of High Energy Physics* 2014.7 (July 2014). ISSN: 1029-8479. DOI: 10.1007/jhep07(2014)079. arXiv: 1405.0301 [hep-ph].

[229] A. Banfi et al. "Optimisation of variables for studying dilepton transverse momentum distributions at hadron colliders". In: *The European Physical Journal C* 71.3 (Mar. 2011). ISSN: 1434-6052. DOI: 10.1140/epjc/s10052-011-1600-y. arXiv: 1009.1580 [hep-ex].

[230] M. Vesterinen and T.R. Wyatt. "A novel technique for studying the Z boson transverse momentum distribution at hadron colliders". In: *Nuclear Instruments and Methods in Physics Research Section A: Accelerators, Spectrometers, Detectors and Associated Equipment* 602.2 (Apr. 2009), pp. 432–437. ISSN: 0168-9002. DOI: 10.1016/j.nima.2009.01.203. arXiv: 0807.4956 [hep-ex].

[231] Markus A. Ebert et al. *Drell-Yan $q_T$ Resummation of Fiducial Power Corrections at $N^3LL$*. 2020. arXiv: 2006.11382 [hep-ph].

[232] Ansgar Denner et al. "Low-virtuality photon transitions $\gamma^* \to f\bar{f}$ and the photon-to-jet conversion function". In: *Physics Letters B* 798 (Nov. 2019), p. 134951. ISSN: 0370-2693. DOI: 10.1016/j.physletb.2019.134951. arXiv: 1907.02366 [hep-ph].

[233] Rabah Abdul Khalek et al. "Phenomenology of NNLO jet production at the LHC and its impact on parton distributions". In: (May 2020). arXiv: 2005.11327 [hep-ph].

[234] Lance J. Dixon. "A brief introduction to modern amplitude methods". In: *Theoretical Advanced Study Institute in Elementary Particle Physics: Particle Physics: The Higgs Boson and Beyond*. 2014, pp. 31–67. DOI: 10.5170/CERN-2014-008.31. arXiv: 1310.5353 [hep-ph].

[235] Henriette Elvang and Yu-tin Huang. *Scattering Amplitudes*. 2013. arXiv: 1308.1697 [hep-th].

[236] Nima Arkani-Hamed, Tzu-Chen Huang, and Yu-tin Huang. *Scattering Amplitudes For All Masses and Spins*. 2017. arXiv: 1709.04891 [hep-th].

[237] Stephen J. Parke and T.R. Taylor. "An Amplitude for $n$ Gluon Scattering". In: *Phys. Rev. Lett.* 56 (1986), p. 2459. DOI: 10.1103/PhysRevLett.56.2459.

[238] Adrian Signer. "One-loop corrections to five-parton amplitudes with external photons". In: *Physics Letters B* 357.1-2 (Aug. 1995), pp. 204–210. ISSN: 0370-2693. DOI: 10.1016/0370-2693(95)00905-z. arXiv: hep-ph/9507442 [hep-ph].

[239] Adrian Signer. "Helicity method for next-to-leading order corrections in QCD". PhD thesis. ETH Zürich, 1995.

[240] Zvi Bern, Lance Dixon, and David A. Kosower. "One-loop amplitudes for e+e− to four partons". In: *Nuclear Physics B* 513.1-2 (Mar. 1998), pp. 3–86. ISSN: 0550-3213. DOI: 10.1016/s0550-3213(97)00703-7. arXiv: hep-ph/9708239 [hep-ph].

[241] Zoltan Kunszt, Adrian Signer, and Zoltán Trócsányi. "One-loop helicity amplitudes for all $2 \to 2$ processes in QCD and N = 1 supersymmetric Yang-Mills theory". In: *Nuclear Physics B* 411.2-3 (Jan. 1994), pp. 397–442. ISSN: 0550-3213. DOI: 10.1016/0550-3213(94)90456-1. arXiv: hep-ph/9305239 [hep-ph].

[242] Zvi Bern, Abilio De Freitas, and Lance Dixon. "Two-Loop Helicity Amplitudes for Gluon-Gluon Scattering in QCD and Supersymmetric Yang-Mills Theory". In: *Journal of High Energy Physics* 2002.03 (Mar. 2002), pp. 018–018. ISSN: 1029-8479. DOI: 10.1088/1126-6708/2002/03/018. arXiv: hep-ph/0201161 [hep-ph].

[243] C. Anastasiou et al. "Two-loop QCD corrections to massless quark–gluon scattering". In: *Nuclear Physics B* 605.1-3 (July 2001), pp. 486–516. ISSN: 0550-3213. DOI: 10.1016/s0550-3213(01)00195-x. arXiv: hep-ph/0101304 [hep-ph].

[244] Zvi Bern, Abilio De Freitas, and Lance J. Dixon. "Two loop helicity amplitudes for quark gluon scattering in QCD and gluino gluon scattering in supersymmetric Yang-Mills theory". In: *JHEP* 06 (2003). [Erratum: JHEP 04, 112 (2014)], p. 028. DOI: 10.1088/1126-6708/2003/06/028. arXiv: hep-ph/0304168.

[245] E.W. Nigel Glover and Maria Elena Tejeda-Yeomans. "Two-loop QCD helicity amplitudes for massless quark-massless gauge boson scattering". In: *Journal of High Energy Physics* 2003.06 (June 2003), pp. 033–033. ISSN: 1029-8479. DOI: 10.1088/1126-6708/2003/06/033. arXiv: hep-ph/0304169 [hep-ph].